DISSERTATION

MULTIPHOTON SPATIAL FREQUENCY MODULATED IMAGING

Submitted by

Keith Wernsing

Department of Electrical and Computer Engineering

In partial fulfillment of the requirements

For the Degree of Doctor of Philosophy

Colorado State University

Fort Collins, Colorado

Summer 2023

Doctoral Committee:

Advisor: Randy Bartels

Jeff Squier
Jesse Wilson
Thomas Borch

ABSTRACT

MULTIPHOTON SPATIAL FREQUENCY MODULATED IMAGING

Far-field optical microscopy has seen significant development in the last 20 years in its ability to resolve specimen information beyond the diffraction limit. However, nearly all of these super-resolution techniques are predicated on the use of fluorescence as the contrast mechanism in the sample. While the variety of fluorophores available for labeling a sample are a widely-utilized tool, in many instances non-fluorescent contrast mechanisms also provide valuable information. Multiphoton microscopy is one route to probing non-fluorescent contrast mechanisms. It has the benefit of sampling multiple contrast mechanisms at once, including second- and third-harmonic generation and Raman vibrational characteristics, as well as autofluorescence and labeled fluorescence. However, development of super-resolving techniques for coherent scattering processes like harmonic generation or coherent Raman excitation has lagged behind that of incoherent scattering processes like fluorescence.

In this work I present the first technique to simultaneously enhance resolution in both real-state (e.g., fluorescence) and virtual-state (e.g. harmonic generation) molecular excitation mechanisms, known as multiphoton spatial-frequency modulated imaging (MP-SPIFI). Standard SPIFI works by projecting spatial cosine patterns onto the sample and gathering object spatial frequency information. Multiphoton SPIFI generates harmonics of these cosine patterns and therein gathers information beyond the frequency passband of the microscope. We demonstrate our initial results with two-photon fluorescence and SHG. An extensive model is built describing the super-resolved image formation process. We then present a method for extending the native, 1D resolution enhancement into two dimensions for an isotropic enhancement. Finally, we present development of two femtosecond, amplified pulsed laser sources tailored to boost SNR in multiphoton processes, through parabolic pulse amplification, and

chirped pulse fiber broadening, in order to deliver the high average power & high peak power required by MP-SPIFI for driving nonlinear processes across a line-focus geometry.

ACKNOWLEDGEMENTS

I would first like to thank my advisor, Randy Bartels, a walking encyclopedia of optics and fountain of ideas, for the opportunity to learn in rich detail the two fields of microscopic imaging and ultrafast optics, and for his practical guidance in developing, modeling, and communicating scientific ideas.

I would also like to thank my committee members, Jeff Squier, Jesse Wilson, and Thomas Borch, for their support and encouragement during my graduate studies. In addition, Dan Kane of Mesa Photonics has been a big support in this process.

I am very grateful for my colleagues in the Bartels lab. First of all, thank you to Jeffrey Field, a good friend and mentor in the field of nonlinear microscopy. My fellow students in the Bartels lab - David Winters, David Smith, Scott Domingue, Patrick Stockton, and Robby Stokoe - have provided stimulating discussions, encouragement, and helped to keep things light. Many thanks to Scott, for his mentorship in femtosecond fiber laser development. I am also grateful for the work of Philip Schlup, Greg Futia, and David Winters, which laid a foundation for that which is presented here.

Finally, I would also like to extend a huge thank you to my family. My children Elizabeth, Nathaniel and Josephine amaze me and help me truly enjoy the day to day moments in life. Many extended family members have helped us out significantly over the years. And the biggest thank you of all is to my wife Sarah, a kind and true soul, for partnering with me on this adventure.

TABLE OF CONTENTS

LIST OF TABLES

LIST OF FIGURES

CHAPTER 1

INTRODUCTION: NEW TOOLS FOR NONLINEAR, LABEL-FREE MICROSCOPY

The optical microscope is an indispensable tool for the modern biologist. In its most basic form, it provides a simple window into the micron-scale spatial organization in organisms. In the dozens of advanced instruments currently available, the biologist can select a tool for its emphasis on certain features, such as resolution or depth-resolving capability. The physics underlying electromagnetic wave propagation through a material provide a rich toolbox for measuring various qualities of the sample. Variations in optical phase, amplitude, polarization, and propagation direction can be read out from the collected signal, and converted into information about the sample. Moreover, light can be converted into new frequencies, or colors, by the sample, which can then separated from the incident field with spectral filters. For each variation in the collected field just mentioned, a handful of different physical mechanisms could be the underlying cause, and therefore it is important to understand which process is being generated, and how to optimize the corresponding signal.

A wealth of human knowledge has been generated up to this point through the measurement of two particular contrast mechanisms: transmitted intensity (known as 'wide-field' or 'bright field' microscopy) and fluorescence intensity. The former corresponds to the standard, historical microscope, still widely used today. The latter is a more recent phenomenon, undergoing intense development over the last 50 years. These techniques require only simple optical setups for basic measurements (the complexity of the objective lens being taken for granted), and have formed the backbone of biological imaging for the past few decades.

Why has fluorescence microscopy, in particular, become the predominant biological imaging tool? One reason has to do with its ease of use. Fluorescent signals are spectrally separated from the excitation light due to the Stokes shift in the molecule, leading to high contrast images thanks to the development of spectral filters with astounding out-of-band rejection, often

leaking only 1 part in a million (OD 6). Converting a basic wide-field microscope into a fluorescence microscope can be as easy as installing in-line spectral filters on the excitation & detection beam paths, in order to enforce the spectral separation between illumination & detection frequencies.

A second reason has to do with specificity. Significant work over many decades (and resulting in many Nobel prizes) has produced a bevy of fluorescent dyes and proteins, such that by dying or transfecting a specimen, the biologist can specifically label various microscopic structures with tailor-made fluorophores. This allows for multicolored images with structural and molecular specificity [1].

Third, fluorescence microscopy has been the primary contrast mechanism in the wide development of resolution-enhancing tools. The confocal microscope is a widely-used workhorse instrument primarily used for out-of-focus rejection, which can also give a modest improvement in resolution of up to $\approx \sqrt{2}$ in practical setups [2, 3]. Structured illumination microscopy returns a lateral resolution improvement of 2x [4]. Beyond this, 10x improvements have been demonstrated with point spread function engineering strategies like STED [5, 6], or with statistical localization strategies such as PALM [7, 8] & STORM [9]. These 'super-resolution' approaches, loosely defined here as those with resolution improvements 2x and above, are all predicated on the use of a contrast mechanism that responds only to the intensity of illumination light, as opposed to the underlying electric field, and were developed with fluorescence in mind as that contrast agent.

However, a significant disadvantage of transmission and fluorescence imaging is the intensive sample preparation required. Thin slices are needed to minimize scattering, which would otherwise present a scrambled picture of emitted spatial positions upon recording at the camera. However, very thin slices can be practically transparent. Therefore, one must resort to a means of enhancing contrast. In brightfield microscopy, for example, the standard practice in pathology for examining cancerous tissue is to extract a biopsy, slice it into sections, fix it with wax on flat glass slide, dissolve the wax, and then apply an H&E stain to generate the contrast

(a practice that has been in use for 100 years). In fluorescence microscopy, as discussed above, most research biologists use some form of applied fluorescent contrast, which involves conjugating fluorescent dyes or breeding organisms with genetically modified fluorescent proteins. Indeed, actively labeling specific structures with stains or fluorophores in order to achieve the desired structural specificity in the image recording process comes with the significant cost of altering the biology from its natural state. Therefore, despite the wealth of human knowledge gained by using these preparation techniques, they cannot make the leap into *in vivo* applications where the natural form of the sample must be preserved to the highest degree possible - especially so for human medicine. For this reason, there is great interest in the development of *label-free* biological microscopy.

1.1 Label-Free Optical Microscopy

Despite the ubiquity of bright-field and fluorescence imaging, a large assortment of contrast mechanisms exist which exploit native contrast mechanisms within the sample. For example, variations in optical phase, polarization, Raman scattering, and harmonic generation (HG) across a sample can each be measured to provide informative spatial maps of a sample. Along with native fluorescence from molecules such as NADH and FAD, these techniques comprise a broad paradigm known as *label-free* imaging. By relaxing the requirements of sample preparation, label-free techniques open up important pathways in research and medicine. By avoiding dyes, stains,and transfected organisms, freshly excised *ex vivo* biological matter can be studied in a more natural and/or timely state. Perhaps most importantly, label-free imaging enables the important goal of minimally invasive *in vivo* imaging [10–13].

One tradeoff with label-free microscopy, however, is that the complexity is often shifted from sample preparation toward the instrumentation and data processing (wherein the instrumentation complexity includes both the illumination source and the imaging optics). Nevertheless, tremendous progress has been made in developing many label-free techniques into viable, and in some cases, clinical imaging strategies. Below, I briefly list some of the most important methods to date:

Table 1.1: A brief list of endogenous optical contrast mechanisms used in various forms of microscopy.

Linear Excitation:	Nonlinear Excitation:
Spontaneous Raman	Coherent Raman Scattering
Phase Imaging	Harmonic Generation
Polarization Resolved	Multiphoton Autofluorescence
Optical Coherence Tomography	

1.1.1 Linear Excitation Contrast Mechanisms

Linear excitation mechanisms take place when the light-matter interaction responds in a linear fashion to the input field or input intensity. An important distinction must be made between coherent and incoherent processes. In an incoherent process, the sample responds to the illumination intensity - that is, the photon density. Illumination photons are absorbed, and if the relaxation process is radiative, photons are emitted with random direction, phase, and polarization. In a coherent process, the sample responds to the illumination electric field. The field (or photon flux) measured after the sample is coherent in that it retains a direction, polarization, and defined phase relationship across its spatial and/or temporal extent.

Phase imaging and polarization-resolved imaging are rather straightforward, as they measure changes in the optical phase delay or polarization state induced by passage through the sample [11]. As phase information is lost upon photoelectron conversion at optical detectors, due to the rapid phase oscillation period (a few fs) relative to electron time-scales (ps), measuring optical phase delay must be achieved interferometrically, by measuring the signal field with a reference field at the camera.

Optical coherence tomography (OCT) has found wide use in the ophthalmology community, and has rapidly progressed into a commercially available, clinical tool. The novelty of OCT is its use of coherence length as a contrast mechanism, a rarely-used feature in optical microscopy. Broadband light has a coherence length on the order of a few microns, and can only produce interference with a reference broadband field if their optical path lengths differ by less than the coherence length. Therefore, by scanning the path length of a reference field,

and interfering it with backscattered light coming from a multitude of biological layers, one can map out the depth profile of the sample. This can also be performed by synthetic broadband illumination with a swept source.

Spontaneous Raman scattering probes the atomic bonds within molecules by depositing a bit of energy into a molecule and exciting various vibrational energy states. The excited vibrational energies can be determined optically by measuring the spectrum of inelastically scattered photons while illuminating with a continuous wave (CW) source, and computing the difference in photon energy between excitation source and scattered light. Raman vibrations allow for molecular specificity because molecular structure is unique, and therefore the strength and frequency of vibrational oscillation between adjacent atomic nuclei varies with their nuclear size, proximity, and orientation.

1.1.2 Non-Linear Excitation Contrast Mechanisms

A particular subset of label-free contrast mechanisms are the result of coherent *nonlinear* scattering. In this case, the incident field is localized in time in the form of a pulse, and the resulting high intensity drives the sample's polarizability nonlinearly. This results in incident energy that is scattered into new optical frequencies. Harmonic generation (HG) and coherent Raman scattering (CRS) are common examples of coherent nonlinear scattering contrast mechanisms used in label-free imaging and spectroscopy. Second harmonic generation (SHG) is commonly used to visualize collagen proteins, which form the structure of the extracellular matrix [14, 15]. Third harmonic generation (THG) responds to changes in the local index of refraction, and is used to map boundary layers, for example, between lipids and surrounding cytoplasm [16]. Molecular Raman vibrations are well-known for their ability to provide spectroscopic signatures of the illuminated region [17, 18].

Certain label-free imaging modalities are easily multiplexed together. Multiphoton laser scanning microscopy (MP-LSM) using focused femtosecond laser pulses, which are rapidly scanned across a sample to form an image, can induce multiple nonlinear processes at once, such as SHG, THG, and two- and three-photon excitation fluorescence (2PEF, 3PEF) of aut-

ofluorophores [19]. The signal from these contrast mechanisms can be easily separated with dichroic filters and directed to individual single-pixel detectors, such as photomultiplier tubes (PMTs). Due to the relatively low cost of PMTS and other single pixel detectors, compared to scientific cameras used in wide-field detection, it is much more feasible to probe multiple contrast mechanisms at once. If one takes the extra step of generating a pulse pair, then coherent Raman scattering can be probed as well. Clever implementations of label-free multiplexed MP-LSM have recently allowed for novel applications like intraoperative monitoring of human cancerous tissue during surgery [20].

MP-LSM is also widely celebrated for its ability to penetrate through scattering media. Utilizing near-infrared excitation wavelengths, where tissue is typically less scattering and absorbing, combined with the ballistic gating mechanism required for a multiphoton interaction [21,22] imaging depths have exceeded 4-6 scattering lengths, with demonstrations through 1mm of murine brain tissue, both *ex vivo* and *in vivo* [23,24].

1.2 Extending Specificity and Super-Resolution to Label-Free Contrast Mechanisms

Despite intense development and impressive results thus far, many label-free contrast mechanisms still lack some of the fantastic developments enjoyed by fluorescence imaging. In particular, the advent of far-field super-resolution microscopy over the last 25 years has been largely predicated on fluorescence contrast with engineered fluorophores. (While native fluorophores like NADH and FAD can in principle be resolved with modern SR techniques, they aren't as photostable as the engineered fluorophores developed to undergo thousands of absorption & emission cycles before bleaching out).

Moreover, moving away from the specific labeling of molecular species with fluorescent tags has required other methods of imaging with molecular specificity. Raman vibrational spectroscopic imaging has long been targeted for this effort, as it is based on the molecular vibrational frequencies of molecules, with each molecule having a unique set of vibrational frequencies. However, Raman signals are often very weak, and therefore significant effort has gone into developing coherent Raman scattering in the focus of a microscope objective. To date, CARS

and SRS have produced molecular images with high sensitivity in the mid-to-high wavenumber region of the Raman spectrum, but a high-sensitivity technique is still needed for the low-wavenumber region.

The current benefits of multiphoton microscopy - deep tissue, label-free, multimodal signals - would be significantly enhanced with the advancement of far-field super-resolution methods beyond fluorescence. Ideally, an SR method would provide resolution enhancement across both coherent and incoherent nonlinear scattering mechanisms. Two-photon excitation fluorescence STED [25] and SIM have been demonstrated [26, 27] using adaptations of these standard SR techniques. However, only a few publications have presented evidence [28, 29] or put forth ideas [30] for coherent nonlinear scattering super-resolution.

It was mentioned that label-free modalities often place a higher burden on the optical instrumentation used for imaging. This is especially true for the nonlinear excitation mechanisms, which require pulsed laser sources. Pulsed sources are more complicated to build, and require great care in the management of pulse dispersion through an optical system in order to generate a high quality (high peak power) excitation at the sample. There is a need to develop both higher average power and higher peak power pulsed laser sources that can offset scattering losses, and allow for extended illumination geometries like line-focus or defocused-point excitation schemes. Ideally, these sources have center wavelengths that are situated in low-scattering windows for biological tissues.

1.3 Super-Resolved Far-Field Optical Microscopy

Super-resolution has made a dramatic impact on far-field optical microscopy since the early 2000's. Since Ernst Abbe introduced the standard recipe for microscope resolution in the 1870's [31–33], microscope makers had been constrained to the resolution limit given by $d = \lambda/2NA$. This simple formula allows for three means of optimization: decreasing the wavelength λ, or increasing the numerical aperture of the objective lens through its two parameters, $NA = n\sin(\theta)$, where n the refractive index of the immersion medium between lens and sample, and θ is the angle between the optic axis and the most steeply inclined ray emanating from the sample that

is captured by the lens. For many years, this formula was considered something akin to a law in optical microscopy.

However, conceptual publications in the mid-1990's showed that optical physicists were reframing this law into a mere barrier that represented the limiting case under conventional illumination and detection [5, 7, 34]. Within a few years, a startling number of techniques had demonstrated clever circumventions of the resolution limit set by diffraction, as framed by Abbe all those years ago. Techniques like stimulated emission depletion (STED) microscopy [6], structured illumination microscopy (SIM) [4, 35], photo-activated localization microscopy (PALM) [8], stochastic optical reconstruction microscopy (STORM) [9], and ground state depletion (GSD) microscopy [36] rapidly reframed the concept of what was possible with optical far-field microscopy. The impact of this work resulted in the Nobel Prize in Chemistry in 2014.

Broadly speaking, these super-resolution (SR) techniques fall into two classes. The first approach uses controlled spatial patterns of illumination in order to isolate signal generation to sub-diffraction-limited spatial sizes. In STED, a point-scanning technique, a standard diffraction limited TEM00 focal spot is reduced in size through the clever use of an overlapping donut beam, which de-excites molecules on the periphery of the focus and therefore generates a sub-diffraction-limited focal volume of fluorescing molecules. Structured illumination microscopy (SIM) [4] is a wide field technique that projects a single spatial frequency across a sample at various orientations and phases, and computationally achieves a 2x resolution improvement. The second class of techniques, dubbed localization microscopy, is based on consideration of the sample as composed of discrete molecules, which though embedded in an ensemble, can be individually and sequentially made to turn on, give signal, and turn off. Using standard wide-field illumination, each molecule's individual contribution to a wide-field image is precisely and sequentially pinpointed. Then, a single composite image is formed of all individual emitters. This class of techniques was made possible by the advent of photo-switchable fluorescent probes, which lie dormant until activated by a certain optical wavelength. After that, they can be regularly excited to fluoresce, until they are not needed anymore, and are switched off. The

precision of localization is based on the number of photons obtained from each molecule, and the number of frames of acquisition for determining the mean location.

Despite their differences, all of these techniques employ a single unifying feature - their reliance on the ability to manipulate the real electronic states of particular signal molecules. In fact, nearly all SR techniques to date presume a fluorescent signal generated from the sample, or at least require a real-state electronic excitation (e.g., absorption). This is because the resolution-enhancing schemes are implemented by controlling the optical intensity at the sample, designed with the foreknowledge that these incoherent scattering processes are only sensitive to the overall intensity of the illumination light. While their applicability has dovetailed nicely with the ubiquity of fluorescent imaging in the life sciences, it turns out that they cannot be applied to coherent scattering processes.

1.4 This Dissertation

The present situation motivates a need for tools that can probe endogenous, coherent contrast mechanisms with greater spatial resolution, and ideally, with molecular specificity. In this work I present a handful of developments serving to advance these capabilities in nonlinear microscopy. In particular, we present the first technique to uniformly enhance resolution in both real-state (e.g., fluorescence) and virtual-state (e.g. harmonic generation) molecular excitation mechanisms, known as multiphoton spatial-frequency modulated imaging (MP-SPIFI). In order to deliver the intensity required for driving nonlinear processes across a line-focusing geometry, I describe two fiber-based methods for generating high repetition rate, high peak power femtosecond pulse trains. An extensive model is built to describe the MP-SPIFI image formation process. Next, I demonstrate how to extract information from the multiple simultaneous images formed by MP-SPIFI microscopy, and subsequently combine this information to generate a composite image with a resolution enhancement approaching the theoretical limit of the technique. Finally, I demonstrate a method for extending the native, 1D resolution enhancement in MP-SPIFI into two dimensions for an isotropic enhancement.

1.4.1 Author Contribution Statement

This dissertation contains collaborative that was jointly performed by Keith Wernsing, Jeff Field, and Randy Bartels. At the end of chapter, contribution statements list the impact made by these contributors and others. Contributors are listed by the following initials: K.A.W. (Keith Wernsing), Jeff Field (J.J.F.), Randy Bartels (R.A.B.), David Winters (D.G.W.), Scott Domingue (S.R.D.), Alyssa M. Allende Motz (A.M.A.M.), Keith DeLuca (K.F.D.), Dean Levi (D.H.L.), Jennifer DeLuca (J.G.D.), Michael Young (M.D.Y.), and Jeff Squier (J.A.S.).

For the entirety of this project, R.A.B. acquired funding, provided laboratory resources, and supervised. R.A.B. and the doctoral committee provided editorial feedback for this dissertation. I would also like to gratefully acknowledge custom data acquisition software used in this work that was written by David Winters, Greg Futia, and Philip Schlup.

1.4.2 Permissions to Use Previously Published Work

Sections of this dissertation that contain text drawn from jointly published articles are noted at the conclusion of corresponding chapters. Material from Ref. [62], Ref. [64] and Ref. [99] is reprinted with permission from the publisher. The authors retain copyright to Ref. [51], and material from [51] is used with the implicit permission therein.

CHAPTER 2

FUNDAMENTALS OF IMAGING THEORY

2.1 Optical Wave Behavior from Maxwell's Equations

In this chapter a few basic building blocks of optical imaging theory are derived. The goal is to have these tools available for microscope design and analysis. Throughout this chapter, light is treated as an electromagnetic wave. This is in contrast to a geometric description using rays, or a quantum description using photons. We start with Maxwell's Equations in differential form:

$$\nabla \cdot \mathbf{D} = \rho \tag{2.1}$$

$$\nabla \cdot \mathbf{B} = 0 \tag{2.2}$$

$$\nabla \times \mathbf{E} = -\frac{\partial \mathbf{B}}{\partial t} \tag{2.3}$$

$$\nabla \times \mathbf{H} = \mathbf{J} + \frac{\partial \mathbf{D}}{\partial t} \tag{2.4}$$

The first equation, historically known as Gauss' Law, describes the electric flux density $\mathbf{D}$ due to static charge, ρ. The second equation dictates that magnetic flux density $\mathbf{B}$ is always zero, and therefore implies there is no such thing as a magnetic charge that can be isolated. The third equation, Faraday's Law, relates a time-varying magnetic flux $\mathbf{B}$ to a curling electric field $\mathbf{E}$. The fourth equation, Ampere's Law, relates a curling magnetic field $\mathbf{H}$ to the sum of electric current $\mathbf{J}$ and a time-varying electric flux density $\mathbf{D}$. The electric flux density is also known as the electric displacement field.

The $\mathbf{D}$ and $\mathbf{B}$ flux densities incorporate the electric and magnetic properties of materials, respectively. In general, materials can have an intrinsic magnetization, $\mathbf{M}$, and polarization, $\mathbf{P}$, which can vary with location in the material and are thus also vector fields. The following constitutive formulas relate the material properties $\mathbf{M}$ and $\mathbf{P}$ and the fields $\mathbf{H}$ and $\mathbf{E}$ to the flux densities:

$$\mathbf{B} = \mu_0 \mathbf{H} + \mu_0 \mathbf{M} \tag{2.5}$$

$$\mathbf{D} = \epsilon_0 \mathbf{E} + \mathbf{P} \tag{2.6}$$

The convention is to scale magnetization by μ_0, but to fold ϵ_0 into polarization. Electric current is related to the electric field through a medium's conductivity, σ:

$$\mathbf{J} = \sigma \mathbf{E} \tag{2.7}$$

The fields $\mathbf{D}$, $\mathbf{B}$, $\mathbf{E}$, and $\mathbf{H}$ can all vary in strength across various points in space and time, and therefore they have a 4-dimensional dependence, e.g. $\mathbf{E}(\mathbf{r}, t)$. Moreover, they can vary in spatial direction at each of those 4D points, and therefore they are best described mathematically as a vector field with 3 directional components, e.g. $\mathbf{E}(\mathbf{r}, t) = \mathsf{E}_x(\mathbf{r}, t)\hat{x} + \mathsf{E}_y(\mathbf{r}, t)\hat{y} + \mathsf{E}_z(\mathbf{r}, t)\hat{z}$ in a Cartesian coordinate system.

The scope of this work deals with electromagnetic wave propagation in the optical regime. Materials will be dielectrics at optical frequencies, and therefore we set free currents and magnetizations to zero. The electric field vector will be the main quantity of interest. Therefore we reformulate Maxwell's equations into an equation for the $\mathbf{E}$-field only. By setting $\mathbf{M}$ and $\mathbf{J}$ to zero, equations (2.3) and (2.4) can be rewritten:

$$\nabla \times \mathbf{E} = -\mu_0 \frac{\partial \mathbf{H}}{\partial t} \tag{2.8}$$

$$\nabla \times \mathbf{H} = \frac{\partial}{\partial t}(\epsilon_0 \mathbf{E} + \mathbf{P}) \tag{2.9}$$

Taking the curl of (2.8),

$$\nabla \times \nabla \times \mathbf{E} = -\mu_0 \frac{\partial}{\partial t}(\nabla \times \mathbf{H}) \tag{2.10}$$

and substituting (2.9) into (2.10),

$$\nabla \times \nabla \times \mathbf{E} = -\mu_0 \frac{\partial^2}{\partial t^2} (\epsilon_0 \mathbf{E} + \mathbf{P}) \tag{2.11}$$

Finally, we make use of the mathematical vector identity $\nabla \times \nabla \times \mathbf{A} = \nabla (\nabla \cdot \mathbf{A}) - \nabla^2 \mathbf{A}$ to recast (2.11) as:

$$\nabla (\nabla \cdot \mathbf{E}) - \nabla^2 \mathbf{E} = -\mu_0 \frac{\partial^2}{\partial t^2} (\epsilon_0 \mathbf{E} + \mathbf{P}) \tag{2.12}$$

In this work, we won't be concerned with free charge generating electric fields. Thus, we can use Maxwell's first equation (2.1) (Gauss' Law) with $\rho = 0$, simplifying (2.12) into something starting to resemble a wave equation:

$$\nabla^2 \mathbf{E} - \mu_0 \frac{\partial^2}{\partial t^2} (\epsilon_0 \mathbf{E} + \mathbf{P}) = 0 \tag{2.13}$$

When the medium responds in a linear fashion to an incident field, the polarization field is simply:

$$\mathbf{P} = \epsilon_0 \chi_e \mathbf{E} \tag{2.14}$$

where χ_e is the material's electric susceptibility, and in general is a matrix, for example, containing different responses along each axis in a biaxial crystal. In a homogeneous medium, such as amorphous glass, it is a scalar quantity. Physically, the electric susceptibility of a material is a measure of how strongly it responds to an incident electric field, $\mathbf{E}$. This can be derived from classical models that depict the ensemble of bound electrons in a static medium being driven about their mean location by an incident field [37, 38]. This moving charge generates radiation, $\mathbf{P}$, which together with the incident field $\mathbf{E}$ creates a delayed (or 'displaced') field $\mathbf{D}$ propagating through the medium. In optics, it is common to wrap the electric susceptibility χ_e into a relative permittivity ϵ_r, which is just a scaling against the permittivity of vacuum, ϵ_0. The total permittivity ϵ is then wrapped into the index of refraction:

$$\epsilon = \epsilon_0 \epsilon_r = \epsilon_0 \left(1 + \chi_e\right) \tag{2.15}$$

$$n = \sqrt{\epsilon} \tag{2.16}$$

Technically, n is defined as $n = \sqrt{\epsilon\mu}$, although for non-magnetic materials $\mu = 1$ and Eqn. (2.16) holds. The index of refraction is especially useful because it allows us to see that Maxwell's equations lead to a wave equation for the electric field in a dielectric medium:

$$\nabla^2 \mathbf{E} - \frac{n^2}{c^2} \frac{\partial^2 \mathbf{E}}{\partial t^2} = 0 \tag{2.17}$$

where the wave velocity is c/n in the medium. Although not shown here, Maxwell's equations dictate that the copropagating electric and magnetic fields oscillate in a direction transverse to the direction of propagation [37]. It often makes sense to choose a coordinate system to match the expected form of propagation in order to eliminate one of the three polarization directions for the field. For example, for beam-like propagation, a Cartesian system with the propagation direction set along z reduces the possible electric field components to E_x and E_y. For spherically expanding or converging waves, a spherical-polar coordinate system centered on the origin of those waves forces the radial field component E_ρ to zero. In cases where the electric field remains polarized in one direction only (e.g. $\hat{x}$), we can eliminate vector notation and use a scalar treatment.

A fundamentally important solution to the wave equation is the propagating plane wave:

$$\mathbf{E} = Re\left\{\mathbf{E_0} \mathrm{e}^{\mathrm{i}(\mathbf{k}\cdot\mathbf{r} - \omega t)}\right\} \tag{2.18}$$

which describes the field as a traveling time-harmonic plane wave, with a complex amplitude E_0 denoting magnitude and phase offset.

Another important solution occurs when we limit the electric field to a time-harmonic quantity, but let the spatial component remain general:

$$\mathbf{E} = Re\left\{\mathbf{E}(\mathbf{r})\mathrm{e}^{-\mathrm{i}\omega t}\right\} \tag{2.19}$$

Plugging this solution (2.19) into the wave equation (2.17), and exchanging the order of linear operations,

$$Re\left\{\nabla^2\mathbf{E}(\mathbf{r})\mathrm{e}^{-\mathrm{i}\omega t} - \frac{n^2}{c^2}\frac{\partial^2}{\partial t^2}\mathbf{E}(\mathbf{r})\mathrm{e}^{-\mathrm{i}\omega t}\right\} = 0 \tag{2.20}$$

We note that if the quantity inside the brackets is zero, then the real and imaginary parts must independently be zero. Therefore it is sufficient to find the solution to the term inside the brackets. The temporal derivative operator acting on this field yields $\partial^2/\partial t^2 \rightarrow -\omega^2$, and then the temporal phase cancels. The remaining field distribution is a function of space:

$$\nabla^2\mathbf{E}(\mathbf{r}) + \frac{n^2\omega^2}{c^2}\mathbf{E}(\mathbf{r}) = 0 \tag{2.21}$$

$$\left[\nabla^2 + k^2\right]\mathbf{E}(\mathbf{r}) = 0 \tag{2.22}$$

Equation (2.22) is the well-known the Helmholtz Equation. It is an important result because it governs the behavior of a monochromatic field in a homogeneous medium.

We note that we have chosen to represent the real-valued electric field in complex form, which is easier to work with in many regards. We can work with the complex field in this way so long as we undertake only linear operations upon it, and at the end take the real part of the solution to return the observable $\mathbf{E}$. For nonlinear operations upon the field, we must use the real-valued field $\mathbf{E}$ to obtain accurate results. For the remainder of this work, we will assume the field is a time-harmonic sinusoid as in Eqn. (2.19). Henceforth, we will simply use the complex field $\mathbf{E}$, with the implicit meaning that the real component of $\mathbf{E}$ must be selected in order to return to the observable field $\mathbf{E}$.

2.2 Optical Intensity

We will make use of the optical intensity throughout this work, especially in the focal region of a microscope where it is used to stimulate an object and generate a signal containing infor-

mation about the object. The intensity of an electromagnetic wave describes the power flux at a given surface. It is found by way of the Poynting vector, which is the result of applying the principle of energy conservation in Maxwell's Equations with Poynting's Theorem. The Poynting vector describes the direction of power flow in an electromagnetic wave via the cross-product between the electric and magnetic fields:

$$\mathbf{S}(\mathbf{r}, t) = \mathbf{E}(\mathbf{r}, t) \times \mathbf{H}(\mathbf{r}, t) \tag{2.23}$$

which describes the fact that power flows in a direction orthogonal to the plane defined by the electric and magnetic vectors. The Poynting vector has units of W / m^2, with the physical meaning of power flux through a surface. For time-harmonic fields where $\mathbf{E}$ is given by Eqn. (2.19) and, similarly, $\mathbf{H} = Re\left\{\mathbf{H}(\mathbf{r})e^{-i\omega t}\right\}$, the Poynting vector can be manipulated into the form:

$$\mathbf{S}(\mathbf{r}, t) = \frac{1}{2}\mathrm{Re}\left\{\mathbf{E}(\mathbf{r}) \times \mathbf{H}^*(\mathbf{r})\right\} + \frac{1}{2}\mathrm{Re}\left\{\mathbf{E}(\mathbf{r}) \times \mathbf{H}(\mathbf{r})e^{-i2\omega t}\right\} \tag{2.24}$$

where we see that the instantaneous power flux has a time-stationary component, and a component that oscillates at twice the optical frequency ω. In most cases of interest the time-averaged power flux is desired. Averaging the Poynting vector over one oscillation period gives

$$\langle \mathbf{S}(\mathbf{r}, t) \rangle_t = \frac{1}{T}\int_0^T \mathbf{S}(\mathbf{r}, t)\, \mathrm{d}t = \frac{1}{2}\mathrm{Re}\left\{\mathbf{E}(\mathbf{r}) \times \mathbf{H}^*(\mathbf{r})\right\} \tag{2.25}$$

The optical intensity is defined as the magnitude of the time-averaged Poynting vector:

$$I = \left| \langle \mathbf{S}(\mathbf{r}, t) \rangle_t \right| = \frac{1}{2}\left|\mathrm{Re}\left\{\mathbf{E}(\mathbf{r}) \times \mathbf{H}^*(\mathbf{r})\right\}\right| \tag{2.26}$$

Propagating electromagnetic waves in an isotropic medium are fundamentally transverse waves, with the **E** and **H** fields orthogonal to one another in the plane transverse to propagation direction. Therefore the sine term in the cross-product is unity, and we are left with the product of magnitudes:

$$\mathbf{E}(\mathbf{r}) \times \mathbf{H}^*(\mathbf{r}) = \left|\mathbf{E}(\mathbf{r})\right|\left|\mathbf{H}^*(\mathbf{r})\right| \sin\Theta = \left|\mathbf{E}(\mathbf{r})\right|\left|\mathbf{H}(\mathbf{r})\right| \tag{2.27}$$

E and **H** also maintain a constant amplitude ratio, and remain in phase, as they propagate. Using the relationships between field magnitudes $\left|\mathbf{H}\right| = \left|\mathbf{B}\right|/\mu$ and $\left|\mathbf{B}\right| = \left|\mathbf{E}\right|/c$, we can write the intensity in terms of the complex electric field only:

$$I = \frac{1}{2}\left|\mathbf{E}(\mathbf{r})\right|\left|\mathbf{H}(\mathbf{r})\right| = \frac{n\epsilon_0 c}{2}\left|\mathbf{E}(\mathbf{r})\right|^2 \tag{2.28}$$

The intensity, like the Poynting vector, measures power flux with SI units of $\mathrm{W/m^2}$. For a vector electric field **E**, the intensity is computed by taking the inner product of the vector field components. For simplicity in this work, we will often neglect the scaling terms $cn\epsilon_0/2$ and compute the intensity as $I = |\mathbf{E}|^2$.

2.3 The Fourier Transform

This dissertation will make frequent use of a powerful tool known as the Fourier transform. The Fourier transform is a way of examining the frequency content of some entity of interest - in our case, the electric field. It is like a library of sinusoids, and it compares the field of interest against each sinusoid in its library to determine, first, how much of each frequency exists in the field, and second, if the identified frequency has a shift (or delay) such that it's crests are shifted away from the zero location in the independent variable. The result is a complex number that varies with frequency, with the magnitude and phase corresponding to the amplitude and shift respectively. Mathematically, the Fourier transform takes the form of a projection. In terms of time and optical frequency, we have:

$$\mathbf{E}(\nu) = \int_{-\infty}^{\infty} \mathbf{E}(t)\mathrm{e}^{-\mathrm{i}2\pi\nu t}\mathrm{d}t \tag{2.29}$$

$$\mathbf{E}(t) = \int_{-\infty}^{\infty} \mathbf{E}(\nu)\mathrm{e}^{\mathrm{i}2\pi\nu t}\mathrm{d}\nu \tag{2.30}$$

Equation (2.29) is the Fourier transform from time to frequency, and equation (2.30) is the inverse Fourier transform from frequency to time. Often one prefers to work in angular fre-

quency, $\omega = 2\pi\nu$. While ν and t are true conjugate variables, one can transform between t and ω by modifying the Fourier transform relations to account for the scaling between ω and ν, using $\mathrm{d}\nu = \frac{1}{2\pi}\mathrm{d}\omega$. Following convention, we move the $1/2\pi$ scaling factor to the transform over time [38, 39]. The Fourier transform pair becomes:

$$\mathbf{E}(\omega) = \frac{1}{2\pi}\int_{-\infty}^{\infty} \mathbf{E}(t)\mathrm{e}^{-\mathrm{i}\omega t}\mathrm{d}t \tag{2.31}$$

$$\mathbf{E}(t) = \int_{-\infty}^{\infty} \mathbf{E}(\omega)\mathrm{e}^{\mathrm{i}\omega t}\mathrm{d}\omega \tag{2.32}$$

A spectrometer measures a quantity proportional to $|\mathbf{E}(\nu)|^2$, where phase information is lost, but the magnitude of each spectral component, or color, of the field is measured.

We may also make a similar transformation from space, $\mathbf{r}$, to spatial frequency $\mathbf{f_r}$ or angular spatial frequency $\mathbf{k}$. While $\mathbf{E}(\nu)$ has a nice physical meaning, spatial frequency in the Fourier transform can seem abstract. For sure, spatial frequencies exist in nature - think of the spacing of pickets along a fence, or the lines on a sheet of paper, or the rulings on a diffraction grating, all having the units of $1/m$. However, when using the Fourier transform, it is more intuitive to think of the spatial Fourier transform as mapping from space to direction. This concept will be explored more fully in Section 2.6.1. For now, we write out the spatial Fourier transform and inverse Fourier transform for space and spatial frequency:

$$\mathbf{E}(\mathbf{f_r}) = \int_{-\infty}^{\infty} \mathbf{E}(\mathbf{r})\mathrm{e}^{-\mathrm{i}2\pi\mathbf{f_r}\cdot\mathbf{r}}\mathrm{d}^3\mathbf{r} \tag{2.33}$$

$$\mathbf{E}(\mathbf{r}) = \int_{-\infty}^{\infty} \mathbf{E}(\mathbf{f_r})\mathrm{e}^{\mathrm{i}2\pi\mathbf{f_r}\cdot\mathbf{r}}\mathrm{d}^3\mathbf{f_r} \tag{2.34}$$

and for space and angular spatial frequency:

$$\mathbf{E}(\mathbf{k}) = \frac{1}{(2\pi)^3}\int_{-\infty}^{\infty} \mathbf{E}(\mathbf{r})\mathrm{e}^{-\mathrm{i}\mathbf{k}\cdot\mathbf{r}}\mathrm{d}^3\mathbf{r} \tag{2.35}$$

$$\mathbf{E}(\mathbf{r}) = \int_{-\infty}^{\infty} \mathbf{E}(\mathbf{k})\mathrm{e}^{\mathrm{i}\mathbf{k}\cdot\mathbf{r}}\mathrm{d}^3\mathbf{k} \tag{2.36}$$

Some authors prefer to write a transformed variable, such as $E(k)$, with a tilde or other such notation to denote its Fourier transformation and distinguish it from $E(r)$. However, in this work we will often utilize a multivariable field that has been transformed in some dimensions and not others, such as $E(f_x, f_y, z)$. Therefore, we will always use E for the field, and we will always write the dependent variables, except when it is obvious which variables are being treated.

2.4 The Electric Field as a Summation of Plane Waves

The total electric field with frequency ω at a location in space can be written as the sum of tilted plane waves present at that location. This is evident by the linearity principle - if a single plane wave (Eqn. (2.18)) solves the electric field wave equation (Eqn. (2.17)), then a linear sum of plane waves must also be a solution. Why would we write the total field this way? Since plane waves are mathematically easy to manipulate, this 'decomposition' of the total field is a powerful tool that enables easier computation of electric field propagation from one location to another. These locations can be transverse planes, like in an imaging system, or source points and focal points. This act of calculating monochromatic diffracting optical fields in a homogeneous medium is known as decomposing the initial electric field into its angular spectrum. The "angular spectrum" refers to a continuum of plane waves, each one propagating in a unique direction. The total field is composed of these plane waves propagating in all directions, where the variation in amplitude and phase of each plane wave is manipulated to generate the total field. Writing the field at a position $\mathbf{r} = (x, y, z)$ as a summation of plane waves takes the form:

$$E(\mathbf{r}, t) = \sum_j E_{0_j} e^{i\phi_j} \exp\{[i(\mathbf{k_j} \cdot \mathbf{r} - \omega t)]\} \tag{2.37}$$

Here, the j^{th} plane wave is propagating in a direction along the vector wavenumber $\mathbf{k_j}$. It has amplitude E_{0_j} and relative phase offset ϕ_j. These last two bits of information can be combined into the complex number $\tilde{E}_j = E_{0_j} e^{i\phi_j}$.

We note that we have written the field as a scalar quantity for simplicity, but in general it is a vector quantity. Maxwell's equations tell us that light is a transverse electromagnetic wave; thus

every propagating plane wave has a field amplitude $\mathbf{E_{0_j}}$ pointing in a direction transverse to its propagation direction along the vector wavenumber $\mathbf{k_j}$. When this amplitude points along one axis of the coordinate system, we can treat the field as a scalar quantity. However, when the direction of the transverse oscillation is projected onto a mixture of coordinate system directions, we must treat the field amplitude, and therefore the field itself, as a vector quantity. The vector electric field is written:

$$\mathbf{E}(\mathbf{r}, t) = \sum_j \tilde{\mathbf{E}}_\mathbf{j} \exp\{[\mathrm{i}(\mathbf{k_j} \cdot \mathbf{r} - \omega t)]\}, \tag{2.38}$$

where the scalar phasor $\tilde{E}_j$ has become a vector quantity $\tilde{\mathbf{E}}_\mathbf{j}$, where the amplitude and phase offset are projected onto the three axes of the coordinate system:

$$\tilde{\mathbf{E}} = E_{0_x} \mathrm{e}^{\mathrm{i}\phi_x} \hat{x} + E_{0_j} \mathrm{e}^{\mathrm{i}\phi_y} \hat{y} + E_{0_j} \mathrm{e}^{\mathrm{i}\phi_z} \hat{z} \tag{2.39}$$

Thus, more generally, the electric field can be described by a summation of plane waves of varying amplitude, direction, delay, and polarization.

The Fourier transform connection between space & the angular spectrum

When we write the total field in terms of plane wave components, we can immediately see a connection to the Fourier transform operation. This is because the complex form of propagating plane waves has the same form as a Fourier transform kernel. In the limit of moving from a discrete set $\mathbf{k_j}$ to a continuum of angular directions $\mathbf{k}$, we recognize the summation above becomes an (inverse) Fourier transform integral.

$$\mathbf{E}(\mathbf{r}, t) = \mathrm{e}^{-\mathrm{i}\omega t} \int_\mathbf{k} \tilde{\mathbf{E}}(\mathbf{k}) \mathrm{e}^{\mathrm{i}\mathbf{k}\cdot\mathbf{r}} \mathrm{d}^3\mathbf{k} \tag{2.40}$$

Therefore we can recognize the set of complex numbers $\tilde{\mathbf{E}}(\mathbf{k})$ as the Fourier transform of the spatial field given by $\mathbf{E}(\mathbf{k})$ in Equations (2.35) and (2.36). $\mathbf{E}(\mathbf{k})$ is simply a collection of complex numbers containing the amplitude and phase information for each angled plane wave in the spectrum. As such, the inverse relationship exists as well. Therefore in order to decompose a

given complex field into its constituent plane wave angular spectrum, we can simply take the spatial Fourier transform. In many cases, it is more convenient to decompose a given field into its angular spectrum representation with a Fourier transform, apply some operations to the field, and then reconstitute the field with an inverse Fourier transform.

Tapping into the rich toolset of Fourier transforms lends great power to the angular spectrum approach. For example, thus far, we have thought about the k variable as describing plane wave propagation directions. However, conjugate Fourier variables are often conceived of as frequencies. Therefore, in the literature, many people describe k as a "angular spatial frequency" and f_r as a "linear spatial frequency." Does this make physical sense? It turns out it does. As an anecdotal example, if you have two plane waves propagating in the $y = 0$ plane, one along the optic axis with direction $\mathbf{k} = (0, k_z)$ and the other at an angle with a direction (k_x, k_z), they will interfere to produce a sinusoidal intensity pattern with the spatial frequency $\cos(k_x x)$. Describing a field as a sum of spatial frequencies is a way of saying that we have used the Fourier transform to synthesize a field from a collection of angled plane waves.

2.5 Propagation Geometry

Before proceeding further, it is helpful to define our system geometry clearly. In many applications involving the propagation of light, there is a well-defined linear sense of direction, such as through a microscope or telescope, or along the trajectory of a free-space laser beam. In these systems, Cartesian or cylindrical coordinates are the natural choice. The convention is to define the z axis as the central direction of propagation, known as the optic axis.

In other situations, it is helpful to switch to a spherical-polar coordinate system in order to describe inwardly or outwardly propagating spherical waves to or from a source point. The spherical-polar system is the best fit for deriving the free-space Green's function due to a point radiator. We will utilize this coordinate system to describe high numerical aperture focusing into a concentrated focal volume.

This work is primarily focused on the spatiotemporal distribution of light propagating through a microscope imaging system. We will work primarily in the Cartesian coordinate system. Field

distributions in certain transverse planes will be the primary species of interest, or in thin volumes around these transverse planes.

The Helmholtz constraint

With the central axis of propagation defined along z, we can move forward to obtain an important result. By replacing the spatial field in the Helmholtz Equation (2.22) with it's three-dimensional Fourier transform,

$$\left[\nabla^2 + k^2\right] \int \mathbf{E}(\mathbf{f_r}) e^{i2\pi \mathbf{f_r}\cdot\mathbf{r}} d^3\mathbf{f_r} = 0 \tag{2.41}$$

and moving the operators inside the integral, we find:

$$\int \mathbf{E}(\mathbf{f_r}) e^{i2\pi \mathbf{f_r}\cdot\mathbf{r}} \left(-k_x^2 - k_y^2 - k_z^2 + k^2\right) d^3\mathbf{f_r} = 0 \tag{2.42}$$

Unless all spatial frequency components $\mathbf{E}(\mathbf{f_r})$ are zero, the term in brackets must equate to zero, and this allows us to write the axial spatial frequency k_z in terms of the wavenumber and lateral spatial frequencies:

$$k_z = \sqrt{k^2 - k_x^2 - k_y^2} \tag{2.43}$$

In a homogeneous medium with index n, the wavenumber k is $2\pi n/\lambda_0$, and thus we can recast k_z in terms of the vacuum wavenumber k_0 as:

$$k_z = \sqrt{n^2 k_0^2 - k_x^2 - k_y^2} \tag{2.44}$$

Recalling our assumption of a monochromatic field propagating in a homogeneous medium, see that knowledge of the optical wavelength λ_0, the medium index n, and the transverse spatial frequencies k_x and k_y serve to fully define the axial propagation magnitude k_z. This is known as the Helmholtz constraint.

2.6 Optical Field Propagation in a Homogeneous Medium (Diffraction)

The central question of diffraction in an optical apparatus with a Cartesian sense of direction is, if I know the transverse field at an arbitrary starting plane, can I predict the field in a subsequent transverse plane some distance farther down the optic axis? Now that we have shown that a Fourier decomposition over space results in an angular spectrum of plane waves, let us move forward to the next step: determining the field some distance downstream of the initial source plane. This is the essence of computing the optical phenomenon of diffraction.

2.6.1 Field Propagation using the Angular Spectrum

In order to compute the propagated field, let us return to the Helmholtz Equation (2.22). We recall that this was derived from Maxwell's equations under our assumptions of a linear, source-free, non-magnetic, uniform dielectric medium (such as air or glass), and under the additional assumption that the field is time-harmonic at an angular frequency ω. We will make use of a mixed-space form of the field, where the transverse dependence has been Fourier transformed, but the axial dependence remains a function of space:

$$\mathbf{E}(x,y,z) = \int\int \mathbf{E}(f_x,f_y,z)\mathrm{e}^{\mathrm{i}2\pi(f_x x+f_y y)}\mathrm{d}f_x\mathrm{d}f_y \tag{2.45}$$

Substituting Eqn. (2.45) into the Helmholtz Equation (2.22), we have:

$$\nabla^2\left[\int\int \mathbf{E}(f_x,f_y,z)\mathrm{e}^{\mathrm{i}2\pi(f_x x+f_y y)}\mathrm{d}f_x\mathrm{d}f_y\right] + k^2\left[\int\int \mathbf{E}(f_x,f_y,z)\mathrm{e}^{\mathrm{i}2\pi(f_x x+f_y y)}\mathrm{d}f_x\mathrm{d}f_y\right] = 0 \tag{2.46}$$

We can move the Laplacian operator ∇^2 and k^2 inside the integrals, and then drop the integration as the integrand must be zero. After evaluating the spatial second derivatives required by the Laplacian operator, $\nabla^2 = \frac{\partial^2}{\partial x^2} + \frac{\partial^2}{\partial y^2} + \frac{\partial^2}{\partial z^2}$, we have

$$\left[\frac{\partial^2\mathbf{E}}{\partial z^2} + \mathbf{E}(f_x,f_y,z)\left[-4\pi^2\left(f_x^2+f_y^2\right)\right] + k^2\mathbf{E}(f_x,f_y,z)\right]\mathrm{e}^{\mathrm{i}2\pi(f_x x+f_y y)} = 0 \tag{2.47}$$

which simplifies to a one-dimensional, second-order ordinary differential equation in z:

$$\frac{\partial^2 \mathbf{E}}{\partial z^2} + \left(k^2 - k_x^2 - k_y^2\right)\mathbf{E} = 0 \tag{2.48}$$

which has the solution:

$$\mathbf{E}\left(f_x, f_y, z\right) = \mathbf{E}\left(f_x, f_y, 0\right)\exp\left[\mathrm{i}\sqrt{k^2 - k_x^2 - k_y^2}\, z\right] = \mathbf{E}\left(f_x, f_y, 0\right)\exp\left[\mathrm{i}k_z z\right] \tag{2.49}$$

where we have recognized that $k^2 - k_x^2 - k_y^2 = k_z^2$ from the Helmholtz constraint (2.43). Equation (2.49) is a powerful result. It states that the transverse field at a position z along the optic axis can be computed exactly if we know the transverse field at some starting plane we designate as $z = 0$. The transfer function for propagation through a homogeneous medium, given by $\exp\left[\mathrm{i}\sqrt{k^2 - k_x^2 - k_y^2}\, z\right]$ is named the angular spectrum propagator:

$$\mathcal{H}\left(f_x, f_y, z\right) = \exp\left[\mathrm{i}k_z z\right] = \exp\left[\mathrm{i}\sqrt{k^2 - k_x^2 - k_y^2}\, z\right] \tag{2.50}$$

It is important to state that Eqn. (2.49) is valid at high numerical aperture propagation, or in other words, for fields with large propagation angles relative to the optic axis. One caveat, however, is that propagation is limited to spatial frequencies that obey the condition $k_x^2 + k_y^2 \leq k^2$. Otherwise, the argument of the exponential becomes real, signifying exponential decay of the initial field. In this way, propagation can be considered a low pass filter of transverse spatial frequencies.

Finally, by using Eqn. (2.49) in Eqn. (2.45), we see that the field at any arbitrary location (x, y, z) can be computed from an initial transverse field $\mathbf{E}(x, y, 0)$ and the angular spectrum propagator, $\mathcal{H}$, followed by inverse Fourier Transform:

$$\mathbf{E}(x, y, z) = \int\int \mathbf{E}\left(f_x, f_y, 0\right)\mathrm{e}^{\mathrm{i}2\pi\left(f_x x + f_y y + f_z z\right)}\mathrm{d}f_x \mathrm{d}f_y \tag{2.51}$$

The paraxial approximation

In the case of paraxial propagation, by which we mean the field is contained within small angles relative to the optic axis, the angular spectrum propagator can be simplified. We can rearrange the equation for k_z given by the Helmholtz constraint in Equation (2.43), and expand the square root in a Taylor series to first order:

$$k_z = k\sqrt{1-\frac{k_\perp^2}{k^2}} \approx k\left(1-\frac{1}{2}\frac{k_\perp^2}{k^2}\right) \tag{2.52}$$

The field propagator in Eqn. (2.50) with k_z given by Eqn. (2.52) becomes:

$$\mathcal{H}(k_\perp, z) = \mathrm{e}^{\mathrm{i}kz}\mathrm{e}^{-\frac{\mathrm{i}k_\perp^2}{2k}z} \tag{2.53}$$

The field propagator in this case is commonly referred to as the Fresnel propagator. In linear spatial frequency coordinates, where

$$f_z = \sqrt{n^2/\lambda_0^2 - f_\perp^2} \tag{2.54}$$

the Fresnel propagator is

$$\mathcal{H}\left(f_\perp, z\right) = \mathrm{e}^{\mathrm{i}kz}\mathrm{e}^{-\mathrm{i}\pi\frac{\lambda_0}{n}f_\perp^2 z} \tag{2.55}$$

The far-field approximation

Another important simplification of the general diffracted field in (2.51) occurs when we examine the field very far away from the source distribution in the plane $z = 0$.

Mandel and Wolf [39] derive a general solution to this integral for the case when $\mathbf{E}(x, y, z)$ is examined in the far field ($r \to \infty$). Mandel and Wolf derive their result both by the method of stationary phase, and by using Rayleigh's diffraction integral of the first kind, and show both results are equivalent. The method of stationary phase is simply a way of looking at the far-field, where sums of rapidly oscillating waves from different source points mostly cause total

destructive interference. However, for the non-zero field points, the method of stationary phase seeks a few "critical points" in the source plane that are generally responsible for constructive interference in the far-field. The resulting far-field expression is:

$$E_\infty(x,y,z) = -2\pi \mathrm{i} k \frac{z}{r} \frac{\mathrm{e}^{\mathrm{i}kr}}{r} E\left(k_x, k_y; z=0\right)_{k_x=\frac{kx}{r},\, k_y=\frac{ky}{r}} \tag{2.56}$$

where $k = 2\pi/\lambda$. Rearranging Eqn. (2.56), the mixed-space transverse field at $z = 0$ can be determined directly from it's far field under a coordinate scaling:

$$E\left(k_x, k_y; z=0\right) = \frac{\mathrm{i}}{2\pi k} \frac{r}{z} r \mathrm{e}^{-\mathrm{i}kr} E_\infty(x = r k_x/k,\, y = r k_y/k,\, z) \tag{2.57}$$

We also mention that using Eqns. (2.35) and (2.33), where $E\left(k_x, k_y\right) = 1/(2\pi)^2 E\left(f_x, f_y\right)$, the far field in terms of linear spatial frequency is:

$$E_\infty(x,y,z) = \frac{-\mathrm{i}}{\lambda} \frac{z}{r} \frac{\mathrm{e}^{\mathrm{i}kr}}{r} E\left(f_x, f_y; z=0\right)_{f_x=\frac{x}{\lambda r},\, f_y=\frac{y}{\lambda r}} \tag{2.58}$$

The paraxial far-field: Fraunhofer Diffraction

We next combine the paraxial and far-field approximations by constraining the far-field result $E_\infty(\mathbf{r})$ in (2.58) to transverse positions near the optic axis. This is equivalent to making the approximation $z \approx r$, where the distant spherical surface is essentially a plane at z, resulting in the Fraunhofer diffraction equation:

$$E_\infty(x,y,z) = \frac{\mathrm{e}^{\mathrm{i}kz}}{\mathrm{i}\lambda z} E\left(f_x, f_y; z=0\right)_{f_x=\frac{x}{\lambda z},\, f_y=\frac{y}{\lambda z}} \tag{2.59}$$

In the Fraunhofer regime, the transverse far-field is simply a scaled Fourier transform of the transverse source field $E(x,y,0)$. In other words, there is a direct map between source field direction and far field transverse position.

2.6.2 Field Propagation using the Fresnel Diffraction Integral

An alternative method of computing electric field propagation through a linear, homogeneous medium is by using the Fresnel diffraction integral. This method predates the Fourier representation of fields as used in the angular spectrum approach, and instead it works with fields in real space only. Like the angular spectrum approach, it computes solutions at various transverse planes of the optical system. References [40, 41] provide derivations of the Fresnel diffraction integral following the historical progression of work by Fresnel, Kirchhoff, Rayleigh, Sommerfeld, and others. In this section, I will instead show how the Fresnel Diffraction Integral can be derived using angular spectrum propagation.

For simplicity, let us assume a scalar field. As usual, we require that the field is propagating in a linear, homogeneous, non-magnetic dielectric medium. We also assume our field is monochromatic with a harmonic time dependence, as in (2.19). We seek to compute the field in a transverse plane at axial position z, downstream of our starting transverse plane at $z = 0$, where we desire a functional form for E at z that depends only on real-space transverse variables x and y. We denote the transverse coordinates in the starting plane (x_0, y_0), and in the downstream plane, (x_1, y_1). Using Eqn. (2.49) with the paraxial (Fresnel) approximation for k_z,

$$E(x_1, y_1) = \mathcal{F}^{-1}\left[\mathcal{F}\left[E(x_0, y_0)\right] \mathrm{e}^{\mathrm{i}k_z z}\right] \tag{2.60}$$

$$= \int_{f_x, f_y} \left[\int_{x_0, y_0} E(x_0, y_0) \mathrm{e}^{-\mathrm{i}2\pi[f_x x_0 + f_y y_0]} \mathrm{d}x_0 \mathrm{d}y_0\right] \mathrm{e}^{\mathrm{i}kz} \mathrm{e}^{-\mathrm{i}\pi\lambda f_x^2 z} \mathrm{e}^{\mathrm{i}2\pi[f_x x_1 + f_y y_1]} \mathrm{d}f_x \mathrm{d}f_y \tag{2.61}$$

Integrating first over f_x and f_y,

$$E(x_1, y_1) = \frac{\mathrm{e}^{\mathrm{i}kz}}{\mathrm{i}\lambda z} \int_{x_0, y_0} E(x_0, y_0) \, \mathrm{e}^{\frac{\mathrm{i}\pi}{\lambda z}\left[(x_0 - x_1)^2 + (y_0 - y_1)^2\right]} \mathrm{d}x_0 \mathrm{d}y_0 \tag{2.62}$$

and expanding the quadratic terms in the exponential,

$$E(x_1, y_1) = \frac{\mathrm{e}^{\mathrm{i}kz}}{\mathrm{i}\lambda z} \mathrm{e}^{\frac{\mathrm{i}\pi}{\lambda z}(x_1^2 + y_1^2)} \int_{x_0, y_0} E(x_0, y_0) \, \mathrm{e}^{\frac{\mathrm{i}\pi}{\lambda z}(x_0^2 + y_0^2)} \, \mathrm{e}^{-\mathrm{i}2\pi\left[\frac{x_1}{\lambda z} x_0 + \frac{y_1}{\lambda z} y_0\right]} \mathrm{d}x_0 \mathrm{d}y_0 \tag{2.63}$$

Equation (2.63) is the Fresnel diffraction integral. It computes the transverse field $E(x_1, y_1)$ at the plane z directly from the field $E(x_0, y_0)$ at $z = 0$, under the paraxial approximation. We can see that the solution takes the form of a Fourier transform of the product between $E(x_0, y_0)$ and a quadratic phase, with scaled conjugate variables $f_{x_0} = x_1/\lambda z$ and $f_{y_0} = y_1/\lambda z$.

The Fraunhofer Diffraction Integral

A simpler diffraction integral can be obtained when we examine the field close to the optic axis after it has propagated very far away, e.g. $z \to \infty$. Near the optic axis, x_0 and y_0 are small, and thus x_0^2/z and y_0^2/z terms are much smaller than x_0/z and y_0/z and $1/z$, and can safely be ignored. In physical terms, the wavefront curvature in both regions is taken to be nominally flat. This is the Fraunhofer diffraction regime, and the Fraunhofer diffraction formula is:

$$E(x_1, y_1, z) = \frac{e^{ikz}}{i\lambda z} \int_{x_0, y_0} E(x_0, y_0, 0)\, e^{-i2\pi\left[\frac{x_1}{\lambda z} x_0 + \frac{y_1}{\lambda z} y_0\right]} dx_0 dy_0 \tag{2.64}$$

$$= \frac{e^{ikz}}{i\lambda z} E(f_{x_0}, f_{y_0}, 0)_{f_{x_0} = \frac{x_1}{\lambda z},\, f_{y_0} = \frac{y_1}{\lambda z}} \tag{2.65}$$

which matches the result we obtained using the angular spectrum propagation method in Eqn. (2.59).

2.7 Optical Field Propagation in Simple Lens Systems

We now seek to model electric field behavior as it propagates through a simple lens system. We will first derive the effect of a simple lens on a paraxial field. Then, we will combine this with the results of Section 2.6 for propagation in a homogeneous medium in order to demonstrate the effects of lenses in the so-called $2f$ and $4f$ configurations, which form the basis of the microscopes discussed in this work.

2.7.1 Propagation through a thin lens

Rather than treating a lens with a simple ray trace utilizing Snell's law for refraction, we instead seek to compute the total phase accumulation at every transverse position (x, y) imparted by the lens. We will follow Goodman's treatment [41], and make the approximation that the lens is thin enough that we can ignore transverse displacements of the field as it propagates through

the lens from surface to surface. Thus, it is a simple matter of computing the total phase accumulation along z for every transverse position (x, y). We assume spherical surfaces, with front and back surfaces having radii of curvature R_1 and R_2, respectively. For the first surface, we assign transverse planes to the z locations where R_1 intersects the optic axis and where it intersects the system aperture (e.g. at $x = \pm 12.5$mm for a 25 mm diameter lens), with the distance between these planes d_1. We then do the same for the second spherical surface defined by R_2. Radii of curvature are positive if the sphere defining the surface has its centerpoint downstream (increasing z) of the point where the surface intersects the optic axis, or in other words, is a convex surface. We can segment the distance d_1 into two pieces: d_{1i} in the incident medium and d_{1g} in glass. We repeat this process for the second surface, $d_2 = d_{2g} + d_{2i}$, with the total distance $d = d_1 + d_2$. The glass thicknesses d_{1g} and d_{2g} are found with the help of the Pythagorean relationship. For convex or concave first surfaces,

$$\text{convex}: \quad d_{1g}(x,y) = d_1 - \left(R_1 - \sqrt{R_1^2 - (x^2+y^2)}\right) \qquad (R_1 > 0) \tag{2.66}$$

$$\text{concave}: \quad d_{1g}(x,y) = -R_1 - \sqrt{R_1^2 - (x^2+y^2)} \qquad (R_1 < 0) \tag{2.67}$$

where in the latter case, $-R_1$ was used for the absolute distance $|R_1|$ since $R_1 < 0$ in our convention. Repeating this analysis for the second surface,

$$\text{convex}: \quad d_{2g}(x,y) = d_2 - \left(-R_2 - \sqrt{R_2^2 - (x^2+y^2)}\right) \qquad (R_2 < 0) \tag{2.68}$$

$$\text{concave}: \quad d_{2g}(x,y) = R_2 - \sqrt{R_2^2 - (x^2+y^2)} \qquad (R_2 > 0) \tag{2.69}$$

The total phase accumulation along z for any given transverse position (x, y) is

$$\phi(x,y) = k_0 \left[n_i \, d_{1i}(x,y) + n_g \, d_{1g}(x.y) + n_g \, d_{2g}(x,y) + n_i \, d_{2i}(x.y) \right] \tag{2.70}$$

$$= k_0 n_i \left(d - d_g\right) + k_0 n_g d_g \tag{2.71}$$

where n_i and n_g are the indices of refraction of the incident medium and the glass, respectively. For lens diameters that are small relative to the lens radii of curvature, $x \ll R_1$ and $y \ll R_1$, and so we can perform a binomial expansion on the radical, $\sqrt{1-\frac{(x^2+y^2)}{R^2}} \approx 1-\frac{1}{2}\frac{(x^2+y^2)}{R^2}$. We note that when factoring R out of the radical for a negative surface radius, we must make sure to use $\sqrt{R^2} = -R$. With this approximation in hand, we can render the phase functions for various lens types. For example, a double convex lens has the phase accumulation

$$\phi(x,y) = k_0 n_g d - k_0 \left(n_g - n_i\right) \frac{x^2+y^2}{2}\left(\frac{1}{R_1} - \frac{1}{R_2}\right) \tag{2.72}$$

and a double concave lens has the phase accumulation

$$\phi(x,y) = k_0 n_i d - k_0 \left(n_g - n_i\right) \frac{x^2+y^2}{2}\left(\frac{1}{R_1} + \frac{1}{R_2}\right) \tag{2.73}$$

We see that if we drop the term that is constant across (x,y) in each of (2.72) and (2.73), the expressions are the same. This can be justified as we are assuming thin lenses and thus d is very small. The same result is obtained for other geometries like meniscus lenses or plano-convex lenses. Moreover, using the common definition for focal length given by

$$f = \left(n_g - n_i\right)\left(\frac{1}{R_1} + \frac{1}{R_2}\right) \tag{2.74}$$

all spherical singlets at low NA can be modeled as the following quadratic phase function applied in a single transverse plane:

$$t_{lens} = \exp\{\mathrm{i}\phi(x,y)\} = \exp\left\{-\mathrm{i}k_0 \frac{x^2+y^2}{2f}\right\} \tag{2.75}$$

where f is positive or negative depending on the combination of radii R_1 and R_2 and indices n_g and n_i in Eqn. (2.74). This powerful result lends itself easily to wave optics propagation through lens systems, as we will see next.

2.7.2 Coherent 2F Propagation

We will now examine what happens when a lens is placed in the $2f$ configuration. In this geometry, the input field is situated at the front focal plane of the lens, and we desire to know the output field in the back focal plane of the lens. The recipe for computing this result is simple: propagate the field a distance z_1 from the plane $z = 0$ to the lens plane, apply the lens transmission function, then propagate a distance z_2 to the plane at $z = z_1 + z_2$ [40, 41]. We will use the Fresnel integral for paraxial propagation. The field at the output plane is the product of the field $E(x_1, y_1)$, which has been propagated from $z = 0$ to $z = z_1$, and the lens phase transmission function, occurring in the plane $z = z_1$:

$$E(x_2, y_2) = \mathrm{e}^{\mathrm{i}kz_2} \frac{-\mathrm{i}}{\lambda z_2} \mathrm{e}^{\frac{\mathrm{i}\pi}{\lambda z_2}(x_2^2+y_2^2)} \int_{x_1,y_1} t_{lens}(x_1, y_1)\, E(x_1, y_1)\, \mathrm{e}^{\frac{\mathrm{i}\pi}{\lambda z_2}(x_1^2+y_1^2)}\, \mathrm{e}^{-\mathrm{i}2\pi\left[\frac{x_2}{\lambda z_2}x_1 + \frac{y_2}{\lambda z_2}y_1\right]} \mathrm{d}x_1 \mathrm{d}y_1 \tag{2.76}$$

where $E(x_1, y_1)$ is given by Eqn. (2.63) with $z = z_1$ and t_{lens} is given by Eqn. (2.75). Exchanging the order of integration,

$$\begin{aligned} E(x_2, y_2) = \quad & \mathrm{e}^{\mathrm{i}k(z_1+z_2)} \frac{-1}{\lambda^2 z_1 z_2} \mathrm{e}^{\frac{\mathrm{i}\pi}{\lambda z_2}(x_2^2+y_2^2)} \int_{x_0,y_0} E(x_0, y_0)\, \mathrm{e}^{\frac{\mathrm{i}\pi}{\lambda z_1}(x_0^2+y_0^2)} \\ & \times \int_{x_1,y_1} \mathrm{e}^{\frac{\mathrm{i}\pi}{\lambda}(x_1^2+y_1^2)\left(\frac{1}{z_1}+\frac{1}{z_2}-\frac{1}{f}\right)}\, \mathrm{e}^{-\mathrm{i}2\pi\left[\frac{x_2}{\lambda z_2}+\frac{x_0}{\lambda z_1}\right]x_1}\, \mathrm{e}^{-\mathrm{i}2\pi\left[\frac{y_2}{\lambda z_2}+\frac{y_0}{\lambda z_1}\right]y_1} \mathrm{d}x_1 \mathrm{d}y_1 \mathrm{d}x_0 \mathrm{d}y_0 \end{aligned} \tag{2.77}$$

We notice the term $\frac{1}{z_1} + \frac{1}{z_2} - \frac{1}{f}$ in the quadratic phase term inside the integration over (x_1, y_1). When set equal to zero, this is the lensmaker's equation for finding the image planes under single lens imaging [40]. However, we are interested in the case where we set $z_0 = z_1 = f$. In other words, we want to look at the relationship between the front and back focal planes of the lens. The integration over x_1 and y_1 can be performed analytically, yielding

$$E(x_2, y_2) = \quad \mathrm{e}^{\mathrm{i}2kf} \frac{-1}{\lambda^2 f^2} \mathrm{e}^{\frac{\mathrm{i}\pi}{\lambda f}(x_2^2+y_2^2)} \int_{x_0,y_0} E(x_0, y_0)\, \mathrm{e}^{\frac{\mathrm{i}\pi}{\lambda f}(x_0^2+y_0^2)} \left[\mathrm{i}\lambda f\, \mathrm{e}^{-\frac{\mathrm{i}\pi}{\lambda f}(x_2+x_0)^2}\, \mathrm{e}^{-\frac{\mathrm{i}\pi}{\lambda f}(y_2+y_0)^2}\right] \mathrm{d}x_0 \mathrm{d}y_0 \tag{2.78}$$

Expanding the terms $(x_2 + x_0)^2$ and $\left(y_2 + y_0\right)^2$ leads to cancellation of all quadratic phase terms. The result is

$$E(x_2, y_2) = \frac{e^{i2kf}}{i\lambda f} \int_{x_0, y_0} E(x_0, y_0)\, e^{-i2\pi\left[\frac{x_2}{\lambda f} x_0 + \frac{y_2}{\lambda f} y_0\right]} dx_0 dy_0 \tag{2.79}$$

which contains a Fourier transform of $E(x_0, y_0)$ with conjugate variables $f_{x_0} = x_2/\lambda f$ and $f_{y_0} = y_2/\lambda f$. This remarkable result can be summarized succinctly: the transverse field distribution in the back focal plane of a lens with focal length f is a scaled Fourier transform of the transverse field in the front focal plane.

Equation (2.79) lies at the heart of Fourier optics. In the absence of a lens, the Fourier transform of a field can only be obtained by allowing the field to diffract a great distance to the far-field - the Fraunhofer regime - where each tilted plane wave in the angular spectrum emanating from the plane $z = 0$ eventually dominates the field summation at a far-field coordinate (x_1, y_1). However, with the addition of a lens, the Fourier spectrum can be obtained in a vastly shorter distance: $2f$. This provides a powerful tool for manipulating fields in an optical system, and we will use this tool extensively.

Finally, a few notes about this result. We have assumed the lens is immersed in the same medium on both sides, e.g. air, through n_i in Eqn. (2.75). Moreover, we have assumed that the aperture of the lens is large enough that it does not play a role in shaping the field distribution. Finally, we assumed paraxial fields.

2.7.3 Coherent 4F Propagation and Imaging

The $2f$ lens configuration can be used as a building block in optical systems. Placing two lenses in series, with the back focal plane of the first lens coinciding with the front focal plane of the second lens, results in the well-known $4f$ imaging configuration [40]. In essence, the input field is Fourier transformed, then Fourier transformed again to return a copy of the original field. The 4f imaging system has certain useful features relative to single lens imaging. First of all, the field wavefront is reimaged along with the field magnitude, whereas single lens imaging

results in additional quadratic phase (wavefront curvature). Secondly, there is easy access to the spatial frequency distribution of the input field in at the back focal plane of the second lens. This can be used to manipulate the way that light propagates through the second lens to the image plane. In the simplest example, a circular aperture limits high spatial frequencies. A ring aperture can allow for only high spatial frequencies to propagate, or a phase plate can be used to delay certain spatial frequencies relative to others. Modern microscopes make heavy use of $4f$ imaging configurations, where the first lens is referred to as the tube lens, and the second lens is an infinity-corrected objective lens. The objective can have high numerical aperture focusing, and in combination with a longer focal length (paraxial) tube lens, can provide high magnification.

We start by two applications of Eqn. (2.79). We set the back focal plane of lens 2 to be coincident with the front focal plane of lens 1. Lens 2 is therefore a distance f_2 away from $E(x_2, y_2)$, and has transverse coordinates (x_3, y_3), although thanks to Eqn. (2.79) the fields in the lens planes do not need to be computed. The front focal plane of lens 2 contains the field $E(x_4, y_4)$. The $4f$ imaging system is therefore described by

$$E(x_4, y_4) = \frac{e^{i2kf_2}}{i\lambda f_2} \int_{x_2, y_2} \mathcal{P}(x_2, y_2)\, E(x_2, y_2)\, e^{-i2\pi\left[\frac{x_4}{\lambda f_2} x_2 + \frac{y_4}{\lambda f_2} y_2\right]} dx_2 dy_2 \tag{2.80}$$

where $E(x_2, y_2)$ is given by Eqn. (2.79) and we have added a pupil function, $\mathcal{P}$, in the 'Fourier plane'. Often, the pupil function is simply a circular aperture created by the finite diameter of the lenses. Exchanging the order of integration,

$$\begin{aligned} E(x_4, y_4) = \frac{-e^{i2k(f_1+f_2)}}{\lambda^2 f_1 f_2} \int_{x_0, y_0} & E(x_0, y_0) \\ \times \int_{x_2, y_2} & \mathcal{P}(x_2, y_2)\, e^{-i2\pi x_2\left[\frac{x_4}{\lambda f_2} + \frac{x_0}{\lambda f_1}\right]} e^{-i2\pi y_2\left[\frac{y_4}{\lambda f_2} + \frac{y_0}{\lambda f_1}\right]} dx_2 dy_2 dx_0 dy_0 \end{aligned} \tag{2.81}$$

The integration over Fourier plane coordinates (x_2, y_2) results in a transverse Fourier transform of the pupil function, with spatial frequencies $f_{x_2} = \frac{x_4}{\lambda f_2} + \frac{x_0}{\lambda f_1}$ and $f_{y_2} = \frac{y_4}{\lambda f_2} + \frac{y_0}{\lambda f_1}$. Denoting the Fourier representation of the pupil $\mathcal{P}(x, y)$ as $\hat{\mathcal{P}}(f_x, f_y)$, and defining the magnification as

$M = -f_2/f_1$, we have

$$E(x_4, y_4) = \frac{-e^{i2k(f_1+f_2)}}{\lambda^2 f_1 f_2} \int_{x_0,y_0} E(x_0, y_0)\, \hat{\mathcal{P}} \left[\frac{-1}{\lambda f_1} \left(\frac{x_4}{M} - x_0 \right), \frac{-1}{\lambda f_1} \left(\frac{y_4}{M} - y_0 \right) \right] dx_0 dy_0 \tag{2.82}$$

We define a new function, the Coherent Spread Function (CSF), which is a scaled version of the pupil's Fourier representation $\hat{\mathcal{P}}$ [40]:

$$CSF(x, y) = \frac{1}{(\lambda f_1)^2} \hat{\mathcal{P}} \left(\frac{-1}{\lambda f_1} x, \frac{-1}{\lambda f_1} y \right) \tag{2.83}$$

which allows us to write Eqn. (2.82) as a convolution integral:

$$E(x_4, y_4) = \frac{e^{i2k(f_1+f_2)}}{M} \int_{x_0,y_0} E(x_0, y_0)\, CSF \left(\frac{x_4}{M} - x_0, \frac{y_4}{M} - y_0 \right) dx_0 dy_0 \tag{2.84}$$

Thus, the imaged field $E(x_4, y_4)$ is a magnified version of the initial field, with some amount of blurring due to the CSF of the system. In the event of an infinitely large pupil, $\mathcal{P}$, the CSF would become a delta function and a perfect image would result. An equally important result is a quantity known as the Coherent Transfer Function (CTF), which is defined as the Fourier transform of the CSF:

$$CTF(f_x, f_y) = \mathcal{F}\left[CSF(x, y) \right] = \mathcal{P}\left(-f_1 \lambda f_x, -f_1 \lambda f_y \right) \tag{2.85}$$

The CTF is simply the pupil scaled from spatial coordinates into spatial frequency coordinates. Thus, in the Fourier plane, radial position is linearly proportional to spatial frequency. Thus, the canonical circular aperture serves to cut off frequencies above a certain threshold, and therefore serves as a low-pass filter, ultimately limiting the resolution of the image. The CSF and CTF functions are well-known in systems theory, going be other names such as the impulse response and system transfer function.

Writing the $4f$ imaging relationship entirely in the spatial frequency domain, the output field spectrum is a product between the incident field spectrum and the system coherent trans-

fer function:

$$E_4(f_x, f_y) = M\, e^{i2k(f_1+f_2)}\, E_0(M f_x, M f_y)\, CTF(M f_x, M f_y) \tag{2.86}$$

2.8 Electric fields at a High Numerical Aperture Focus

Some forms of microscopy require tightly-focused laser beams utilizing high numerical aperture (NA) objective lenses. This is often the case for laser-scanning techniques, where a tightly confined focal volume is raster-scanned in three dimensions to build up an image [22]. Some forms of super-resolution microscopy require tight foci. An example of a point-scanning super resolution technique is STED microscopy, which require the overlap of a tightly focused laser beam in the TEM00 spatial mode and a second tightly focused beam in the LG01 "doughnut" mode [5]. The numerical aperture refers to the steepest angle, with respect to the optic axis, that the lens will transmit. It is defined by the formula:

$$\mathrm{NA} = n \sin\theta \tag{2.87}$$

where n is the index of refraction in the medium, and θ is the angle of the steepest inclined ray passed by the lens. Objective lenses designed to operate in air can reach NA's up to about 0.85. Water immersion objectives are used for numerical apertures in the 0.9 - 1.1 range, and oil immersion objectives are used to obtain NA's up to about 1.7. For focal conditions exceeding approximately 0.7 NA, the scalar approximation becomes increasingly inaccurate for modeling focal fields. A vector field treatment is required to account for depolarization of the beam as it is refracted at large angles by the objective lens. While there are many ways to compute the field at a high NA focus, in this work we will utilize the Debye-Wolf diffraction integral.

2.8.1 Debye's Concept for Focal Field Computation

To solve for the focal field in the geometric focus of a lens, a century ago Debye proposed the concept of a focus being formed by a spherical converging wave that is decomposed into a spectrum of plane waves. A description in English is related by Debye's thesis advisor Som-

merfeld [42]. The spectrum contains plane waves from all directions within a certain solid angle limited by a circular aperture. Debye provided us with an early example of the plane wave decomposition (angular spectrum) model applied to a specific propagation geometry. Mathematically, Debye's idea can be expressed with an equation of the form:

$$\mathbf{E}(x,y,z) = \int_{\Omega} \mathbf{a}(s_x, s_y) \mathrm{e}^{\mathrm{i}k(s_x x + s_y y + s_z z)} \mathrm{d}\Omega \tag{2.88}$$

where **E** is the field in the focal region, **s** is the spectrum of plane wave directions, and **a** is the strength or magnitude of each plane wave component in the spectrum of directions (s_x, s_y). The integration occurs over the spectrum of directions, ultimately limited by some solid angle Ω [43, 44]. The limiting solid angle can be due to the aperture, or do to the set of s_x and s_y that do not lead to evanescent waves, that is $(s_x, s_y) \in s_x^2 + s_y^2 < 1$.

In subsequent years, some effort was made to test the validity of Debye's model relative to other well-known diffraction models, particularly by Wolf [43–45]. For example, the Huygens-Fresnel diffraction integral computes the focal field by summing the radiation from a set of spherically-emitting points in the aperture of the lens, whereas the Debye diffraction integral approach sums the radiation from a set of plane wave emitters in the aperture. Born and Wolf [46] demonstrate that the Debye integral is derived from the Huygens-Fresnel integral in the approximation that the propagation from the aperture to the focal point is much larger than the wavelength. In terms of computational rigor, it has been found that the Kirchhoff diffraction formula is more accurate under extreme conditions and has a broader range of applications than the Debye formula [45, 47]. Nevertheless, the Debye formula is still used frequently for the special case of computing focusing fields. To prescribe limits to its applicability, Wolf and Li showed that for focal fields with high Fresnel numbers, $N_F \gg 1$, the Debye focal field indeed provides a reasonably accurate model of the focal field [45]. The Fresnel number is based on three parameters related to the focal geometry: $N_F = r_F^2/\lambda f$, where r_F is the circular aperture radius, f the focal length, and λ the wavelength. For most objective lenses in common use, N_F

is indeed $\gg 1$. For example, for a small 1mm radius, and a very short 1mm focal length, light with a 1μm wavelength has a Fresnel number of 1000.

In 1959, Richards and Wolf [44] extended the Debye model from a scalar field treatment to the case where vectorial fields are considered in the aperture and at the focus. Thanks to Wolf's many contributions to understanding the nature of the Debye focal field, the integral is sometimes referred to as the Debye-Wolf integral.

2.8.2 The Debye-Wolf Integral

We will now demonstrate how the Debye-Wolf integral for computing high-NA vector focal fields can be derived from the angular spectrum equations developed in Section 2.6.1. We will follow the analysis provided in Ref. [38], which is a modern version of the classical derivation in Ref. [44] that is designed to easily accommodate laser beams.

The goal is to compute the field in a volume (x, y, z) near the geometric focal point of a high-NA lens. We start with the general diffraction equation given in Eqn. (2.51), which gives the field at an arbitrary location in the focal volume by propagating the angular spectrum of the focal field, $\mathbf{E}(x, y, 0)$, about the focal plane:

$$\mathbf{E}(x, y, z) = \int_{k_x} \int_{k_y} \left[\mathbf{E}(k_x, k_y; 0) \mathrm{e}^{\mathrm{i}k_z z} \right] \mathrm{e}^{\mathrm{i}(k_x x + k_y y)} \mathrm{d}k_x \mathrm{d}k_y \tag{2.89}$$

To proceed, we must know the transverse focal field. This is available to us if we know the far field, thanks to Eqn. (2.57). Rewritten here, it is:

$$\mathbf{E}\left(k_x, k_y; z = 0\right) = \frac{\mathrm{i}}{2\pi k} \frac{r}{z} r \mathrm{e}^{-\mathrm{i}kr} \mathbf{E}_\infty \left(x, y, z\right) \Big|_{x = r\frac{k_x}{k},\ y = r\frac{k_y}{k}} \tag{2.90}$$

This formulation is conceptually clear, because the far-field can be equated to the input field of our high-NA lens. This input field is that which we have brought to the back focal plane of the lens.

To facilitate our analysis, it is helpful to move from a spectrum of spatial frequencies, $\mathbf{k}$, to a spectrum of unit directions, $\mathbf{s}$. We define a normalized wavevector:

$$\mathbf{s} = \mathbf{k}/|\mathbf{k}| = \frac{k_x}{k}\hat{\mathbf{x}} + \frac{k_y}{k}\hat{\mathbf{y}} + \frac{k_z}{k}\hat{\mathbf{z}} = \left(s_x, s_y, s_z\right) \tag{2.91}$$

The Cartesian components of $\mathbf{s}$ have fractional magnitudes such that their vector sum yields a unitary length $|\mathbf{s}| = 1$. Moreover, due to the dispersion relationship in a homogeneous medium, s_z is defined through s_x and s_y as

$$s_z = \pm\sqrt{1 - s_x^2 - s_y^2} \tag{2.92}$$

We will assume forward-propagating waves corresponding to a typical lens illumination, and take the positive square root. We will also only consider far fields, and so we exclude the set of s_x and s_y that lead to evanescent waves, that is $(s_x, s_y) \in s_x^2 + s_y^2 \leq 1$. This makes Eqn. (2.89) take the form:

$$\mathbf{E}(x, y, z) = k^2 \int_{s_x^2+s_y^2\leq 1} \mathbf{E}(k_x = ks_x, k_y = ks_y; 0)\, \mathrm{e}^{\mathrm{i}k\left(s_x x + s_y y + \sqrt{1-s_x^2-s_y^2}\, z\right)} \mathrm{d}s_x \mathrm{d}s_y, \tag{2.93}$$

which is an integral that sums plane waves over a set of unit directions, $\mathbf{s}$, as opposed to a set of spatial frequencies, $\mathbf{k}$. Upon substituting the far field in Eqn. (2.90) into Eqn. (2.93), the field in the focal volume becomes

$$\mathbf{E}(x, y, z) = \frac{\mathrm{i}kr\mathrm{e}^{-\mathrm{i}kr}}{2\pi} \int_{s_x^2+s_y^2\leq 1} \mathbf{E}_\infty\left(x = rs_x, y = rs_y, z = rs_z\right) \frac{1}{s_z}\, \mathrm{e}^{\mathrm{i}k\left(s_x x + s_y y + \sqrt{1-s_x^2-s_y^2}\, z\right)} \mathrm{d}s_x \mathrm{d}s_y \tag{2.94}$$

where we also used $z = rs_z$ which is found by evaluating $r^2 = x^2 + y^2 + z^2$ for $x = rs_x$ and $y = rs_y$ with Eqn. (2.92) . By transforming the differentials using

$$\mathrm{d}\Omega = \frac{\mathrm{d}s_x \mathrm{d}s_y}{s_z} \tag{2.95}$$

we can write the integral over solid angle:

$$\mathbf{E}(x,y,z) = \frac{\mathrm{i}kr\mathrm{e}^{-\mathrm{i}kr}}{2\pi}\int_{\Omega\leq 2\pi}\mathbf{E}_{\infty}(rs_x, rs_y, rs_z)\,\mathrm{e}^{\mathrm{i}k\mathbf{s}\cdot\mathbf{r}}\mathrm{d}\Omega \tag{2.96}$$

Eqn. (2.96) is a rigorous derivation of the concept introduced by Debye (Eqn. (2.88)). In this form, the field in the focal region is entirely defined by summing over directional plane waves which have emanated from the far-field. The total solid angle of plane wave directions is limited to the half space $z \geq 0$ to exclude evanescent waves, but in practice is further limited by a system aperture. The far-field, a sufficient distance away, is written as a function of these plane wave directions, with each plane wave assigned a magnitude. The far field can also include other properties for each tilted plane wave, such as phase delay and polarization state.

While the discussion thus far has been motivated by computing the vector electric field at a high NA focus, the diffraction integral in Eqn. (2.96) is more general. It provides the field in any volume of interest in terms of the forward-propagating tilted plane waves emanating from the far field. Let us now return to the physical problem of focusing with a high NA lens.

The far-field on the Gaussian Reference Sphere

A high NA lens can be modeled as a system that generates constructive interference at the focus by creating an ideal spherically converging field. This spherical field can be thought of as originating at a spherical surface of radius f, where f is the high NA lens focal length.

The use of a reference sphere for a focal field comes from the older description of a classic aplanatic imaging system fulfilling the Abbe sine condition [48], where the sphere is sometimes called the Gaussian reference sphere. Abbe's sine condition is a statement of high-quality imaging from one transverse plane to another. It states that the cone of rays emerging from any point in the transverse object plane should be captured by the imaging system, and that the cone of rays should be reproduced (possibly with angular magnification) in the image space to reproduce the transverse point in the image plane [49]. This results in a system that is free of spherical and comatic aberration (aplanatic) even with wide-angle illumination and collection. For this

result to hold, the cone of rays emerging spherically outward from an object point is captured at a spherical reference surface representing a tube lens, with each ray being redirected to travel parallel to the optic axis. Then, these parallel rays encounter another reference sphere wherein they are redirected to spherically converge toward the focal volume and the transverse image plane located therein. This geometry is a generalization of paraxial optics, where the transverse principal plane representing a lens transformation has been curved into a spherical surface of radius f, situated one focal length from the lens' focal point.

In Debye's model, as we have discussed, this spherically converging field is decomposed into a spectrum of plane wave directions, emanating from a common spherical surface, and arriving in phase at the focus. If f, λ and the aperture radius r_F together ensure that the Fresnel number $N_F \gg 1$, then we can accurately compute the focal region field from the far field using the Debye-Wolf integral. We therefore define a spherical reference surface at a radius $r = f$ to work with.

To use the Debye-Wolf integral, we must next define the far field on this reference sphere. For a spherically converging field, the wavefront normal points toward the geometric focus. We now see why it was helpful to write the far field in terms of unit-fractional direction vectors, as they directly map into the azimuthal and polar angles of a spherical-polar coordinate system:

$$s_x = \sin\theta\cos\phi \tag{2.97}$$

$$s_y = \sin\theta\sin\phi \tag{2.98}$$

$$s_z = \cos\theta \tag{2.99}$$

The differential solid angle in spherical-polar coordinates is:

$$\mathrm{d}\Omega = \sin\theta\,\mathrm{d}\theta\,\mathrm{d}\phi \tag{2.100}$$

The general diffraction integral in Eqn. (2.96), with the far-field now situated on the Gaussian reference sphere, yields the Debye-Wolf integral for a high-NA focus:

$$\mathbf{E}(x,y,z) = \frac{\mathrm{i}kf\,\mathrm{e}^{-\mathrm{i}kf}}{2\pi}\int_{\theta,\phi}\mathbf{E}_\infty(f,\phi,\theta)\,\mathrm{e}^{\mathrm{i}k(x\sin\theta\cos\phi+y\sin\theta\sin\phi+z\cos\theta)}\sin\theta\,\mathrm{d}\theta\,\mathrm{d}\phi \tag{2.101}$$

In some cases it is also helpful to convert the field in the focal volume to a cylindrical coordinate system, where ρ is the radius and φ is the angle in the transverse (x,y) focal plane:

$$x = \rho\cos\varphi \qquad y = \rho\sin\varphi \tag{2.102}$$

We use φ for the azimuthal component of the cylindrical coordinate system used in the focal region in order to avoid confusion with ϕ, the azimuthal component of the spherical polar coordinate system used in the same region. With these changes, the Debye-Wolf integral for the field in the focal volume in cylindrical coordinates can be compactly written with the help of a trigonometric identity:

$$\mathbf{E}(\rho,\varphi,z) = \frac{\mathrm{i}kf\,\mathrm{e}^{-\mathrm{i}kf}}{2\pi}\int_{\theta,\phi}\mathbf{E}_\infty(f,\phi,\theta)\,\mathrm{e}^{\mathrm{i}k\rho\sin\theta\cos(\phi-\varphi)}\mathrm{e}^{\mathrm{i}kz\cos\theta}\sin\theta\,\mathrm{d}\theta\,\mathrm{d}\phi \tag{2.103}$$

The field in the focal volume is defined by the far-field defined on a spherical surface f away. Additionally, in a microscope, the solid angle of the spherical surface is constrained by a planar aperture normal to the optic axis. The solid angle permitted by the aperture is controlled by the polar angle θ, with the maximum angle θ_{max} specified through the NA of the lens using Eqn. (2.87).

Far-field coordinate transformation at the reference sphere

The next step is to determine how a beam of light arriving at the lens aperture is mapped onto the Gaussian reference sphere. In modern laser scanning microscopes, a collimated laser serves as the parallel bundle of rays incident on the reference sphere. Or, in wave optics terms, a collimated beam with a waist incident on the reference sphere has a planar wavefront with the normal to the wavefront (indicating propagation direction) pointing purely in the forward ($\hat{\mathbf{z}}$) direction everywhere along the wavefront. This incident collimated beam will have its elec-

tric field vector pointing in the transverse plane, and therefore can be written as a sum of two polarization states in either Cartesian or cylindrical coordinates:

$$\mathbf{E}_\infty = [\mathbf{E}_\infty \cdot \hat{\mathbf{x}}]\,\hat{\mathbf{x}} \;\; + \;\; \left[\mathbf{E}_\infty \cdot \hat{\mathbf{y}}\right]\hat{\mathbf{y}} \tag{2.104}$$

$$= \left[\mathbf{E}_\infty \cdot \hat{\phi}\right]\hat{\phi} + \left[\mathbf{E}_\infty \cdot \hat{\rho}\right]\hat{\rho} \tag{2.105}$$

At the spherical reference surface, the incoming beam is transformed (via ideal refraction) into one that converges toward the focus at the center of the sphere. Each differential area in the incident beam will obtain a new k vector direction (pointing toward the geometric focus) and a new electric field direction. Thus, a coordinate transformation is needed to map the incident beam in Cartesian or cylindrical coordinate system into a spherical-polar coordinate system best matching the geometry of the focusing field.

It will be most expedient to transform from a cylindrical to a spherical-polar coordinate system. The azimuthal field component is preserved upon refraction, while the radial component is projected purely onto the polar component of a spherical-polar coordinate system. Thus, just inside the reference sphere, the field is a function of the θ and ϕ directions, and as such, can be used as the far field in Eqn. (2.103) in order to compute the field at the focus. The far-field just inside the sphere, in terms of the incident beam, will be of the form

$$\mathbf{E}_\infty(f,\phi,\theta) \propto \left[\mathbf{E}_\infty \cdot \hat{\phi}\right]\hat{\phi} + \left[\mathbf{E}_\infty \cdot \hat{\rho}\right]\hat{\theta} \tag{2.106}$$

although energy conservation still needs to be accounted for to have equality. The area of a patch in the transverse plane is $\mathrm{d}A_1 = \mathrm{d}\rho \times \rho\mathrm{d}\phi$, while the area of that patch projected onto the reference sphere is $\mathrm{d}A_2 = \mathrm{d}\rho/\cos\theta \times \rho\mathrm{d}\phi$. The time-averaged Poynting vector (Eqn. (2.26)), derived directly from Maxwell's Equations, gives the power flux through an area. For optical power to remain constant through the two surfaces, we must have $|\langle\mathbf{S}\rangle_1|\cdot\mathrm{d}A_1 = |\langle\mathbf{S}\rangle_2|\cdot\mathrm{d}A_2$. With Eqn. (2.28), this leads to the expression:

$$|\mathbf{E}_2| = \sqrt{\frac{n_1}{n_2}\cos\theta}\,|\mathbf{E}_1| \tag{2.107}$$

With Equations (2.106) and (2.107), the transformation of the collimated far-field beam from cylindrical to spherical-polar coordinates at a distance f from the origin is:

$$\mathbf{E}_\infty(f,\phi,\theta) = \sqrt{\frac{n_1}{n_2}\cos\theta}\Big[\left[\mathbf{E}_\infty\cdot\hat{\phi}\right]\hat{\phi} + \left[\mathbf{E}_\infty\cdot\hat{\rho}\right]\hat{\theta}\Big] \tag{2.108}$$

We note that transmission coefficients can be added to this expression, but we ignore this on the assumption of good anti-reflection coatings.

We note that $\mathbf{E}_\infty(\rho,\phi,z)$ and $\mathbf{E}_\infty(f,\phi,\theta)$, which are the far fields just before and just inside of the reference sphere, respectively, are both vector fields with Cartesian field directions $\left(\hat{x},\hat{y},\hat{z}\right)$, although the field amplitude in each case is written as a function of cylindrical and spherical-polar coordinates, respectively. To perform the inner products in Eqn. (2.108), we need to express the unit vectors $\hat{\rho}$, $\hat{\phi}$ and $\hat{\theta}$ in terms of unit Cartesian vectors, using the following:

$$\hat{\rho} = \quad \cos\phi\,\hat{\mathbf{x}} + \sin\phi\,\hat{\mathbf{y}} \tag{2.109}$$

$$\hat{\phi} = -\sin\phi\,\hat{\mathbf{x}} + \cos\phi\,\hat{\mathbf{y}} \tag{2.110}$$

$$\hat{\theta} = \quad \cos\theta\cos\phi\,\hat{\mathbf{x}} + \cos\theta\sin\phi\,\hat{\mathbf{y}} - \sin\theta\,\hat{\mathbf{z}} \tag{2.111}$$

The far-field defined just inside the reference sphere, which Cartesian vector components, is therefore expressed in terms of the collimated beam incident on the reference sphere as:

$$\mathbf{E}_\infty(f,\phi,\theta) = \sqrt{\frac{n_1}{n_2}\cos\theta}\left[\mathbf{E}_\infty\cdot\left(-\sin\phi\,\hat{\mathbf{x}}+\cos\phi\,\hat{\mathbf{y}}\right)\begin{bmatrix}-\sin\phi\,\hat{\mathbf{x}}\\ \cos\phi\,\hat{\mathbf{y}}\\ 0\,\hat{\mathbf{z}}\end{bmatrix} + \mathbf{E}_\infty\cdot\left(\cos\phi\,\hat{\mathbf{x}}+\sin\phi\,\hat{\mathbf{y}}\right)\begin{bmatrix}\cos\theta\cos\phi\,\hat{\mathbf{x}}\\ \cos\theta\sin\phi\,\hat{\mathbf{y}}\\ -\sin\theta\,\hat{\mathbf{z}}\end{bmatrix}\right] \tag{2.112}$$

Equation (2.112) can now be inserted into the Debye-Wolf integral in Eqn. (2.103) to compute the focal field in terms of the polarized incident beam.

For the special case of a linearly polarized input, where we use the angle ξ to represent the angle of the transverse polarization vector with respect to x, the transverse far field is

$$\mathbf{E}_\infty = E_\infty \cos\xi\,\hat{\mathbf{x}} + E_\infty \sin\xi\,\hat{\mathbf{y}} \tag{2.113}$$

and upon inserting into Eqn. (2.112), the far field just inside the reference sphere, in spherical polar coordinates, is

$$\mathbf{E}_\infty(f,\phi,\theta;\xi) = E_\infty(x,y)\sqrt{\frac{n_1}{n_2}\cos\theta}\begin{bmatrix} \cos\phi\cos\theta\cos\left(\phi-\xi\right) + \sin\phi\sin\left(\phi-\xi\right)\,\hat{\mathbf{x}} \\ \sin\phi\cos\theta\cos\left(\phi-\xi\right) - \cos\phi\sin\left(\phi-\xi\right)\,\hat{\mathbf{y}} \\ -\sin\theta\cos\left(\phi-\xi\right)\,\hat{\mathbf{z}} \end{bmatrix} \tag{2.114}$$

2.8.3 High NA focal fields for a linearly polarized Gaussian beam

To illustrate the use of the Debye-Wolf integral, we will compute the high-NA focal field for the simple case of a linearly polarized, collimated Gaussian beam with a single mode (TEM00) spatial profile. Such a field has the form:

$$\mathbf{E}_\infty = E_0 \mathrm{e}^{-\rho^2/w_0^2}\hat{\mathbf{x}} \tag{2.115}$$

in the cylindrical coordinate system used at incidence on the reference sphere, with the beam waist given by w_0. In spherical-polar coordinates, which we will use after transforming at the sphere, the incident transverse Gaussian beam can be expressed as

$$\mathbf{E}_\infty = E_0 \mathrm{e}^{-(f\sin\theta)^2/w_0^2}\hat{\mathbf{x}} = f_w(\theta)\hat{\mathbf{x}} \tag{2.116}$$

where $f_w(\theta)$ expresses that the beam waist is a function of polar angle θ. Since the beam is x-polarized, we will use Eqn. (2.114) with $\xi = 0$ to compute the incident field given by Eqn. (2.116)

just inside the reference sphere.

$$\mathbf{E}_{\infty}(f,\phi,\theta) = f_w(\theta)\frac{1}{2}\sqrt{\frac{n_1}{n_2}\cos\theta}\begin{bmatrix}\left(1+\cos\theta-(1-\cos\theta)\cos\left(2\phi\right)\right)\hat{\mathbf{x}}\\ -(1-\cos\theta)\sin\left(2\phi\right)\hat{\mathbf{y}}\\ -2\sin\theta\cos\phi\,\hat{\mathbf{z}}\end{bmatrix} \tag{2.117}$$

Inserting this far field into the integral in Eqn. (2.103) to compute the field in the focal volume,

$$\begin{aligned}\mathbf{E}(\rho,\varphi,z) = \frac{\mathrm{i}kf\mathrm{e}^{-\mathrm{i}kf}}{4\pi}\sqrt{\frac{n_1}{n_2}}\int_{\theta=0}^{\theta_{max}}\int_{\phi=0}^{2\pi} f_w(\theta)\sqrt{\cos\theta}\sin\theta\mathrm{e}^{\mathrm{i}kz\cos\theta}\\ \times\begin{bmatrix}\left(1+\cos\theta-(1-\cos\theta)\cos\left(2\phi\right)\right)\hat{\mathbf{x}}\\ -(1-\cos\theta)\sin\left(2\phi\right)\hat{\mathbf{y}}\\ -2\sin\theta\cos\phi\,\hat{\mathbf{z}}\end{bmatrix}\mathrm{e}^{\mathrm{i}k\rho\sin\theta\cos(\phi-\varphi)}\,\mathrm{d}\theta\mathrm{d}\phi\end{aligned} \tag{2.118}$$

The integral over azimuthal angle can be solved using the definitions of the n^{th}-order Bessel functions:

$$\int_0^{2\pi}\cos\left(n\phi\right)\mathrm{e}^{\mathrm{i}x\cos(\phi-\varphi)}\mathrm{d}\phi = 2\pi\mathrm{i}^n J_n(x)\cos\left(n\varphi\right) \tag{2.119}$$

$$\int_0^{2\pi}\sin\left(n\phi\right)\mathrm{e}^{\mathrm{i}x\cos(\phi-\varphi)}\mathrm{d}\phi = 2\pi\mathrm{i}^n J_n(x)\sin\left(n\varphi\right) \tag{2.120}$$

resulting in the following expression for the field in the focal volume:

$$\begin{aligned}\mathbf{E}(\rho,\varphi,z) = \frac{\mathrm{i}kf\mathrm{e}^{-\mathrm{i}kf}}{2}\sqrt{\frac{n_1}{n_2}}\int_{\theta=0}^{\theta_{max}} f_w(\theta)\sqrt{\cos\theta}\sin\theta\mathrm{e}^{\mathrm{i}kz\cos\theta}\\ \times\begin{bmatrix}\left((1+\cos\theta)J_0(k\rho\sin\theta)+(1-\cos\theta)J_2(k\rho\sin\theta)\cos\left(2\varphi\right)\right)\hat{\mathbf{x}}\\ (1-\cos\theta)J_2(k\rho\sin\theta)\sin\left(2\varphi\right)\hat{\mathbf{y}}\\ -2\mathrm{i}\sin\theta J_1(k\rho\sin\theta)\cos\left(\varphi\right)\hat{\mathbf{z}}\end{bmatrix}\mathrm{d}\theta\end{aligned} \tag{2.121}$$

This expression can be written more compactly by defining the following three integrals [38,44],

$$I_{00} = \int_{\theta=0}^{\theta_{max}} f_w(\theta)\sqrt{\cos\theta}\sin\theta \;\; J_0(k\rho\sin\theta)\mathrm{e}^{\mathrm{i}kz\cos\theta}\,(1+\cos\theta)\,\mathrm{d}\theta \tag{2.122}$$

$$I_{01} = \int_{\theta=0}^{\theta_{max}} f_w(\theta)\sqrt{\cos\theta}\sin^2\theta\, J_1(k\rho\sin\theta)\mathrm{e}^{\mathrm{i}kz\cos\theta}\,\mathrm{d}\theta \tag{2.123}$$

$$I_{02} = \int_{\theta=0}^{\theta_{max}} f_w(\theta)\sqrt{\cos\theta}\sin\theta \;\; J_2(k\rho\sin\theta)\mathrm{e}^{\mathrm{i}kz\cos\theta}\,(1-\cos\theta)\,\mathrm{d}\theta \tag{2.124}$$

resulting in the expression for the focal field:

$$\mathbf{E}(\rho,\varphi,z) = \frac{\mathrm{i}kf\mathrm{e}^{-\mathrm{i}kf}}{2}\sqrt{\frac{n_1}{n_2}}\begin{bmatrix} \left(I_{00}+I_{02}\cos\left(2\varphi\right)\right)\,\hat{\mathbf{x}} \\ I_{02}\sin\left(2\varphi\right)\,\hat{\mathbf{y}} \\ -2\mathrm{i}I_{01}\cos\left(\varphi\right)\,\hat{\mathbf{z}} \end{bmatrix} \tag{2.125}$$

Equation (2.125) gives the vector electric field in the focal region of a high NA lens, for the example input field of a linearly polarized, collimated Gaussian beam incident on the reference sphere of the lens. Despite the trigonometric identities used to simplify the mathematical expressions, the numerical solution of three integrals (I_{00}, I_{01}, I_{02}) over the aperture angle θ is required, which can bottleneck computation time for large numbers of points in the focal volume, where the sample spacing is driven in part by accurately capturing the oscillatory behavior of the Bessel functions. Despite these limitations, the Debye-Wolf integral provides a useful tool for investigating field behavior at a high-NA focus.

In summary, the key details of high-NA focal field computation using the Debye-Wolf integral are the following:

1 Assume an incoming collimated laser beam described in cylindrical coordinates. Being collimated, it is perfectly forward-directional. It's transverse electric field has radial and azimuthal, but not axial, components.

2 Define a reference sphere of radius f, where f is the high-NA lens focal length. The reference sphere will transform the forward-directional input field into an ideal spherically-converging field. A coordinate transformation from cylindrical to spherical-polar coordinates is used. Propagation along $\hat{\mathbf{z}}$ in the cylindrical system is mapped into propagation

along $\hat{\mathbf{r}}$ in the spherical-polar system. Meanwhile, the transverse electric field vectors at each differential area of the input beam are also transformed: azimuthal components are preserved ($\hat{\phi} \rightarrow \hat{\phi}$), while radial components are mapped into polar components ($\hat{\rho} \rightarrow \hat{\theta}$).

3 For a circular pupil, integration over ϕ results in Bessel functions. Integration over the semi-aperture (polar) angle θ is performed numerically. The resultant field in the focal volume is described in cylindrical coordinates, with Cartesian field directions.

2.9 Nonlinear optical interactions

Under a strong enough incident field **E**, a material medium may not physically be able to generate a polarization field **P** that follows the incident field linearly, resulting in only a change in amplitude or phase. The medium's polarization comes from the response of the bound charge distribution averaged over an ensemble of atoms in the volume of interest. For example, for a time-harmonic incident E-field, the charge distribution can be caused to oscillate about its mean location with some phase delay relative to E. However, when driven too strongly, electrons may either break away (ionization) or oscillate with certain limitations on harmonic (sinusoidal) behavior, resulting in waveforms that can be described instead by Fourier summation techniques. To model this behavior, the polarization field can be expanded as a power series:

$$\mathbf{P} = \epsilon_0 \left(1 + \chi_e \mathbf{E} + \chi_e^{(2)} \mathbf{E}^2 + \chi_e^{(3)} \mathbf{E}^3 + ...\right) \tag{2.126}$$

2.10 Spatial Coherence

In this work, we limit our analysis to spatially coherent illumination in the SPIFI microscope. This treatment is in accordance with our experimental work, which was performed with a laser beam. As is well known, lasers exhibit a high degree of spatial coherence. In other words, the phase relationship between different locations in space is well-behaved over long periods of time. Hence, it can be considered deterministic. Coherent light sources – the laser chief among them – exhibit a field with clear directionality and uniform phase oscillation across the wavefront.

This is in contrast to partially coherent and fully incoherent light, where the field phase difference measured at two locations in space does not maintain a steady value over time. This quality is characterized by the mutual intensity function, which is the spatial correlation between the field at two points, averaged over a long period of time [40]. Incoherence is generally due to a light source where points within the source volume generate fields without any relationship in terms of phase and direction. Example light sources include stars, filament bulbs, and fluorescent molecules in a microscopic sample.

Incoherent illumination can be used in a SPIFI microscope, and a $4f$ image relay will produce an image of the modulator disk at the focal plane. However, when the mutual intensity function drops to zero in an area smaller than the total illumination intensity area in the focal plane, then the beam can be thought of as comprising multiple coherence areas. Roughly speaking, field points within a coherence area can generate interference when propagated and overlapped at a new detection plane. However, these field points will not interfere with light originating from a different region in the focal plane that is outside the coherence area. Rather, it is merely the sum of intensities from different coherence regions in the focal plane that yield the total measurable intensity at the new detection plane. This leads to an approach of decomposing a beam into spatially coherent beamlets, propagating each beamlet, and then summing the intensities of each beamlet at the plane of interest. This is a more complicated problem than we treat in this work.

Although we restrict ourselves to spatially coherent light for illuminating the sample, we will treat the signal light emanating from the sample as either coherent or incoherent. This is one of the key features of SPIFI microscopes - the modulated intensity patterns in the focal volume due to coherent beam interference impart a modulated signature onto the signal light emitted by the sample, regardless of the coherence state of the emitted response. This feature enables key advances, like applying holographic reconstruction tools to incoherent fluorescent light [50]. For multiphoton excitation, it enables super-resolution imaging by the same mechanism

for both incoherent two-photon fluorescence, and coherent second harmonic generations [51], which is the main result of this work.

CHAPTER 3

IMAGE FORMATION IN AN MP-SPIFI MICROSCOPE

In this chapter I present the novel mechanism by which multiphoton spatial frequency modulated imaging generates resolution beyond the diffraction limit for both coherent and incoherent optical responses in a sample. I start by describing the image formation process in linear SPIFI through the twin viewpoints of (1) sequential spatial frequency projections and (2) multiplexed frequency modulation. The former is used to show how the patterned illumination in SPIFI, in combination with a nonlinear optical interaction, generates spatial frequencies in the sample greater than the maximum spatial frequency passed by the objective lens. Since the spatial frequency bandwidth is inversely proportional to optical resolution, MP-SPIFI is therefore capable of generating images with finer detail than allowed under standard, diffraction-limited coherent imaging conditions. The theoretical limit yields a resolution approximately 2x better than achievable with standard 2-photon laser-scanning microscopy using the same laser & microscope optics.

3.1 Brief Conceptual Overview

3.1.1 Line Imaging with a Single Pixel and the Fourier Basis

Many imaging instruments measure a quantity that is proportional to the spatially-integrated product of the illumination light and the sample. In the simplest possible form, this can be described mathematically as

$$S(t) \propto \int\int I(x,y,t)\, C(x,y)\, \mathrm{d}x\, \mathrm{d}y \tag{3.1}$$

where the object is described generally as a contrast distribution $C(x,y)$, and I is the illumination intensity. The product of these two quantities is some form of optical signal light, which is transferred to a detector. Unlike a camera, a single pixel detector simply integrates the detected intensity. For example, in laser-scanning microscopy, the illumination is a tightly focused focal volume that is raster scanned across the object. The intensity of the focal volume is propor-

tional to the illumination system's point spread function, $I \propto PSF(x,y)$. Serially scanning this focus across the sample gathers the information for an image, with measured signal S(t):

$$S(x_0,y_0) \propto \int_{x,y} PSF\left(x_0-x, y_0-y\right) C\left(x,y\right) \mathrm{d}x\mathrm{d}y \quad = \quad C\left(x,y\right) \underset{x,y}{*} PSF\left(x,y\right) \tag{3.2}$$

where we have used the real-valued property of the PSF to reverse the sign in the argument of the PSF, allowing us to write the result as a convolution.

In a SPIFI microscope, the illumination is brought to a focus in one dimension, but in the other dimension it consists of a series of spatial patterns represented by a function m, so that the intensity is $I(x(t),y) \propto PSF\left(y\right)\mathrm{m}(x,t)$. The measured signal, after scanning the line focus in y and projecting the temporal sequence of patterns along x, is:

$$S(t,y_0) \propto \int_{x,y} PSF(y_0-y)\,\mathrm{m}(x,t)\,C(x,y)\mathrm{d}x\mathrm{d}y \quad = \quad PSF(y) \underset{y}{*} \int_x \mathrm{m}(x,t)\,C(x,y)\mathrm{d}x \tag{3.3}$$

For a general function, $\mathrm{m}(x,t)$, reconstructing the object, $C(x)$ is an inverse problem whose mathematical treatment depends on the physical model of the object and modulation. In SPIFI, the entire inverse problem is solved by a simple Fourier Transform, which is numerically very fast thanks to the fast Fourier Transform (FFT) algorithm [52]. This is accomplished by strategically choosing the pattern function to contain a term that has the form of the Fourier kernel, $\mathrm{m}(x,t) \propto \mathrm{e}^{2\pi \mathrm{i} f_x(t) x}$, where $f_x(t)$ is a function describing the projected spatial frequency as a function of time. In the case where f_x is a linear function of time, such as $f_x(t) = \kappa t$, then we can write:

$$S(t,y_0) \propto PSF(y) \underset{y}{*} \int C(x,y)\,\mathrm{e}^{2\pi \mathrm{i} \kappa x t}\,\mathrm{d}x \quad = \quad PSF(y) \underset{y}{*} C[f_x(t),y] \tag{3.4}$$

The signal, S, now takes on the appearance of a Fourier transform over x, with the conjugate variable $f_x = \kappa t$. This indicates that S contains information to recover an image of the object by an inverse Fourier Transform of the signal along the x dimension, subject to convolution with the system PSF in y:

$$C(x, y_0) \propto PSF(y) \underset{y}{*} \mathscr{F}_x^{-1}\{S(f_x, y_0)\} \tag{3.5}$$

We present this idealized case in order to demonstrate the key principle of image formation using Fourier basis illumination patterns in a SPIFI microscope. The reader is referred to well-known results [53–55] for images generated in this fashion. In the sections that follow, we will describe the SPIFI microscope in detail, with an emphasis on the exact nature of the illumination patterns in the focal volume, and the resulting imaging properties of the microscope.

3.1.2 Frequency Modulated Imaging

Although we have discussed image formation in the context of Fourier basis projections, the Fourier kernel $\exp[\mathrm{i}2\pi\kappa x t]$ allows for an alternate viewpoint on the imaging process. Instead of the grouping $f_x(t) = \kappa t$, we can write $f_t(x) = \kappa x$, we $f_t(x)$ is a modulation frequency that varies with horizontal position x.

Frequency modulation techniques are often used in conjunction with a single pixel detector, such as a photodiode or photomultiplier tube (PMT), which have high electronic bandwidths. For example, pump-probe spectroscopy typically modulates a laser beam at kHz - MHz rates in order to be well above the 1/f noise regime of most lasers, in order to look for small signals against large background [56]. In contrast, scientific camera readout times limit frame rates to $\sim$ 1 kHz. However, while single pixel detectors can be sampled at MHz or GHz rates, their frame rate is slowed by the serial scanning of point excitation over space. Therefore, a strategy that utilizes single pixel detectors while decreasing the spatial scan dimensionality can generate large frame rates [54].

A complex intensity given by $I = PSF(y) \exp\left[\mathrm{i}2\pi f_t(x) t\right]$ extends the frequency modulation approach to a continuum of x spatial positions along a line focus. The simplest implementation of this idea uses a spinning reticle to impart a range of frequency modulations to a line of illumination light [53]. This idea has also been implemented using a liquid crystal spatial light modulator [55], or an acousto-optic deflector [54], which have the advantage of being non-inertial modulators, albeit at a significant cost increase. In each of these references, modulation was

performed over a 1D array of spatial positions, with line-scanning to form a 2D image. However, it is possible to extend these techniques to a two-dimensional modulation scheme [57].

3.2 SPIFI modulator pattern

How does one form the modulation pattern to represent the Fourier kernel? One approach makes use of a Cartesian spatial light modulator, such as a digital mirror device or a liquid crystal device [55]. The approach we use in this work employs a spinning reticle, where each radial position is linked to a unique modulation frequency [53, 58–60]. The disk can be conceived of as a set of concentric rings, where each ring represents a path that is a cosine modulation with some number of cycles per revolution, $N(r)$. The mask function in polar coordinates, for the ring at radius r with N cycles per revolution, is:

$$\mathrm{m}(r,\phi) = \frac{1}{2} + \frac{1}{2}\cos\big(N(r)\,\phi\big) \tag{3.6}$$

where the factors of $\frac{1}{2}$ take into account the positive semi-definite nature of the modulation. Note that $N(r) = N$ represents the pattern for a standard chopper wheel.

For this work, we choose a simple linear relationship between number of cycles and radius, $N(r) = \Delta_k r$, with Δ_k the scaling factor determining how rapidly the modulation rate scales with radius. Two practical considerations must also be accounted for. In the lab frame, the beam is stationary and the mask is rotated, and therefore at the fixed beam location, the mask presents continuously incremented angular positions. This rotational offset for a spinning disk with angular velocity ω_r, is represented by the temporal parameterization $\phi + \omega_r t$, where the disk is spinning in the clockwise direction when viewed by the approaching laser beam. Secondly, the modulators used here are printed with a binary chrome-on-glass pattern, which we model with the signum function:

$$\mathrm{sgn}(z) = \begin{cases} 1, & \text{if } z \geq 0 \\ -1, & \text{otherwise} \end{cases} \tag{3.7}$$

The mask function for our experiment is therefore given as:

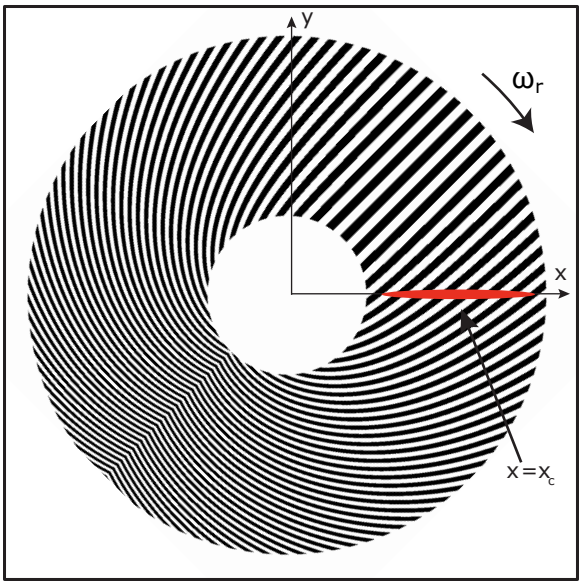

Figure 3.1: SPIFI modulator disk, at angular increment $\Delta\phi = -\pi/4$. A laser line focus is shown at polar coordinate $\phi = 0$, centered at $x = x_o$.

$$\mathrm{m}(r,\phi,t) = \frac{1}{2} + \frac{1}{2}\mathrm{sgn}\left[\cos\left(\Delta_k\, r\, \left(\phi + \omega_r\, t\right)\right)\right] \tag{3.8}$$

which is plotted in Figure (3.1).

This design is known as the Lovell reticle [60]. It's use for imaging was first reported with the modulator placed in the detection path [59]. However, SPIFI utilizes the modulator in the illumination path [53], which in combination with a nonlinear excitation, allows for the unique resolution-enhancing capabilities of MP-SPIFI [51]. To understand how the modulator contributes to resolving beyond the diffraction limit, it is helpful to view the modulator in terms of spatial frequency projections.

Modulator Spatial Frequencies

For a tightly line-focused laser beam positioned along $\phi = 0$, the modulator takes on the appearance of a diffraction grating. This is made clear by transforming the mask cosine argument into Cartesian coordinates, $\mathrm{m}\left(r,\phi\right) \rightarrow \mathrm{m}\left(x,y\right)$. In order to do this, we need to compute the Cartesian angular spatial frequencies [41, 58]:

$$k_x = \frac{\partial \mathrm{m}}{\partial x} = \frac{\partial \mathrm{m}}{\partial r}\frac{\partial r}{\partial x} + \frac{\partial \mathrm{m}}{\partial \phi}\frac{\partial \phi}{\partial x} \qquad k_y = \frac{\partial \mathrm{m}}{\partial y} = \frac{\partial \mathrm{m}}{\partial r}\frac{\partial r}{\partial y} + \frac{\partial \mathrm{m}}{\partial \phi}\frac{\partial \phi}{\partial y} \tag{3.9}$$

Using the trigonometric relations $\phi(x,y) = \mathrm{atan}\left(y/x\right)$ and $r = \sqrt{x^2+y^2}$, we can compute:

$$\frac{\partial \phi}{\partial x} = \frac{-y}{x^2+y^2} = \frac{-\sin(\phi)}{r} \tag{3.10}$$

$$\frac{\partial \phi}{\partial y} = \frac{x}{x^2+y^2} = \frac{\cos(\phi)}{r} \tag{3.11}$$

$$\frac{\partial r}{\partial x} = \frac{x}{\sqrt{x^2+y^2}} = \cos(\phi) \tag{3.12}$$

$$\frac{\partial r}{\partial y} = \frac{y}{\sqrt{x^2+y^2}} = \sin(\phi) \tag{3.13}$$

Thus, a general polar-coordinate cosine argument $\mathrm{m}(r,\phi,t)$ can be recast into Cartesian coordinates with the following angular spatial frequencies:

$$k_x = \cos\phi\frac{\partial \mathrm{m}}{\partial r} - \frac{\sin\phi}{r}\frac{\partial \mathrm{m}}{\partial \phi} \qquad k_y = \sin\phi\frac{\partial \mathrm{m}}{\partial r} + \frac{\cos\phi}{r}\frac{\partial \mathrm{m}}{\partial \phi} \tag{3.14}$$

For our particular reticle design, we have:

$$\frac{\partial \mathrm{m}}{\partial r} = \Delta_k\left(\phi + 2\pi\nu_r t\right) \qquad \frac{\partial \mathrm{m}}{\partial \phi} = \Delta_k r \tag{3.15}$$

where we have used $\omega_r = 2\pi\nu_r$, where ν_r is the rotational rate of the disk, e.g. revolutions per second, measured in Hertz.

The mask transmission function in the vicinity of the laser line focus, along $\phi = 0$, can now be written in Cartesian coordinates as:

$$\mathrm{m}(x,y,t) = \frac{1}{2} + \frac{1}{2}\mathrm{sgn}\left[\cos\left(2\pi\Delta_k\nu_r t x + \Delta_k y\right)\right] \tag{3.16}$$

The fundamental spatial frequencies are given by:

$$f_{g_x}(t) = \Delta_k \nu_r \, t \equiv \kappa \, t \qquad\qquad f_{g_y} = \frac{\Delta_k}{2\pi} \tag{3.17}$$

We see that the line focus experiences a set of two-dimensional gratings. The fundamental grating consists of a time-varying spatial frequency along x and a time-stationary spatial frequency along y. The horizontal grating changes density at the linear rate given by κ. We have used the subscript g to denote that these spatial frequencies correspond to a grating pattern on the modulator.

Of course, the lateral spatial frequency does not increase infinitely. The maximum fundamental lateral spatial frequency on the disk for a given Δ_k can be found by evaluating Equations (3.14) and (3.15) at $\phi = 0$, with the angular increment $\omega_r t = \pi$, resulting in $f_{g_{x,max}} = \Delta_k/2$. This finite bandwidth can be implemented by multiplying the signum function in Equation (3.16) with a rectangular ('boxcar') function, Π_m, where the m subscript associates this function to the mask:

$$\Pi_m = \text{rect}\left(\frac{f_{g_x}}{\Delta_k}\right) = \begin{cases} 1, & |f_{g_x}(t)| \leq \frac{\Delta_k}{2} \\ 0, & \text{otherwise} \end{cases} \tag{3.18}$$

Viewing the mask as a time-varying grating allows us to see SPIFI as a form of single-pixel, coded illumination imaging. The two most common basis sets for coded illumination are the Hadamard and Fourier bases [61]. The SPIFI signal, Eqn. (3.1), which integrates over the product of the object, C(x), and the mask illumination patterns, Eqn. (3.16), is clearly a Fourier basis projection technique.

Modulator Temporal Frequencies

We can group parameters in the mask equation (3.16) a bit differently to see that this modulator also imparts temporal modulation frequencies as expected to an incident line focus.

Defining the temporal modulation rate along the line $(x, 0)$ as

$$\nu_{mod}(x) = \Delta_k \nu_r x \equiv \kappa \, x \tag{3.19}$$

the mask function can be written in a way that emphasizes that it imparts a varying modulation frequency along x at the radial lineout $y = 0$:

$$\mathrm{m}(x, 0, t) = \frac{1}{2} + \frac{1}{2}\mathrm{sgn}\left[\cos\left(2\pi\nu_{mod}(x)\, t\right)\right] \tag{3.20}$$

precisely as planned in the modulator design. According to Eqn. (3.19), the modulation frequency increases at a linear rate κ with increasing x position. This linear change in frequency is often referred to as chirp. The chirp given by κ is a direct consequence of the chirp imparted by the printed mask modulation rate parameter, Δ_k. However, κ can also be flexibly adjusted in the lab via changes to the disk speed, ν_r.

Spatial frequency harmonics from binary printing

The binary nature of the printed modulator creates harmonics of the fundamental set of temporal modulation frequencies. In the spatial frequency projection picture, we have harmonics of the set of fundamental spatial frequencies. To handle this in a mathematically flexible way, we write the sgn(cos( )) function, which is effectively a periodic square wave in x & y, in terms of its Fourier series decomposition. Using Θ as a dummy variable to represent the phase argument in Eqn. (3.16), $\Theta = 2\pi\Delta_k\nu_r\, t x + \Delta_k y$, we can write the mask transmission function as:

$$\begin{aligned}
\mathrm{m} &= \frac{1}{2} + \frac{1}{2}\mathrm{sgn}\left[\cos\Theta\right] && (3.21)\\
&\approx \frac{1}{2} + \frac{2}{\pi}\cos\Theta - \frac{2}{3\pi}\cos 3\Theta + \frac{2}{5\pi}\cos 5\Theta - \frac{2}{7\pi}\cos 7\Theta\ldots && (3.22)\\
&= a_0 + \sum_{j=1}^{\infty} 2a_j \cos j\Theta && (3.23)\\
&= \sum_{j=-\infty}^{\infty} a_j \mathrm{e}^{\mathrm{i}j\Theta} && (3.24)
\end{aligned}$$

where in the last line we used Euler's identity to write the function compactly. The a_j coefficients are given by the formula:

$$a_j = \frac{1}{2}\mathrm{sinc}\left(\frac{j}{2}\right), \quad j \in \mathbb{Z} \tag{3.25}$$

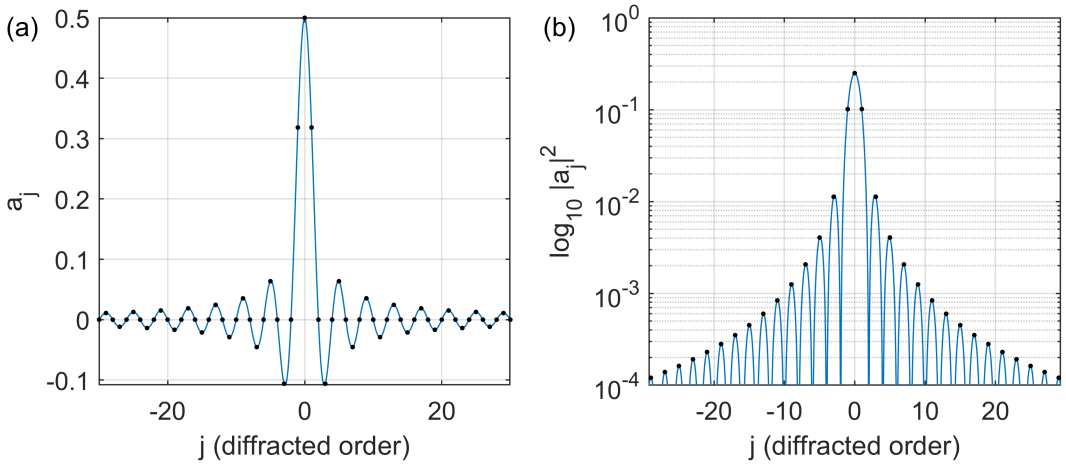

Figure 3.2: Diffracted Order Coefficients a_j for a binary square wave grating with 50% duty cycle at normal incidence. Black dots correspond to $j \in \mathbb{Z}$, which are overlaid on a blue line where j is a continuous distribution for better visualization of the functional forms of a_j and $|a_j|^2$. (a) Field amplitude coefficients a_j for each diffracted order, j. (b) Intensity coefficients, $|a_j|^2$, plotted on log scale.

which is plotted in Fig. 3.2(a). For the square wave grating pattern used here, even-valued j land on zeros of the sinc function, and therefore only odd diffracted orders are generated, as is well-known. Note that we assume the convention $\text{sinc}(u) = \frac{\sin(\pi u)}{\pi u}$. Since the sinc function is symmetric, $\pm j$ pairs share the same coefficient, a_j. For a 50% duty cycle square wave amplitude grating, half of the light intensity is transmitted through the grating apertures, while the other half is reflected backward or absorbed. Thus, the sum over $|a_j|^2$ in Fig. 3.2(b) is 0.5. In the forward direction, the undiffracted $j = 0$ field contains 25% of the total incident power while the $j = \pm 1$ diffracted orders contain about 11% each.

Each harmonic has a maximum spatial frequency imparted by the mask that scales as j times the maximum fundamental spatial frequency. Thus, we introduce a general boxcar window function Π_{m_j} as an extension of Π_m in Eqn. (3.18) :

$$\Pi_{m_j}(f_{g_x}) = \text{rect}\left(\frac{f_{g_x}}{j\,\Delta_k}\right) = \begin{cases} 1, & |f_{g_x}(t)| \le j\frac{\Delta_k}{2} \\ 0, & \text{otherwise} \end{cases} \tag{3.26}$$

The complete mask transmission function, written in Cartesian coordinates, for the region along the radial line at $\phi = 0$, is therefore the temporally-changing Fourier sum of spatial frequency harmonics given by:

$$\mathrm{m}(x, y; t) = \sum_{j=-\infty}^{\infty} \Pi_{m_j} a_j \mathrm{e}^{\mathrm{i}2\pi j \left[f_{g_x}(t)\, x + f_{g_y} y \right]} \tag{3.27}$$

with the amplitude coefficients a_j, window functions Π_{m_j}, and Cartesian spatial frequencies $f_{g_x}(t)$ and f_{g_y} given by Equations (3.25), (3.26), and (3.17), respectively. As the mask rotates at a linear rate, the transmission function in Eqn. (3.27) has the form of a linearly time-varying binary diffraction grating in x, and a time-stationary binary grating in y.

Modulator Manufacturing

The modulators used in this work were designed to fully utilize the 3600 dot-per-inch (DPI) resolution available at the manufacturer (Inlight Gobos, Dallas, TX). At this resolution, the smallest dot size is 7.05μm, and thus the smallest on/off period is 14.1μm, which is a maximum spatial frequency of $f_{x_{max}} = 70.9 \frac{periods}{mm}$. By setting the mask modulation-chirp parameter $\Delta_k = f_{x_{max}}$, this maximum spatial frequency is obtained along the radial lineout at $\phi = 2\pi$, on a mask where ϕ scans the range $(0, 2\pi]$. However, for ease in FFT processing of our raw data, we opted for a zero-centered set of spatial frequencies, such that ϕ scans the range $(-\pi, \pi)$. In this case, the radial lineout with highest spatial frequency occurs at $\phi = \pm\pi$, where $f_x = \Delta_k/2$, utilizing half the available print resolution.

3.3 Computing the Spatiotemporal Illumination Intensity at the Focal Plane

In order to generate the sequence of Fourier basis projections at the focal plane of the microscope, the appropriate mask is designed and installed at a conjugate plane of a $4f$ image relay system. Incident light is focused into a line on the mask in order to sample the modulation pattern, and this modulated line focus immediately after the mask is then image-relayed to the object focal plane, with some demagnification M. Signal light is collected and integrated on

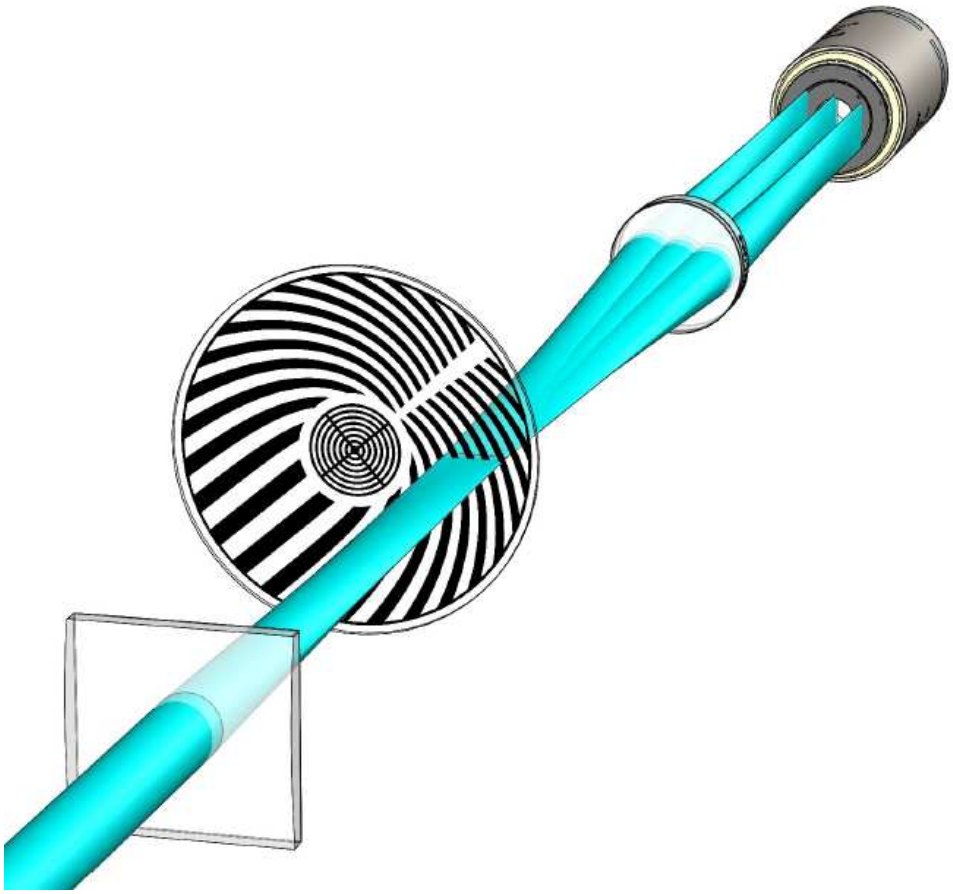

Figure 3.3: 3D visualization of the MP-SPIFI illumination scheme. A collimated laser beam is focused with a cylindrical lens to a radial line on the modulator disk. The mask pattern on the disk is subsequently imaged to the sample plane, by way of transferring the diffracted orders created by the pattern through a $4f$ image relay system consisting of a tube lens and an objective lens. The diffracted orders are subject to spatial filtering at the back aperture of the objective lens. Only the three lowest diffracted orders, $j \in [-1, 0, 1]$ are depicted for simplicity.

a single pixel detector. The SPIFI microscope as a $4f$ image relay system from the mask to the sample is conceptually depicted with a 3D rendering in Fig. 3.3 and with 2D views in the (x, z) and (y, z) planes in Fig. 3.4.

3.3.1 Diffraction from the mask

Assuming the modulator is infinitely thin - justified for a chrome reflective layer - the electric field transmitted through the mask is formed by the product of the incident field and the mask function, $E_m = E_i \, \mathrm{m}$, where m is given by Eqn. (3.27):

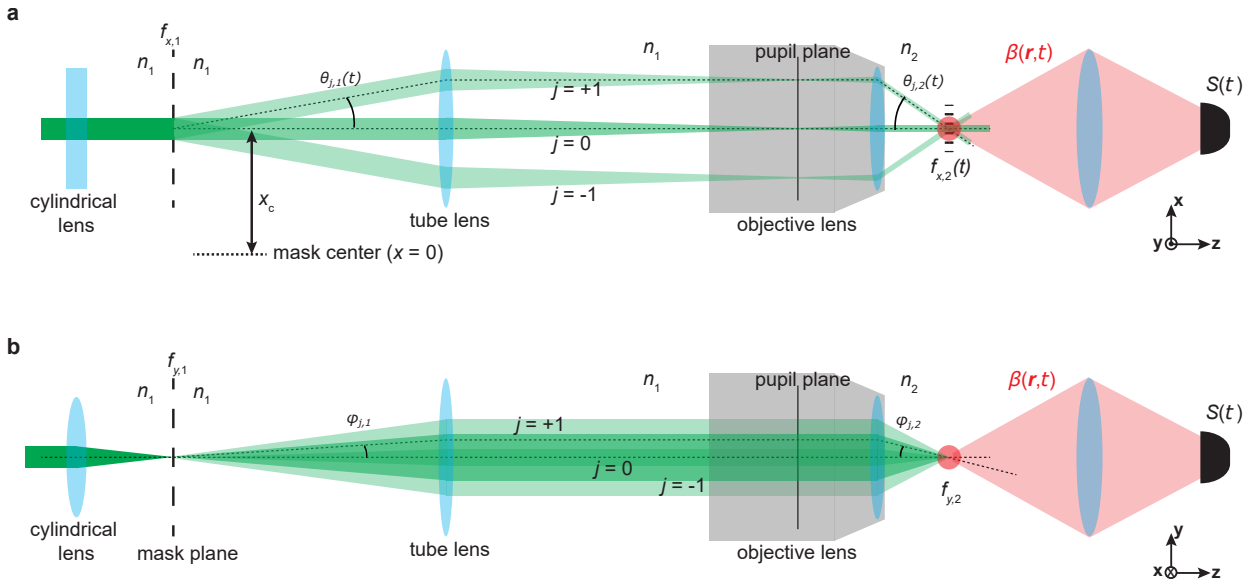

Figure 3.4: MP-SPIFI 4-f imaging system. (a) Looking down on the (x,z) distribution of light in the microscope. The diffracted orders from the mask with time-varying diffraction angle $\theta_{j,1}(t)$ are imaged to the object region with angular magnification, $\theta_{j,2}(t) \approx \theta_{j,1}(t)/M$. (b) Looking at the (y,z) distribution of light in the microscope, from the side. The diffracted orders have a small, time-stationary diffraction angle $\phi_{j,1}$ in the vertical direction from the mask. Reprinted from Ref. [51].

$$E_m = E_i \sum_{j=-\infty}^{\infty} \Pi_{m_j} a_j e^{i2\pi j\left[f_{g_x}(t)\,x + f_{g_y} y\right]} \tag{3.28}$$

In section 3.2 we justified the description of the spinning modulator as a diffraction grating with time-varying spatial frequency in x and time-stationary spatial frequency in y. We should expect a grating to diffract the incident field at normal incidence into multiple orders, with angles given by the grating equation: $\sin\theta = j\lambda f_g$, where λ is the wavelength, f_g is the fundamental grating spatial frequency. Eqn. (3.28) demonstrates that the total field after the mask has indeed become a sum of j discrete copies of the incident field, each traveling in unique directions that differ by the integer factor j. These directions vary in time in x as $\theta_x(t) = \sin^{-1}(j\lambda f_{g_x}(t))$, but are constant in y, $\theta_y = \sin^{-1}(j\lambda f_{g_y})$. The $j = 0$ and $j = \pm 1$ orders are depicted in Figure 3.4. Each a_j coefficient imparts an amplitude scaling to the j^{th} diffracted field.

We neglected one important point in Eqn. (3.28) - namely, the optical axis of the microscope passes through a point $(x,y) = (x_o, 0)$ on the mask, as depicted in Fig. 3.1. Because of this lat-

eral translation between coordinate systems, the transmitted field should actually be written $E_m(x,y) = E_i(x,y)\,\mathrm{m}(x+x_o,y)$, such that the origin of the optic axis is centered at $(x_o,0)$ on the mask. Thus, the total field emerging from the mask is:

$$E_m\left(x,y,t\right) = E_i \sum_{j=-\infty}^{\infty} \Pi_{m_j} a_j \mathrm{e}^{\mathrm{i}2\pi j\left[f_{g_x}(t)\,(x+x_o)+f_{g_y}y\right]} \tag{3.29}$$

The presence of the constant x_o in the phase argument imparts a horizontal phase shift to the spatial frequencies f_{g_x}. As the spatial frequency f_{g_x} changes with time, there is a corresponding translation of the spatial frequency with time. This phase shift plays a key role in the image recovery process, as we will see later.

Although the Fourier series representation of the binary mask pattern in principle allows $j \to \infty$, for any given grating there is an upper limit on the number of diffracted orders that physically propagate to the far field. The dispersion relationship given by the Helmholtz equation places a fundamental constraint on field propagation away from the grating. For a field at normal incidence the transmitted field will have the axial spatial frequency

$$k_z = \sqrt{k^2 - (jk_{g_x})^2 - (jk_{g_y})^2} = k\sqrt{1 - \left[j^2\lambda^2\left(f_{g_x}^2 + f_{g_y}^2\right)\right]} \tag{3.30}$$

If the grating spatial frequencies are high enough that the term in brackets under the radical exceeds 1, then k_z becomes imaginary, and the field attenuates rapidly along z. In other words, the field is evanescent, and will not propagate to the far field. For our modulator designed with chirp parameter $\Delta_k = 70mm^{-1}$, and illumination at $\lambda = 1\mu m$, there is a maximum diffraction angle of about 2 degrees for the first diffracted order. It is not until the $j = 28^{th}$ diffracted order that the maximum spatial frequency imparted by the mask causes the diffracted order to become evanescent at certain scan times near the maximum. However, for mask spatial frequencies close to zero, many more diffracted orders than this will propagate, although their relative energy given by $|a_j|^2$ is negligibly small.

Equipped with a description of the electric field diffracted by the mask, we will now model the propagation of this field through a $4f$ image relay system. The diffracted field at the mask is situated at the back focal plane of the tube lens in the system. This field is relay imaged with demagnification M to the front focal plane of the objective lens (see Fig. 3.4), subject to low-pass filtering by the system pupil. We will take the approach of propagating each diffracted order j through the system, and then reconstituting the total field in the sample region as a linear sum of all diffracted orders. This allows for notational simplicity, and allows us to apply pupil effects uniquely to each order. We shall denote three transverse planes in our analysis - the mask plane, the pupil plane, and the focal plane in the sample region - with the subscripts m, p, and s respectively. We will also write $x_{m_c} = x_o$, as the horizontal offset is simply a constant, and not a variable that becomes involved in the following integration.

3.3.2 2f propagation from Mask to Pupil

Computing propagation in a $4f$ optical setup is equivalent to computing propagation through two $2f$ setups in series. The tube lens is typically a 1"-2" diameter optic with a long focal length between 150 - 250 mm. This low numerical aperture falls comfortably within the paraxial regime, where we can justify the use of the Fresnel diffraction integral to compute propagation from the mask to the pupil. We therefore make use of the field transformation dictated by a paraxial lens in the $2f$ configuration, given by Equation (2.79). Moving from the front focal plane to the back focal plane of our tube lens, the field in the pupil is given by:

$$E_{j,p}\left(x_p, y_p, t\right) = \frac{\mathrm{e}^{\mathrm{i}2kf_1}}{\mathrm{i}\lambda f_1} \int_{x_m, y_m} E_{j,m}\left(x_m, y_m, t\right) \mathrm{e}^{-\mathrm{i}\frac{2\pi}{\lambda f_1}\left[x_p x_m + y_p y_m\right]} \mathrm{d}x_m \mathrm{d}y_m \tag{3.31}$$

Using Eqn. (3.29), a single diffracted order emerging from the mask is:

$$E_{j,m}\left(x_m, y_m, t\right) = E_i\left(x_m, y_m\right) \Pi_{m_j} a_j \mathrm{e}^{\mathrm{i}2\pi j\left[f_{g_x}(t)\,(x+x_o)+f_{g_y} y\right]} \tag{3.32}$$

Inserting this into Eqn. (3.31) and carrying out the integration produces the field at the pupil plane of the $4f$ image relay system:

$$E_{j,p} = \frac{e^{i2kf_1}}{i\lambda f_1}\Pi_{m_j} a_j e^{i2\pi j f_{g_x}(t)\, x_o} \hat{E}_i\left(\frac{x_p}{\lambda f_1} - j f_{g_x}(t)\,,\, \frac{y_p}{\lambda f_1} - j f_{g_y}\right) \tag{3.33}$$

where $\hat{E}_i$ is the transverse 2D Fourier transform of the incident field on the mask, evaluated at the spatial frequencies $\left(f_{x,m}\,,\, f_{y,m}\right) = \left(\frac{x_p}{\lambda f_1} - j f_{g_x}(t)\,,\, \frac{y_p}{\lambda f_1} - j f_{g_y}\right)$. We can also write the pupil field in a slightly different way that emphasizes the fact that the j^{th} diffracted copy of $\hat{E}_i$ has been shifted and scaled:

$$E_{j,p} = \frac{e^{i2kf_1}}{i\lambda f_1}\Pi_{m_j} a_j e^{i2\pi j f_{g_x}(t)\, x_o} \hat{E}_i\left(\frac{1}{\lambda f_1}\left(x_p - x_{p_0,j}(t)\,,\, y_p - y_{p_0,j}\right)\right) \tag{3.34}$$

where x_{p_0} is the time-varying horizontal shift of the j^{th} diffracted order,

$$x_{p_0,j}(t) = j\lambda f_1 f_{g_x}(t) \tag{3.35}$$

and $y_{p_0,j}$ is the time-stationary vertical shift of the j^{th} diffracted order,

$$y_{p_0,j} = j\lambda f_1 f_{g_y} \tag{3.36}$$

We now seek to gain some physical understanding of the diffracted fields in the pupil plane given by Eqns. (3.33) and (3.34). Up to this point we have not specified the form of the field incident on the mask, $E_i(x_m, y_m)$, other than to stipulate that E_i is sufficiently narrow in the y direction at the mask to sample one horizontal spatial frequency at a time as the mask rotates. This requirement allowed us to derive the form of the mask function given in Eqn. (3.27). Figure 3.5 provides an illustration of E_i at the mask and E_p in the pupil plane of the $4f$ system, for the case where E_i is assumed to be a Gaussian laser beam at the mask with a flat wavefront and widths $w_x \gg w_y$. This situation is generated when a collimated beam is focused onto the mask by a cylindrical lens, as depicted in Fig. 3.4.

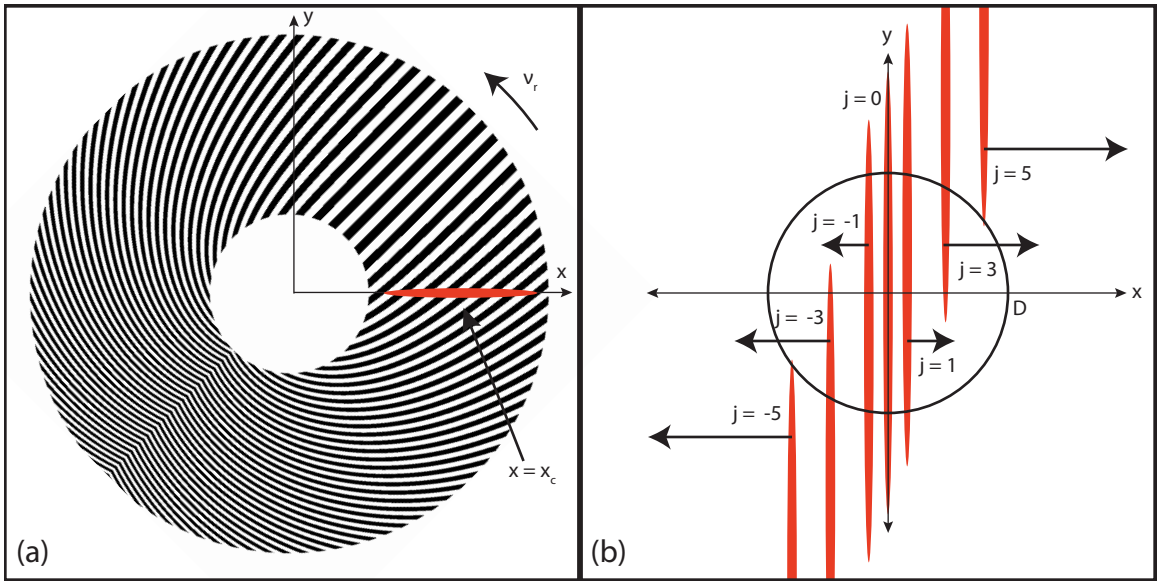

Figure 3.5: (a) The disk modulator, printed as a binary amplitude grating with 50% duty cycle. As the disk rotates, the line focus is diffracted by a binary grating that equates to a superposition of j sinusoidal gratings, each with horizontal time-varying groove density $f_{x_j}(t) = j\,\nu_r\,\Delta_k\,t$, and vertical time-stationary groove density $f_y = j\,\frac{\Delta_k}{2\pi}$. (b) Intensity distribution in a Fourier plane of the mask. Diffracted beams scan horizontally with time. Scan rate scales with j (denoted by magnitude of arrows), as $j\nu_r\Delta_k$. Circular aperture represents the Fourier pupil presented by the back aperture of the system objective lens. (ν_r : disk rotation speed; Δ_k: mask design parameter, corresponding to rate of increase of modulation frequency with radius, $f_m od(x) = \Delta_k x$; D: diameter of objective lens back aperture. Reprinted from Ref. [62] with permission.

Let us examine Eqn. (3.34) as depicted in Figure 3.5(b). First, the lateral line focus at the mask, where the beam profile has widths $w_{x_m} \gg w_{y_m}$, has been transformed into a set of vertical line foci, with widths $w_{y_p} \gg w_{x_p}$. Secondly, we see that the angular directions of the diffracted fields emerging from the mask have been mapped into horizontal and vertical offsets in the Fourier plane. Moreover, the time-varying x-spatial frequency of the mask has the physical effect of causing diffracted orders to scan laterally across the Fourier plane as a function of time. The y-spatial frequency component of the mask imparts only a constant vertical diffraction angle for each beam, which can be useful for spatial filtering.

3.3.3 Filtering of Diffracted Fields at the Pupil

Nearly all realistic microscope scenarios use the full bandwidth of the objective lens for maximum resolution. A careful model must handle the pupil apodization present in this case. Our

microscope is designed such that the maximum fundamental spatial frequency in x imparted by the mask exceeds that of the optical relay system. This ensures that the focusing angles at the sample for the bright $j = \pm 1$ orders will pass through the entire NA of the objective lens, for diffraction-limited x-resolution. Thus, the pupil is as a low-pass spatial frequency filter, and because x-spatial frequencies are associated with scan time, the pupil can also be conceived of as a temporal gating function. As the mask rotates from $\phi = 0$ to $\phi = \pi$, the pupil will sequentially extinguish each scanning diffracted order, from highest to lowest, until only the stationary zero-order beam remains.

It is evident from examination of Figure 3.5(b) that if the diffracted orders scan to the edge of the pupil, then the aperture also vertically truncates each of the scanning beams in a time-varying fashion. This has important implications for the fields transferred to the sample plane, which we will discuss in Chapter 7.

Pupil Approximation in SPIFI

The highly anamorphic beams generated in SPIFI lend themselves to a simple approximation at the pupil. Being very narrow in x, we can easily assume that each horizontally scanning beam is so thin that it experiences no horizontal apodization at any scan position, until at the pupil boundary it is simply extinguished. This can be represented by a rectangle function, $\text{rect}\left[\frac{x_{p_0,j}(t)}{2x_c}\right]$, which serves as a window limiting the maximum horizontal offset. Meanwhile, being very tall in y, each scanning beam experiences a rectangular aperture of time-varying height in the vertical direction. This height is given by the geometric chord across the circle at each x-scan position. The pupil aperture can therefore be written as the product of independent rectangle functions:

$$\mathcal{P}(x_p, y_p; t) = \Pi_{x_j}\Pi_{y_j} = \text{rect}\left[\frac{x_{p_0,j}(t)}{2x_c}\right]\ \text{rect}\left[\frac{y_p}{2y_{c,j}(t)}\right] \tag{3.37}$$

The rectangle functions Π_{x_j} and Π_{y_j} are explicitly defined as:

$$\Pi_{x_j}(t) \quad = \quad \text{rect}\left[\frac{x_{p_0,j}(t)}{2x_c}\right] \quad = \quad \begin{cases} 1, & |x_{p_0,j}(t)| \leq x_c \\ 0, & \text{otherwise} \end{cases} \tag{3.38}$$

$$\Pi_{y_j}(t) \quad = \quad \text{rect}\left[\frac{y_p}{2y_{c,j}(t)}\right] \quad = \quad \begin{cases} 1, & |y_p| \leq y_{c,j}(t) \\ 0, & \text{otherwise} \end{cases} \tag{3.39}$$

The horizontal pupil cutoff is simply $x_c = r_c$. The vertical pupil cutoff for a circular aperture of radius r_c varies with the beam's x-position as:

$$y_{c,j}(t) = \text{Re}\left\{\sqrt{r_c^2 - x_{p_0,j}^2(t)}\right\} \tag{3.40}$$

This is depicted in Fig. 3.6.

3.3.4 Scalar Focal Fields in the Paraxial Limit

In subsequent sections we will employ a rigorous model for high NA focusing with vector fields, by mapping the field components onto the aplanatic focal sphere in the pupil. However, in this section, we seek a scalar solution for low to moderate NA focusing, providing intuition in a rapid fashion through simplified computations. We will do so using our simple approximation for the diffracted fields in the system Fourier plane. The field in the pupil is the product of $E_{j,p}$ given by Eqn. (3.33) and the pupil aperture $\mathcal{P}(x_p, y_p)$. We assume an aberration free system so that $\mathcal{P}$ is real-valued and simply described by the pupil geometry.

We invoke Eqn. (2.79) once again to transfer the field to the focal plane of the objective lens, which has focal length f_2:

$$E_{j,s}(x_s, y_s, t) = \frac{\exp(\text{i}2kf_2)}{\text{i}\lambda f_2} \int_{x_p}\int_{y_p} \mathcal{P}(x_p, y_p)\, E_{j,p}(x_p, y_p, t)\, \text{e}^{-\text{i}\frac{2\pi}{\lambda f_2}(x_p x_s + y_p y_s)}\, \text{d}x_p \text{d}y_p \tag{3.41}$$

where $E_{j,p}$ is given by Eqn. (3.34) and the aperture function $\mathcal{P}$ is given by Eqns. (3.37) - (3.39). In full detail,

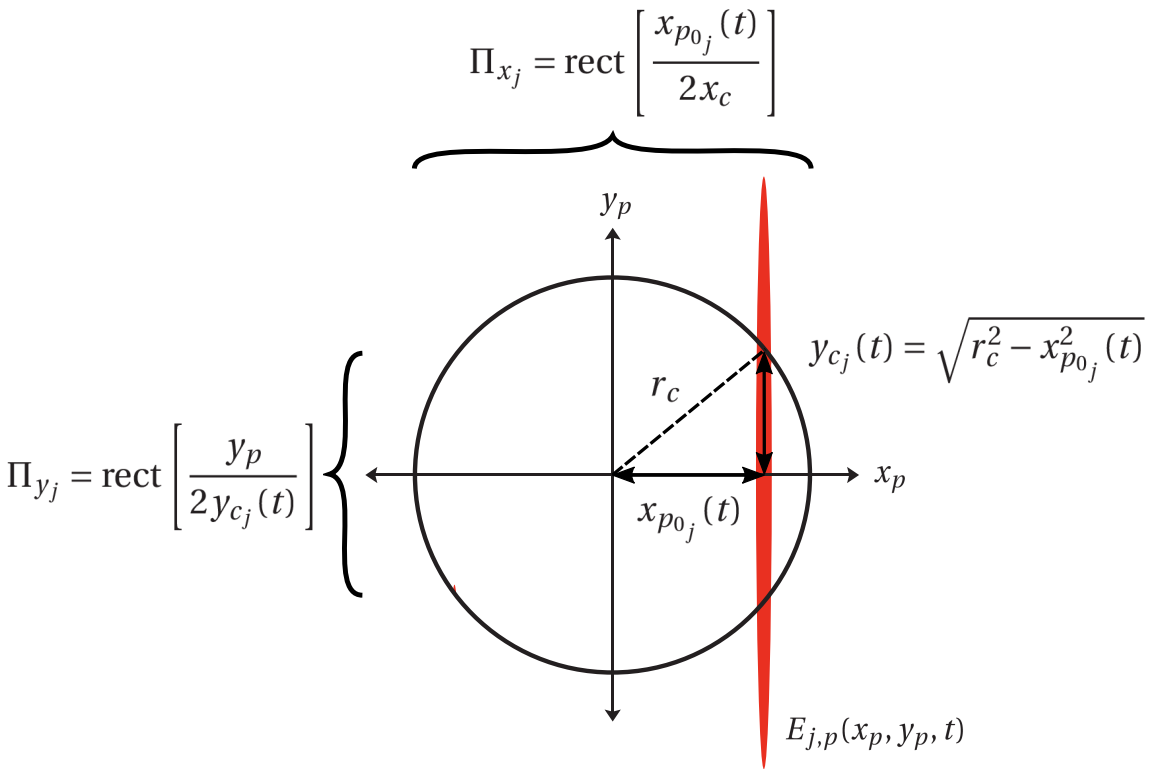

Figure 3.6: Pupil Approximation in SPIFI. We plot only one diffracted order $E_{j,p}$ in the pupil plane for clarity. $E_{j,p}$ is very narrow in x and very broad in y, therefore we can approximate the pupil as rectangle functions in x_p and y_p. $E_{j,p}$ scans horizontally across the pupil as a function of scan time, with position $x_{p_{0_j}}(t) = j\lambda f_1 f_{g_x}(t)$ given by Eqn. (3.35). In the vertical direction, the pupil is approximately a rectangle function with maximum width at $t = 0$ and a progressively decreasing width as $t \to t_c$.

$$E_{j,s}(x_s, y_s, t) = \frac{e^{i2k(f_1+f_2)}}{-\lambda^2 f_1 f_2} \Pi_{m_j} \Pi_{x_j} a_j e^{i2\pi j f_{g_x}(t) x_o} \tag{3.42}$$

$$\times \int_{x_p} \int_{y_p} \hat{E}_i \left(\frac{1}{\lambda f_1} \left(x_p - x_{p_{0,j}}(t), y_p - y_{p_{0,j}} \right) \right) e^{-i\frac{2\pi}{\lambda f_2}(x_p x_s + y_p y_s)} \, dx_p dy_p \tag{3.43}$$

A number of simplifications can be made. First, on-axis phase accumulation $\exp\left(i2k(f_1 + f_2)\right)$ is inconsequential here and can be ignored. Secondly, for an optical system where the mask diffraction is large enough to cause all diffracted orders to scan beyond the system pupil, the binary mask gating function becomes inconsequential:

$$\Pi_{m_j}\Pi_{x_j} \rightarrow \Pi_{x_j} \tag{3.44}$$

In other words, the pupil imposes the stricter gating function for the range of horizontal spatial frequencies.

Third, we make the following variable substitutions to simplify the integration:

$$x'_p = \frac{1}{\lambda f_1}\left(x_p - x_{p_0,j}(t)\right) \qquad\qquad y'_p = \frac{1}{\lambda f_1}\left(y_p - y_{p_0,j}\right) \tag{3.45}$$

where the pupil offset positions $x_{p_0,j}(t)$ and $y_{p_0,j}$ are defined in (3.35) and (3.36). Finally, we also make the assumption that the incident field and its 2D transform are separable in Cartesian coordinates, so that $\hat{E}_i = \hat{E}_{i_x}\hat{E}_{i_y}$.

The equation for the j^{th} diffracted order at the sample plane is:

$$E_{j,s}\left(x_s, y_s, t\right) = \frac{-a_j\Pi_{x_j}}{f_2/f_1}\mathrm{e}^{\mathrm{i}2\pi j f_{g_x}(t)\,x_o}\mathrm{e}^{\mathrm{i}2\pi j\frac{f_1}{f_2}\left(f_{g_x}(t)\,x_s + f_{g_y}\,ys\right)} \tag{3.46}$$

$$\times \int_{x'_p} \hat{E}_{i_x}(x'_p)\,\mathrm{e}^{\mathrm{i}2\pi\left(\frac{f_1}{f_2}x_s\right)x'_p}\,\mathrm{d}x'_p \tag{3.47}$$

$$\times \int_{y'_p} \hat{E}_{i_y}(y'_p)\Pi_{y_j}\,\mathrm{e}^{\mathrm{i}2\pi\left(\frac{f_1}{f_2}y_s\right)y'_p}\,\mathrm{d}y'_p \tag{3.48}$$

We will separate the focal field into three distinct components, which will shall refer to throughout the rest of this work. These components are outlined by Eqns. (3.46) – (3.48). The focal field for the j^{th} diffracted order is:

$$E_{j,s}\left(x_s, y_s, t\right) = v_{j,s}\left(x_s, y_s, t\right)\, p_x\left(x_s\right)\, p_{y_j}\left(y_s, t\right), \tag{3.49}$$

The first component, given by (3.46), is a plane wave field for the j^{th} diffracted order. The range of tilted plane waves described by this field is parameterized by t and capped by the gating function Π_{x_j}. We use the magnification, defined as:

$$M = -f_2/f_1 \tag{3.50}$$

to write the plane wave field component as:

$$v_{j,s}\left(x_s, y_s, t\right) = \frac{a_j}{M}\Pi_{x_j} \mathrm{e}^{\mathrm{i}2\pi j\left[f_{gx}(t)\, x_o - \frac{f_{gx}(t)}{M} x_s - \frac{f_{gy}}{M} y_s\right]} \tag{3.51}$$

The second component is the integral over x'_p in (3.47). This is simply an inverse Fourier transform of $\hat{E}_{i_x}$, returning a demagnified image of the horizontal field distribution incident on the mask. We will label this stationary field distribution p_x:

$$p_x(x_s) \;=\; \int_{x'_p} \hat{E}_{i_x}(x'_p)\, \mathrm{e}^{-\mathrm{i}2\pi\left(\frac{x_s}{M}\right)x'_p}\, \mathrm{d}x'_p \;=\; E_{i_x}\left(\frac{x_s}{M}\right) \tag{3.52}$$

The third component is the integral over y'_p in (3.48). It is complicated by the vertical pupil clipping function Π_{y_j}, which varies with time. The pupil imposes a constraint on the ability to form an image of the tight vertical field distribution E_{i_y} incident at the mask. The variable p_{y_j} is introduced to describe the integral as the spatial profile in the vertical direction at the sample plane. This spatial distribution is influenced by the form of $\hat{E}_{i_y}$ and the time-varying clipping by the aperture:

$$p_{y_j}(y_s, t) = \int_{y'_p} \Pi_{y_j}\left(y'_p, t\right) \hat{E}_{i_y}\left(y'_p\right) \mathrm{e}^{-\mathrm{i}2\pi\left(\frac{y_s}{M}\right)y'_p}\, \mathrm{d}y'_p \tag{3.53}$$

All together, the total electric field in the sample plane is the sum over diffracted orders:

$$E_s\left(x_s, y_s, t\right) = \sum_{j=-N}^{N} E_{j,s}(x_s, y_s, t) \tag{3.54}$$

where N is the highest diffracted order that is imaged to the sample plane, as discussed in Section 3.3.1. The intensity due to the total scalar field is

$$I_s\left(x_s, y_s, t\right) = \left| \sum_{j=-N}^{N} E_{j,s}(x_s, y_s, t) \right|^2 \tag{3.55}$$

Focal Field Vertical Distributions p_y for 3 common cases

We now examine the form of the focal field line focus. We will investigate 3 common pupil distributions in the vertical direction: an underfilled aperture, an aperture overfilled by a plane wave, and an aperture overfilled by a Gaussian beam. The vertical field distribution, $p_{y_j}(y_s, t)$, is given by the integral in Eqn. (3.53), where the physical problem is to compute each of the diffracted fields in the focal plane when they are clipped by the aperture in a time-varying fashion. In general, numerical techniques are required to evaluate the Eqn. (3.53). However, for these three cases of interest we can compute an analytic solution.

1. An underfilled aperture

First of all, in the idealized case where the vertical field distribution is much smaller than the aperture, we can ignore the pupil in the y direction and the integral in (3.53) is simply another scaled inverse Fourier transform, meaning that $p_{y_j}(y_s, t) = p_y(y_s) = E_{i_y}(y_s/M)$. The solution for the vertical distribution is constant with order j and scan time t while within the aperture along x. The solution for the j^{th}-order diffracted field imaged to the sample plane is:

$$E_{j,s}\left(x_s, y_s, t\right) = \frac{a_j}{M}\Pi_{x_j} \mathrm{e}^{\mathrm{i}2\pi j\left[f_{g_x}(t)\,x_o - \frac{f_{g_x}(t)}{M}x_s - \frac{f_{g_y}}{M}y_s\right]} E_{i_x}\left(\frac{x_s}{M}\right) E_{i_y}\left(\frac{y_s}{M}\right) \tag{3.56}$$

Although a simplified case, the physical information contained in Eqn. (3.56) illustrates some fundamental properties of the $4f$ imaging system. First of all, the incident field has been imaged and scaled by M in size, causing the field amplitude to increase by a factor $1/M$. Secondly, the phase terms tell us that the tilted angle of propagation with respect to the optic axis, caused by diffraction at the mask, has increased by a factor $1/M$, and is flipped about the optic axis, as a simple ray trace would predict. (Note $|M| \ll 1$ for a typical tube lens / objective lens setup). Third, these diffraction angles multiplicatively increase with diffraction order, j. Fourth, the pupil gating function Π_{x_j} in the x direction limits the range of field diffraction angles passed through the system from the mask to the sample plane. Fifth, the linear phase accumulation rate due to the offset x_o of the mask center from the beam center does not scale with magnifi-

cation. One way to understand why this is true is to view this phase accumulation in terms of the temporal modulation frequency at the center position of the field distribution at the mask x_o. Using Eqn. (3.19), $\nu_{mod}(x_o) = \kappa x_o \equiv \nu_o$, and we can write the phase accumulation due to the beam offset x_o in temporal terms:

$$\exp\left[\mathrm{i}2\pi\, j\, f_{g_x}(t)\, x_o\right] = \exp\left[\mathrm{i}2\pi\, j\kappa\, t\, x_o\right] = \exp\left[\mathrm{i}2\pi\, j\nu_o\, t\right] \tag{3.57}$$

Using (3.57) in (3.56), it is evident that the center temporal modulation frequency imparted by the mask will not change with spatial magnification. Since the beam extent along x given by E_{i_x} is demagnified from mask plane to sample plane, we can infer that the range of temporal modulation frequencies remains the same after the image relay, but the spatial distribution of temporal modulation frequencies along x is more densely packed in the sample plane than the mask plane due to the system demagnification, M.

2. An aperture overfilled by a plane wave

We next consider more realistic scenarios where the diffracted orders $E_{j,p}$ in the pupil plane overfill the aperture in the vertical direction. We must now account for the clipping function Π_{y_j} when evaluating the integral in Eqn. (3.53). After using the replacement y'_p, Eqn. (3.45), in the definition of Π_{y_j}, Eqn. (3.39), we have:

$$\Pi_{y_j}(t) = \mathrm{rect}\left[\frac{y'_p + j f_{g_y}}{2\left(\frac{y_{c,j}(t)}{\lambda f_1}\right)}\right] = \begin{cases} 1, & -\frac{y_{c,j}(t)}{\lambda f_1} \le y'_p + j f_{g_y} \le \frac{y_{c,j}(t)}{\lambda f_1} \\ 0, & \text{otherwise} \end{cases} \tag{3.58}$$

For the next two cases, we exploit the fact that the rectangle function simply moves the limits of integration. The limits move from $y'_p = \pm\infty$ to $y'_p = \pm\frac{y_{c,j}(t)}{\lambda f_1} - j f_{g_y}$. For simplicity, we will ignore the small vertical offset, $j f_{g_y} \to 0$.

Our second case occurs when the spatial extent of $\hat{E}_{iy}(y'_p)$ overfills the aperture so greatly that it can be treated as a plane wave within the pupil, and thus replaced with a constant, which

we set equal to 1. Evaluating Eqn. (3.53), we find that the vertical profile at the focal plane is a sinc function:

$$\begin{aligned} p_{y_j}(y_s,t) &= \int_{-\infty}^{\infty} \Pi_{y_j}\left(y'_p,t\right) \mathrm{e}^{-\mathrm{i}2\pi\left(\frac{y_s}{M}\right)y'_p}\,\mathrm{d}y'_p = \int_{\frac{-y_{c,j}(t)}{\lambda f_1}}^{\frac{y_{c,j}(t)}{\lambda f_1}} \mathrm{e}^{-\mathrm{i}2\pi\left(\frac{y_s}{M}\right)y'_p}\,\mathrm{d}y'_p \\ &= \frac{2y_{c,j}(t)}{\lambda f_1}\mathrm{sinc}\left[\frac{2y_{c,j}(t)}{M\lambda f_1}y_s\right] \end{aligned} \tag{3.59}$$

where $\mathrm{sinc}(x) = \sin(\pi x)/(\pi x)$. The sinc function, with its decaying oscillations away from $y_s = 0$, describes the ringing behavior due to diffraction of a coherent field from a hard edge. Moreover, according to Eqn. (3.59), as the vertical cutoff in the pupil plane $y_{c,j}(t)$ decreases as a beam moves from $x_p = 0$ to $x_p = x_c$, two dynamic effects are imposed on the focal field in the sample plane. One, the field peak amplitude, related to energy throughput, is diminished by progressively stronger clipping in the pupil. Two, the width of the vertical sinc profile increases: the first zero of the sinc function occurs at $y_s = M\lambda f_1/(2y_{c,j}(t))$, so as $y_{c,j}$ diminishes with time, the first zero increases. Near the edges of the aperture, $y_{c,j}$ is nearly zero, and thus $p_y(y_s)$ is essentially a very weak plane wave in the focal plane.

3. An aperture overfilled by a Gaussian beam

The third case of interest occurs for a Gaussian laser beam profile in the vertical direction. For a tight Gaussian focus incident on the mask, $E_{i_y} = \exp\left(-y_m^2/w_{y_m}^2\right)$, it's transform is also a Gaussian, $\hat{E}_{i_y} = w_{y_m}\sqrt{\pi}\exp\left[-\left(\pi w_{y_m} f_{y,m}\right)^2\right]$. Evaluating Eqn. (3.53), and again converting the rect function Π_{y_j} into a change in the limits of integration, we have:

$$p_{y_j}(y_s,t) = \sqrt{\pi}w_{y_m}\int_{-\frac{y_{c,j}(t)}{\lambda f_1}}^{\frac{y_{c,j}(t)}{\lambda f_1}} \mathrm{e}^{-\left(\pi w_{y_m} y'_p\right)^2} \mathrm{e}^{-\mathrm{i}2\pi\left(\frac{y_s}{M}\right)y'_p}\,\mathrm{d}y'_p \tag{3.60}$$

By completing the square in the argument of the exponential,

$$\mathrm{e}^{-(\pi w_{y_m})^2 y'^2_p + (\mathrm{i}2\pi\frac{y_s}{M})y'_p - \left(\frac{\mathrm{i}y_s}{Mw_{y_m}}\right)^2 + \left(\frac{\mathrm{i}y_s}{Mw_{y_m}}\right)^2} = \mathrm{e}^{-\left[\pi w_{y_m} y'_p - \frac{\mathrm{i}y_s}{Mw_{y_m}}\right]^2} \mathrm{e}^{\left(\frac{\mathrm{i}y_s}{Mw_{y_m}}\right)^2} \tag{3.61}$$

and separating the integral into two parts, such that

$$p_{y_j}(y_s,t) = \sqrt{\pi} w_{y_m} \mathrm{e}^{\left(\frac{\mathrm{i}y_s}{Mw_{y_m}}\right)^2} \left[\int_{-\frac{y_{c,j}(t)}{\lambda f_1}}^{0} \mathrm{e}^{-\left[\pi w_{y_m} y'_p - \frac{\mathrm{i}y_s}{Mw_{y_m}}\right]^2} \mathrm{d}y'_p + \int_{0}^{\frac{y_{c,j}(t)}{\lambda f_1}} \mathrm{e}^{-\left[\pi w_{y_m} y'_p - \frac{\mathrm{i}y_s}{Mw_{y_m}}\right]^2} \mathrm{d}y'_p \right] \tag{3.62}$$

and furthermore making the substitution $y''_p = \pi w_{y_m} y'_p - \frac{\mathrm{i}y_s}{Mw_{y_m}}$, while also reversing the order of integration in the first integral,

$$p_{y_j}(y_s,t) = \frac{1}{\sqrt{\pi}} \mathrm{e}^{\left(\frac{\mathrm{i}y_s}{Mw_{y_m}}\right)^2} \left[-\int_{0}^{-\frac{\pi w_{y_m} y_{c,j}(t)}{\lambda f_1} - \frac{\mathrm{i}y_s}{Mw_{y_m}}} \mathrm{e}^{-y''^2_p} \mathrm{d}y''_p + \int_{0}^{\frac{\pi w_{y_m} y_{c,j}(t)}{\lambda f_1} - \frac{\mathrm{i}y_s}{Mw_{y_m}}} \mathrm{e}^{-y''^2_p} \mathrm{d}y''_p \right] \tag{3.63}$$

we find that the form of the integrals can be made to match the definition of the Error Function, defined as:

$$\mathrm{Erf(z)} \equiv \frac{2}{\sqrt{\pi}} \int_0^{\mathrm{z}} \mathrm{e}^{-s^2} \mathrm{d}s \tag{3.64}$$

where z denotes a complex argument. The resulting vertical component of the j^{th} sample plane field, $p_{y_j}(y_s,t)$, is a demagnified copy of the Gaussian input field, but modulated by half the difference of two Error Functions:

$$p_{y_j}(y_s,t) = \mathrm{e}^{-\left(\frac{y_s}{Mw_{y_m}}\right)^2} \frac{1}{2} \left[\mathrm{Erf}\left(\frac{\pi w_{y_m} y_{c,j}(t)}{\lambda f_1} - \frac{\mathrm{i}y_s}{Mw_{y_m}} \right) - \mathrm{Erf}\left(-\frac{\pi w_{y_m} y_{c,j}(t)}{\lambda f_1} - \frac{\mathrm{i}y_s}{Mw_{y_m}} \right) \right] \tag{3.65}$$

This modulating term provides the 'ringing' from the hard aperture on the focal field, as did the sinc function function in the plane wave case.

3.3.5 Scalar CTFs for the Diffracted Orders

At any instant of time, the $4f$ image relay system is performing coherent imaging of each diffracted field exiting the mask plane, subject to filtering by the system coherent transfer function. To determine the CTF for a given order at a given time, we first write out the transverse

Fourier representation of $E_{j,s}$ in a general way:

$$\hat{E}_{j,s}(f_{x,s}, f_{y,s}) = \int_{x_s}\int_{y_s} E_{j,s}(x_s, y_s)\mathrm{e}^{-\mathrm{i}2\pi(f_{x,s}x_s + f_{y,s}y_s)}\mathrm{d}x_s\mathrm{d}y_s \tag{3.66}$$

where $E_{j,s}(x_s, y_s)$ is given by Eqn. (3.41). By integrating first over x_s and y_s, followed by x_p and y_p, the 2D spectral field is:

$$\begin{aligned}\hat{E}_{j,s}(f_{x,s}, f_{y,s}) = -Ma_j\Pi_{m_j}\mathrm{e}^{\mathrm{i}2\pi v_o t}\hat{p}_x\left(-Mf_{x,s} - jf_{g_x}\right)\hat{p}_y\left(-Mf_{y,s} - jf_{g_y}\right) \\ \times\mathcal{P}\left(-\lambda f_2 f_{x,s}\,, -\lambda f_2 f_{y,s}\right) \qquad (3.67)\end{aligned}$$

$$= M\hat{E}_{j,m}\left(Mf_{x,s}, Mf_{y,s}\right)CTF\left(f_{x,s}, f_{y,s}\right) \tag{3.68}$$

where $\hat{E}_{j,m}$ is the transverse Fourier transform of the mask field in Eqn. (3.32). In Equation (3.68) we see a product between a demagnified copy of the mask field and a filter given by the aperture function $\mathcal{P}$. This filter is the coherent transfer function, described in Section 2.7.3. The filter's spatial frequency coordinates are a scaled version of the aperture coordinates, as described in Equation (2.85):

$$CTF\left(f_{x,s}, f_{y,s}\right) = \mathcal{P}\left(x_p, y_p\right)\Big|_{(x_p,y_p)=-f_1\lambda(f_{x,s},f_{y,s})} \tag{3.69}$$

The one difference between the CTFs in Eqn. (2.85) and Eqn. (3.69) is that in the latter, we have defined the CTF in terms of the spatial frequency content of the second lens of focal length f_2.

The CTF is directly related to the pupil geometry in the Fourier plane [40]. Adapting the equations for the pupil aperture $\mathcal{P}$ given in Equations (3.37), (3.38), and (3.39), the CTFs in each Cartesian direction are:

$$CTF_{x_j}\left(f_{g_x}(t)\right) = \text{rect}\left[\frac{j f_{g_x}(t)/M}{2f_{x_c}}\right] = \begin{cases} 1, & |j f_{g_x}(t)/M| \leq f_{x_c} \\ 0, & \text{otherwise} \end{cases} \tag{3.70}$$

$$CTF_{y_j}\left(f_y, t\right) = \text{rect}\left[\frac{f_y}{2f_{y_{c,j}}(t)}\right] = \begin{cases} 1, & |f_y| \leq f_{y_{c,j}}(t) \\ 0, & \text{otherwise} \end{cases} \tag{3.71}$$

The rectangle functions switch state when the lateral and vertical spatial frequency components encounter the cutoff frequency of the system pupil $f_c = NA/\lambda$. Because $E_j(t)$ contains only one lateral spatial frequency per unit time, CTF_{x_j} provides a finite range of lateral spatial frequencies that can be scanned through temporally. Conversely, $E_j(t)$ contains a bandwidth of vertical spatial frequencies at any one time. The role of $CTF_{y_j}(f_y, t)$ is that of a low-pass filter on the vertical spatial frequency bandwidth; this filter varies with time for scanning beams $E_{|j|\geq 1}$. The filter allows the maximum bandwidth $\Delta f_y = [-f_c : f_c]$ at time $t = 0$, with progressively stronger low-pass filtering as scan time progresses from $t = 0$ in either direction to $|t| = t_c/j$. The vertical frequency support for a circular aperture of radius NA/λ varies with the beam's instantaneous lateral spatial frequency $f_x = j f_{g_x}(t)/M$ according to the equation:

$$f_{y_{c,j}}(t) = \sqrt{\left(\frac{NA}{\lambda}\right)^2 - \left(\frac{j f_{g_x}(t)}{M}\right)^2} \tag{3.72}$$

3.3.6 Vector Focal Fields at High NA

In a scalar, paraxial approach, we can use Eqn. (3.41) to compute the fields in the sample plane. However, for moderate to high NA focusing, a better model uses aplanatic focusing with vector fields, which we developed in Section 2.8 according to the principles of the angular spectrum of plane waves, resulting in the Debye-Wolf integral (Eqn. (2.103)).

In Section 2.8, we used a linearly polarized, collimated Gaussian beam as an example input field. For an MP-SPIFI microscope, we take the input field at the reference sphere of the high NA lens to be the temporally-scanning set of diffracted orders in the Fourier plane of the $4f$ image

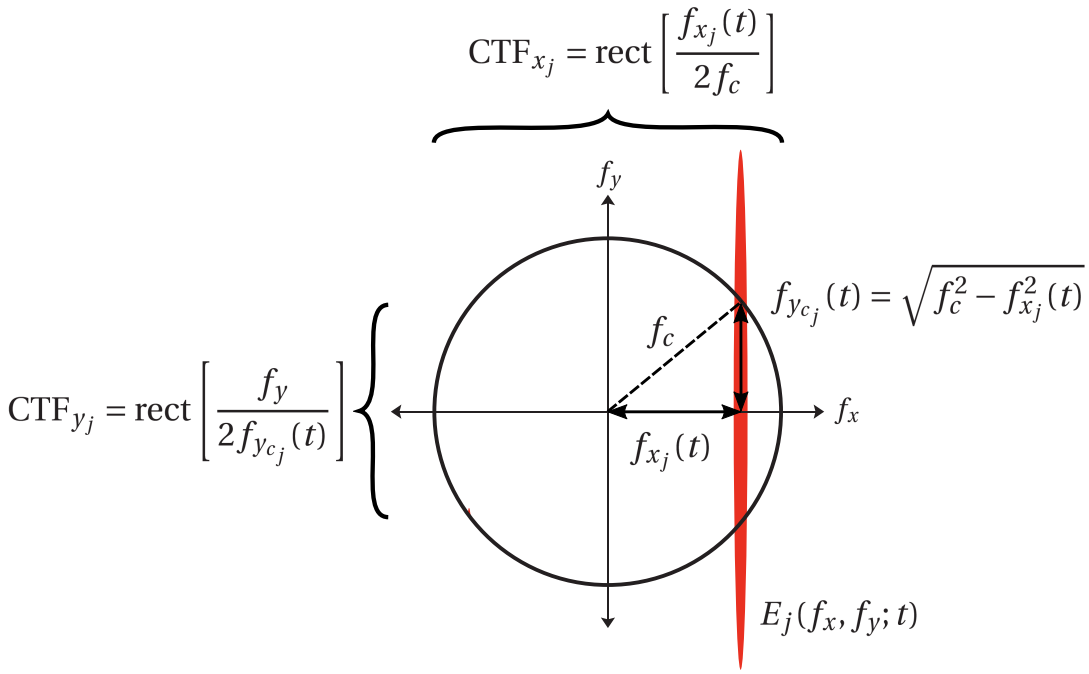

Figure 3.7: The $4f$ system CTF for diffracted order E_j can be decomposed into two Cartesian directions. Because the diffracted orders are very narrow in x and very broad in y, the CTF can be approximated as rectangle functions in f_x and f_y. The pupil cutoff frequency is $f_c = \mathrm{NA}/\lambda$. The scanning horizontal spatial frequency for diffracted order E_j is $f_{x_j}(t) = j f_{g_x}(t)/M = j\kappa t/M$. The width of the vertical CTF varies with scan time. We plot only one diffracted order E_j for clarity.

relay system, depicted at one time instant in Fig. 3.5(b). The equation for each diffracted order in the Fourier plane is given by Eqn. (3.33) or (3.34); the total field is the sum over j.

We note that this approach is a small violation of the premises undergirding the Debye-Wolf integral as described in Section 2.8. That is, the input field $\mathbf{E}_\infty$ defined in Eqn. (2.112) is that which is defined on the reference sphere of the lens; the reference sphere corresponds to the paraxial principal plane generalized to a high NA system. In contrast, we are taking the field in the Fourier plane of the tube lens / objective lens $4f$ relay system as the input field. To resolve this difference, we could simply propagate the Fourier plane field distribution a distance f_2 to the location where the reference sphere intercepts the optic axis. However, we would then violate a separate premise of the Debye-Wolf integral formula, which is that the field intercepting the reference sphere should be collimated. In the SPIFI microscope, the diffracted order fields

in the Fourier plane are collimated in $\hat{y}$ but tightly focused in $\hat{x}$. However, they do have a waist in $\hat{x}$ and are briefly collimated over a short Rayleigh range in the Fourier plane. For simplicity, we simply take the Fourier plane as the far-field input as if it were itself incident on the reference sphere. While imperfect, this enables us to gain insight into the focal field distribution when large angles and polarized fields generate discrepancies from the predictions of the scalar, paraxial approach.

The vectorial electric field of each diffracted beam in the object region is:

$$\mathbf{E}_{j,s}(\mathbf{r},t) = E_{x,j,s}(\mathbf{r},t)\,\hat{\mathbf{x}} + E_{y,j,s}(\mathbf{r},t)\,\hat{\mathbf{y}} + E_{z,j,s}(\mathbf{r},t)\,\hat{\mathbf{z}} \tag{3.73}$$

The Debye-Wolf integral (Eqn. (2.103)) must be solved numerically for each diffracted order. For the j^{th} order, the focal field is:

$$\mathbf{E}_{j,s}(\rho,\varphi,z) = \frac{\mathrm{i}kf\,\mathrm{e}^{-\mathrm{i}kf}}{2\pi} \int_{\phi=0}^{2\pi} \int_{\theta=0}^{\theta_{max}} \mathbf{E}_{\infty,j}(f,\phi,\theta)\,\mathrm{e}^{\mathrm{i}k\rho\sin\theta\cos(\phi-\varphi)}\mathrm{e}^{\mathrm{i}kz\cos\theta}\sin\theta\,\mathrm{d}\theta\,\mathrm{d}\phi \tag{3.74}$$

We will assume a linearly polarized far-field on the reference sphere, given by Eqn. (2.114),

$$\mathbf{E}_{\infty,j}(f,\phi,\theta;\xi) = E_{\infty,j}(x,y)\sqrt{\frac{n_1}{n_2}\cos\theta}\begin{bmatrix} \cos\phi\cos\theta\cos\left(\phi-\xi\right) + \sin\phi\sin\left(\phi-\xi\right)\,\hat{\mathbf{x}} \\ \sin\phi\cos\theta\cos\left(\phi-\xi\right) - \cos\phi\sin\left(\phi-\xi\right)\,\hat{\mathbf{y}} \\ -\sin\theta\cos\left(\phi-\xi\right)\,\hat{\mathbf{z}} \end{bmatrix} \tag{3.75}$$

and as discussed above we will use the field in the Fourier plane (Eqn. (3.34) with (3.35) and (3.36)) of the $4f$ image relay system as the transverse far-field input:

$$E_{\infty,j}(x,y) \quad = \quad E_{j,p}\left(x_p,y_p,t\right) \quad = \quad \frac{a_j}{\mathrm{i}\lambda f_1}\mathrm{e}^{\mathrm{i}2\pi j f_{g_x}(t)\,x_o}\hat{E}_i\left(\frac{1}{\lambda f_1}\left(x_p - x_{p_0,j}(t)\,,\,y_p - y_{p_0,j}\right)\right) \tag{3.76}$$

The j^{th} diffracted order has a temporal dependence in the Fourier plane, as it's lateral center position x_{p_0} is varying linearly with time. In using Eqn. (3.34), we have assumed the case where every diffracted order has a spatial window larger than the aperture of the objective lens, so that

the binary window function $\Pi_{m_j} \rightarrow 1$, and we have neglected the linear axial phase accumulation $\exp\left(\mathrm{i}2kf_1\right)$.

For a Gaussian laser beam with unit amplitude incident on the mask,

$$E_{i_y} = \exp\left(-x_m^2/w_{x_m}^2\right)\exp\left(-y_m^2/w_{y_m}^2\right) \tag{3.77}$$

it's Fourier transform is also a Gaussian, given by:

$$\hat{E}_{i_y} = w_{x_m} w_{y_m} \pi \exp\left[-\left(\pi w_{x_m} f_{x,m}\right)^2\right] \exp\left[-\left(\pi w_{y_m} f_{y,m}\right)^2\right] \tag{3.78}$$

so that the j^{th} diffracted order in the Fourier plane has a Gaussian form given by:

$$E_{\infty,j}(x,y,t) = \frac{a_j w_{x_m} w_{y_m} \pi}{\mathrm{i}\lambda f_1} \mathrm{e}^{\mathrm{i}2\pi j f_{g_x}(t) x_o} \exp\left[-\left(\frac{x_p - x_{p_0,j}(t)}{w_{x_p}}\right)^2\right] \exp\left[-\left(\frac{y_p - y_{p_0,j}}{w_{y_p}}\right)^2\right] \tag{3.79}$$

where the transverse offsets $x_{p_0,j}(t)$ and $y_{p_0,j}$ are given by Equations (3.35) and (3.36) and the field widths in the Fourier plane are

$$w_{p_x} = \frac{\lambda f_1}{\pi w_{x_m}} \qquad\qquad w_{p_y} = \frac{\lambda f_1}{\pi w_{y_m}} \tag{3.80}$$

The transverse Gaussian beam arriving at the high NA lens reference sphere given by Equation (3.79) must now be converted to spherical-polar coordinates in order to use Eqn. (3.75) in Eqn. (3.74). The transverse Cartesian variables (x_p, y_p) in Eqn. (3.79) are converted to spherical coordinates using the transformation

$$x_p = f_2 \sin\theta \cos\phi \tag{3.81}$$

$$y_p = f_2 \sin\theta \sin\phi \tag{3.82}$$

so that the far-field on the reference sphere is completely specified in spherical-polar coordinates:

$$E_{\infty,j}(f_2,\phi,\theta,t)=\frac{a_j w_{x_m} w_{y_m}\pi}{\mathrm{i}\lambda f_1}\mathrm{e}^{\mathrm{i}2\pi j f_{g_x}(t)\,x_o}\mathrm{e}^{-\left(\frac{f_2\sin\theta\cos\phi-x_{p_0,j}(t)}{w_{x_p}}\right)^2}\mathrm{e}^{-\left(\frac{f_2\sin\theta\sin\phi-y_{p_0,j}}{w_{y_p}}\right)^2} \tag{3.83}$$

The far-field in Eqn. (3.83) is then used as the input to Eqn. (3.74) to compute the field in the focal region for each diffracted order j.

The total spatiotemporal vector field in the focal region is obtained after numerically computing Eqn. (3.74) for each diffracted order j, at every scan time t. The total electric field along each Cartesian direction is found by summing the respective component contributed by each diffracted order:

$$\mathbf{E}_s(\mathbf{r},t) = \sum_j \left[E_{x,j,s}(\mathbf{r},t)\,\hat{\mathbf{x}}+E_{y,j,s}(\mathbf{r},t)\,\hat{\mathbf{y}}+E_{z,j,s}(\mathbf{r},t)\,\hat{\mathbf{z}}\right] \tag{3.84}$$

$$= E_{x,s}(\mathbf{r},t)\,\hat{\mathbf{x}}+E_{y,s}(\mathbf{r},t)\,\hat{\mathbf{y}}+E_{z,s}(\mathbf{r},t)\,\hat{\mathbf{z}} \tag{3.85}$$

where $\mathbf{r}=\left(\rho,\varphi,z\right)$. Equation (3.85) is the generalized version of the total scalar field given in Eqn. (3.54). The intensity in the focal region, computed as described in Section 2.2, is the inner product of the electric field vectors:

$$I_s(\mathbf{r},t) = \left|\sum_j E_{x,j,s}(\mathbf{r},t)\right|^2+\left|\sum_j E_{y,j,s}(\mathbf{r},t)\right|^2+\left|\sum_j E_{z,j,s}(\mathbf{r},t)\right|^2 \tag{3.86}$$

3.4 Light-Matter Interaction and Contrast Mechanisms

In our microscope we measure optical signals that are generated by the interaction of the illumination intensity and the material properties of the object. The signal light, $\beta(\mathbf{r},t)$, arising from this interaction can follow the intensity linearly:

$$\beta(\mathbf{r},t)=I(\mathbf{r},t)C(\mathbf{r}) \tag{3.87}$$

where $C(\mathbf{r})$ represents the object as a stationary spatial contrast function, and the intensity $I(\mathbf{r},t)$ can be described with a scalar (Eqn. (3.55)) or vector (Eqn. (3.86)) model.

However, some forms of optical contrast are the result of the object responding to the optical intensity in a nonlinear fashion. For example, under saturated absorption excitation (SAX), an object's absorbing capabilities will respond linearly in regions of low intensity illumination, but will not be able to absorb in regions of high intensity illumination to the same proportion, because all of the available absorbers in those regions will have been activated [63]. To describe this generally, one can write that the signal light is a function of the illumination intensity:

$$\beta(\mathbf{r}, t) = f\left[I(\mathbf{r}, t)\right] C(\mathbf{r}) \tag{3.88}$$

In this work, we focus on multiphoton excitation mechanisms which are typically integer powers of the illumination intensity. Physically, this corresponds to processes such as second & third harmonic generation, or two- and three-photon excited fluorescence. The signal light under a nonlinear excitation of order η can be represented by raising $I(\mathbf{r}, t)$ to the integer power η:

$$\beta(\mathbf{r}, t) = \left[I(\mathbf{r}, t)\right]^{\eta} C(\mathbf{r}) \tag{3.89}$$

$C(\mathbf{r})$ is a general distribution function that can be adapted to a particular optical excitation mechanism, with associated scalar constants folded in. For a second-order multiphoton process, such as second harmonic generation (SHG) and two-photon excited fluorescence (TPEF), ignoring polarization effects and assuming a static contrast function, the signal light is then $\beta(\mathbf{r}, t) = I^2(\mathbf{r}, t)\, C(\mathbf{r})$ where $C(\mathbf{r}) = \left|\chi^{(2)}(\mathbf{r})\right|^2$ for SHG, and where $\chi^{(2)}(\mathbf{r})$ is the second-order nonlinear susceptibility tensor for the molecules in the specimen. For TPEF, $C(\mathbf{r})$ describes the spatial distribution of fluorescent molecules. In both cases we have absorbed proportionality constants such as two-photon cross section into $C(\mathbf{r})$ for simplicity.

3.5 Illuminating the Object with Spatial Frequencies Beyond the Cutoff

In this section we demonstrate how the illumination scheme probes the object with spatial frequencies beyond the cutoff spatial frequency of coherent $4f$ imaging system. We will use the scalar form for the diffracted fields in the focal plane for simplicity and clarity.

The super-resolving mechanism in MP-SPIFI occurs in the horizontal dimension. To avoid distraction, we will make a few simplifying assumptions about the vertical field distribution. First of all, we will neglect the small vertical offset $y_{p_0,j}$ of each diffracted order $E_{j,p}$ in the Fourier plane, which is equivalent to letting $f_{g_y} \to 0$ (Equations (3.34) and (3.36)). Secondly, we assume that the vertical field profiles $p_{y_j}(y_s,t)$ are constant for all scan time. Physically, this can be achieved by a rectangular aperture in the Fourier plane. The two assumptions together imply that the vertical field profiles are the same for all diffracted orders j. Together with the temporal form of the linear phase accumulation (Eqn. (3.57)) provided by the mask, the focal field is

$$E_{j,s}\left(x_s,y_s,t\right) = \frac{a_j \Pi_{x_j}(t)}{M} \mathrm{e}^{\mathrm{i}2\pi j\left[\nu_o t - \frac{f_{g_x}(t)}{M} x_s\right]} p_x(x_s)\, p_y(y_s) \tag{3.90}$$

Without any time dependence in the vertical field distributions, the intensity of the scalar field using Eqn. (3.55) is separable in x and y:

$$I(x_s,y_s,t) = I(y_s)\; I(x_s,t) \tag{3.91}$$

$$= \left|p_y(y_s)\right|^2 \cdot \left|p_x(x_s)\right|^2 \cdot \left| \sum_{j=-N}^{N} \frac{a_j \Pi_{x_j}(t)}{M} \mathrm{e}^{\mathrm{i}2\pi j\left[\nu_o t - \frac{f_{g_x}(t)}{M} x_s\right]} \right|^2 \tag{3.92}$$

The quantity within the summation over j is nothing more than a set of plane waves, which change propagation angle continuously with t, since $f_{g_x} = \kappa t$. The velocity of the changing angle scales with j. The limit on range of angles is provided by the pupil, represented by Π_{x_j}, defined in (3.38). we can compute $I(x,y,t)$ in the object region as a sum over pairs of tilted plane waves:

$$I(x_s,y_s,t) = \left|p_y(y_s)\right|^2 \left|p_x(x_s)\right|^2 \sum_{j=-N}^{N} \sum_{k=-N}^{N} v_j^*(x_s,t)\, v_k(x_s,t), \tag{3.93}$$

We can also simplify this notation into a product of intensities:

$$I(x_s, y_s t) = P_y(y_s)\, P_x(x_s)\, V(x_s, t) \tag{3.94}$$

where P_x is the stationary lateral intensity profile imaged from the mask, P_y is the vertical intensity profile, subject to apodization by the system pupil, and V is the modulated intensity pattern due to interference from the set of j tilted plane waves:

$$P_y(y_s) = \left| p_y(y_s) \right|^2 \tag{3.95}$$

$$P_x(x_s) = \left| p_x(x_s) \right|^2 \tag{3.96}$$

$$V(x_s, t) = \left| \sum_{j=-N}^{N} v_j(x_s, t) \right|^2 = \sum_{j=-N}^{N} \sum_{k=-N}^{N} v_j^*(x_s, t)\, v_k(x_s, t) \tag{3.97}$$

A nonlinear intensity I^η results in a discrete sum of harmonic spatial cosine functions in the plane wave component, V^η:

$$I^\eta(x_s, y_s, t) = P_y^\eta(y_s)\, P_x^\eta(x_s)\, V^\eta(x_s, t) \tag{3.98}$$

$$= P_y^\eta(y_s)\, P_x^\eta(x_s) \sum_{q=0}^{2\eta N} 2 H_q(t) \cos\left(2\pi q \nu_o t - 2\pi q (\kappa t / M) x_s\right) \tag{3.99}$$

Equation (3.99) is rich in physical information. At a snapshot in time, t, there is a constant background intensity corresponding to the $q = 0$ term. Overlaid on this is a fundamental cosine intensity pattern with spatial frequency $f_x(t) = \kappa t / M$, and a spatial phase shift $\phi_x(t) = 2\pi \nu_o x_o t$. Each harmonic cosine intensity pattern overlays a spatial frequency $f_x(t) = q\kappa t / M$ that is q times denser than the fundamental, with a phase offset that has shifted the harmonic fringes q times farther than the fundamental. The amplitude of each cosine pattern is contained in the set of functions $H_q(t)$. We shall see that the $H_q(t)$ functions are built up from combinations of diffracted order amplitudes and windows, a_j and $\Pi_{x_j}(t)$, and that each $H_q(t)$ function is distinct from the others. Finally, for the integer nonlinearity η, the total number of cosine harmonics is given by twice the product of the highest diffracted order and the nonlinearity, $q_{max} = 2\eta N$.

3.5.1 2-photon illumination intensity for diffracted orders j = $\{-1, 0, 1\}$

For the remainder of this chapter, we will assume the simplified case where only three diffracted orders propagate to the sample plane: the zero-order undiffracted field, and the two first order diffracted fields. This can be accomplished by spatial filtering of the higher diffracted orders, by using a true gray-scale amplitude mask, or by using a phase mask. For a well-aligned system, the zero-order propagates along the optic axis, and the $j = \pm 1$ fields have the same cut-off time t_c and window function Π_{x_1} due to their symmetry about the optic axis. For a 2-photon illumination intensity, $\eta = 2$, $q_{max} = 4$.

The plane wave component of the illumination intensity using (3.51) & (3.97) is:

$$\begin{aligned} V(x_s,t) &= \left[\frac{1}{4} + \frac{3}{\pi^2}\Pi^2_{x_1}(t)\right] \\ &+ \left[\frac{2}{\pi}\Pi_{x_1}(t)\right]\cos\left[2\pi\,\nu_o\,t - 2\pi\,f_x(t)\,x_s\right] \\ &+ \left[\frac{1}{\pi^2}\Pi^2_{x_1}(t)\right]\cos\left[4\pi\,\nu_o\,t - 4\pi\,f_x(t)\,x_s\right] \end{aligned} \tag{3.100}$$

For a second-order nonlinear process, the nonlinear plane wave illumination intensity is:

$$\begin{aligned} V^2(x_s,t) &= \left[\frac{1}{16} + \frac{3}{\pi^2}\Pi^2_{x_1}(t) + \frac{6}{\pi^4}\Pi^4_{x_1}(t)\right] \\ &+ \left[\frac{1}{\pi}\Pi_{x_1}(t) + \frac{12}{\pi^3}\Pi^3_{x_1}(t)\right]\cos\left[2\pi\,\nu_o\,t - 2\pi\,f_x(t)\,x_s\right] \\ &+ \left[\frac{3}{\pi^2}\Pi^2_{x_1}(t) + \frac{8}{\pi^4}\Pi^4_{x_1}(t)\right]\cos\left[4\pi\,\nu_o\,t - 4\pi\,f_x(t)\,x_s\right] \\ &+ \left[\frac{4}{\pi^3}\Pi^3_{x_1}(t)\right]\cos\left[6\pi\,\nu_o\,t - 6\pi\,f_x(t)\,x_s\right] \\ &+ \left[\frac{2}{\pi^4}\Pi^4_{x_1}(t)\right]\cos\left[8\pi\,\nu_o\,t - 8\pi\,f_x(t)\,x_s\right] \end{aligned} \tag{3.101}$$

This can be written compactly as:

$$V^2(x_s,t) = \sum_{q=0}^{4} H_q(t)\cos\left[2\pi\,q\,\nu_o\,t - 2\pi\,q\,f_x(t)\,x_s\right] \tag{3.102}$$

and the total 2-photon illumination intensity using Eqn. (3.99) is:

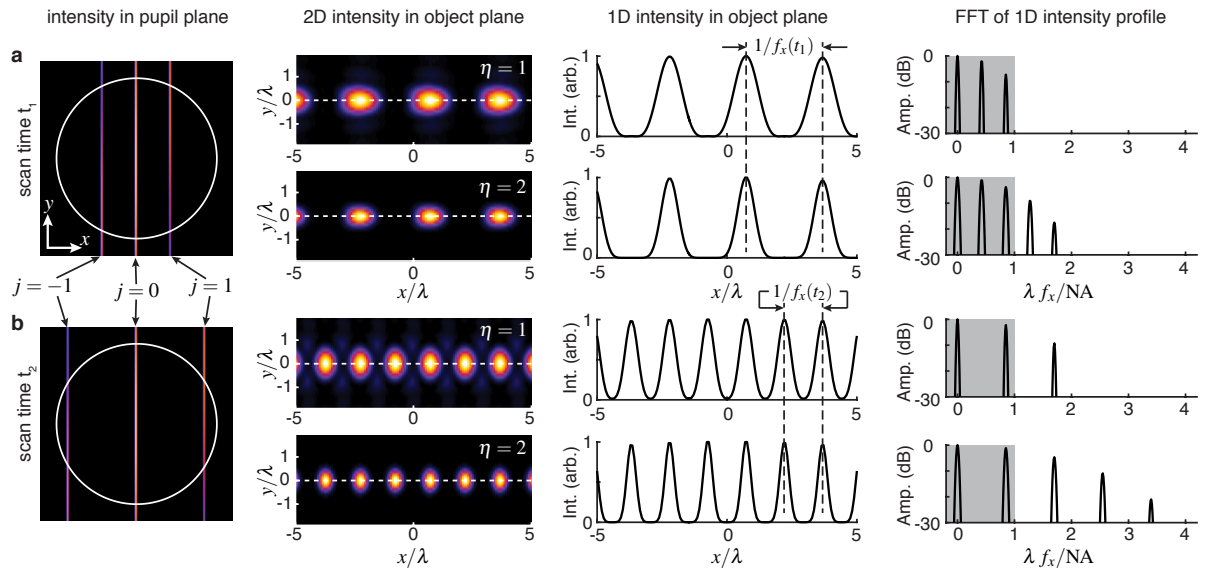

Figure 3.8: The illumination intensity pattern at two snapshots in time, (a) t_1 and (b) t_2, during a single temporal scan of the MP-SPIFI signal, $S(t)$. The left column shows the intensity at the rear pupil of the objective lens, where the white circle represents the pupil. The second column displays the illumination intensity in the focal plane of the objective lens. The illumination intensity for both linear and second-order nonlinear contrast generation are shown for each snapshot in time. The third column displays the intensity along the x-axis in the object plane, as indicated by the dashed lines in the second column. Finally, the fourth column shows the fast Fourier transform (FFT) of the 1D intensity line-outs, where the gray boxes represent the passband of the illumination objective lens. Note that the amplitude information in the frequency domain is symmetric about $f_x = 0$, but we display only the positive spatial frequencies to save space. The spacing between the $j = \pm 1$ beams and the $j = 0$ beam dictates the fundamental spatial frequency of the illumination intensity in the object plane. At time t_1, the $j = \pm 1$ beams are relatively close to the $j = 0$ beam in the pupil plane, and the resulting intensity in the object plane has a low spatial frequency, $f_x(t_1)$. At time t_2, the $j = \pm 1$ beams are separated from the $j = 0$ beam by twice the distance as at time t_1, thereby producing an intensity pattern with twice the spatial frequency, $f_x(t_2)$. The illumination intensities in the focal plane (column 2) were computed using the Debye-Wolf integral. Reprinted from Ref. [51].

$$I^2(x_s, y_s, t) = P_x^2(x_s)\, P_y^2(y_s) \sum_{q=0}^{4} H_q(t) \cos\left[2\pi\, q\, \nu_o\, t - 2\pi\, q\, f_x(t)\, x_s\right] \tag{3.103}$$

The spatial resolution of a microscope is determined by the set of spatial frequencies that the system can capture. In a conventional imaging system, the range of spatial frequencies that can be collected is limited by the numerical aperture (NA) of the objective lens and the wavelength of light. For a coherent illumination source of wavelength λ, the largest spatial frequency passed by the objective lens is $f_{x,c} = \mathrm{NA}/\lambda$. Assuming that all spatial frequencies are passed

by the objective lens with equal amplitude, the spatial resolution for a coherent imaging system is $\delta x = \lambda/(2\,\mathrm{NA}) = (2\,f_{x,c})^{-1}$. Acquiring super-resolved images is equivalent to collecting specimen information beyond this range of spatial frequencies. Equations (3.100) and (3.101) demonstrate that the harmonic cosine terms ($q \geq 2$) in linear and two-photon excitation project spatial frequencies onto the sample that exceed the coherent system cutoff frequency by a factor $q \times f_{x,c}$.

Under linear excitation, the fundamental lateral spatial frequency projected onto the sample is physically manifested through interference of the $j = \pm 1$ orders with the zero order, where the semi-aperture angle between the $j = \pm 1$ orders and the zero order is given by $\theta_2(t)$ in Fig.3.4. Interference between the $j = +1$ and $j = -1$ orders also takes place, and generates twice the maximal spatial frequency at the cutoff time $t_c = f_c/\kappa$, because the $j = \pm 1$ orders interfere at an angle $2 \times \theta_2(t)$ in the sample plane. With nonlinear excitation, harmonics of these two physical interference patterns are also generated.

3.6 Super-Resolved Image Reconstruction

In this section we show how specimen information corresponding to spatial frequencies up to $q \times f_{x,c}$ beyond the conventional limit is measured and processed into a super-resolved image. We continue with the scalar model and simplifying assumptions used in the previous section.

A portion of the signal light $\beta(\mathbf{r}, t)$ emitted by the sample is collected with a lens and directed onto a large-area single pixel detector. Folding the collection efficiency into the contrast function for simplicity, the collected signal is:

$$S(t) = \int_{x,y} \beta(x, y, t)\,\mathrm{d}x\,\mathrm{d}y = \int_{x,y} I^{\eta}(x, y, t)\,C(x, y)\,\mathrm{d}x\,\mathrm{d}y \tag{3.104}$$

The illuminated sample area is a line focus in the vertical direction, . The sample can be scanned vertically to build up a 2D image as described in Section 3.1. Using Eqn. (3.98) for the multiphoton excitation intensity, and using the scan variable y_0 for the vertical location in the sample,

$$S(t, y_0) = \int_{x,y} C(x, y - y_0)\, P_y^{\eta}(y)\, P_x^{\eta}(x)\, V^{\eta}(x, t) \mathrm{d}x\, \mathrm{d}y \tag{3.105}$$

The point spread function in the vertical direction is given by the real-valued intensity profile $P_y^{\eta}(y_s)$. If $P_y^{\eta}(y)$ is symmetric, then $P_y^{\eta}(y - y_0) = P_y^{\eta}(y_0 - y)$ and we have a formal convolution. This is akin to conventional multiphoton microscopy. Without making that assumption, we take the Fourier transform of (3.105) with respect to the scan vector y_0. This gives a product of the spatial-frequency distributions in f_y between the vertical profile and the specimen.

$$S\left(t, f_{y_0}\right) = -\hat{P_y^{\eta}}(f_{y_0}) \int_x C\left(x, -f_{y_0}\right)\, P_x^{\eta}(x)\, V^{\eta}(x, t) \mathrm{d}x\, \mathrm{d}y \tag{3.106}$$

To determine the point spread function of the image reconstruction process in the horizontal direction, we will now suppress the y-component for simplicity. The 1D signal measured at one position y_0 is:

$$S(t) = \int P_x^{\eta}(x)\, V^{\eta}(x, t)\, C(x)\, \mathrm{d}x \tag{3.107}$$

$$= \int P_x^{\eta}(x)\, C(x) \sum_{q=0}^{2\eta N} 2 H_q(t) \cos\left(2\pi q \nu_o t - 2\pi q (\kappa t / M) x\right) \mathrm{d}x \tag{3.108}$$

For simplicity, we absorb the horizontal intensity profile into the object, $P_x^{\eta}(x) C(x) \rightarrow C(x)$. (The profile can be later removed from a reconstructed object via deconvolution). The integration over space performed by the large area single pixel detector, in combination with the spatial sinusoidal modulations, demonstrates that the illumination & collection scheme together generates mathematical projections of the object using Fourier basis functions. More specifically, a harmonic set of projections are collected simultaneously with the fundamental projection at each snapshot in time. Expanding each of the q cosine functions into complex exponentials using Euler's formula, we find that we measure a linear sum of terms:

$$S(t) = S_0(t) + S_{1+}(t) + S_{1-}(t) + \ldots + S_{q_{max}+}(t) + S_{q_{max}-}(t) \tag{3.109}$$

The $q = 0$ term is a background term with a slow temporal dependence through its window function, which only contains information on the overall strength of the contrast function.

$$S_0(t) = 2\,H_0(t)\int C(x)\mathrm{d}x = c_0 H_0(t) \tag{3.110}$$

The remaining terms contain spatial object information. The q^{th} positive exponent term is:

$$S_{q+}(t) = H_q(t)\mathrm{e}^{\mathrm{i}2\pi q\nu_o t}\int \mathrm{e}^{-\mathrm{i}2\pi q\kappa x t/M}C(x)\mathrm{d}x \tag{3.111}$$

where the $H_q(t)$ functions are unique envelopes determined by the combination of field amplitudes a_j and pupil windowing functions $\Pi_{x_j}(t)$ for each contributing diffracted order at time t. We recognize the integral in (3.111)as a Fourier transform of the spatial object C(x), with conjugate variable $q\kappa\,t/M$. Replacing the Fourier integral with the object's spatial frequency representation,

$$S_{q+}(t) = H_q(t)\mathrm{e}^{\mathrm{i}2\pi q\nu_o t}\,\hat{C}_x(q\kappa\,t/M)) \tag{3.112}$$

The entire real measured signal, using (3.110) and (3.112) for the terms in (3.109), can be written as a sum of $2\eta N$ terms, where N is the highest diffracted order j considered:

$$S(t) = S_0(t) + \sum_{q=1}^{2\eta N}\left[H_q(t)\mathrm{e}^{\mathrm{i}2\pi q\nu_o t}\hat{C}_x(q\kappa\,t/M) + \text{c.c.}\right] \tag{3.113}$$

We have assumed C(x) is real-valued, and therefore $\hat{C}_x$ displays conjugate spectral symmetry. The shaping functions $H_q(t)$ are also real, unless aberration is present in the system. We see that over the course of a temporal scan, $S_{q+}(t)$ is a measurement of the object's spatial frequency distribution, $\hat{C}_x$, as apodized by the shaping function $H_q(t)$. The phase term describes a sinusoidal temporal carrier frequency oscillating at temporal harmonic $q\,\nu_o = q\Delta_k\nu_r x_o$ under the envelope formed by $H_q(t)\hat{C}_x(q\kappa\,t/M)$. Assuming that we can isolate $S_{q+}(t)$ from the total measured time trace, $S(t)$, we can then access the object information $\hat{C}_x$ in order to form a reconstruction of the object, $C(x)$. In fact, this isolation is made possible due to the linear phase

accumulation with time, which dictates that the Fourier transform of $S_{q+}(t)$ will be shifted to a sideband centered at $\nu = q\nu_o$.

To clarify how SPIFI collects specimen spatial frequency information beyond the system cutoff, we drop the temporal parameter, which only serves as an index for grating density and grating phase shift for a constantly spinning mask. The temporal window function for each first diffracted order, $\Pi_{x_1}(t)$, can be written in terms of the lateral spatial frequency coordinate in the Fourier plane, given by $f_x(t) = \kappa t/M$. The composite window functions, $H_q(t)$ in (3.100) & (3.101), directly depend on Π_{x_1} and therefore can also be written as $H_q(f_x)$. Secondly, we replace $\nu_o t$ in the phase argument of (3.112) with $Mf_x x_o$. The total measured signal becomes:

$$S(f_x) = S_0(f_x) + \left[\sum_{q=1}^{2\eta N} H_q(f_x) \mathrm{e}^{\mathrm{i}2\pi q M f_x x_o} \hat{C}_x(q f_x) + \text{c.c.}\right] \tag{3.114}$$

and the q^{th} positive sideband term in the summation is:

$$S_{q+}(f_x) = H_q(f_x) \mathrm{e}^{\mathrm{i}2\pi[qMx_o]f_x} \hat{C}(q f_x) \tag{3.115}$$

Examination of (3.115) reveals object information encoded in the form of a lateral spatial frequency distribution. Therefore a one-dimensional image of the object can be recovered through a Fourier transform of (3.115). The phase terms in Eqn. (3.115) play an important role in isolating the object information contained in each $\hat{C}(q f_x)$. The linear phase increase with f_x, at a rate qMx_o, will result in a shift of the image to qMx_o. Invoking the convolution, scaling, and shifting properties of the transform, the result is

$$S_{q+}(x) = h_q(x + qMx_o) \otimes \frac{1}{q} C\left(\frac{x}{q}\right) \tag{3.116}$$

A Fourier transform over the entire measured signal (3.114), being a linear operation, is equivalent to a Fourier transform over every term in $S(f_x)$. The total transformed signal is therefore:

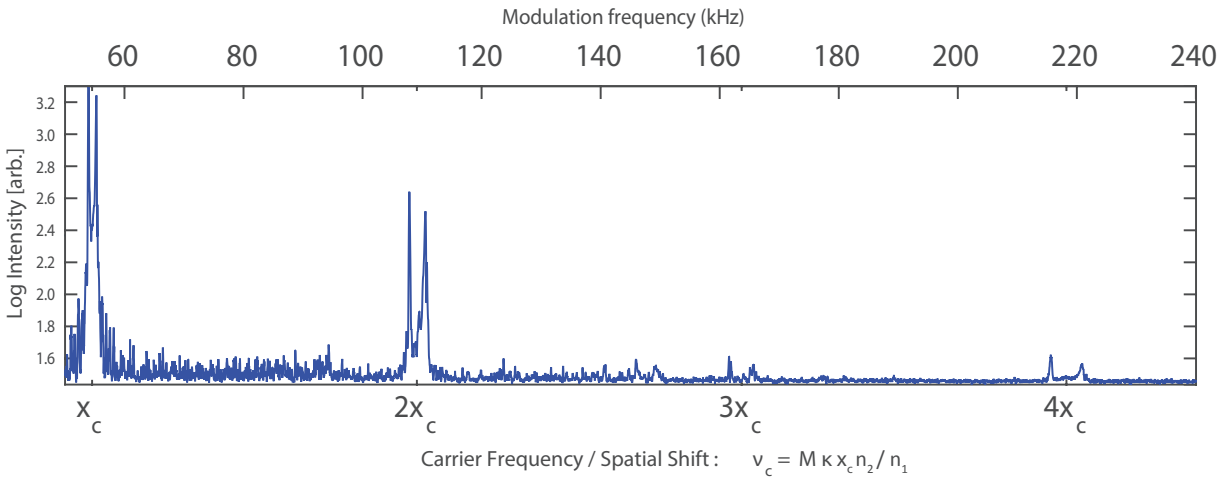

Figure 3.9: Simultaneous line images, at corresponding carrier modulation frequencies. Each image order, q, has a spatial shift and fractional bandwidth that scale with q. Object is a cross-section through a 15um shell-stained bead. Reprinted from Ref. [62] with permission.

$$S(x) = c_0 h_0(x) + \sum_{q=1}^{2\eta N} \frac{1}{q} \left(h_q(x - qMx_o) + h_q(x + qMx_o) \right) \otimes C\left(\frac{x}{q}\right) \tag{3.117}$$

The Fourier transform of the measured signal contains q = $2\eta N$ unique images, spatially separated by integer multiples of the distance Mx_o. Each of the q images is convolved with a unique point spread function, $h_q(t)$. The q^{th} image is dilated by a factor of q along the spatial axis with respect to image q = 1, and therefore, is sampled q times more finely. This is readily observed in Figure 3.9, for a 2nd-order nonlinear excitation.The four 1D images in Figure 3.9 are the result of an FFT operation on the measured signal S(t), where the spatial separation and spatial dilation as a function of q are evident. We display only the positive sideband, as the images in the negative sideband are redundant.

To rigorously compare the imaging properties of each image $S_{q+}(x)$ in the transformed signal, we need to take the final step of slicing out each image and mapping the set of images onto the same spatial axis. To understand why the set of images are on harmonically dilated x-axes, we recognize that every composite window function, $H_q(t)$, has the same temporal cutoff t_c, due to the moment at which the $j = \pm 1$ beams scan beyond the physical pupil. However, under

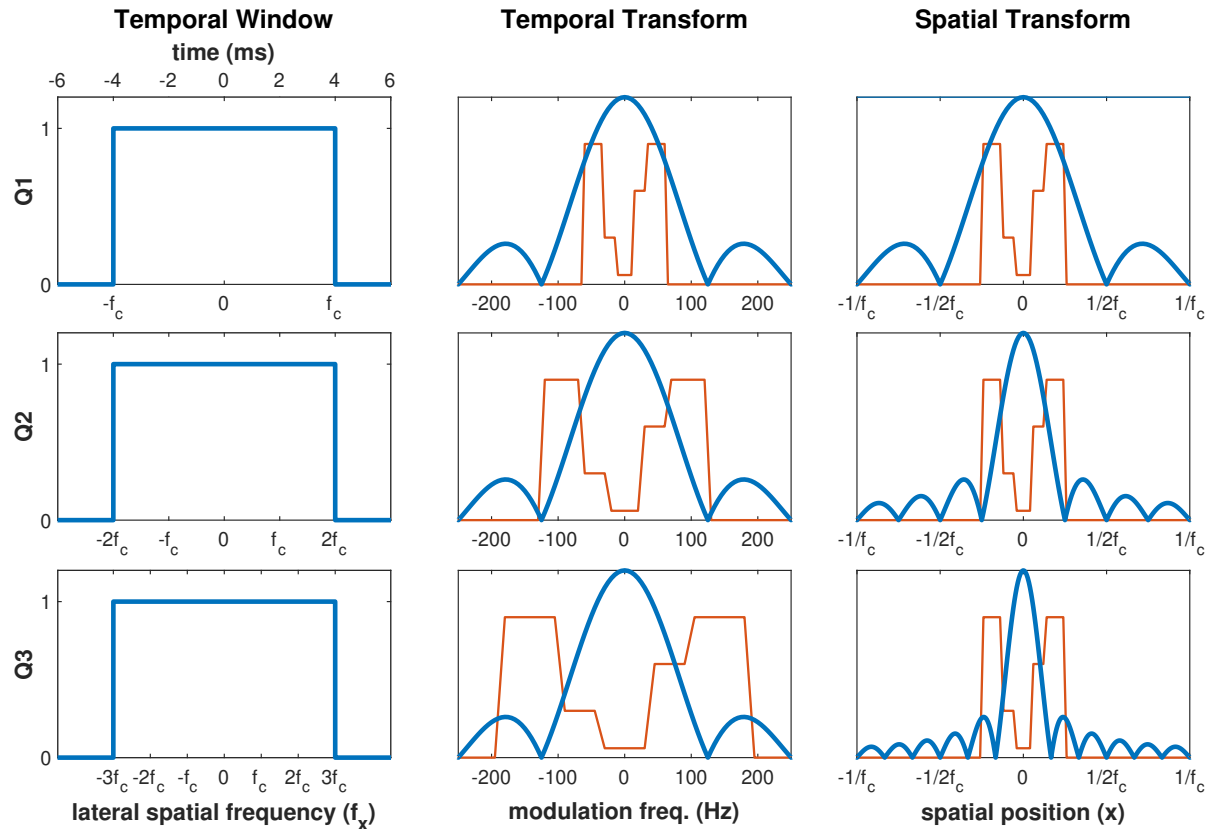

Figure 3.10: Image Dilation with harmonic image order, q, for the idealized case of rectangular apodization functions $H_q(t)$ for every image order. Left column: Under the temporal envelope of $H_q(t)$, the range of projected spatial frequencies increases by q relative to the fundamental. Center column: After an FFT of the raw temporal signal, the demodulated PSFs (blue) have the same width, but the images (red) are dilated. Right column: Rescaling each higher image order onto the fundamental x-axis means that the PSFs narrow at a rate 1/q relative to the fundamental, as expected from the set of projected spatial frequencies.

the envelope described by $H_q(t)$, the range of spatial frequencies projected increases with q according to $f_x, c, q \in [-qNA/\lambda, qNA/\lambda,]$. This is demonstrated in Fig.3.10 for the idealized case of $H_q(t)$ being rectangular for every order, q.

Proceeding, we utilize the spatial separation between images to window each image in turn, and downshift it to the origin. The q^{th} image is:

$$S_{q+}(x) = \frac{1}{q} h_q(x) \otimes C(\frac{x}{q}) \tag{3.118}$$

Making the variable substitution $\frac{x'}{q} \rightarrow x$, we arrive at the final expression:

$$S_{q+}(x) = \frac{1}{q} h_q\left(qx\right) \otimes C\left(x\right) \tag{3.119}$$

We see that MP-SPIFI takes the familiar form of a linear shift-invariant (LSI) imaging system, where the q^{th} image, $S_{q+}(x)$, is a rendering of the object, C(x), blurred by a point spread function whose spatial extent is contracted by a factor of 1/q. The Fourier transform of Eqn. (3.119) is

$$S_{q+}(f_x) = H_q\left(f_x / q\right) \hat{C}(f_x), \tag{3.120}$$

where we recognize $H_q(f_x)$ as the OTF for image S_{q+}. Our choice of variable for this combination of window functions becomes clear.

Taken together, Equations (3.119) & (3.120) demonstrate the super-resolving capability inherent in multiphoton SPIFI. The optical transfer functions, $H_q(f_x)$, for each successive image order extend out to q times the reach of the fundamental order. Therefore, they sample object information q times beyond the diffraction limit. Because the q^{th} image samples a spatial frequency content in the object that is q times larger than the Abbe-limited image at the fundamental, we see that the system contains the ability to resolve an object beyond the diffraction limit [51]. In the limit that all of the individual $h_q(x)$ PSFs are the same, then the q^{th} PSF resolves the object 1/q times more finely than the first order SPIFI PSF (which corresponds to the Abbe limited imaging condition). In practice, the set of point spread functions $h_q(x)$ are all somewhat different, as they are comprised of various combinations of beam amplitudes a_j and pupil windowing functions $\Pi_{x_j}(t)$.

In conclusion, we have presented the image formation process in an MP-SPIFI microscope. We have modeled the focal plane illumination intensity due to the coherent addition of temporally varying, spatially coherent diffracted fields using both a scalar and vector field approach. Image reconstruction from the time-sequence of harmonic lateral spatial frequency projections was shown to contain specimen spatial frequency information beyond the system cutoff frequency, enabling super-resolved imaging in the lateral dimension.

Author Contributions

The mathematical models to describe MP-SPIFI illumination and image reconstruction in this chapter were developed by K.A.W., J.J.F. and R.A.B. Specifically, R.A.B. and J.J.F. adapted the plane wave diffraction model from Ref. [58] for application to multiphoton excitation. K.A.W. applied $2f$ propagation analysis and developed scalar models for the pupil. K.A.W., J.J.F. and R.A.B. developed the mathematical model demonstrating resolution enhancement with image order. J.J.F. adapted the Debye vector focusing model to SPIFI. Sections 3.4 and 3.5 use text from Ref. [51] and Section 3.6 uses text from Ref. [62]. J.J.F. made Figures 3.4 and 3.8.

CHAPTER 4

4D STRUCTURE OF THE SPATIOTEMPORAL FOCAL VOLUME INTENSITY

In previous chapters our model of the spatio-temporal SPIFI illumination scheme was limited to the focal plane. This approach allowed us to model the illumination intensity in a line focus geometry for nonlinear excitation with reasonable accuracy. However, nonlinear microscopy is often used for interrogating thick specimens, due to the ballistic gating effect that provides some immunity to scatter. In a typical laser-scanning multiphoton microscope, the sample or the tight focal volume is raster-scanned in 3D to build up a volume image. In this chapter, we develop a model for SPIFI imaging where the object is scanned in two dimensions, y and z, while projections are used in the x direction to form a 3D image.

We develop a model describing the 4D illumination intensity due to any pair of interfering fields E_j and E_k in the focal volume, where these field pairs all originate as diffracted orders from the spinning modulator that have been imaged to the sample focal volume. This 4D illumination intensity is described over the 3D sample volume, as it evolves with modulator scan time. With a few approximations, we show that the 4D dynamic intensity for any beam pair effectively synthesizes a 3D optical transfer function (OTF) that describes the entire imaging properties of the microscope for illumination with that beam pair. We show that this OTF is directly related to the spectral intensity, and that the spectral intensity can be formed as a convolution between a plane wave term and a spatial envelope term. The ability to cast the imaging process into that of a linear, shift-invariant system, complete with an OTF, gives a convenient and well-understood point of reference for comparing the imaging properties to various other imaging techniques, such as wide-field, laser-scanning confocal, and so on. Moreover, it allows for rapid modeling of imaging performance for a given set of lenses, SPIFI mask parameters, and samples. Illumination with 3 or more beams is handled as a linear sum of beam-pair interactions. These results are the primary outcome of this chapter.

4.1 Motivation: Analytic model for Imaging Thick Specimens

A numerical computation of the SPIFI signal collection process for a 3D specimen is relatively straightforward once the 2D focal plane field distribution has been calculated. Thanks to the angular spectrum propagator, propagating a transverse field along the optical axis is easily handled (Equations (2.49) and (2.50)). Moreover, we have already fully defined the transverse focal field using both scalar and vector field models (Equations (3.54) and (3.85)).

A numerical study of the 3D spatial intensity distribution as a function of mask scan time t can be carried out by Fourier transforming the transverse focal field into lateral spatial frequency coordinates, applying the angular spectrum propagator to fill out a 3D space in (f_x, f_y, z), and then inverse Fourier transforming the result to generate the 3D spatial field distribution in (x, y, z). By repeating this process for each temporal position of the spinning mask, a 4D illumination field hypercube is created. This 4D cube can then be used to compute overlap integrals with the object $C(\mathbf{r})$ to simulate signal collection $S(t)$.

For imaging thick specimens, an additional two scan vectors are needed in order to simulate specimen translation in y and z. The three-dimensional $S(t, y_0, z_0)$ can then be converted into a 3D image of the thick specimen. Needless to say, computer processing time for six-dimensional datasets can be quite high. Computation times are bottlenecked further if one uses the high-NA vector field computations that were discussed in Section 3.3.6, because of the numerical integrals involved just to generate the initial transverse field at a single time. Numerical simulations in our lab, with distributed computations on a GPU, have required > 8 hours for certain datasets [64].

Instead, we turn to analytic models using scalar fields for speed and simplicity. For accuracy with scalar field models, we restrict our attention to low & moderate NA lenses. For flexibility, we make use of the paraxial approximation for axial phase accumulation - that is, the Fresnel propagator in Eqn. (2.55) - which allows for analytic Fourier transforms between z and f_z.

We also turn to the tools of optical imaging theory to simplify our approach to the image formation process. With some manipulation, we show that the SPIFI projection scheme can

be cast into a form recognizable in linear systems theory [40, 41]. That is, the specimen can be regarded as a set of frequencies input into the system, and at the output, the frequencies passed by the system (with possible attenuation and delay) are collected, resulting in a representation of the specimen subject to the system's filtering - in other words, an image. In optics, the application of linear systems theory to an imaging system results in the system being described by an Optical Transfer Function (OTF) for spatially incoherent light or a Coherent Transfer Function (CTF) for spatially coherent light passing through the system. For a $4f$ imaging system consisting of two lenses in the $2f$ configuration placed in series, we have already derived the equation for a CTF filtering an object field to produce an image field (Equation (2.86)). For an intensity-based imaging process, the OTF works in the same way:

$$S(\mathbf{f_r}) = OTF(\mathbf{f_r})C(\mathbf{f_r}) \tag{4.1}$$

A second important property is shift-invariance, which means that the linear transfer occurs faithfully and equivalently, no matter what transverse position (or shift from the origin) is interrogated. In the spatial domain, this means that the coherent spread function (CSF) or point spread function (PSF) is the same for all transverse positions in the object plane. Linear and shift-invariant (LSI) optical systems are easy to characterize through their transfer functions or point spread functions, which also makes different types of LSI imaging systems easy to compare.

The analysis we present in this chapter shows that the SPIFI microscope behaves as a linear, shift-invariant (LSI) system [64]. Therefore, we are able to derive an optical transfer function (OTF) relationship for the microscope that relates the sample under study to the reconstructed image formed by the optical system. The availability of an OTF, and its corresponding point spread function (PSF), then allow us to rapidly compute imaging performance for a given set of lenses and SPIFI mask parameters. The OTF also allows us to rapidly compute the expected image for a given object.

4.1.1 Secondary Applications

In previous chapters, we assumed that the illumination intensity was focused to a line, and we ignored the effect of out-of-focus light. However, a full account of the illumination intensity throughout the three-dimensional sample volume can better predict the collected photon flux at the single-element detector. This becomes especially interesting in the case of a relaxed focus, where the illumination volume is better described as a light sheet than a line focus.

In one important application, we turn our attention to a SPIFI microscope where only the $j = [0, 1]$ diffracted orders propagate to the sample, and the line focus in y is relaxed into a light sheet extending over the (x, z) plane. Under this illumination scheme, the intensity encodes axial propagation phase onto a thick sample through a chirped-frequency intensity modulation [58, 65], which provides a unique chirped modulation signature for every point in the (x, z) space. The remarkable outcome is the ability to perform digital holography on a distribution of incoherent emitters, such as fluorophores. To capture its importance, this technique was given its own acronym - CHIRPT (Coherent Holographic Image Reconstruction by Phase Transfer). As a demonstration of this capability, our group recently performed optical diffraction tomography on a fluorescent sample [50]. These works utilized a plane wave interference model, which was constructed to understand how the spatial phase of the interfering fields generates the uniquely labeling modulation intensity patterns in the (x, z) plane [58]. However, the spatial envelope of the illumination intensity, which determines the thickness and usable axial extent of the light sheet, was left untreated. Our work in this chapter allows us to circumscribe a boundary on holographic propagation in CHIRPT. For example, with Gaussian beams, the recorded signal light can be numerically propagated in a region around the focus, up to an axial limit (such as the confocal parameter of the intensity envelope in the (y, z) plane), where beyond this distance, signals from emitters in nearby y planes are mixed into the reconstruction.

Another important outcome is the ability to predict circular apodization by the system pupil. As we have shown, the back aperture actually contains vertical line cursors that scan in x (see Fig. 3.5)b). Because the aperture height changes with scan time, we realize a roll-off in vertical

frequency support. Practically speaking, this means that the real-space focal fields in the sample volume can have an intensity envelope in (y,z) that can vary from a line focus, to a light sheet, to a collimated beam as a function of scan time. For beam pair interactions involving the zero-order beam, the envelope is gated to quasi-static region. For beam pair interactions involving scanning beams, the intensity envelope can vary dramatically. In the future, knowledge of these time-varying focal volumes can be utilized in the image reconstruction process in a tomographic approach.

4.2 Comparison to experimental and numerical results

We start with a direct comparison of results. Figure 4.1 demonstrates both the speed and accuracy of this analytic 3D model in comparison to experimental data and to a forward computational model. Figure 4.1(a) shows a 2D image of a 15-μm diameter shell stained fluorescent bead in a commercially available slide (LifeTechnologies, FocalCheck™ Slide 1, Well A1). The image was collected in the (x,z) plane by scanning the bead axially and collecting 1D images in the $\hat{x}$ dimension. The experimental parameters are the same as described in [65]. Briefly, a continuous wave laser source at 532 nm was used to illuminate the specimen. A modulator mask with $\Delta_k = 70/\text{mm}$ was illuminated with a line focus and image relayed with a demagnification of 95× to the focal plane of a 0.8 NA, air-immersion objective lens (Zeiss N-Achroplan 50×/0.8 NA Pol) to create the CHRIPT intensity pattern. Images were collected and processed as described in Ref. [65].

The image in Fig. 4.1(b) was computed with a numerical simulation of the CHIRPT image formation process. At each time instance in the simulation, the 3D synthesized intensity was computed with a Gaussian beam model that includes wavefront shearing as a function of scan time. The fluorescence emitted from the specimen was computed by taking the product of the synthesized intensity and the object. From the emitted fluorescence, the photocurrent at time t was computed by performing a 3D trapezoidal integration of the fluorescent intensity. This process was repeated for all time points and axial positions in the image to compute a signal similar to the demodulated time trace, $S_{1+}(t)$. A Fourier transform of this computed data with

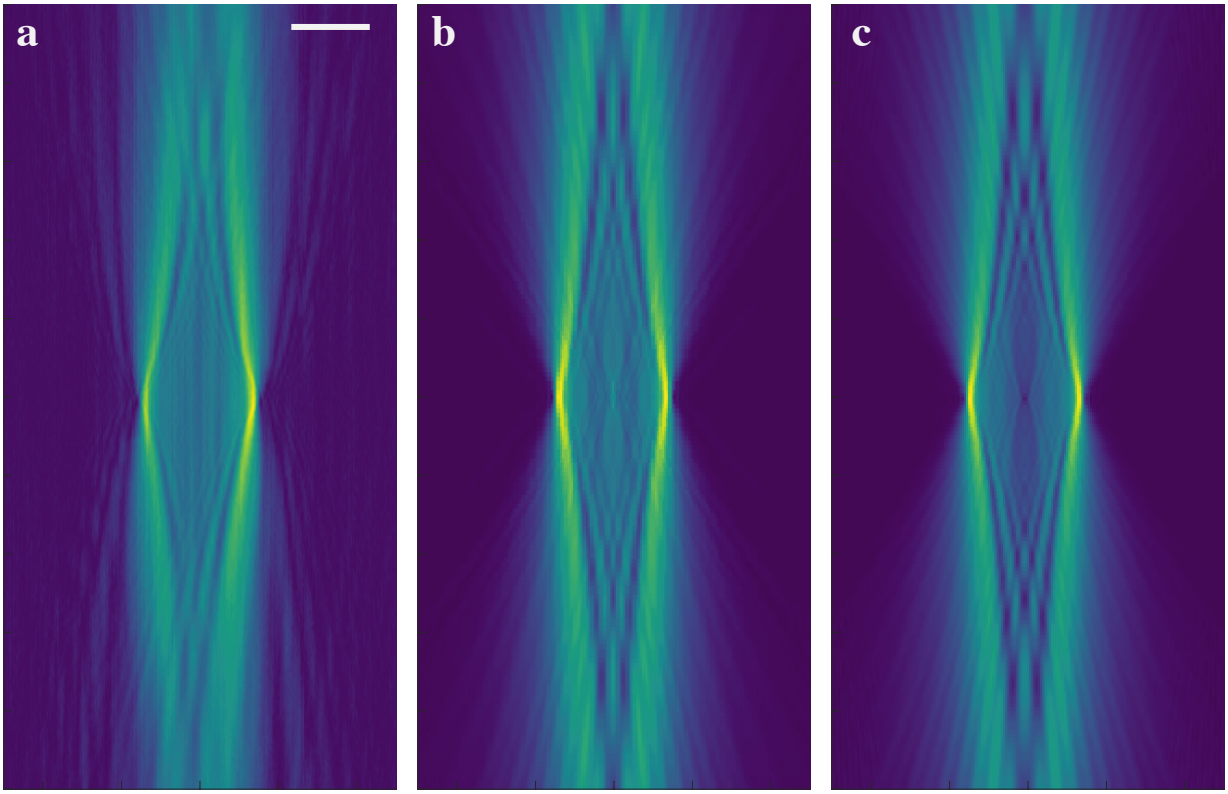

Figure 4.1: 2D lateral-axial images of a 15 μm diameter shell stained fluorescent microsphere. (a) Experimental data. (b) A numerically simulated 2D image computed as described in the text. Total computation time was approximately 4.5 hours. (c) A 2D image extracted from a 3D image computed using the analytic theory presented in this chapter. Computation time for the complete 3D image was approximately two minutes. Note that the spatial and temporal sampling density in panels (b) and (c) are identical. Scale bar: 10 μm. Reprinted with permission from Ref. [64] ©The Optical Society.

respect to the scan time revealed a simulated image of the object. The simulation was carried out on a desktop PC containing a graphical processing unit (GPU; NVIDIA GeForce GTX Titan) to parallelize the simulation, and took approximately 4.5 hours to complete.

Finally, the image in Fig. 4.1(c) was computed from the analytic theory presented in this chapter. The illumination intensity was formed by the product of a plane-wave intensity and Gaussian profile intensity at each time point in the simulation according to the assumptions made in this chapter, and Fourier transformed to generate an OTF. A 3D image was computed using the Fourier convolution theorem – the OTF was multiplied by a Fourier-space represen-

tation the object, followed by an inverse 3D Fourier transform. On a laptop computer with no GPU parallelization, this process took approximately two minutes of computation time.

The excellent agreement between the three images in Fig. 4.1 demonstrates that the approximations used to arrive at closed expressions for the OTF in this chapter are valid under most imaging conditions. Although higher-order effects such as shearing of the wavefront of the scanning beam were ignored in the analytic model, the resulting simulated image matched the experimentally collected image remarkably well.

4.3 Imaging with Plane Waves in Focal Volume

In this section we will compute the fields in the focal volume under the simplified assumption that the illumination is a time-sequence of tilted plane waves. A plane wave analysis is presented first in order to build intuition for the spatial beam analysis to follow. Optical transfer functions are presented for linear intensity patterns caused by the interference of pairs of tilted plane waves with their k-vectors in the lateral-axial plane. We examine the special case of CHIRPT, which contains holographic information in the measured signal.

We use the results of Section 3.3, where we computed the 4f image relay of each diffracted order from the mask, modeled as time-varying tilted plane waves, under the assumption of no pupil effects on the propagating fields. Since we are now working exclusively in the sample region, we will drop the s subscripts on the spatial coordinates.

4.3.1 Plane wave propagation through the Focal Volume

The plane wave component of the j^{th} diffracted order at the focal plane is given by Eqn. (3.51). To compute the field for each diffracted order in the volume around the focal plane (displaced from $z = 0$), we will use the angular spectrum representation of the monochromatic transverse field. Converting the j^{th} diffracted plane wave field into transverse Fourier space,

$$v_j\left(f_x, f_y, t\right) = \frac{a_j \Pi_{x_j}}{M} \exp\left[\mathrm{i}2\pi\left(j f_{g_x}(t)\right) x_o\right] \delta\left(f_x + \frac{j f_{g_x}(t)}{M}\right) \delta\left(f_y + \frac{j f_{g_y}}{M}\right) \tag{4.2}$$

We can now apply the Fresnel propagator (2.55) to examine the field on either side of the focal plane:

$$v_j\left(f_x,f_y,z,t\right) = v_j\left(f_x,f_y,0,t\right)\mathcal{H}\left(f_x,f_y,z\right) \tag{4.3}$$

$$= \frac{a_j\Pi_{x_j}}{M}\exp\left[\mathrm{i}2\pi\left(jf_{g_x}(t)\right)x_o\right]\delta\left(f_x+\frac{jf_{g_x}(t)}{M}\right)\delta\left(f_y+\frac{jf_{g_y}}{M}\right)\mathrm{e}^{\mathrm{i}kz}\mathrm{e}^{-\mathrm{i}\pi\lambda\left(f_x^2+f_y^2\right)z} \tag{4.4}$$

From here, it is helpful to look at the field both in complete real-space coordinates ($\overrightarrow{r}$) and in complete Fourier-space coordinates ($\overrightarrow{f_r}$). Transforming the transverse variables back to real space, the δ functions make the integration trivial. The real-space diffracted field is:

$$v_j\left(\mathbf{r},t\right) = \frac{a_j\Pi_{x_j}}{M}\mathrm{e}^{\mathrm{i}2\pi jv_ot}\mathrm{e}^{-\mathrm{i}2\pi j\frac{f_{g_x}}{M}(t)x}\mathrm{e}^{-\mathrm{i}2\pi j\frac{f_{g_y}}{M}y}\mathrm{e}^{\mathrm{i}kz}\mathrm{e}^{-\mathrm{i}\pi\lambda\frac{j^2}{M^2}\left(f_{g_x}^2(t)+f_{g_y}^2\right)z} \tag{4.5}$$

Propagating away from the focal plane, the field picks up an axial phase component that varies quadratically with lateral spatial frequency. Physically, this means that the plane wave propagation direction follows a parabolic trajectory as it moves through the focal volume. The $j=0$, $j=1$, and $j=-1$ diffracted orders are given by:

$$v_0 = \frac{a_0}{M}\mathrm{e}^{\mathrm{i}kz} \tag{4.6}$$

$$v_{1+} = \frac{a_1\Pi_{x_1}}{M}\mathrm{e}^{\mathrm{i}2\pi v_ot}\mathrm{e}^{-\mathrm{i}2\pi\frac{f_{g_x}(t)}{M}x}\mathrm{e}^{-\mathrm{i}2\pi\frac{f_{g_y}}{M}y}\mathrm{e}^{\mathrm{i}kz}\mathrm{e}^{-\mathrm{i}\pi\lambda\frac{1}{M^2}\left[f_{g_x}^2(t)+f_{g_y}^2\right]z} \tag{4.7}$$

$$v_{1-} = \frac{a_1\Pi_{x_1}}{M}\mathrm{e}^{-\mathrm{i}2\pi v_ot}\mathrm{e}^{\mathrm{i}2\pi\frac{f_{g_x}(t)}{M}x}\mathrm{e}^{\mathrm{i}2\pi\frac{f_{g_y}}{M}y}\mathrm{e}^{\mathrm{i}kz}\mathrm{e}^{-\mathrm{i}\pi\lambda\frac{1}{M^2}\left[f_{g_x}^2(t)+f_{g_y}^2\right]z} \tag{4.8}$$

We see that the $j=0$ order propagates on-axis, contains no temporal modulation, and accumulates only linear axial phase as it propagates. In contrast, the $j=\pm1$ orders propagate at time-varying horizontal angles, time stationary vertical angles, and accumulate both linear & quadratic axial phase. The quadratic component varies with time as it depends on $f_x(t)$ through the Helmholtz equation.

To look at the field in spatial frequency space, where a tilted plane wave becomes a single point, we take the Fourier transform over z of Eqn. (4.4):

$$v_j(\mathbf{f_r}, t) = \frac{a_j \Pi_{x_j}}{M} e^{i2\pi j \nu_o t} \delta\left(f_x + \frac{j f_{g_x}(t)}{M}\right) \delta\left(f_y + \frac{j f_{g_y}}{M}\right) \delta\left(f_z - \frac{1}{\lambda}\left(1 - \frac{\lambda^2}{2}\frac{j^2}{M^2}\left(f_{g_x}^2(t) + f_{g_y}^2\right)\right)\right) \quad (4.9)$$

The temporal parameterization causes a locus of points to be swept out in a parabolic arc in (f_x, f_z), since $f_x \propto t$ and $f_z \propto t^2$.

In our idealized sinusoidal amplitude mask, three diffracted orders $j \in [-1, 0, 1]$ propagate to the sample plane. However, in the CHIRPT illumination scheme, the $j = -1$ order is blocked before reaching the sample. Computing the illumination intensity for each scheme, we have:

$$\text{CHIRPT}: \quad I = |v_0 + v_1|^2 \quad (4.10)$$

$$\text{SPIFI}: \quad I = |v_0 + v_1 + v_{-1}|^2 \quad (4.11)$$

In both cases, the illumination intensity contains a component with temporal modulations from the mask, and one without: $I = I_{DC} + I_{AC}$. In CHIRPT, I_{AC} is very simple, and contains the terms:

$$\text{CHIRPT}: \quad I_{AC} = v_0^* v_1 + v_0 v_1^* = I_{1+} + I_{1-} \quad (4.12)$$

where the $\pm$ subscripts refer to the presence of the linear phase term $\exp[\pm i2\pi\kappa t x_o]$, which allows for isolation of image-containing information at a sideband after Fourier transformation. The information in I_+ and I_- is redundant, as they are merely complex conjugates of one another. We typically select the positive sideband term I_+ for analysis.

To compute the measured signal, let us assume that the sample is embedded in a medium of the same index of refraction as the immersion medium expected by the objective lens.

$$S(t) = \int C\left(\vec{r}\right) I\left(\vec{r}, t\right) d^3\vec{r} \quad (4.13)$$

Since the sideband-generating components $\exp[\pm i2\pi\nu_o t]$ are not a function of space, they move outside the integral. Therefore since the illumination intensity is the linear sum $I =$

$I_{DC} + I_{1+} + I_{1-} + ...$, it follows that the measured signal is $S(t) = S_{DC} + S_{1+} + S_{1-} + ...$, where any sideband component such as S_{1+} or S_{1-} can be extracted for the information it contains about $C(\overrightarrow{r})$.

4.3.2 Chirped Signals Give Axial Location Information

Let us now focus on the CHIRPT illumination scheme for simplicity, where only the $j \in [0,1]$ orders are allowed to propagate to the sample plane. The illumination intensity at the first positive sideband is:

$$I_{1+} = v_0^* v_1 = \frac{a_0 a_1 \Pi_{x_1}}{M^2} e^{i2\pi f_{gx}(t)\, x_o} e^{-i2\pi \frac{f_{gx}(t)}{M} x} e^{-i2\pi \frac{f_{gy}}{M} y} e^{-i\pi\lambda\left[\left(\frac{f_{gx}(t)}{M}\right)^2 + \left(\frac{f_{gy}}{M}\right)^2\right] z} \tag{4.14}$$

We will employ the temporal frequency viewpoint for a moment to gain physical intuition. Let us assume that we can engineer the experiment to eliminate the static vertical spatial frequency, such that $f_{g_y} = 0$. Reorganizing the variables in Eqn. (4.14), we can write:

$$S_{1+}(t) = \int C\left(\overrightarrow{r}\right) \frac{a_0 a_1 \Pi_{x_1}}{M^2} e^{i2\pi\kappa[x_o - x/M]t} e^{-i2\pi \frac{\lambda\kappa^2}{2M^2} z\, t^2} d^3\overrightarrow{r} \tag{4.15}$$

where we can write the temporal modulation frequency given by the lateral position $\nu(x) = \kappa\,[x_o - x/M]$. Moreover, there is a temporal chirp parameter given by the axial position, $c(z) = -\left(\lambda\kappa^2\right)/\left(2M^2\right) z$. Thus, if the object is a single point emitter $C(x,z) = \delta(x-x_0)\delta(y-y_0)\delta(z-z_0)$, then the resultant measured signal is a chirped temporal waveform,

$$S_{1+}(t) \propto \Pi_{x_1}(t) e^{i2\pi\nu(x_0)\,t} e^{i2\pi c(z_0)\,t^2} \tag{4.16}$$

encoding information about the object in the x and z directions. (We note that the measured signal yields no object information in y, which is the subject of later work in this chapter). Looking at the measured signal, an emitter before the focal plane ($z_0 < 0$) has an upchirped signature, and an emitter beyond the focal plane generates a downchirped signature. (This is the reason for the name "CHIRPT"). This expression captures the nature of CHIRPT imaging: an emitter's

lateral position is encoded by a modulation frequency, and its axial location is encoded by the strength of the chirp imparted upon that modulation frequency. It is a remarkable feature that the nature of the plane wave interference itself generates axial location information, and not anything having to do with localized focusing of the intensity. This would not be possible in a SPIFI illumination scheme where the $j = -1$ order also propagated to the sample, as an equivalent axial phase term with opposite sign would be generated, canceling out the quadratic axial phase information [58, 66]. Finally, we note that a collection of point emitters results in a linear sum of chirped waveforms at the detector.

4.3.3 CHIRPT OTF for Plane Wave Illumination

In the preceding section we discussed how CHIRPT encodes (x, z) information about a volume object $C(\overrightarrow{r})$, even while compressing this 2D information into a 1D data stream at the single pixel detector. How does one recover this dimensionality in order to reconstruct a 2D object $C(x, z)$?

Let us start by rewriting the measured signal, where the sample 'center' (which can be arbitrary, but makes sense for something like a delta emitter) is displaced z_0 from the center of the illumination intensity. Examining the information-bearing component,

$$S_{1+}(t, z_0) = \int C\left(x, y, z - z_0\right) I_{1+}\left(\overrightarrow{r}, t\right) \mathrm{d}^3\overrightarrow{r} \tag{4.17}$$

where we have again assumed $f_{g_y} = 0$ in I_{1+}, and that the object exists in the (x, z) plane only, so that $C(y) = \delta(y)$. Making a change of variables $z' = z - z_0$, we find that:

$$S_{1+}(t, z_0) = \frac{a_0 a_1 \Pi_{x_1}}{M^2} \mathrm{e}^{\mathrm{i}2\pi\nu_o t} \mathrm{e}^{-\mathrm{i}2\pi\left[\lambda f_{g_x}^2(t)/2M^2\right] z_0} \int C(x, z') \mathrm{e}^{-\mathrm{i}2\pi\frac{f_{g_x}(t)}{M}x} \mathrm{e}^{-\mathrm{i}2\pi\left[\lambda f_{g_x}^2(t)/2M^2\right] z'} \mathrm{d}x\mathrm{d}z' \tag{4.18}$$

After demodulating from the sideband, ignoring scaling constants, and solving the integral,

$$S_{1+}(t,z_0) \propto \Pi_{x_1}(t)\, \mathrm{e}^{-\mathrm{i}2\pi\left[\lambda f_{g_x}^2(t)/2M^2\right]z_0}\, \hat{C}\left(f_x(t), f_z(t)\right) \tag{4.19}$$

where the lateral spatial frequency is $f_x(t) = f_{g_x}(t)/M$ and the axial spatial frequency is $f_z(t) = \lambda f_{g_x}^2(t)/2M^2$. As we know, the mask steps through f_{g_x} linearly with time, and therefore $f_z \propto f_{g_x}^2$ has a parabolic shape. We can thus conclude that each temporal point in the measurement is probing the object's spatial frequency content along a parabolic arc in (f_x, f_z) in the plane $f_y = 0$. In essence, CHIRPT is sequentially measuring voxels in the Fourier space of the object's spatial distribution. This is in contrast to laser-scanning microscopy, which sequentially measures voxels in real space, $\vec{r}$. At this point, let us more explicitly write the lateral spatial frequency in place of time, since the former is simply a linear function of the latter, $f_x(t) \propto t$. The signal is thus:

$$S_{1+}(f_x(t),z_0) \propto \Pi_{x_1}(f_x(t))\, \mathrm{e}^{-\mathrm{i}2\pi[\lambda f_x^2(t)/2]z_0}\, \hat{C}\left(f_x(t), f_z(f_x(t))\right) \tag{4.20}$$

Equation (4.20) is the key result for CHIRPT microscopy. We see that the measurement is a mixed-space (f_x, z_0) quantity that contains three key components: an upper boundary on the maximum spatial frequency projected ($\Pi_{x_1}(f_x(t))$), a quadratic axial phase proportional to the displacement from illumination center $\exp\left[-\mathrm{i}2\pi[\lambda f_{g_x}^2/2M^2]z_0\right]$, and a sampling of the object's spatial frequency content along the arc $(f_x, f_z) = (f_{g_x}/M, \lambda f_{g_x}^2/2M^2)$. There are a few different ways to interpret this result.

1. The displacement variable z_0 can be a scan vector. By mechanically varying z_0, one probes and collects defocus phase from emitters' central positions.

2. Alternately, recognizing the 1D measured signal exists in (f_x, z) space, one can immediately apply a numerical angular spectrum propagator to fill out the 2D space along z. This computation will act on the measured propagation phase to refocus, or further defocus, the intensity measured at position z_0.

3. One can rewrite the signal entirely temporally, where modulation frequency and chirp encode emitter positions (as in the previous section). One can then perform a fit to these parameters to localize emitter positions.

In the spatial framework of (1) or (2) above, whether mechanical scanning or numerical propagation is utilized to fill out a 2D space, one can then IFFT $S_{1+}(f_x, z_0)$ from f_x to x in order to reconstruct the 2D object C(x,z). Alternatively, one can FFT from z_0 to f_{z_0} in order to examine the 2D transfer function of the imaging system. This will give:

$$\hat{S}_{1+}(f_x, f_{z0}) \propto \Pi_{x_1}(f_x)\, \delta\left(f_{z_0} + \frac{\lambda f_{g_x}^2}{2M^2}\right) \hat{C}\left(f_x, f_{z_0}\right) \tag{4.21}$$

$$= OTF_{1+}\left(f_x, f_{z_0}\right) \hat{C}\left(f_x, f_{z_0}\right) \tag{4.22}$$

Thus we have derived the plane wave OTF for CHIRPT, which takes the form of a parabolic arc centered at the origin:

$$OTF_{1+}(f_x, f_{z0}) = \Pi_{x_1}(f_x)\, \delta\left(f_{z0} + \frac{\lambda f_{g_x}^2(t)}{2M^2}\right) \tag{4.23}$$

This is depicted in Fig. 4.2(a).

The fact that CHIRPT measures defocus phase and therefore allows numerical refocusing is a significant feature. It is clearly a holographic measurement. What's more, and this can't be overstated, the object contrast function is not limited to a coherent response as in standard holography. Even if the object has an incoherent response, such as fluorescence, it is the coherence of the illuminating light, imprinted upon the object spatial distribution through chirped temporal modulations, that allows for holographic refocusing of incoherent emission [50, 58, 65]. (This is the reasoning behind the CHIRPT acronym: Coherent Holographic Image Reconstruction by Phase Transfer).

That being said, there are important limitations to the holographic capability in CHIRPT. First of all, it only allows for holographic refocusing in one lateral dimension (x). In the vertical dimension, it does not allow for holographic refocusing, nor does it even offer spatial resolution. To gain spatial resolution in y, one must move away from plane wave interference and

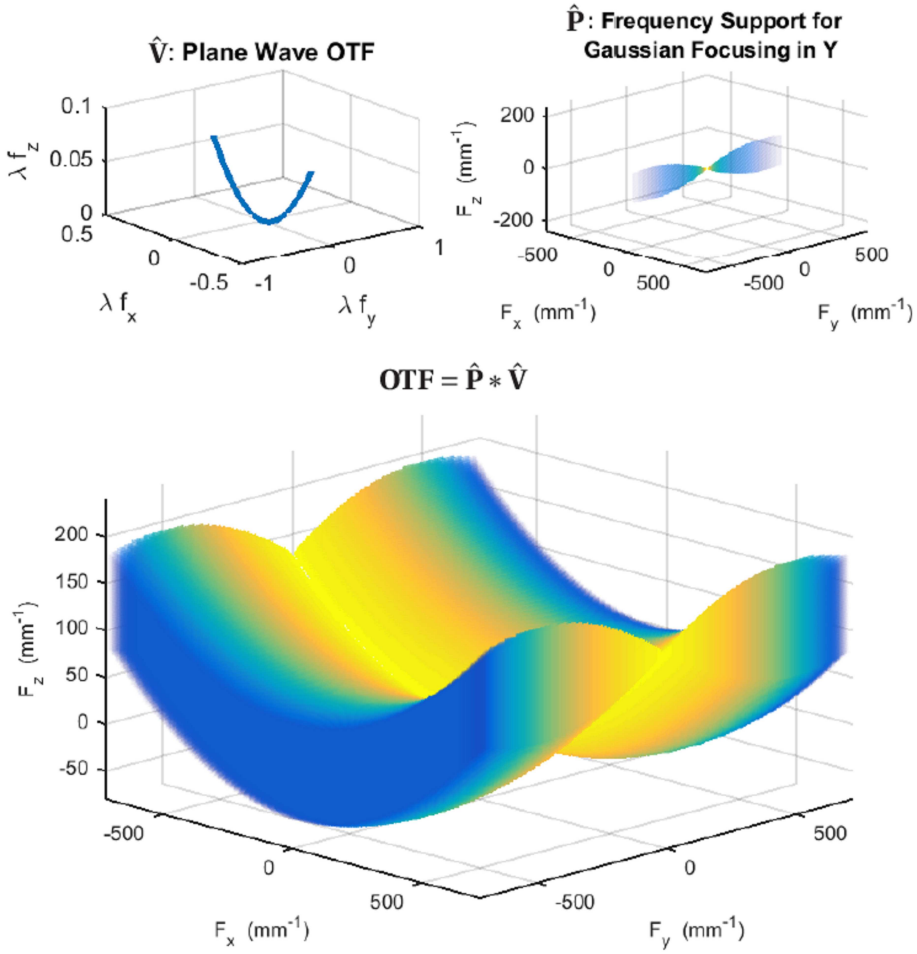

Figure 4.2: (a) The OTF, $\hat{V}$, for CHIRPT imaging under the plane wave approximation. (b) The OTF, $\hat{P}$, due to line focusing in the $\hat{y}$ direction. (c). The 3D OTF for CHIRPT imaging with line-focused spatial beams.

utilize vertically-focused light sheets. This has been how the experimental results have been demonstrated thus far. With a light sheet, the depth of focus is inversely related to how tightly the light is focused in y. Thus, in CHIRPT,there is a tradeoff between spatial resolution in y, and the depth of field in z over which one can perform holographic refocusing. Accurately modeling the light-sheet focusing utilized in experimental demonstrations of CHIRPT is the subject of the latter part of this chapter.

4.3.4 SPIFI OTFs for Plane Wave Illumination

In order to understand the importance of the axial defocus phase measured by CHIRPT, it is helpful to also examine the SPIFI measured signal, where all three diffracted orders ($j \in [-1,0,1]$) propagate to the sample plane. The first sideband intensity is:

$$\begin{aligned} I_{1+} &= v_0^* v_1 + v_0 v_{-1}^* \\ &= \frac{a_0 a_1 \Pi_{x_1}}{M^2} e^{i2\pi v_o t} e^{-i2\pi \frac{f_{g_x}(t)}{M} x} e^{-i2\pi \frac{f_{gy}}{M} y} \left[e^{-i\pi\lambda \frac{1}{M^2}\left[f_{g_x}^2(t)+f_{g_y}^2\right] z} + e^{\ i\pi\lambda \frac{1}{M^2}\left[f_{g_x}^2(t)+f_{g_y}^2\right] z} \right] \end{aligned} \tag{4.24}$$

The symmetry of the two diffracted orders, v_{1+} and v_{1-}, scanning through equal but opposite angles about the optic axis, causes their respective interference with the on-axis zero order v_0 to generate quadratic axial phases with opposite sign. This destroys the ability to locate an emitter in z with a unique chirped temporal signature. To see this, let us assume a point emitter, $C(x,z) = \delta(x - x_0, y, z - z_0)$. The measured, isolated sideband signal $S_{1+}(t) = \int C\left(\overrightarrow{r}\right) I_{1+}\left(\overrightarrow{r}, t\right) d^3\overrightarrow{r}$ becomes

$$S_{1+}(t) \propto \Pi_{x_1}(t) e^{i2\pi \frac{f_{g_x}(t)}{M} x_0} \cos\left(\pi\lambda \frac{f_{g_x}^2(t)}{M^2} z_0\right) = \Pi_{x_1}(t) e^{i2\pi \frac{f_{g_x}(t)}{M}(t) x_0} \frac{1}{2}\left(e^{i\pi\lambda \frac{f_{g_x}^2(t)}{M^2} z_0} + e^{-i\pi\lambda \frac{f_{g_x}^2(t)}{M^2} z_0} \right) \tag{4.25}$$

where we have again assumed $f_{g_y} = 0$. If we first apply a propagator to the 1D signal to fill out the z direction in (f_x, z) space, and then inverse Fourier transform $S_{1+}(f_x, z)$ over f_x, we find that the reconstructed 2D image has placed twin emitters at equal distances across the focal plane from each other: $S_{1+}(x,z) \propto \delta(x - x_0, z - z_0) + \delta(x - x_0, z + z_0)$.

The OTF for the SPIFI image extracted from the first sideband, S_{1+}, displays dual arcs in (f_x, f_{z_0}) space, one for each pair of interference terms [66]. Using the same development as in the case of CHIRPT, the OTF for first-order SPIFI is:

$$OTF_{1+}(f_x(t), f_{z0}) = \Pi_{x_1}(f_x(t)) \left[\delta\left(f_{z0} + \frac{\lambda f_{g_x}^2(t)}{2M^2} \right) + \delta\left(f_{z0} - \frac{\lambda f_{g_x}^2(t)}{2M^2} \right) \right] \tag{4.26}$$

At the second positive sideband the intensity is the product of both first-diffracted orders:

$$I_{2+} = v_{-1}^{*} v_1 = \frac{a_1^2 \Pi_{x_1}^2}{M^2} \mathrm{e}^{\mathrm{i}2\pi(2f_{g_x}(t))x_o} \mathrm{e}^{-\mathrm{i}2\pi(2f_{g_x}(t)/M)x} \mathrm{e}^{-\mathrm{i}2\pi\left(2f_{g_y}/M\right)y} \tag{4.27}$$

where we observe, first, that the axial phase component has disappeared completely. Secondly, the projected spatial frequencies $f_{gx} = 2\kappa t/M$ and $f_{g_y} = 2\Delta_k/(2\pi M)$ are increased by a factor of two. Physically, this is due to their equal but opposite propagation angles, generating interference at twice the spatial frequency when compared to each of them interfering with the on-axis zero order. The measured, demodulated signal for a point emitter $C = \delta(x - x_0)\delta(y)\delta(z - z_0)$, which with our preceding assumption $f_{g_y} = 0$, is

$$S_{2+}(t) = \int C(\overrightarrow{r}) I_{2+}(\overrightarrow{r}, t) \mathrm{d}^3\overrightarrow{r} = \frac{a_1^2 \Pi_{x_1}^2}{M^2} \mathrm{e}^{\mathrm{i}2\pi(2f_{g_x}(t))x_0} \tag{4.28}$$

The transfer function is simply $OTF_{2+} = \Pi_{x_1}\left(2f_x(t)\right)$, showing while the system probes twice the lateral spatial frequency, there is no information about axial emitter position preserved through phase. This is because the (x, z) fringe pattern formed by the interference between v_1 and v_{-1} is always symmetric about $x = 0$, since the beams always interfere at equal but opposite angles in the (x, z) plane for all scan times t. Emitters that are axially displaced from one another will all contribute to the measured signal in the same way. Thus, axial information for 2^{nd} order SPIFI must occur through another means, such as confocal detection, computed tomography, or optical sectioning with an intensity envelope, e.g. through a line focus. We handle focusing envelopes next.

4.4 Imaging with Spatial Beams in the 3D Focal Volume

Having looked at transfer functions for the explicit cases of CHIRPT and SPIFI using tilted plane wave illumination with the 3 lowest diffracted orders, we now generalize our model in two ways. First, we now explicitly include spatial beam profiles in our model. Second, we can examine any pair of diffracted orders that propagate to the sample.

4.4.1 The 3D OTF for Laser Scanning Microscopy

To begin our formulation of imaging with focused beams, we start by way of examining a 3D point focus, as used in laser scanning microscopy (LSM). In an LSM model, the object is scanned in 3 dimensions relative to the localized illumination intensity, $I(\overrightarrow{r})$ (or vice-versa). The signal light, generated by the linear interaction between the object and illumination, is collected and spatially integrated on a single pixel detector:

$$S(\overrightarrow{r}_s) = \int_{\overrightarrow{r}} C(\overrightarrow{r} - \overrightarrow{r_s})\, I(\overrightarrow{r})\, \mathrm{d}^3\overrightarrow{r} \tag{4.29}$$

Taking the Fourier transform over the scan vector results in:

$$\hat{S}(\overrightarrow{f}_{r_s}) = -\hat{C}(-\overrightarrow{f}_{r_s})\, \hat{I}(\overrightarrow{f}_{r_s}) \tag{4.30}$$

Other than the trivial sign flip in the spatial frequency vector, we can see that $-\hat{I}$ acts as a linear system transfer function acting on the input object frequency content $\hat{C}(-\overrightarrow{f}_{r_s})$ and producing a filtered form of the frequency content, $\hat{S}$. The negated spectral intensity is therefore a system transfer function:

$$OTF(\overrightarrow{f}_{r_s}) = -\hat{I}(\overrightarrow{f}_{r_s}) \tag{4.31}$$

We can instead anticipate the sign flip by saying that the programmed scan position r_0 will in fact interrogate $-r_0$ in the object:

$$S(\overrightarrow{r}_s) = \int_{\overrightarrow{r}} C\left(-\left(\overrightarrow{r} - \overrightarrow{r_s}\right)\right) I(\overrightarrow{r})\, \mathrm{d}^3\overrightarrow{r} = \int_{\overrightarrow{r}} C\left(\overrightarrow{r_s} - \overrightarrow{r}\right) I(\overrightarrow{r})\, \mathrm{d}^3\overrightarrow{r} \quad = \quad C(\overrightarrow{r}) * I(\overrightarrow{r}) \tag{4.32}$$

which results in a convolution integral, and a clean product in spatial frequency space:

$$\hat{S}(\overrightarrow{f}_{r_s}) = \hat{C}(\overrightarrow{f}_{r_s})\, \hat{I}(\overrightarrow{f}_{r_s}) \tag{4.33}$$

In other words, the spectral intensity is the system optical transfer function:

$$OTF(\overrightarrow{f}_{r_s}) = \hat{I}(\overrightarrow{f}_{r_s}) \tag{4.34}$$

Since the tight focal volume is the same for all transverse scan positions, the system is also shift-invariant. Thus, the class of laser-scanning microscopy techniques are on the same formal footing as wide-field imaging techniques. The image mechanism is conceptually clear - probing the object with a small, finite focal volume returns an image, with the caveat that sample features smaller than the focal volume are blurred out. In other words, the object is convolved with a small blurred spot.

4.4.2 The 3D OTF for any SPIFI beam pair

We will now show that SPIFI imaging also results in LSI system behavior. Specifically, every pair of diffracted orders generates an intensity pattern over time that results in a unique OTF for that illumination beam pair.

We use Equation (4.31), where we now give the illumination intensity a temporal dependence to account for the series of illumination patterns projected onto the sample at a given scan position $\overrightarrow{r}_s$. The collected signal takes the same form as in LSM, with an additional temporal dependence:

$$S(\overrightarrow{r}_s, t) = \int_{\overrightarrow{r}} C(\overrightarrow{r} - \overrightarrow{r_s})\, I(\overrightarrow{r}, t)\, \mathrm{d}^3\overrightarrow{r} \tag{4.35}$$

As before, we can separate the signal, and the illumination intensity, into terms that are isolated at sidebands upon Fourier transformation of the signal. For two diffracted orders E_j and E_k produced at the mask, the modulator phase shift on E_j and E_k means that the illumination will have a temporal carrier frequency at a harmonic $(k-j)\nu_o$. In some cases multiple pairs of beams will contribute to the same sideband, in which case the isolated signal is a sum of beam pair signals. The complex signal due to the $(k-j)^{th}$ beam pair is:

$$S_{j,k}(\overrightarrow{r}_s, t) = \int_{\overrightarrow{r}} C(\overrightarrow{r} - \overrightarrow{r_s})\, I_{j,k}(\overrightarrow{r}, t)\, \mathrm{d}^3\overrightarrow{r} \tag{4.36}$$

To account for the presence of spatially confined beams, we write the fields in the focal volume as a simple product of a spatial profile p and a plane wave component v:

$$E_j\left(\overrightarrow{r},t\right) = p_j\left(\overrightarrow{r},t\right)\, v_j\left(\overrightarrow{r},t\right) \tag{4.37}$$

$$E_k\left(\overrightarrow{r},t\right) = p_k\left(\overrightarrow{r},t\right)\, v_k\left(\overrightarrow{r},t\right) \tag{4.38}$$

The profile intensity component is

$$P_{j,k} = p_j^* p_k, \tag{4.39}$$

which represents a spatial intensity envelope, determined by the region of overlap of the two field amplitudes. The plane wave intensity component is

$$V_{j,k} = v_j^* v_k = \left(\Pi_{x_j}(t)\mathrm{e}^{\mathrm{i}2\pi\overrightarrow{f}_{r\,j}(t)\cdot\overrightarrow{r}}\right)^* \left(\Pi_{x_k}(t)\mathrm{e}^{\mathrm{i}2\pi\overrightarrow{f}_{r\,k}(t)\cdot\overrightarrow{r}}\right) = \Pi_{x_j}(t)\,\Pi_{x_k}(t)\,\mathrm{e}^{\mathrm{i}2\pi\Delta\overrightarrow{f}_r(t)\cdot\overrightarrow{r}}, \tag{4.40}$$

where $\Delta\overrightarrow{f_r} = \overrightarrow{f}_k - \overrightarrow{f}_j$ refers to the difference in plane wave directions of the two interfering beams in the sample plane. This difference results in sinusoidal modulations at the difference spatial frequency $\Delta\overrightarrow{f_r}$. The binary window functions Π_x are real-valued. Their product is a new binary window function

$$\Pi_{x_{j,k}}(t) \quad = \quad \Pi_{x_j}(t)\,\Pi_{x_k}(t) \quad = \quad \begin{cases} \Pi_{x_j}(t), & |j| \geq |k| \\ \Pi_{x_k}(t), & |k| > |j| \end{cases} \tag{4.41}$$

where the higher diffracted order, which has the quicker temporal transit through the pupil, determines the temporal window used for this beam-pair interaction. We are interested in the range of lateral spatial frequencies that are projected during the window 'on' time. This range is determined by the frequency difference

$$\Delta f_x(t) = k f_{g_x}(t) - j f_{g_x}(t) \tag{4.42}$$

for the diffracted orders j and k, which will have a maximum difference of

$$\Delta f_x(t)_{[\max]} = \frac{|k-j|}{\mathrm{Max}\left[|j|,|k|\right]} \cdot f_c \tag{4.43}$$

Thus the horizontal spatial frequency window for two arbitrary diffracted orders j and k is

$$\Pi_{x_{j,k}}\left(\Delta f_x(t)\right) = \mathrm{rect}\left[\frac{\Delta f_x(t)}{2 \cdot \Delta f_x(t)_{[\max]}}\right] \tag{4.44}$$

The intensity due to this beam pair interaction is

$$I_{j,k} = \left(v_j\, p_j\right)^* \left(v_k\, p_k\right) = v_j^*\, v_k \times p_j^*\, p_k = V_{j,k}\, P_{j,k} \tag{4.45}$$

$$= \Pi_{x_{j,k}}\left(\Delta f_x(t)\right) \mathrm{e}^{\mathrm{i}2\pi\Delta\vec{f}_r(t)\cdot\vec{r}}\, P_{j,k}(\vec{r},t) \tag{4.46}$$

The spectral intensity will therefore be a 3D convolution:

$$\hat{I}_{j,k}\left(\vec{f_r},t\right) = \hat{V}_{j,k}\left(\vec{f_r},t\right) \underset{\vec{f_r}}{*} \hat{P}_{j,k}\left(\vec{f_r},t\right) = \Pi_{x_{j,k}}\left(\Delta f_x(t)\right) \left[\mathscr{F}\left[P(\vec{r},t)\right] \underset{\vec{f_r}}{*} \mathscr{F}\left[\mathrm{e}^{\mathrm{i}2\pi\Delta\vec{f}_r(t)\cdot\vec{r}}\right]\right] \tag{4.47}$$

The complex signal (Equation (4.36)) is now written:

$$S_{j,k}(\vec{r}_s,t) = \Pi_{x_{j,k}}\left(\Delta f_x(t)\right) \int_{\vec{r}} C(\vec{r}-\vec{r_s})\, P_{j,k}(\vec{r},t)\, \mathrm{e}^{\mathrm{i}2\pi\Delta\vec{f}_r(t)\cdot\vec{r}}\, \mathrm{d}^3\vec{r} \tag{4.48}$$

Upon Fourier transform over the sample translation vector $\vec{r}_s$, just as in Eqn. (4.30), the measurement has a representation in the spatial frequency domain

$$S_{j,k}(\vec{f}_{r_s},t) = -\hat{C}(-\vec{f}_{r_s})\, \hat{I}_{j,k}(\vec{f}_{r_s},t) \tag{4.49}$$

$$= -\hat{C}(-\vec{f}_{r_s})\, \Pi_{x_{j,k}}\left(\Delta f_x(t)\right) \left[\mathscr{F}\left[P(\vec{r},t)\right] \underset{\vec{f_r}}{*} \mathscr{F}\left[\mathrm{e}^{\mathrm{i}2\pi\Delta\vec{f}_r(t)\cdot\vec{r}}\right]\right] \tag{4.50}$$

For beams that underfill the vertical aperture, or are clipped in a time-constant fashion, we can

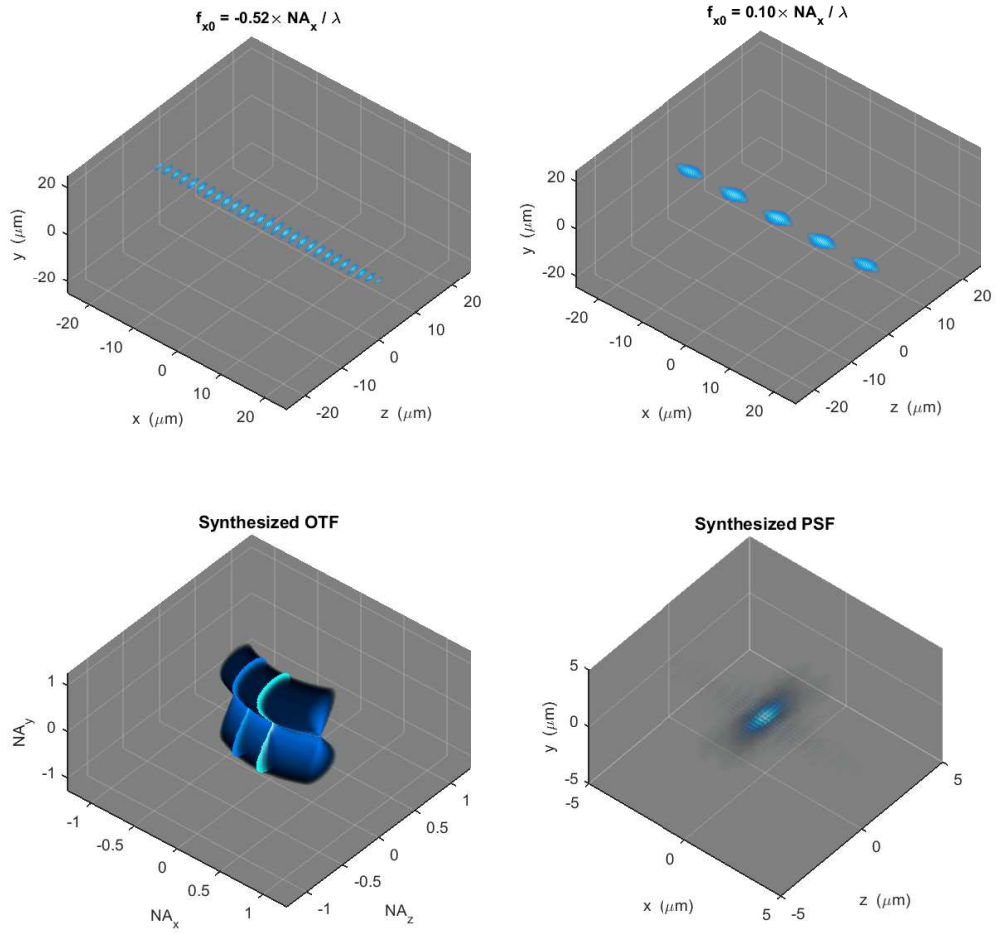

Figure 4.3: Synthesized 3D OTF and PSF in CHIRPT imaging ($j \in [0,1]$) with a line focus. Top row: Line focus illumination at two snapshots in time, modulated by the x spatial frequency projection corresponding to each time. Bottom left: The 3D OTF synthesized from the set of hourglass-shaped slices corresponding to each line-focused x cosine projection in the set of illumination patterns. The two slices corresponding to the projections in the top row are highlighted. Bottom right: The synthesized PSF of the imaging system, realized by Fourier transform of the OTF.

make the approximation that the intensity envelope does not vary much in time. Furthermore, since the microscope is designed to focus the intensity in the y direction, but keep the illumination collimated in x (in order to generate a line focus or a light sheet), we can assume that the

intensity profile is roughly constant in x across the region of illumination. Thus, let us write the intensity envelope P, which in general varies in 3D as the diffracted orders rotate through the sample volume in time, more simply as $P(\vec{r}, t) \approx P(y, z)$. In other words, we are approximating that the spatial volume of the intensity envelope is time-stationary. With this approximation in hand, the 3D spatial Fourier transform over the envelope becomes:

$$\hat{P}_{j,k} = \mathscr{F}\left[P_{j,k}(\vec{r}, t)\right] = \mathscr{F}\left[P_{j,k}(y, z)\right] = \delta(f_{x_s})\hat{P}_{j,k}(f_{y_s}, f_{z_s}) \tag{4.51}$$

Meanwhile, the 3D spatial Fourier transform over the phase term containing the interference information is:

$$\mathscr{F}\left[\mathrm{e}^{\mathrm{i}2\pi\Delta\vec{f}_r(t)\cdot\vec{r}}\right] = \delta\left(\vec{f}_{r_s} - \Delta\vec{f}_r(t)\right) \tag{4.52}$$

Putting these together, the spectral intensity is

$$\hat{I}_{j,k}(\vec{f}_{r_s}, t) = \Pi_{x_{j,k}}\left(\Delta f_x(t)\right)\left[\delta(f_{x_s})\hat{P}_{j,k}(f_{y_s}, f_{z_s}) \underset{\vec{f}_r}{*} \delta\left(\vec{f}_{r_s} - \Delta\vec{f}_r(t)\right)\right] \tag{4.53}$$

$$= \Pi_{x_{j,k}}\left(\Delta f_x(t)\right)\delta\left(f_{x_s} - \Delta f_x(t)\right)\left[\hat{P}_{j,k}(f_{y_s}, f_{z_s}) \underset{f_y, f_z}{*} \delta\left(f_{y_s} - \Delta f_y\right)\delta\left(f_{z_s} - \Delta f_z(t)\right)\right] \tag{4.54}$$

We now utilize further physical information about the microscope's illumination configuration. First of all, the vertical spatial frequency difference Δf_y is a constant, given by the mask pattern density as $f_{y_j} = j\Delta_k/(2\pi M)$. In many cases it is fine to approximate this as zero. The convolution over f_y simply returns the vertical profile $\hat{P}_{j,k}(f_y)$:

$$\hat{I}_{j,k}(\vec{f}_{r_s}, t) = \Pi_{x_{j,k}}\left(\Delta f_x(t)\right)\delta\left(f_{x_s} - \Delta f_x(t)\right)\left[\hat{P}_{j,k}(f_{y_s}, f_{z_s}) \underset{f_z}{*} \delta\left(f_{z_s} - \Delta f_z(t)\right)\right] \tag{4.55}$$

Inserting this expression into our collected spectral signal, Equation (4.49), we have

$$S_{j,k}(\vec{f}_{r_s}, t) = -\hat{C}(-\vec{f}_{r_s})\,\Pi_{x_{j,k}}\left(\Delta f_x(t)\right)\delta\left(f_{x_s} - \Delta f_x(t)\right)\left[\hat{P}_{j,k}(f_{y_s}, f_{z_s}) \underset{f_z}{*} \delta\left(f_{z_s} - \Delta f_z(t)\right)\right] \tag{4.56}$$

We see that, just as in the 1D treatment of SPIFI, the object's x spatial frequency information is scanned sequentially by the sequence of projections $\delta\left(f_{x_s} - \Delta f_x(t)\right)$ formed by the two interfering beams. The time dependence can be expressed simply as a parameterization of the lateral and axial spatial frequency variables:

$$S_{j,k}(\vec{f}_{r_s}, t) = S_{j,k}\left(f_{x_s}(t), f_y, f_{z_s}(t)\right) \tag{4.57}$$

Moreover, because the illumination pattern is very broad in x, and information along x can be found through the temporal projections $\Delta f_x(t)$, there is no need to physically scan the specimen in x with a translation stage. Instead, the 'scan' over object horizontal information occurs in spatial frequency space through the sequence of cosine patterns. We also note in passing that $\Delta f_z(t)$ is a function of $\Delta f_x(t)$ through the Helmholtz equation. We see that the spectral signal displays the form of an LSI system,

$$S_{j,k}\left(f_{x_s}(t), f_{y_s}, f_{z_s}(t)\right) = \hat{C}(-\vec{f}_{r_s})\, OTF\left(f_{x_s}(t), f_{y_s}, f_{z_s}(t)\right) \tag{4.58}$$

where the Optical Transfer Function is given by

$$OTF\left(f_{x_s}(t), f_{y_s}, f_{z_s}(t)\right) = -\Pi_{x_{j,k}}\left(\Delta f_x(t)\right)\delta\left(f_{x_s} - \Delta f_x(t)\right)\left[\hat{P}_{j,k}(f_{y_s}, f_{z_s}) \underset{f_z}{*} \delta\left(f_{z_s} - \Delta f_z(t)\right)\right] \tag{4.59}$$

$$= -\hat{P}_{j,k} \underset{\vec{f}_r}{*} \hat{V}_{j,k} \tag{4.60}$$

where $\hat{P}_{j,k}$ and $\hat{V}_{j,k}$ are given by Equations (4.51) and (4.52), respectively. Thus, the OTF is the negative of the spectral intensity, $OTF = -\hat{I}_{j,k}$, just as in the case of LSM (Eqn. (4.31)).

Equation (4.60) is a key result of this chapter. It states that when we move to a model using spatially-confined fields, we can simply convolve the frequency support of the intensity envelope with the plane wave OTF, to form the full 3D OTF. This process is depicted in Figure 4.2 for the $j \in [0,1]$ pair of diffracted orders. The spectral profile $\hat{P}(f_y, f_z)$ is convolved with a 3D delta

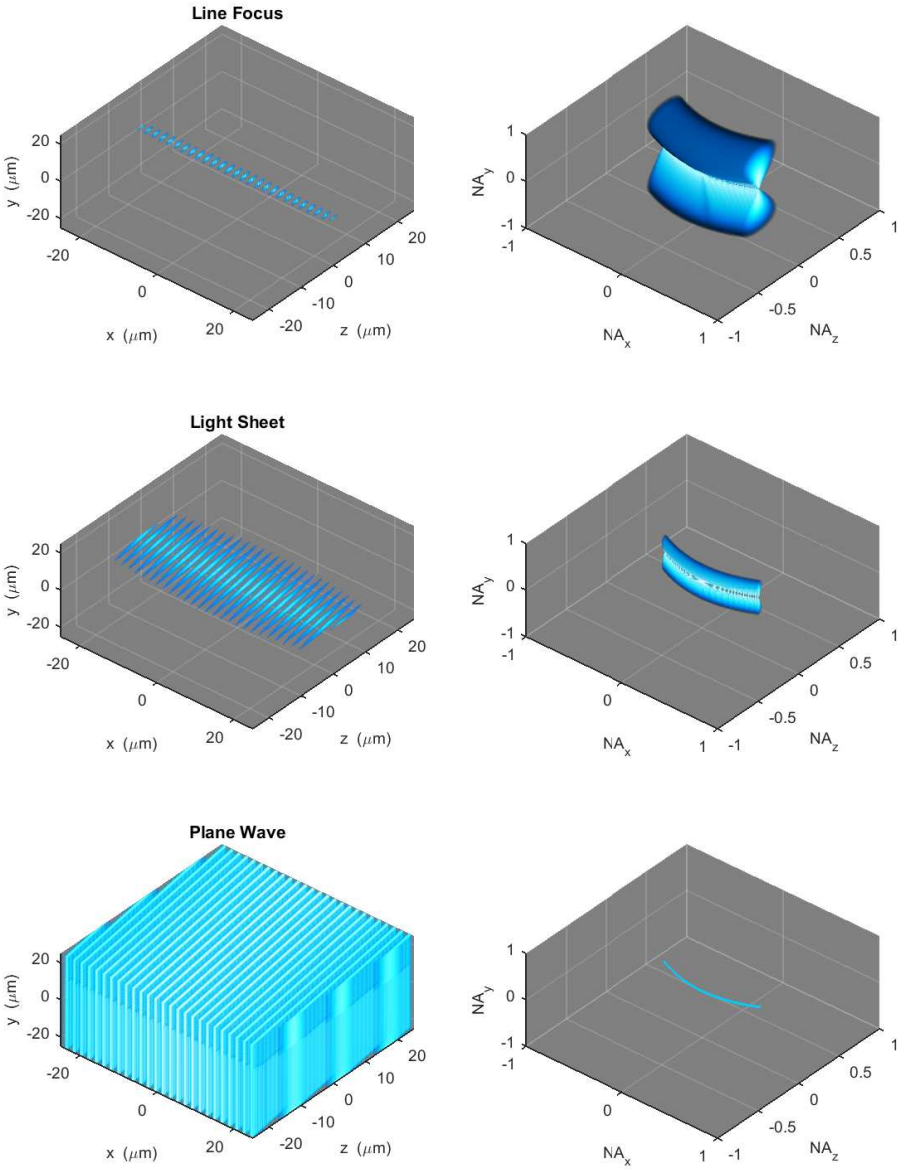

Figure 4.4: Illumination conditions and corresponding OTFs for 3 focal geometries in the CHIRPT imaging configuration. Top row: a tight line focus. Middle row: a soft line focus (light sheet). Bottom row: afocal plane wave illumination. Illumination intensities in the left column are at one snapshot in time; OTFs in right column are synthesized from the full range of scan times. We observe the convolution of focal support $\hat{P}(f_y, f_z)$ with the plane wave OTF $\hat{V}(f_x, f_z)$, and the decreasing size of $\hat{P}$ as the focus is softened.

function, where the location of the delta function moves along a line in (f_x, f_z) defined by the set of interfering tilted plane waves in the range of the beam pair E_j and E_k .

In Figure 4.3, we demonstrate how the line focus at two snapshots in time, modulated by cosine patterns along x, contributes to the OTF that is synthesized over the scan time t. At each snapshot in time, an hourglass-shaped spectral profile $\hat{P}(f_y, f_z)$ with vanishing width in f_x is generated by the line focus and probes the object's frequency content. As time progresses, these slices in (f_y, f_z) are translated along an arc is the (f_x, f_z) plane. When the temporal scan is finished, 3D spatial frequency information has been collected about the specimen. This 3D information can be Fourier transformed to display a system point spread function.

The spatial bandwidth associated with the vertical focusing plays a key role in determining the 3D OTF. The (y, z) profile of the focusing envelope leads to a certain size and shape of the profile distribution in (f_y, f_z). This is pictorially depicted in Fig. (4.4) for the $j \in [0, 1]$ pair of diffracted orders, where we show three focusing geometries: a tight line focus, a soft line focus (light sheet), and afocal plane wave illumination. The corresponding OTFs with focusing exhibit the characteristic hour-glass shape in the (f_y, f_z) plane, convolved along the plane wave arc in the (f_x, f_z) plane. Under plane wave illumination, the focal support vanishes.

4.4.3 An Analytic Expression for the 3D OTF

In Section 4.4.2 we derived the microscope 3D OTF for any two interfering beams that are generated by diffraction from the spinning modulator. We took a 'top-down' approach, where we started with the form of the measured signal, and applied approximations based on our knowledge of the interfering fields to derive the OTF. We found that the OTF for beam pair E_j and E_k is directly derived from the spectral intensity $\hat{I}_{j,k}(\mathbf{r}, t)$, and that the spectral intensity can be expressed as a convolution between a spatial profile component and a plane wave interference component. Object information in y and z is found by scanning the sample; object information in x is found through the sequence of cosine projections. The result was that the 3D OTF can be computed numerically for any vertical spectral profile $\hat{p}_y(f_y)$ on the interfering

fields. Unfortunately, computing a numerical convolution can be quite slow, especially in 3D dimensions.

In this section, we produce an analytic function for $\hat{I}_{j,k}$ (and thus the OTF) without a convolution operation. This expression for the OTF is fundamentally built up from pair-wise products of diffracted fields. This result works for field vertical beam profiles p_y that have an analytic Fourier transform - that is, $\hat{p}_y(f_y)$ has a functional form. We derive a function in f_y and f_z that can be fed into $\hat{p}_y$ as an argument. This allows for the rapid computation and plotting of the OTF for various beam-pair interactions. We use the pupil approximation in Section 3.3.3, and a center-difference coordinate transform for the vertical beam profiles which is common to wide-field OTF calculations [40]. Since the total SPIFI illumination intensity is formed by summing over products of field pairs (Eqn. (3.93)), this is a general approach that can be scaled for the number of diffracted orders present in the sample focal volume.

The complex intensity due to two interfering beams in the focal volume is:

$$I_{j,k}(\boldsymbol{r};t) \quad = \quad E_j^* E_k = \left(\int_{f'_\perp} \hat{E}_j\left(f'_\perp, z\right) \mathrm{e}^{\mathrm{i}2\pi f'_\perp \dot{\rho}} \right)^* \left(\int_{f''_\perp} \hat{E}_k\left(f''_\perp, z\right) \mathrm{e}^{\mathrm{i}2\pi f''_\perp \dot{\rho}} \right), \tag{4.61}$$

where each mixed-space 3D field inside the integral is:

$$\hat{E}_j\left(f_\perp, z\right) \quad = \quad \hat{E}_j\left(f_\perp\right) CTF_j\left(f_\perp\right) \mathcal{H}\left(f_\perp, z\right) \tag{4.62}$$

where the CTF applies the 4-f filtering constraint to the spectral field in the focal plane, and is unique for each diffracted order. The field is then propagated in the $\pm z$ direction in order to fill out the sample volume with the coherent Fresnel propagator, $\mathcal{H}$, given by Eqn. (2.55). The CTF is the product

$$CTF_j = CTF_{x_j}\left(f_{g_x}(t)\right) CTF_{y_j}\left(f_y, t\right) \tag{4.63}$$

where the CTFs in each Cartesian direction are defined in Equations (3.70) and (3.71).

Now, rather than just numerically propagate the apodized field $\hat{E}_j CTF_j$ with the Fresnel propagator $\mathcal{H}$ to fill out the focal volume, we show a way to quickly obtain an analytic expression for $\hat{I}(\boldsymbol{f_r})$, and thus the OTF, when the vertical field profile $\hat{p}(f_y)$ in the pupil has an analytic form. The focal plane field $E_{j,s} = p_x(x_s)p_y(y_s,t)v_j(x_s,y_s t)$, with $v_j(x_s,y_s t)$ given by Eqn. (3.51). (We neglect Π_{x_j} in (3.51) because the pupil is handled by the CTFs in this treatment). The focal plane field has the transverse Fourier transform:

$$\hat{E}_{j,s}(f_x,f_y) = \frac{a_j}{M}\mathrm{e}^{\mathrm{i}2\pi j f_{g_x} x_o}\hat{p}_x\left(f_x + \frac{j f_{g_x}}{M}\right)\hat{p}_y\left(f_y + \frac{j f_{g_y}}{M}\right) \tag{4.64}$$

In Eqn. (4.64), we can make our usual assumptions that the pupil profiles are very thin in x, $\hat{p}_x \approx \delta_x$, and also that the small constant offset in y can be ignored, $f_{g_y} \approx 0$. We then use the fields in Equations (4.62) and (4.64) to compute the complex intensity for the beam pair given by Equation (4.61). We note CTF_x does not depend on f_x, but rather on $f_{g_x}(t)$, and moves outside the integrals. Moreover, it is completely equivalent to the pupil function Π_{x_j}, and so we now opt to use the latter for familiarity. The integrations over f_x' and f_x'' are trivial, and we define a plane-wave field in (x,z) to group the following terms:

$$v_j(x,z;t) = \frac{a_j \Pi_{x_j}(t)}{M}\mathrm{e}^{\mathrm{i}2\pi j\left[f_{g_x}x_o - \frac{f_{g_x}}{M}x\right]}\mathrm{e}^{-\mathrm{i}\pi\lambda\left(\frac{j f_{g_x}}{M}\right)^2 z} \tag{4.65}$$

which is the same as Eqn. (4.5), where we have let $f_{g_y} = 0$. The plane wave intensity is:

$$V_{j,k}(x,z;t) = v_j^* v_k = \frac{a_j a_k \Pi_{x_{j,k}}\left(\Delta f_x(t)\right)}{M^2}\mathrm{e}^{\mathrm{i}2\pi(k-j)f_{g_x}\left[x_o - \frac{x}{M}\right]}\mathrm{e}^{-\mathrm{i}\pi\lambda(k^2-j^2)\left(\frac{f_{g_x}}{M}\right)^2 z} \tag{4.66}$$

The remaining components of the illumination intensity consist of the (y,z) focal profile as dictated by the beam shape and aperture. The complex intensity for the beam pair is

$$I_{j,k} \quad = \quad V_{j,k}\int_{f_y'}\int_{f_y''}\hat{p}_j^*(f_y')\hat{p}_k(f_y'')CTF_{y_j}^*(f_y')CTF_{y_k}(f_y'')\mathrm{e}^{\mathrm{i}2\pi\left(f_y'' - f_y''\right)y}\mathrm{e}^{-\mathrm{i}\pi\lambda\left(f_y''^2 - f_y'^2\right)z} \tag{4.67}$$

We now utilize a center-difference coordinate transform in the vertical coordinate, which is a technique used to calculate the OTF for a wide-field, incoherent-illumination microscope [40], since it enables a simple calculation in the paraxial regime. We define center and difference spatial frequency variables:

$$f_{ce} = \frac{f_y' + f_y''}{2}, \qquad f_{di} = f_y'' - f_y' \tag{4.68}$$

The differentials have a one-to-one mapping $\mathrm{d}f_y'\mathrm{d}f_y'' = \mathrm{d}f_{ce}\mathrm{d}f_{di}$. For ease of notation, we also group the pupil function and the vertical field profile into one distribution:

$$\hat{\mathrm{p}}(f_y) = \hat{p}(f_y)\, CTF_y(f_y) \tag{4.69}$$

The expression for the complex intensity becomes:

$$I_{j,k} = V_{j,k} \int_{f_{ce}} \int_{f_{di}} \hat{\mathrm{p}}_j^* \left(f_{ce} - \frac{f_{di}}{2} \right) \hat{\mathrm{p}}_k \left(f_{ce} + \frac{f_{di}}{2} \right) \mathrm{e}^{\mathrm{i}2\pi f_{di} y} \mathrm{e}^{-\mathrm{i}2\pi\lambda f_{ce} f_{di} z} \tag{4.70}$$

In order to ultimately form the OTF, we will need to calculate the spatial Fourier transform of I:

$$\hat{I}_{j,k}(\boldsymbol{f_r}; t) = \int_{\boldsymbol{r}} I_{j,k}(\boldsymbol{r}; t) \mathrm{e}^{-\mathrm{i}2\pi \boldsymbol{f_r} \cdot \boldsymbol{r}} \mathrm{d}^3 \boldsymbol{r} \tag{4.71}$$

The integrals over x and y act on linear phase terms to produce delta functions. Subsequent integration over f_{di} reduces the complex spectral intensity to:

$$\hat{I}_{j,k}(\boldsymbol{f_r}; t) = \int_z \hat{V}_{j,k}(f_x, z) \int_{f_c} \hat{\mathrm{p}}_j^* \left(f_{ce} - \frac{f_y}{2} \right) \hat{\mathrm{p}}_k \left(f_{ce} + \frac{f_y}{2} \right) \mathrm{e}^{-\mathrm{i}2\pi (f_z + \lambda f_{ce} f_y) z} \tag{4.72}$$

Integration over z produces another delta function of the form:

$$\int_z \mathrm{e}^{-\mathrm{i}\pi\lambda (k^2 - j^2) \left(\frac{f_{gx}}{M} \right)^2 z} \mathrm{e}^{-\mathrm{i}2\pi (f_z + \lambda f_{ce} f_y) z} \mathrm{d}z = \frac{1}{\lambda |f_y|} \delta \left[f_{ce} + \frac{1}{\lambda f_y} \left(f_z + \frac{\lambda f_{g_x}^2}{2} \frac{k^2 - j^2}{M^2} \right) \right], \tag{4.73}$$

which allows for a final integration over f_{ce}. The resultant spectral intensity is:

$$\hat{I}_{j,k}(\boldsymbol{f_r};t) = \frac{a_j a_k \Pi_{x_{j,k}}\left(\Delta f_x(t)\right)}{M^2} \mathrm{e}^{\mathrm{i}2\pi(k-j)f_{g_x}x_o}\delta\left(f_x + \frac{k-j}{M}f_{g_x}\right) \\ \times \frac{1}{\lambda|f_y|}\hat{p}_j^*\left[\frac{-f_y}{2} - \frac{1}{\lambda f_y}\left(f_z + \frac{\lambda f_{g_x}^2}{2}\frac{k^2-j^2}{M^2}\right)\right]\hat{p}_k\left[\frac{f_y}{2} - \frac{1}{\lambda f_y}\left(f_z + \frac{\lambda f_{g_x}^2}{2}\frac{k^2-j^2}{M^2}\right)\right] \quad (4.74)$$

where the temporal dependence in f_{g_x} is understood. We can simplify this large expression by writing the argument for $\hat{p}$ as a convolution in f_z with a delta function:

$$\hat{I}_{j,k}(\boldsymbol{f_r};t) = \frac{a_j a_k \Pi_{x_j}\Pi_{x_k}}{M^2} \mathrm{e}^{\mathrm{i}2\pi(k-j)f_{g_x}x_o}\delta\left(f_x + \frac{k-j}{M}f_{g_x}\right)\delta\left(f_z + \frac{\lambda f_{g_x}^2}{2}\frac{k^2-j^2}{M^2}\right) \\ \underset{f_z}{*} \quad \left(\frac{1}{\lambda|f_y|}\hat{p}_j^*\left[\frac{-f_y}{2} - \frac{f_z}{\lambda f_y}\right]\hat{p}_k\left[\frac{f_y}{2} - \frac{f_z}{\lambda f_y}\right]\right) \quad (4.75)$$

The result is a familiar expression for the spectral intensity - a convolution along the f_z coordinate between a plane wave interference term, and a vertical focusing profile.

$$\hat{I}_{j,k}(\boldsymbol{f_r};t) \quad = \quad \hat{V}_{j,k}(f_x,f_z) \underset{f_z}{*} \hat{P}_{j,k}(f_y,f_z) \quad (4.76)$$

where the plane-wave spectral intensity is:

$$\hat{V}_{j,k}(f_x,f_z) = \frac{a_j a_k \Pi_{x_{j,k}}\left(\Delta f_x(t)\right)}{M^2} \mathrm{e}^{\mathrm{i}2\pi(k-j)f_{g_x}x_o}\delta\left(f_x + \frac{k-j}{M}f_{g_x}\right)\delta\left(f_z + \frac{\lambda f_{g_x}^2}{2}\frac{k^2-j^2}{M^2}\right) \quad (4.77)$$

and the spectral intensity profile is:

$$\hat{P}_{j,k}(f_y,f_z) = \frac{1}{\lambda|f_y|}\left[\hat{\mathrm{p}}_j^*\left(-\frac{\mathrm{f_y}}{2} - \frac{\mathrm{f_z}}{\lambda \mathrm{f_y}}\right)\hat{\mathrm{p}}_k\left(\frac{\mathrm{f_y}}{2} - \frac{\mathrm{f_z}}{\lambda \mathrm{f_y}}\right)\right] \quad (4.78)$$

Thus, as long as one has an analytic expression for the 1D vertical field profiles $\hat{p}_y(f_y)$ in the pupil, the complete spectral intensity for any pair of diffracted order interaction products can be computed analytically using Eqns. (4.76) – (4.78). The analytic solution has a $1/|f_y|$ factor that causes the OTF to diverge along $f_y = 0$, which can present numerical issues. For Figures 4.5

and 4.6, we replaced values along $f_y = 0$ with an average of the adjacent pixels. Total computation time for the six OTFs in Figure 4.6 was 3 seconds on a modern laptop computer, whereas the 3D rendering took approximately 1.5 minutes. OTF grid sizes were 101 x 514 x 514.

4.4.4 Demonstration for CHIRPT beam pair with Gaussian profiles

To demonstrate the application of our analytic OTF expression, let us consider the CHIRPT beam pair with diffracted orders $j = [0, 1]$. For a complex intensity at the first image sideband, we have $E_{j,k} = E_j^* E_k$ where $j = 0$ and $k = 1$. The plane wave intensity component (Eqn. (4.77) is:

$$\hat{V}_{0,1}(f_x, f_z) = \frac{a_0 a_1 \Pi_{x_1}\left(\Delta f_x(t)\right)}{M^2} \mathrm{e}^{\mathrm{i}2\pi f_{g_x} x_o} \delta\left(f_x + \frac{f_{g_x}}{M}\right) \delta\left(f_z + \frac{\lambda f_{g_x}^2}{2M^2}\right) \tag{4.79}$$

where the lateral spatial frequency difference scales as $\Delta f_x(t) = 1 \cdot f_{g_x}(t) - 0 \cdot f_{g_x}(t) = \kappa t$. The temporal window is $\Pi_{x_{0,1}} = \Pi_{x_0} \Pi_{x_1} = \Pi_{x_1}$ because the zero-order beam is always on. The range of projected spatial frequencies is $[-f_c : f_c]$ as given by Eqns. (4.43) and (4.44). The projection information has the linear phase shift $f_{g_x} x_o$ which corresponds to a location at the first harmonic sideband after Fourier transform of a real signal.

For a Gaussian beam vertical field profile $p_y(y) = \exp\left[y^2 / w_y^2\right]$, and no clipping in the system pupil such that $\hat{\mathrm{p}}(f_y) = \hat{p}(f_y)$ by Eqn. (4.69), the analytic transform is $\hat{p}_y(f_y) = \sqrt{\pi} w_y \exp\left[\pi^2 w_y^2 f_y^2\right]$. The intensity profile for the beam pair interaction (Eqn. (4.78)) is:

$$\hat{P}_{0,1}(f_y, f_z) = \frac{1}{\lambda |f_y|} \left[\hat{\mathrm{p}}_0^*\left(-\frac{\mathrm{f_y}}{2} - \frac{\mathrm{f_z}}{\lambda \mathrm{f_y}}\right) \hat{\mathrm{p}}_1\left(\frac{\mathrm{f_y}}{2} - \frac{\mathrm{f_z}}{\lambda \mathrm{f_y}}\right)\right] \tag{4.80}$$

$$= \frac{\pi w_y^2}{\lambda |f_y|} \mathrm{e}^{-\pi^2 w_y^2 \left[\frac{f_y^2}{2} + \frac{2}{\lambda} \frac{f_z^2}{f_y^2}\right]} \tag{4.81}$$

The OTF for this beam pair is

$$OTF_{0,1}(\mathbf{f_r}) = -\hat{I}_{0,1}(\mathbf{f_r}) = -\hat{V}_{0,1}(f_x, f_z) \underset{f_z}{*} \hat{P}_{0,1}(f_y, f_z) \tag{4.82}$$

$$= -\frac{a_0 a_1 \Pi_{x_1}}{M^2} \frac{\pi w_y^2}{\lambda |f_y|} e^{i2\pi f_{g_x} x_o} \delta\left(f_x + \frac{f_{g_x}}{M}\right) \left[\delta\left(f_z + \frac{\lambda f_{g_x}^2}{2M^2}\right) \underset{f_z}{*} e^{-\pi^2 w_y^2 \left[\frac{f_y^2}{2} + \frac{2}{\lambda}\frac{f_z^2}{f_y^2}\right]}\right] \tag{4.83}$$

The convolution of the profile function with a delta function simply results in a shift of the profile function to the location of the delta function:

$$OTF_{0,1}(\mathbf{f_r}) = -\frac{a_0 a_1 \Pi_{x_1}}{M^2} \frac{\pi w_y^2}{\lambda |f_y|} e^{i2\pi f_{g_x} x_o} \delta\left(f_x + \frac{f_{g_x}}{M}\right) \exp\left[-\pi^2 w_y^2 \left(\frac{f_y^2}{2} + \frac{2}{\lambda} \frac{\left(f_z + \frac{\lambda f_{g_x}^2}{2M^2}\right)^2}{f_y^2}\right)\right] \tag{4.84}$$

To compute this OTF, one simply creates a temporal vector that parameterizes the set of spatial frequencies imparted by the grating, $f_{g_x}(t)$. The vertical-axial spectral profile $\hat{P}_{0,1}(f_y, f_z)$ is computed for each shift in f_z imparted by $f_{g_x}(t)$. These slices are assembled into a 3D space $(f_x(t), f_y, f_z)$ for direct visualization of the OTF. A normalized version of Equation (4.84) has been used to generate Figures 4.2, 4.3 and 4.4.

4.4.5 Demonstration for 2nd-order SPIFI beam pair with Gaussian profiles

In 2^{nd} order SPIFI, we have the beam pair $j = [-1, 1]$. To extract the complex signal at the positive second harmonic sideband, we let $j = -1$ and $k = 1$. The plane wave intensity component (Eqn. (4.77) is:

$$\hat{V}_{-1,1}(f_x, f_z) = \frac{a_1^2 \Pi_{x_1}^2 \left(\Delta f_x(t)\right)}{M^2} e^{i2\pi 2 f_{g_x} x_o} \delta\left(f_x + \frac{2}{M} f_{g_x}\right) \delta\left(f_z\right) \tag{4.85}$$

where the axial dependence on f_{g_x} has disappeared since $k^2 - j^2 = 0$. The lateral spatial frequency difference scales as $\Delta f_x(t) = 1 \cdot f_{g_x}(t) - (-1) \cdot f_{g_x}(t) = 2\kappa t$. The temporal window is $\Pi_{x_{-1,1}} = \Pi_{x_{-1}} \Pi_{x_1} = \Pi_{x_1}$ as they are the same. The range of projected lateral spatial frequencies is $[-2f_c : 2f_c]$ as given by Eqns. (4.43) and (4.44). The projection information has the linear phase shift $2 f_{g_x} x_o$ which corresponds to a location at the second harmonic sideband after Fourier

transform of a real signal. Again, we assume Gaussian field profiles without clipping by the aperture. The OTF is

$$OTF_{-1,1}(\mathbf{f_r}) = -\hat{I}_{-1,1}(\mathbf{f_r}) = -\hat{V}_{-1,1}(f_x, f_z) \underset{f_z}{*} \hat{P}_{-1,1}(f_y, f_z) \tag{4.86}$$

$$= -\frac{a_1^2 \Pi_{x_1}^2}{M^2} \frac{\pi w_y^2}{\lambda |f_y|} e^{i2\pi f_{g_x} x_o} \delta\left(f_x + \frac{2f_{g_x}}{M}\right) \left[\delta\left(f_z\right) \underset{f_z}{*} e^{-\pi^2 w_y^2 \left[\frac{f_y^2}{2} + \frac{2}{\lambda}\frac{f_z^2}{f_y^2}\right]}\right] \tag{4.87}$$

$$= -\frac{a_1^2 \Pi_{x_1}^2}{M^2} \frac{\pi w_y^2}{\lambda |f_y|} e^{i2\pi f_{g_x} x_o} \delta\left(f_x + \frac{2f_{g_x}}{M}\right) e^{-\pi^2 w_y^2 \left[\frac{f_y^2}{2} + \frac{2}{\lambda}\frac{(f_z)^2}{f_y^2}\right]} \tag{4.88}$$

The second-order SPIFI OTF given by Eqn. (4.88) is plotted in the top-right panel of Figure 4.6. The hourglass-shaped vertical-axial spectral intensity profile is simply translated along the f_x for each projected spatial frequency $\delta(f_x + 2f_{g_x}(t)/M)$, without any translation in the axial direction.

4.4.6 Verification with Gaussian beam forward model

Gaussian beams have quadratic phase terms and analytic Fourier transforms, and therefore they can be used in a physical forward model to compute the 3D focal field. This can serve as a verification of our results in the previous sections which relied heavily on imaging theory. We will make similar approximations based on physical reasoning in this forward model as we did in our derivation of beam-pair OTFs. For simplicity we will compute the OTF for the CHIRPT beam pair $j = [0, -1]$.

We use Eqn. (3.49) to describe the imaging of each diffracted beam, E_j, to the microscope focal plane, where p_x and p_y are now defined as standard Gaussian envelopes:

$$p_x(x)\, p_y(y) = e^{-\frac{x^2}{w_x^2}} e^{-\frac{y^2}{w_y^2}} \tag{4.89}$$

where the widths have a large aspect ratio $w_x \gg w_y$ to describe the line focus geometry, and we use $w = w_s = w_m/M$ for the widths in the focal plane. Furthermore, we neglect the static

vertical grating tilt, $f_{g_y} \rightarrow 0$, and we use f_{g_x}/M for the demagnified grating spatial frequency in the sample plane.

To describe axial propagation away from the focal plane, we Fourier transform the field to lateral spatial frequency space, multiply by the Fresnel propagator using Eqn. (2.55), and inverse Fourier transform back to real space. Our assumption of Gaussian field profiles allows these transforms to be computed analytically. For the moment, we will ignore the prefactors $a_j \Pi_{x_j}/M \exp\left[\mathrm{i}2\pi j f_{g_x} x_o\right]$. The j^{th} field propagating away from the focal plane is:

$$E_j(\boldsymbol{r};(t)) = \frac{1}{\sqrt{A_y}} \exp\left(\frac{-y^2}{w_y^2}\frac{1}{A_y}\right)\exp\left(\mathrm{i}kz\right) \\ \times \frac{1}{\sqrt{A_x}} \exp\left(\frac{-x^2}{w_x^2}\frac{1}{A_x}\right)\exp\left(\frac{-\mathrm{i}2\pi j(f_{g_x}(t)/M)x}{A_x}\right)\exp\left(-\pi^2 w_x^2 j^2 (f_{g_x}/M)^2\left(1-\frac{1}{A_x}\right)\right) \tag{4.90}$$

where $A_{x,y} = 1 + \mathrm{i}\frac{\lambda z}{\pi w_{x,y}^2} = 1 + \mathrm{i}\frac{z}{z_{Rx,y}}$ is the complex Gaussian beam parameter, and z_{Rx} and z_{Ry} are the Rayleigh distances in the x and y dimensions. We see that the x-z dependence of the field contains a standard Gaussian field, and some additional terms due to the lateral, time-dependent phase tilt $f_{g_x}(t)$:

$$E_{\text{gauss}}(x,z) = \frac{1}{\sqrt{A_x}} \exp\left(-\frac{x^2}{w_x^2}\frac{1}{A_x}\right) \tag{4.91}$$

$$E_{\text{tilt}}(x,z;t) = \exp\left(-\pi^2 w_x^2 j^2 (f_{g_x}/M)\right)^2\left(1-\frac{1}{A_x}\right)\exp\left(\frac{-\mathrm{i}2\pi j(f_{g_x}(t)/M)x}{A_x}\right) \tag{4.92}$$

We next utilize the fact that the fields are at least roughly collimated in the x-dimension over some axial region of interest, which we can express mathematically $\frac{z^2}{z_{Rx}^2} << 1$. In order to exploit this in our analysis, we first expand A_x according to the relationships:

$$\frac{1}{\sqrt{A_x}} = \frac{1}{\left(1+\frac{z^2}{z_{Rx}^2}\right)^{1/4}} \mathrm{e}^{\frac{\mathrm{i}}{2}\tan^{-1}\left(\frac{z}{z_{Rx}}\right)}, \qquad \frac{1}{A_x} = \frac{1}{1+\frac{z^2}{z_{Rx}^2}} - \mathrm{i}\frac{z}{\left(1+\frac{z^2}{z_{Rx}^2}\right)z_{Rx}} \tag{4.93}$$

Substituting these expressions into (4.91) & (4.92), and then making the approximation $\frac{z^2}{z_{Rx}^2} << 1$, we are left with the simplified expressions:

$$E_{\text{gauss}}(x,z) \approx \mathrm{e}^{\frac{\mathrm{i}}{2}\tan^{-1}\left(\frac{z}{z_{Rx}}\right)} \exp\left(-\frac{x^2}{w_x^2}\right) \exp\left(\mathrm{i}\frac{x^2 z}{w_x^2 z_{Rx}}\right) \tag{4.94}$$

$$E_{\text{tilt}}(x,z;t) \approx \exp\left[-\left(\pi w_x j \frac{f_{g_x}}{M}\frac{z}{z_{Rx}}\right)^2\right] \exp\left(\frac{-2\pi j \frac{f_{g_x}}{M} xz}{z_{Rx}}\right) \exp\left(-\mathrm{i}\pi\lambda\left(j\frac{f_{g_x}}{M}\right)^2 z\right) \exp\left(-\mathrm{i}2\pi j \frac{f_{g_x}}{M} x\right) \tag{4.95}$$

Furthermore, the Guoy phase and quadratic focusing phase in (4.94) are negligible in typical setups, where the axial extent of the light sheet, dictated by the y-focusing, limits the range of z to much less than z_{Rx}. (We can take the y confocal parameter, $2\,z_{Ry}$, as a measure of the axial extent of the light sheet). The three remaining real-valued exponentials can be collected into a single quantity, which describes rotation of the profile in the (x,z) plane. Putting the expression back together for the j^{th} diffracted field, Eqn. (4.90) is now expressed as:

$$\begin{aligned} E_j(\boldsymbol{r};t) = &\frac{1}{\sqrt{A_y}} \exp\left(\frac{-y^2}{w_y^2}\frac{1}{A_y}\right) \exp\left(\mathrm{i}kz\right) \\ &\times \exp\left(-\mathrm{i}2\pi j \frac{f_{g_x}}{M} x\right) \exp\left(-\mathrm{i}\pi\lambda\left(\frac{j f_{g_x}}{M}\right)^2 z\right) \exp\left(\frac{-\left(x + j\lambda\frac{f_{g_x}}{M} z\right)^2}{w_x^2}\right) \end{aligned} \tag{4.96}$$

where we can see the connection to our general derivation by assigning the following components to plane wave and profile terms, respectively:

$$v_j(x,z;t) = \exp\left(-\mathrm{i}2\pi j \frac{f_{g_x}}{M} x\right) \exp\left(\mathrm{i}kz\right) \exp\left(-\mathrm{i}\pi\lambda\left(\frac{j f_{g_x}}{M}\right)^2 z\right) \tag{4.97}$$

$$p_j(\boldsymbol{r};t) = \frac{1}{\sqrt{A_y}} \exp\left(\frac{-y^2}{w_y^2}\frac{1}{A_y}\right) \exp\left(\frac{-\left(x + j\lambda\frac{f_{g_x}}{M} z\right)^2}{w_x^2}\right) \tag{4.98}$$

We recognize (4.97) as the 2D lateral-axial plane-wave field, and (4.98) defines a localized volume profile. The plane wave component contains a linear phase sweep through x, and a cor-

responding quadratic phase sweep through z. The profile component contains a standard focused Gaussian beam in y, which dictates the height and axial extent of the light sheet, along with a collimated Gaussian profile in x that shears across the x-z plane in the direction dictated by the phase tilt, $f_{g_x}(t)$, imparted by the mask. However, in our general OTF derivation, we also made the approximation that the field envelopes are practically plane waves in x ($w_x \to \infty$), with small scan angles such that p_0 and p_1 are roughly the same for all scan angles ($x - j\lambda(f_{g_x}/M)z \approx x$). Applying these approximations here, the field profile becomes a function of the vertical focusing only.

At this point, it is helpful to reintroduce the neglected prefactors for a complete solution.

$$v_j(x,z;t) = \frac{a_j \Pi_{x_j}}{M} \mathrm{e}^{\mathrm{i}2\pi j f_{g_x}\left(x_o - \frac{x}{M}\right)} \mathrm{e}^{\mathrm{i}kz} \mathrm{e}^{-\mathrm{i}\pi\lambda\left(\frac{j f_{g_x}}{M}\right)^2 z} \tag{4.99}$$

$$p_j(y,z) = \frac{1}{\sqrt{A_y}} \exp\left(\frac{-y^2}{w_y^2}\frac{1}{A_y}\right) \tag{4.100}$$

The CHIRPT complex intensity readily available at the first sideband is:

$$I_{1+} = E_0^* E_1 = \left(v_0 p_0\right)^* v_1 p_1 = V_{1+} P_{1+} \tag{4.101}$$

where the plane wave and profile intensities are:

$$V_{1+}(x,z;t) = \frac{a_0 a_1 \Pi_{x_1}}{M^2} \mathrm{e}^{\mathrm{i}2\pi f_{g_x}\left(x_o - \frac{x}{M}\right)} \mathrm{e}^{-\mathrm{i}\pi\lambda\left(\frac{f_{g_x}}{M}\right)^2 z} \tag{4.102}$$

$$P_{1+}(y,z) = \frac{1}{\sqrt{1+\frac{z}{z_{Ry}}}} \mathrm{e}^{\frac{-2y^2}{w_y^2}\frac{1}{1+\frac{z}{z_{Ry}}}} \tag{4.103}$$

In the plane wave intensity V_{1+}, we can drop the phase offset $\exp\left(\mathrm{i}2\pi f_{g_x} x_o\right)$ after isolating the complex sideband. Fourier transforming V_{1+} and P_{1+} to the spatial frequency domain:

$$\hat{V}_{1+}(f_x, f_z; t) = \frac{a_0 a_1 \Pi_{x_1}}{M^2} \delta\left(f_x + \frac{f_{g_x}(t)}{M}\right) \delta\left(f_z + \frac{\lambda}{2}\frac{f_{g_x}^2(t)}{M^2}\right) \tag{4.104}$$

$$\hat{P}_{1+}(f_y, f_z) = \frac{\pi w_y^2}{\lambda |f_y|} \exp\left[-\pi^2 w_y^2 \left(\frac{f_y^2}{2} + \frac{2}{\lambda^2}\frac{f_z^2}{f_y^2}\right)\right] \tag{4.105}$$

The OTF is the convolution in f_z of (4.104) and (4.105):

$$OTF_{1+} = -\hat{V}_{1+} * \hat{P}_{1+} = -\frac{a_0 a_1 \Pi_{x_1}}{M^2} \frac{\pi w_y^2}{\lambda |f_y|} \delta\left(f_x + \frac{f_{g_x}(t)}{M}\right) \exp\left[-\pi^2 w_y^2 \left(\frac{f_y^2}{2} + \frac{2}{\lambda^2}\frac{\left(f_z + \frac{\lambda f_{g_x}^2}{2M^2}\right)^2}{f_y^2}\right)\right] \tag{4.106}$$

Using the fact that Gaussian beams provide analytic Fourier transforms, we have independently verified the validity of Eqn. (4.84) with (4.106).

4.5 Dynamic Apodization at the Pupil plane

Nearly all realistic microscope scenarios use the full bandwidth of the objective lens for maximum resolution. A careful model must handle the pupil apodization present in this case. In Ch. 3, we employed a rigorous focusing model for high NA focusing with vector fields, by mapping the field components onto the aplanatic focal sphere in the pupil. However, in keeping with the spirit of this chapter, we seek a scalar solution for low to moderate NA focusing, providing intuition in a rapid fashion through simplified computations. We will do so using a simple approximation for the diffracted fields in the system Fourier plane.

4.5.1 Dynamic Vertical-Axial Frequency Support

The general model for the intensity profile support, $\hat{P}(f_{y_s}, f_{z_s})$ used in our derivation of the OTF, can encompass both a component due to the input beam profiles, and a component due to the unique coherent transfer function (CTF) that varies with time for each diffracted order j:

$$\hat{P}(f_y, f_z; t) = \left(\hat{p}_0(f_y, f_z) CTF_0(f_y, f_z)\right)^* \left(\hat{p}_1(f_y, f_z) CTF_1(f_y, f_z; t)\right) \tag{4.107}$$

The CTF is directly related to the pupil geometry in the Fourier plane [40]. In SPIFI, the pupil affects the "hourglass" shape of each $\hat{P}(f_y, f_z)$ slice, seen in Figure 4.3, such that the set of slices are no longer the same for every scan time t. This directly corresponds to the geometry of vertical "line-cursor" foci being multiplied by the circular pupil, and losing spatial frequency bandwidth in f_y as scan time increases, as seen in Figure 3.5(b).

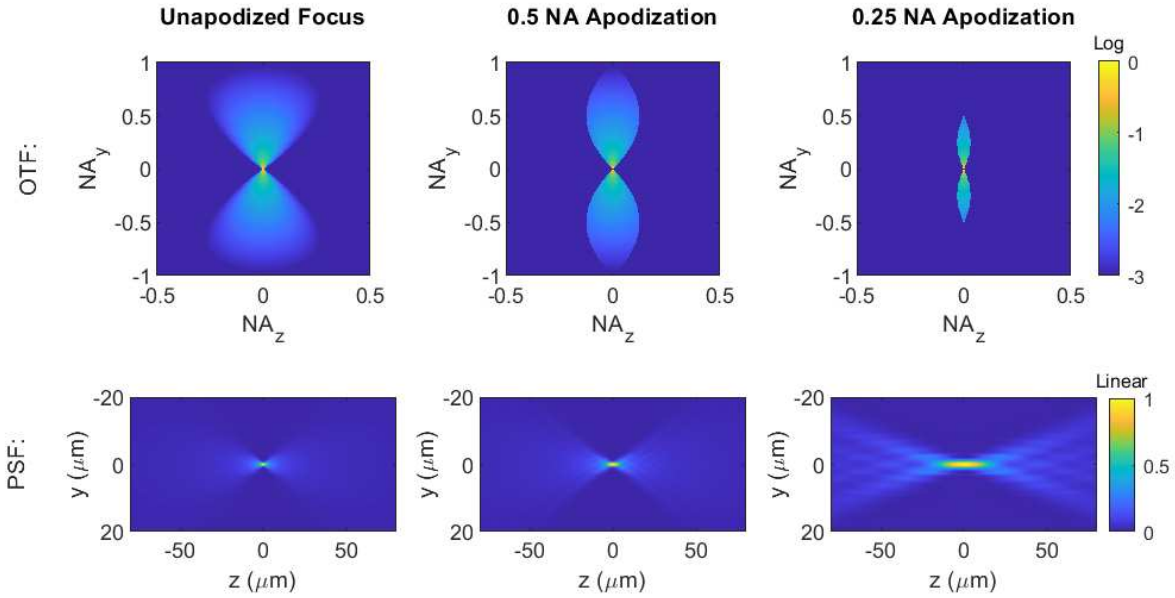

Figure 4.5: Variable Apodization in Vertical Focusing with beam scan position in the back aperture. Field $p(y,z)$ is a Gaussian with fill factor = 1 when positioned at the center of the pupil of a 0.5 NA objective lens, $\lambda = 1\mu m$. Left: An infinitely large pupil; Center: at pupil center, NA = 0.5; Right: Halfway between pupil center and edge, NA = 0.25. Top Row: Optical Transfer Functions, plotted on log scale. Bottom Row: Focal Intensity, $I(y,z)$, on a linear scale. All PSFs and OTFs have been normalized for visualization, therefore the energy loss due to apodization is not represented.

The OTFs under pupil apodization are plotted in Figures 4.5 and 4.6. We readily see that the presence of the pupil serves to truncate the f_y, f_z intensity distribution to a finite range, as expected. Whereas without apodization, the OTF contains the same vertical support at all horizontal scan angles, with apodization we see the vertical support dissipating when the scan beams approach the edge of the pupil.

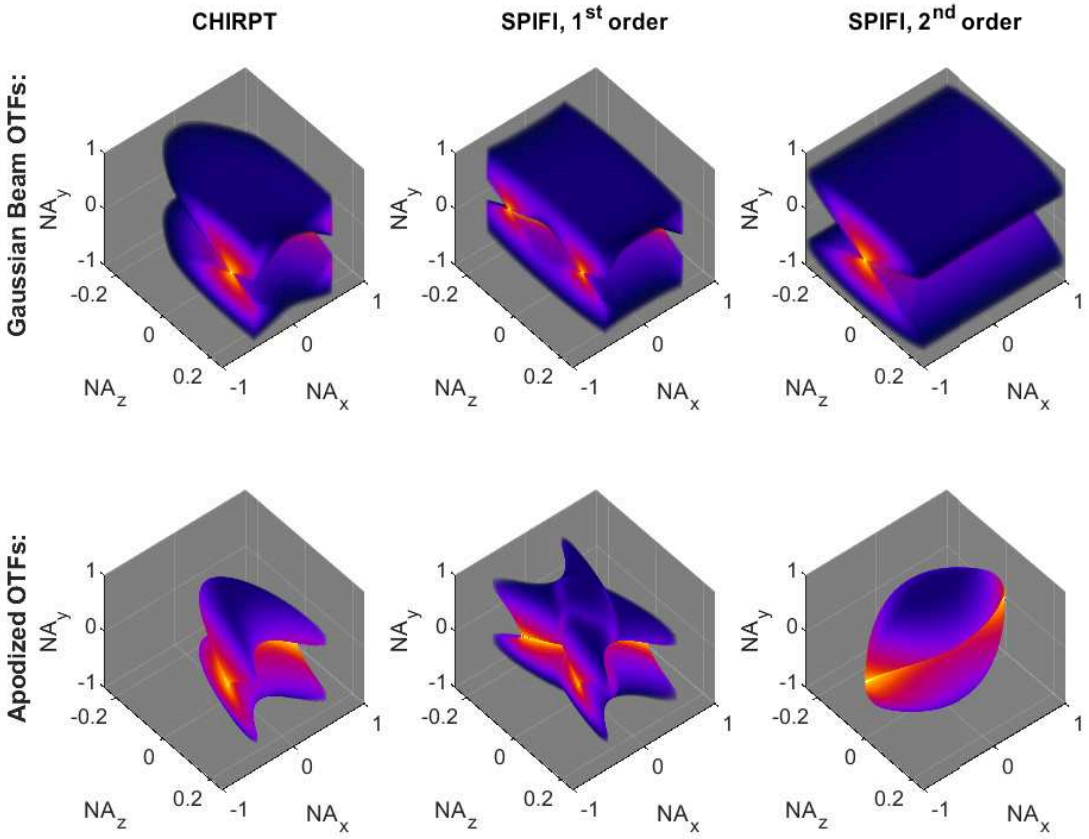

Figure 4.6: 3D OTFs for CHIRPT and SPIFI. Simulation using Gaussian beam with fill factor of 1 in the y direction when positioned at the pupil center of 0.5 NA objective lens; $\lambda = 1\mu m$. OTFs are normalized and plotted on a log scale with range [-3,0]. Note that for 2^{nd}-order SPIFI, the f_x range is doubled compared to CHIRPT and 1^{st}-order SPIFI; however, the support in the y direction is completely extinguished at the end of this range.

4.5.2 Dynamic Focal Volumes

The 'roll-off' in vertical frequency support with scan time is due to the diffracted orders being progressively clipped by the aperture. The geometry of vertical "line-cursor" foci being multiplied by the circular pupil, as seen in Figure 3.5(b), results in less spatial frequency bandwidth in f_y as scan time increases. The result is changing dimensions of the light sheet in the focal volume. As scan beams travel away from the center of the pupil, their focal properties in (y,z) move from a line focus, to a light sheet, to a plane wave before being completely extinguished. Nevertheless, for CHIRPT and first-order SPIFI, this is not of great concern, because

the intensity profile is gated by the undiffracted $j = 0$ field, which is stationary and focusing at full vertical NA. The net effect is that the intensity profile maintains fairly consistent dimensions over the scan range, but the magnitude drops off with scan angle.

However, second-order SPIFI images are formed by the two scanning $j = \pm 1$ beams alone. Thus, the illumination intensity is not gated by the zero-order beam, and therefore the illumination volume varies significantly over the range of the scan, meaning that signal light from nearby emitters in y and z can be coupled into the bucket detection for high x spatial frequency projection times. This doesn't seem to be a huge problem in experimental data, however, perhaps because at time zero the DC sample information is probed finely in y, localizing it in space. There are also workarounds - for one, a confocal detection can be implemented with a slit, effectively gating the collected light to the line focus region for all scan times. Secondly, a more flexible imaging model than the FFT can be used to incorporate this information appropriately. In the future, knowledge of these time-varying focal volumes can be utilized in the image reconstruction process in a tomographic approach.

4.6 Conclusion

In this chapter we presented a model for the spatiotemporal illumination intensity formed in a CHIRPT or SPIFI microscope, across three spatial dimensions and varying with time. Using a scalar, paraxial approach, we found analytic expressions that enable rapid computation of the complex illumination intensity in SPIFI that leads to image formation. We did this by isolating the vertical and horizontal field components of the mask-diffracted electric field. In the sample plane, the horizontal field is a linear sequence of spatial frequency projections, whereas the vertical field is a simultaneous projection of spatial frequencies passed by the system. We also examined the effect of an illumination envelope that varies in size due to the changing apodization imposed by the microscope pupil with scan time. This model enables a more complete picture to emerge of the field-sample interaction, and how image information is recorded and used to reconstruct an image. This approach can serve as a guide when moving to higher NA imaging scenarios, and can be used for model-based imaging approaches where measured

traces are fit to a model. The fields and intensities here can easily be input into a multiphoton model to then compute nonlinear field-sample interactions.

Author Contributions

K.A.W., J.J.F., and R.A.B. developed the 4D scalar mathematical model for CHIRPT illumination, which led to the work published in Ref. [64]. Figure 4.1 and portions of text in Section 4.2 are reprinted with permission from Ref. [64]. J.J.F., D.G.W., and R.A.B. developed the plane wave model (Ref. [58]) reviewed in Section 4.3. K.A.W. developed the analytic 4D spatiotemporal illumination model for any beam pair, generalized to include dynamic apodization, and the resulting imaging system OTF described in Sections 4.4 and 4.5.

CHAPTER 5

PULSED FEMTOSECOND FIBER SOURCES FOR HIGH-FLUENCE MULTIPHOTON LINE IMAGING

In a typical multiphoton laser-scanning microscope (MP-LSM), single nanojoule pulses are typically more than sufficient to drive two- and three-photon nonlinear processes at moderate to high NA. However, extending the point-focus illumination volume into a line geometry decreases the fluence accordingly, and thereby the local peak power available to drive nonlinearities. In addition, the axial confinement degrades as well. In MP-SPIFI, laser power is further reduced at the mask; a binary transmission mask like those used in this work transmit only 50% of the incident light. The illumination intensity at the sample consists of a spatially modulated light sheet that contains harmonic spatial frequencies corresponding to different image orders - the great bulk of the illumination intensity drives the 0th (DC) and 1st order light sheets. The 4th order light sheet, yielding the highest resolution image, is generated from a tiny fraction of the available illumination intensity. Experimentally, we found that we needed to drive our laser amplifier at its maximum output in order to see the 4th order image rise above the noise floor [51]. This source, replicated after that reported in [67], generated approximately 1.3W of average power, corresponding to 25nJ pulses with 150fs duration (167kW of peak power).

In order to boost the signal-to-noise in our imaging process, we therefore explored two routes to generate higher peak power laser pulses. The first technique is a conversion of our initial PM fiber amplifier into one that supports parabolic pulse amplification. The second technique performs chirped pulse spectral broadening from a commercial high energy source.

5.1 Parabolic Pulse Amplification in MOPA configuration

A review of recent work in femtosecond Yb:fiber lasers showed a striking parallel between our in-house master-oscillator-power-amplifier (MOPA) Yb:fiber sources, and those reported elsewhere that employed a form of parabolic pulse amplification regime [68, 69]. In both cases,

the seed pulse launched into the amplifier is spectrally filtered to a few nanometers, and undergoes spectral broadening while amplifying in the fiber. Our motivation for this architecture was based on a study in our group [70] that showed that all-normal-dispersion (ANDi) fiber lasers, also known as Dissipative Soliton lasers [71, 72], have the lowest relative-intensity-noise (RIN) in the center of their optical spectrum. Supercontinuum generated from the spectral center was much more stable than that generated from the entire spectrum. Consequently, our group built very stable fiber amplifiers while seeding with a few-nm spectrally-filtered pulse. The idea behind these amplifiers is that a narrow-band seed pulse injected into the fiber amplifier remains narrow enough during most of its amplification to prevent the accumulation of nonlinear phase. Towards the end of the fiber, the pulse has increased in energy enough to start driving spectral broadening via self-phase modulation (SPM), with the caveat that the combination of nonlinear phase accumulation via SPM is still small enough to easily compress the pulse with a standard grating compressor. For these amplifiers to work well, the amount of passive fiber on either side of the gain fiber is kept very short, especially on the output side (<10cm). Empirically, pulses from these sources can reproduce the oscillator bandwidth (roughly 25nm FHWM), while still remaining compressible to near the transform limit with a grating compressor.

Parabolic pulse amplification, also known as similariton amplification, corresponds to a situation where a laser pulse with a parabolic temporal profile undergoes amplification in the presence of positive group velocity dispersion (GVD), and maintains it's same parabolic shape as the pulse profile increases both in amplitude and in duration [73–75]. The latter increase corresponds to the generation of new colors at the edges of the pulse. The remarkable feature of these pulses is the very linear chirp of the colors comprising the pulse - a noteworthy result considering the amount of higher-order dispersion that fiber-based amplifiers typically impart on a pulse. Moreover, others have shown that the similariton regime is a nonlinear attractor, and therefore if you can tip your pulses in that direction, the amplification should be stable [76]. While the theoretical solutions for parabolic pulse are driven by the interplay of gain and GVD, in practice, real fiber amplifiers also impart higher-order dispersion, stimulated Raman scatter-

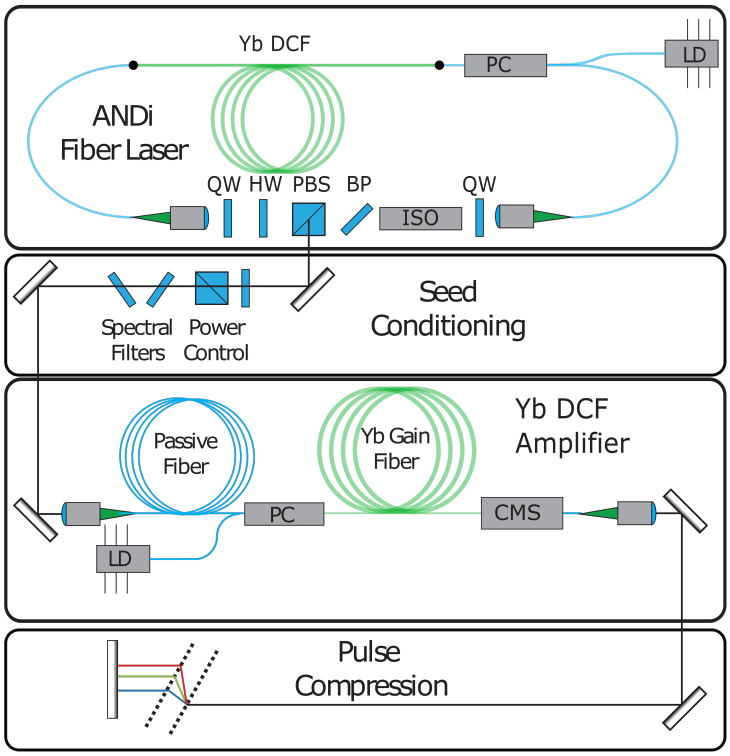

Figure 5.1: Schematic of Yb:fiber nonlinear amplifier. DCF: double-clad fiber; QW: quarter-wave plate; HW: half-wave plate, PBS: polarizing beam splitter; BP: birefringent plate.

ing, and the dopant ions have a finite gain bandwidth that will limit the process. Nevertheless, researchers have recently produced fantastic results, including the folding of this amplification process inside a laser oscillator [68], generating compressible pulses extending across the entire Yb gain bandwidth, corresponding to 40fs pulse durations. An interesting feature in the co-propagating pump configuration is that the center of the gain bandwidth shifts to the long-wavelength side of the spectrum as the seed amplifies and the pump attenuates along the fiber length, due to the decreasing ratio of Yb^{3+} ions in the excited vs. ground state.

A straight-forward rework of our in-house MOPAs yielded much more intense pulses through parabolic pulse amplification. Adding approximately 2.5m of passive 10/125PM fiber before the gain segment allowed for the seed pulse to evolve into a parabolic temporal shape. The seed pulses, derived from an ANDi oscillator running at 65 MHz with 25nm bandwidth, were spectrally filtered to a 4nm FWHM quasi-Gaussian shape using two Semrock Maxline spectral

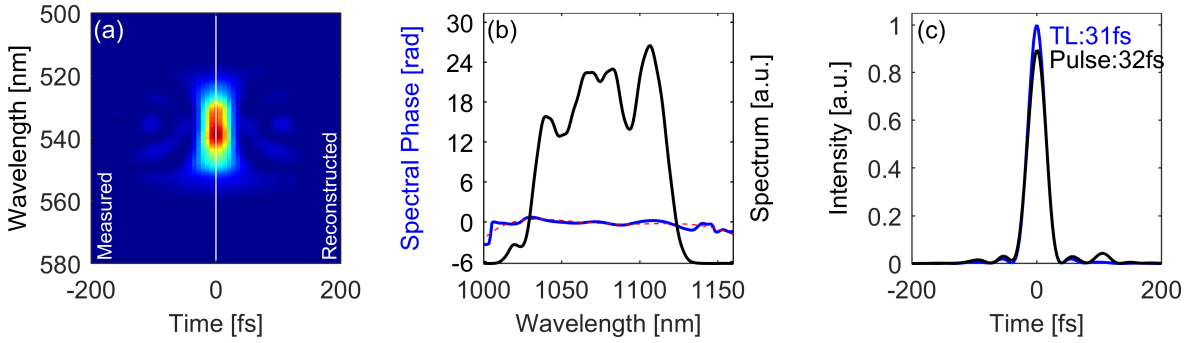

Figure 5.2: SHG-FROG pulse measurement for parabolic pulse amplifier with evolving gain bandwidth.

filters. Power control with a half waveplate (HWP) and polarizing beam splitting cube (PBS) was also used to tune the seed's peak power to ensure that it evolved into a parabolic shape at the start of the gain segment. The gain fiber is nearly single-mode 10/125 double clad polarization-maintaining fiber produced by Leikki, and available through Thorlabs (Yb1200-10/125DC-PM). Compression was done with a Treacy grating compressor using a pair of high efficiency holographic gratings (Lightsmyth, T-1000-1040) and a retroreflecting prism (Thorlabs, PS915H-B). Pulse characterization using a home-built SHG-FROG with an all-reflective geometry revealed very clean pulses with 30 - 40 fs durations, as seen in Fig. 5.2. This amplification process accommodated further power scaling, before being limited by damage to fiber components and decrease in pulse quality. Overall, this source generated 4.4W after the compressor (77nJ pulse energies), yielding peak powers on the order of 2 MW - more than 10x greater than we had achieved previously.

A numerical model was constructed using the split-step implementation of the Generalized Nonlinear Schrödinger Equation (GNLSE) equation, which is discussed more fully in Sec. 5.2.3, along with a model for the Yb:fiber gain medium as a two-level system [77]. Dispersion and absorption and emission cross-sections as a function of wavelength were obtained from the manufacturer. Numerical results are displayed in Fig. 5.3, demonstrating relatively good agreement with experimental pulses measured by SHG-FROG in Fig. 5.2.

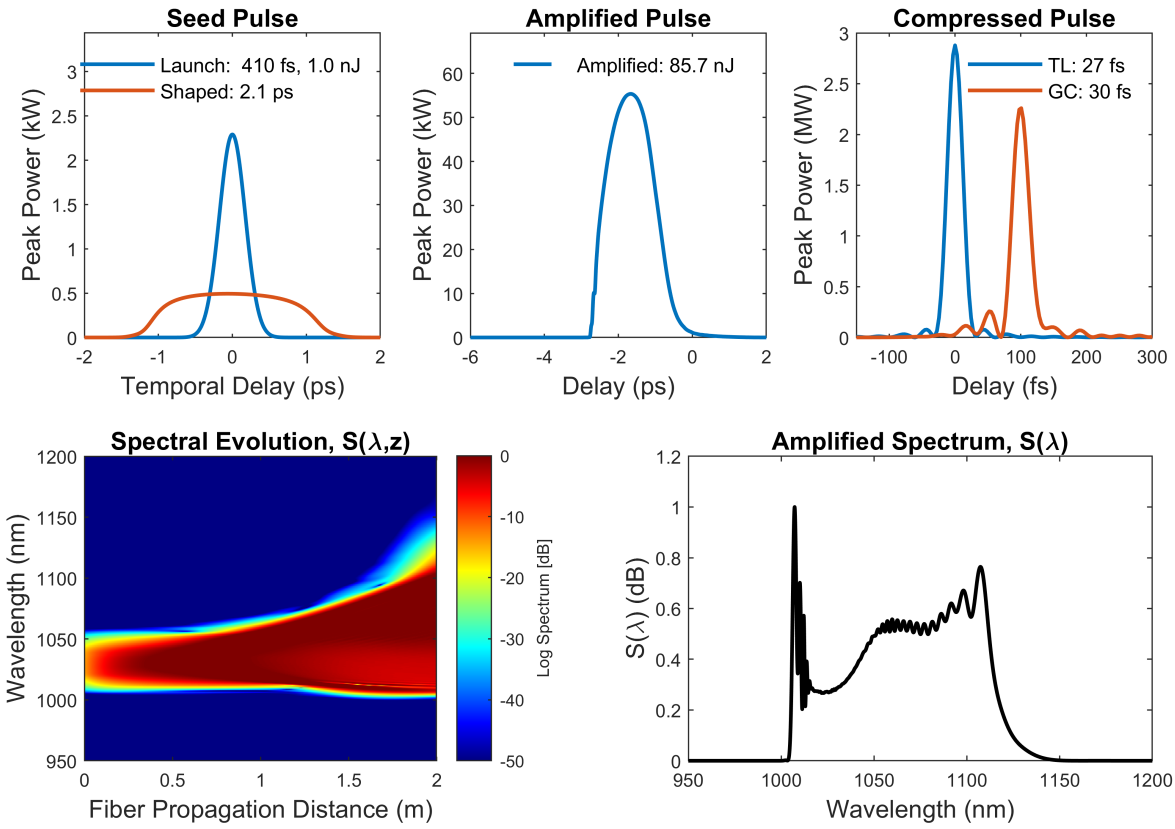

Figure 5.3: Modeling Results for the parabolic pulse amplifier with evolving gain bandwidth. Pump laser was assumed to be 9W at 976nm, with the seed pulses at 67 MHz repetition rate. The seed was shaped by passage through 3m of passive fiber, before amplification in a 2m gain fiber. A Treacy grating compressor (GC) was simulated and the grating separation numerically optimized for comparison with the transform-limited pulsed duration.

5.1.1 Broadband NIR Ultrafast Pulses converted into the Visible

Many applications in microscopy require visible light to excite single-photon transitions, most often to probe specific fluorophores. Broadband visible light sources can be used in conjunction with chromatic excitation filters to stimulate multiple fluorophores, or to monitor a sample's absorption spectrum. However, broadband coherent sources can also be used to excite multiphoton transitions in the case where an absorption peak is centered in the ultraviolet. For all of these reasons, we sought to convert our high intensity NIR pulses into broadband visible light.

One immediate result of our efforts was a novel microscope that reconstructs the $\chi^{(2)}$ nonlinear susceptibility of microscopic samples [78]. Our broadband, pulsed NIR laser output was split into two arms; one arm traveled to the sample plane to generate second-harmonic generation at the sample, while the other was frequency-doubled in a thin SHG crystal. The SHG from the sample was then combined with the SHG from the external crystal onto a camera, where the coherent spatial interference was exploited in an off-axis holography configuration. A reconstruction algorithm developed by our partners at the University of Illinois converted the measured SHG holographic images into a map of the χ^2 nonlinear susceptibility. The algorithm also succeeded in improving the axial sectioning of the reconstructed object.

Two key enabling features of the microscope apparatus were the broadband optical spectrum, and a broad spectrum of transverse spatial frequencies due to a high-NA laser focus. Combined, this allowed for a large range of phase-matching conditions in the sample. We note that the sample was purposely positioned at a defocused location relative to the laser focus. This unusual approach was useful for generating wide-field illumination with a large diversity of illumination directions (high NA).

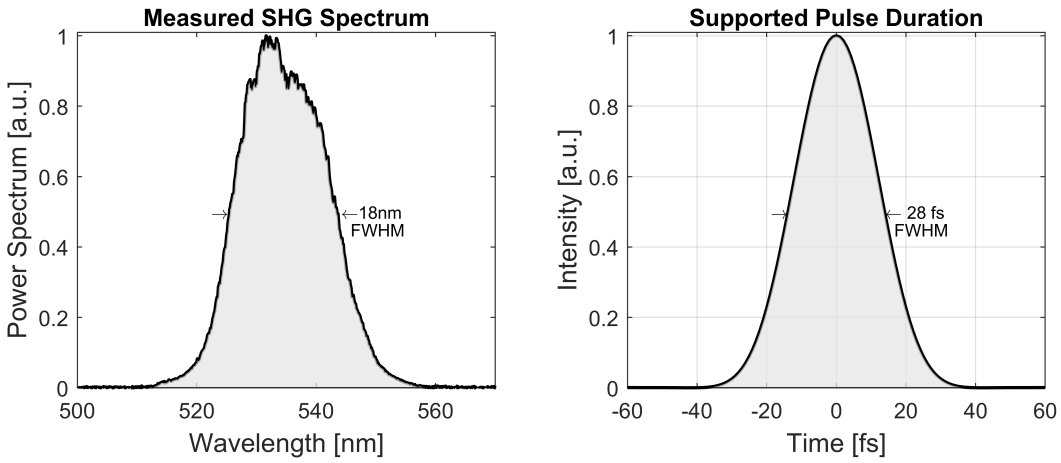

Figure 5.4: Demonstration of SHG generation with 200um BBO crystal

5.2 Chirped Pulse Spectral Broadening

5.2.1 Introduction

Laser pulse compression below 20 femtoseconds requires a power spectrum exceeding 22 THz in bandwidth. With the exception of Ti:Sapphire Kerr-lens modelocked (KLM) lasers, no laser gain medium has the gain bandwidth necessary to generate such pulses directly from an oscillator. Therefore, a common strategy is to exploit nonlinear optical processes that generate additional bandwidth, followed by a compression scheme to ensure the shortest pulse available from the bandwidth.

Utilizing this strategy, femtosecond pulses of initially moderate durations (>100 fs) can be compressed to sub-20fs durations by driving self-phase modulation (SPM) in a controlled fashion. Spectral broadening with low energy (0.1-10 nJ) ultrafast pulses is easily attained with engineered microstructured fibers that possess anomalous dispersion over a broad spectral range. Unfortunately, scaling this supercontinuum process to higher pulse energies is infeasible because of fiber damage, pulse-breakup into higher-order solitons, and spectral decoherence when high soliton number pulses are launched [79]. In contrast, nonlinear fiber propagation under normal dispersion can handle greater pulse energies, with the added benefit of maintaining a high degree of temporal coherence in the broadened spectrum, especially in the cases of short fiber lengths and sub-picosecond seed pulses [80].

Normal dispersion spectral broadening is not limited to extended confinement in optical fiber, however. In recent years, laser pulses above the 1 μJ threshold have been used to demonstrate spectral broadening in precisely built multi-pass Herriott cells [81, 82], and in sequences of glass plates displaced from a focus [83–85]. These approaches must account for spatial Kerr lensing in tandem with spectral broadening. Recent efforts to reach the μJ level with fiber have made use of gas-filled negative-curvature hollow-core fibers [86], which allow for mode field diameters of many 10's of μm, with very low accumulated dispersion due to the low index of gas. However, as with many photonic crystal fibers, the end faces are extremely sensitive to damage

under slight misalignment, and as others have reported, the output spectrum can be relatively unstable [85].

In this work we report on a robust pulse compression strategy for pulse energies in the 100nJ regime. In this range, pulses of few hundred femtosecond durations (typical of gain media like Yb and Er), have too low an intensity to drive appreciable SPM in Kagome fiber or in bulk material, yet much too high an intensity to generate controlled, SPM-dominated spectra in a single mode fiber of practical length. Therefore, we explore a strategy of stretching and shaping the launch pulse, such that we limit the nonlinear phase accumulation to the SPM regime while still using a practical fiber length - in our case, about 7cm. We demonstrate clean pulse compression to sub-20fs using both negatively or positively chirped launch pulses. This approach deviates from standard practice, where typically a compressed pulse is launched in order to generate maximum bandwidth. Our system is intended to be simple, tunable, and low cost, and therefore we use simple optics to shape the launch pulse and a standard off-the-shelf fiber. Moreover, while others [87, 88] have demonstrated the compressibility of spectra generated by SPM and extended by wavebreaking, those efforts require an expensive programmable pulse shaper to account for the large spectral phase accumulation present in the WB portion of the spectrum. Therefore, with a mind toward a simple, robust system, we constrain ourselves to the SPM-dominated regime, which can be compressed with a simple dispersion compensation tool - in our case, a standard prism compressor.

One drawback of an extended medium like glass fiber is the large higher-order dispersion picked up by the pulse once the spectral broadening has significantly reduced the dispersion length. Maintaining very small amounts of higher order spectral dispersion is crucial for clean temporal compression after the fiber, and therefore, ideally one would use the shortest possible fiber. However, it is extremely challenging to work with fiber lengths less than a few centimeters. Therefore, in order to keep the system practical and easy to use, we take as a prerequisite fiber lengths of approximately 7 cm, such that the front end of the fiber can be connecterized, polished, and fitted to a collimator, in order to ensure stable mounting and high efficiency cou-

pling, and the exit fiber tip can be rigidly held. However, at these fiber lengths, a transform-limited 100 nJ pulse of even a moderate duration (100-300 fs) will rapidly break down. Instead of scaling the energy back in order to maintain compressible SPM, the key feature of our approach is to impart controllable chirp on the launch pulse, reducing the peak power while carrying high energy through the fiber.

Chirped pulse broadening has been studied in the anomalous dispersion regime [89, 90]. Another group [91] discusses chirped-pulse broadening with an Yb source using a ZDW PCF fiber shifted to 1064nm.Generally, these studies have focused on the generation of supercontinuum spectra. However, the compressibility of optical pulses undergoing chirped-pulse spectral broadening has not been rigorously studied.

5.2.2 Experimental Setup & Results

Initial results of our compression scheme are shown in Fig. 5.5, where 84 nJ pulses are compressed to 13 fs. In this case, an SF10 prism was used in the output compression stage. The large dispersion of SF10 glass indicates that the total phase accumulation in the fiber is well-matched out to third-order for this particular nonlinear pulse evolution. The pulse was optimized with simple adjustments to the launch pulse temporal profile, followed by adjustments to the output compressor on the output pulse. This empirical optimization is a benefit of our approach, in that one does not need a transform-limited launch pulse, nor a carefully tailored fiber such as a zero-dispersion, dual-zero dispersion, or dispersion-shifted photonic crystal fiber. Instead, one simply needs a smooth spectral & temporal pulse profile, control over pulse chirp, and a standard normal-dispersion fiber.

Launch Pulse Conditioning

Our laser source, a KM Labs Y-fi HP, consists of an ANDi fiber laser [72] that is directly amplified in a single stage master oscillator power amplifier (MOPA) to 400nJ at the fundamental 59MHz repetition rate. An internal pulse picker allows for repetition rate reduction by 5x or

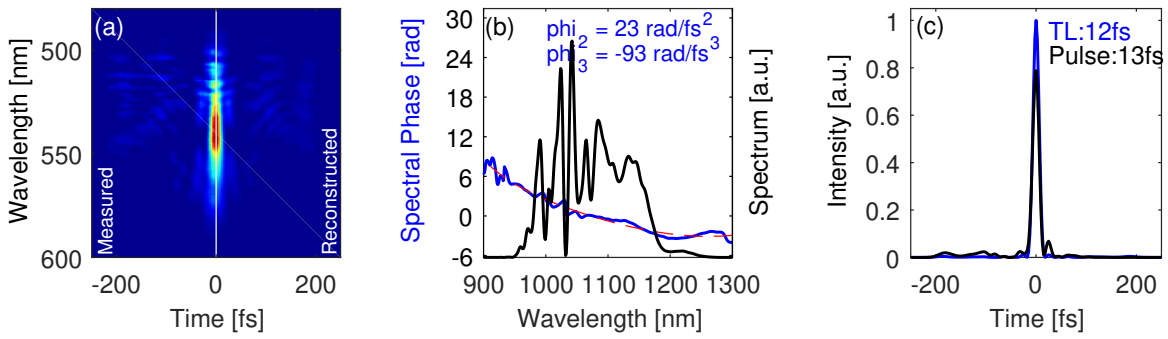

Figure 5.5: (a) Phantom SHG-FROG, with reconstruction overlaid on right half of measurement for visual comparison. (b) Reconstructed pulse power spectrum (black), with reconstructed phase (blue) and 4th order polynomial fit (dashed red). (c) Reconstructed temporal pulse intensity (black) and calculated transform-limited pulse (blue) based on the spectrum in (b), with FWHM durations. The reconstructed pulse amplitude is scaled relative to the TL pulse such that they contain the same energy.

more, with pulse energies in the few μJ range. Output pulse durations are 130fs. We operated the system at both 59 and 10 MHz repetition rates, with equally successful pulse compression.

To shape the launch pulse, we used a simple Lyot Filter, consisting of a birefringent quartz plate and polarizing beam splitter, in order to carve out a smooth, nearly Gaussian spectral shape. This removes the problematic spectral and temporal structure caused by the characteristic 'cat ears' of an ANDi laser, and therefore enables a smooth nonlinear evolution in the fiber. The data in Fig. 5.5 was acquired with a 3mm quartz plate that passed a Gaussian shaped spectrum of roughly 11nm full-width at half-maximum (FWHM). It has also been shown that ANDi lasers exhibit higher spectral noise just inside the cat ears [70]; therefore we intentionally narrowed the filter using a 5mm quartz plate so that those features lied in the nulls of the sinusoidal transmission spectrum of the Lyot filter. The Lyot filter was followed by a 1075 shortpass filter (Edmund optics) and a 1064 longpass filter (Semrock), angle-tuned to reject the residual cat-ears. The data in Fig. 5.7 was acquired with this setup, where the launch pulse spectrum was ~7.5nm FWHM, supporting a 210fs pulse.

To chirp the launch pulse, we employed either a Treacy grating compressor or a Martinez 4-f pulse shaper at various times. While the Martinez compressor was more difficult to align, it's spectral resolution allowed for further apodization by using an iris near the Fourier plane. We

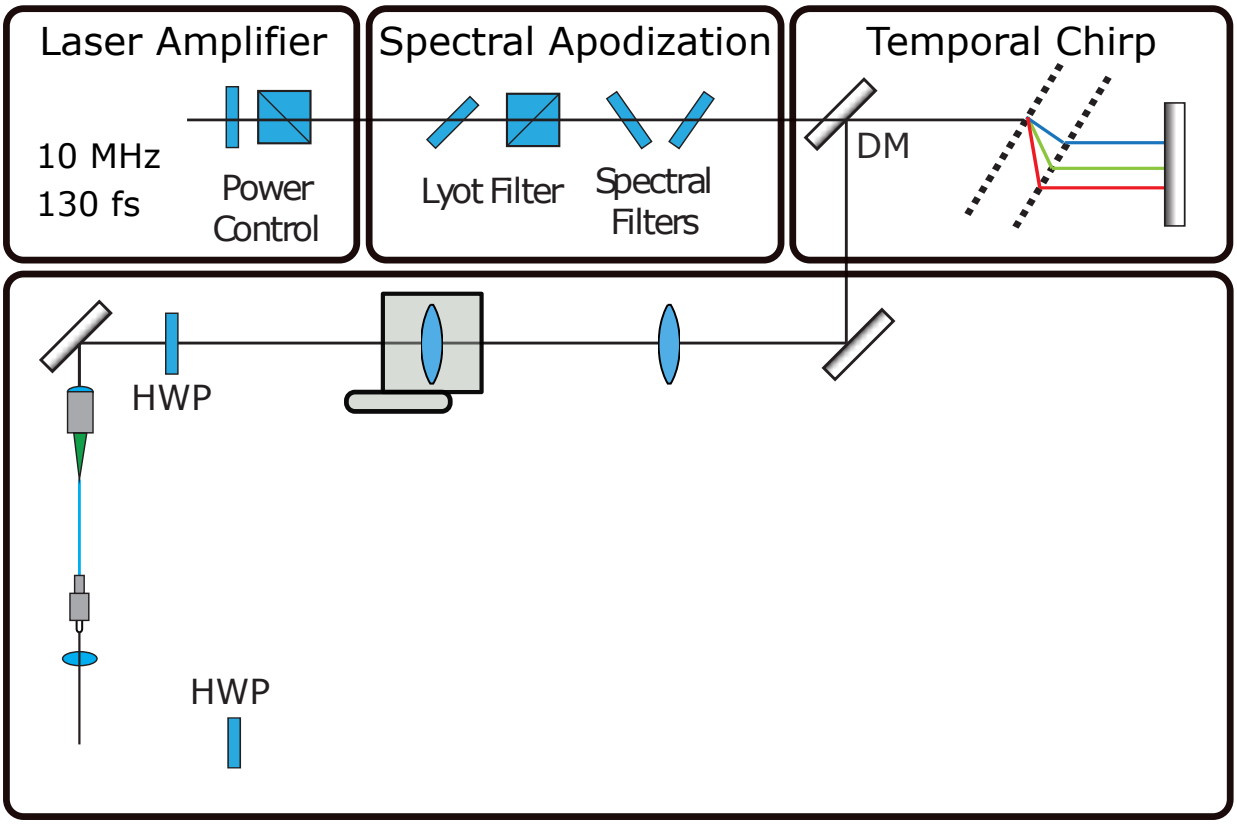

Figure 5.6: Schematic of pulse compression experiment. HWP: half-wave plate, GP: grating pair, RM: roof mirror, ACH: achromatic lens, DM: D mirror, CCM: corner-cube mirror.

note that if one opted to use an SLM device in the Fourier plane, one could tailor both the pulse amplitude and phase at once - albeit at a higher system cost.

Fiber

The broadening fiber is a nearly single mode, polarization-maintaining (PM) fiber (Nufern FUD-3460 or PM1060L), which presents normal dispersion to the pulse centered at 1044 nm. The simple, all-glass fiber allows for more robust power handling than a delicately structured PCF fiber or highly nonlinear fibers – both of which are subject to damage at relatively low average powers and pulse energies. Moreover, the 10.5μm mode field diameter (MFD), accommodates 3x higher pulse energies than standard PM980, while still allowing for easy coupling to the TEM00 mode, yielding excellent beam quality at the output.

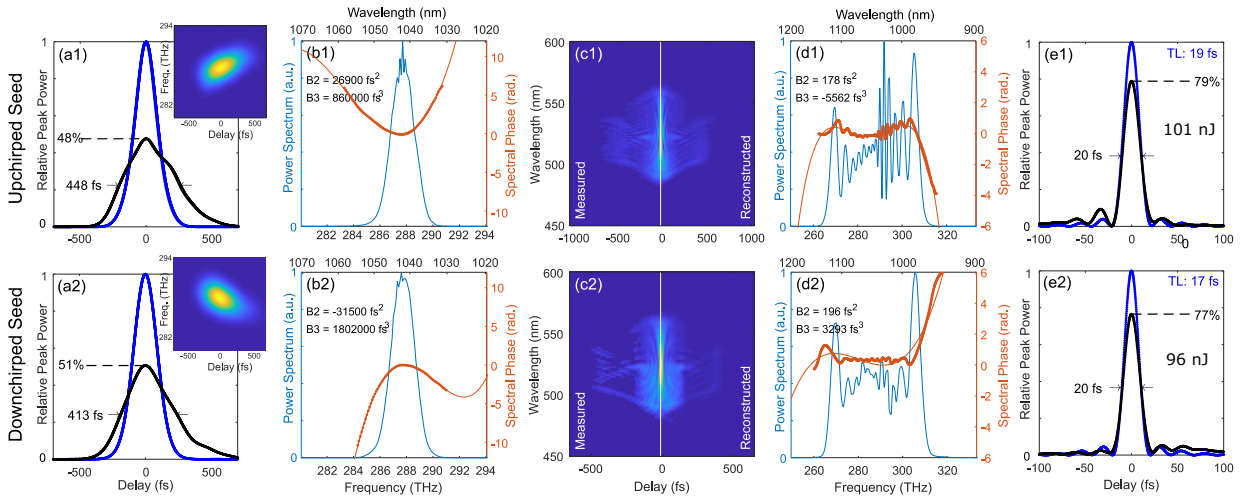

Figure 5.7: Experimental Results of High Peak Power Pulse Compression in PM10/125 fiber measured with SHG-FROG. Top row: positively chirped launch pulse with 153nJ coupled pulse energy. Bottom row: negatively chirped launch pulse with 146nJ coupled pulse energy. (a1,a2) Temporal launch pulse (I(t), black) against the transform-limited launch pulse (blue). Inset: spectrogram. (b1,b2) Launch pulse spectrum, $I(\omega)$, and spectral phase $\phi(\omega)$. (c1,c2) Phantom SHG-FROG trace of the compressed output pulses, with right-half of reconstruction overlaid on right-half of measurement for visual comparison. (d2,d2) Compressed pulse spectrum and phase. (e1,e2) Compressed (black) and transform-limited (blue) output pulses; compressed pulse scaled to contain same energy as TL pulse.

The PM design, using two Panda-style stress rods, imparts a large birefringence, which mitigates polarization modulation instability and nonlinear polarization rotation arising from the weak intrinsic birefringence in standard fibers during the all-normal dispersion broadening process [70, 92]. Coupling to the fiber's slow axis maintains stable polarization and therefore enables modeling in the scalar approximation.

The fiber length of ~ 7cm is chosen by balancing needs in our desire for clean, high quality pulse compression. On one hand, we want an easy-to-use fiber, which calls for a longer fiber. On the other hand, clean compression is predicated on accumulating as little higher order dispersion as possible, and thus shorter fibers are preferred. We note that short fiber lengths and sub-picosecond seed pulses have the added benefit of preserving a high degree of temporal coherence in the broadened spectrum [80]. 7cm presents an optimal tradeoff.

To further enhance power handling, we initially selected an input collimator manufactured by Oz Optics, which consists of an asphere focusing onto a thin glass window soldered to the

fiber input face. The beam waist at the air/glass interface is slightly larger than it would be without the window, reducing the peak-power at the interface and therefore allowing for higher peak-power coupling. The window can also be AR-coated, although it was not in our case. However, we also successfully used homemade epoxied connectors at reduced (10 MHz) repetition rate, with >175nJ incident on the fiber tip, coupled in with an asphere (F220APC-1064, Thorlabs). In either case, fiber coupling efficiency is routinely between 80-84%, such that 100nJ incident on the fiber yields >80nJ pulses at the output. Furthermore, we find that >90% of the output energy is maintained after passing the pulse through a linear polarizer. Due to the strong suppression of polarization rotation by the birefringent fiber, polarization loss can likely be attributed to imperfect coupling to the fiber's slow axis, perhaps made worse by high peak power and high average power in the glass window soldered to the fiber tip.

The distal end of the fiber was held in place using a fiber connector barrel without epoxy (B30126C3), which was clamped and mounted on a z-axis translation stage. We found that the 126μm barrel diameter provided sufficient positional rigidity to the 125μm fiber such that no beam pointing instabilities were noticed after a few meters of propagation. To prepare the fiber end facet, the barrel was translated past the fiber tip, the tip was cleaved with a diamond scribe, and the barrel was moved back until flush with the fiber end face (as evidenced by the disappearance of diffraction rings around the central spatial mode in the far field).

Compression

To compress this newly-generated bandwidth, we employ a single-prism compressor [93], where our strategy of minimizing higher order dispersion allows us to avoid expensive solutions like programmable pulse shapers or custom chirped mirrors, and use a simple, single compression stage. The single prism design keeps the system compact and simplifies alignment for large bandwidths. We note that the efficiency of this device suffers from the six reflections off of the gold-coated corner cube mirror, which limit the compressor efficiency to 73%.

Figure 5.7 demonstrates higher energy measured pulses before and after the fiber compression scheme. In these cases, ~190nJ were incident on the fiber, with ~150nJ throughput and

~100nJ compressed. Remarkably, the chirping scheme works for both positively chirped (top row) and negatively chirped (bottom row) launch pulses. (See the spectrogram insets in panels (a), and spectral phase in panels (b)). In both cases, the compressed pulse reaches the 20 fs threshold, with low pedestal content. For this data, we reduced the repetition rate from 59 MHz to ~10 MHz, in order to minimize thermal issues that scale with higher average power. We also switched to a fused silica prism in order to minimize the third order dispersion from the prism glass. These pulses were carefully characterized with second harmonic generation frequency-resolved optical gating (SHG-FROG) before and after the fiber in order to verify our results with a numerical model.

Combining fiber coupling (80%) and polarization (90%) losses with the compressor efficiency, the compressed pulse contains just over half of the energy in the launch pulse. Therefore a 2x loss in energy, combined with a 10x decrease in compressed pulse duration, yields a peak power improvement of 5x. In our proof-of-principle experiment, the spectral apodization stage also presents a significant energy loss. However, this can be mitigated by use of a near-Gaussian laser source spectrum.

5.2.3 Numerical fiber propagation of chirped pulses

To understand the pulse propagation dynamics, we built a model in Matlab following references [94–96], which uses the split-step propagation method to numerically solve the Generalized Nonlinear Schrödinger Equation (GNLSE) for the electric field temporal envelope $A(T)$ as it propagates down the fiber length:

$$\begin{aligned}\frac{\partial A}{\partial z} = &-\frac{\alpha}{2}A + \sum_{n\geq 2}\frac{\mathrm{i}^{n+1}}{n!}\beta_n\frac{\partial^n A}{\partial T^n} \\ &+\mathrm{i}\gamma\left(1+\frac{\mathrm{i}}{\omega_0}\frac{\partial}{\partial T}\right)A\int_{-\infty}^{\infty}R\left(T'\right)\left|A\left(z,T-T'\right)\right|^2\mathrm{d}T'\end{aligned} \tag{5.1}$$

where the first two terms on the right-hand side of the equation correspond to attenuation α (which we ignore for this short fiber length), and the fiber dispersion modeled as a Taylor expansion with coefficients β_n. For the PM1060L fiber, our model assumes $\beta_2 = 13\,\mathrm{fs}^2$ / mm, and

β_3 = 51 fs^3 / mm. The remaining terms accounts for various nonlinear effects, as they depend on the temporal pulse intensity, $|A(T)|^2$. Impulsive Raman scattering in the glass material is modeled with a convolution of the intensity profile $|A|^2$ with the Raman response $R(T)$. The resultant temporal intensity is multiplied with the fiber nonlinear parameter γ to compute SPM. The pulse envelope temporal derivative term accounts for the self-steepening effect. We take γ to be 0.0022. We note that the temporal delay variable, T, is chosen such that the pulse is centered in the temporal window, allowing us to ignore the group delay term β_1, and simplifying computation.

Following the standard split-step procedure, solving for $A(T)$ at each subsequent position z is broken into two steps. First, the nonlinear term is set to zero, and the linear dispersion operation is computed in the frequency domain. Then, the linear terms are set to zero, and the nonlinear equation is solved in the time domain, with the exception of the Raman convolution integral, which is converted to a multiplication in the frequency domain. A fourth-order Runge-Kutta procedure is used to solve the nonlinear step.

In Figure 5.8 we show the results of our numerical simulation using the measured seed pulses in Fig. 5.7(a), with the measured coupling efficiency and depolarization loss, for the experimental fiber length of 7.25cm. The computed output spectra for both seed pulses show reasonable agreement with the measured data in Fig. 5.7(d). Furthermore, we account for the dispersion of downstream optics, such as the collimating lens and achromatic half-wave plate, and then numerically fit a fourth-order polynomial to the spectral phase, followed by subtraction of β_0, β_1, and β_2 in order to mimic the effect of a quadratic compressor. The numerically compressed pulses in Fig. 5.8(c,f) express good agreement with their measured counterparts.

The combination of negative chirp and normal dispersion (Fig. 5.8(d)) results in the well-known effect of spectral focusing. In our experiment, the nonlinear length is significantly shorter than the dispersion length [96], and as a result the pulse first undergoes rapid spectral compression, before rebroadening far beyond its initial bandwidth. It has been pointed out that Gaussian pulses undergoing spectral focusing exhibit pedestals at the spectral focus [97]. We see this

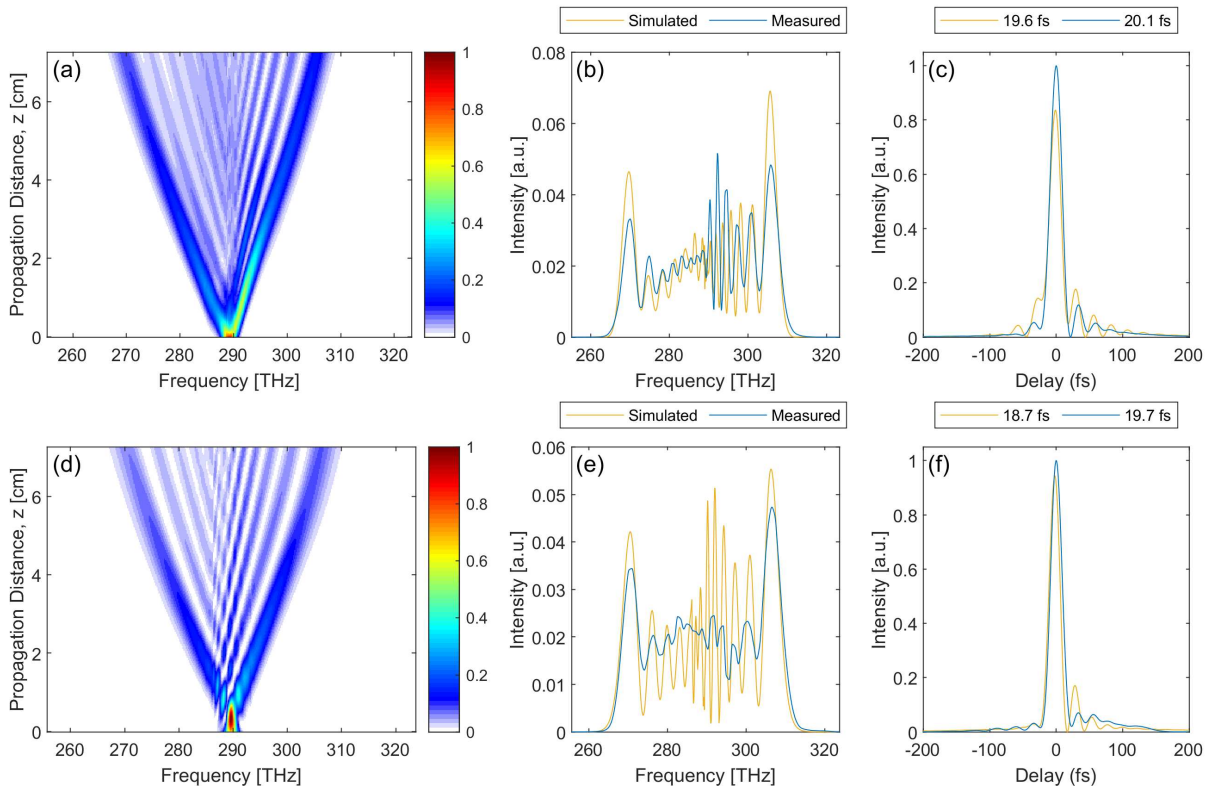

Figure 5.8: Numerical model for pulse propagation using the split-step Fourier method. (a)-(c) Positively chirped launch case, using the measured seed pulse in Figure 1(b). (d)-(f) Negatively chirped launch case, using the seed pulse in Figure 2(b). (a),(d) Spectral intensity as a function of fiber propagation length. (b),(e) Measured & simulated output spectra. (c),(f) Measured & simulated compressed pulses, with simulated pulse compressed by numerical removal of spectral phase up to second-order (GDD).

too in our propagation model, where the pedestals lead to added ripple in the power spectrum in (Fig. 5.8(d)), compared to the smoother, classic SPM spectral modulation seen in (Fig. 5.8(a)). Nevertheless, the overall phase disturbance is quite mild after the full fiber propagation length, as the compressed pulse is very similar for both launch seed chirp conditions.

We next utilize our model to demonstrate the importance of the two control parameters on the launch pulse - spectral shape and temporal duration - that are emphasized in our experiment. As we wish to maintain high energy throughput for the given fiber, we do not explore energy variation here.

First, Figure 5.9 demonstrates the effect of launching the apodized pulse without chirp - that is, the transform-limited pulse. (This 210 fs pulse is displayed in blue in Fig. 5.7(a)). As

expected, the high peak intensity produces an exceedingly large bandwidth, supporting a 7 fs pulse duration. A large wave-breaking pedestal is observed on the blue side of the spectrum, predicated by self-steepening on the trailing edge of the pulse. The large bandwidth sampling the fiber dispersion profile, compounded by the effects of wave-breaking, lead to the accumulation of spectral phase with significant higher-order dispersion. As a result, the output spectral phase cannot be compensated by a standard quadratic compressor [70, 87]. This is depicted in Fig. 5.9(c), where we have numerically removed spectral phase up to second-order as in Fig. 5.8, and plotted the resultant pulse intensity. In short, launching TL pulses at 140 nJ into a 7.25 cm fiber destroys the peak power achievable with a simple pulse compressor.

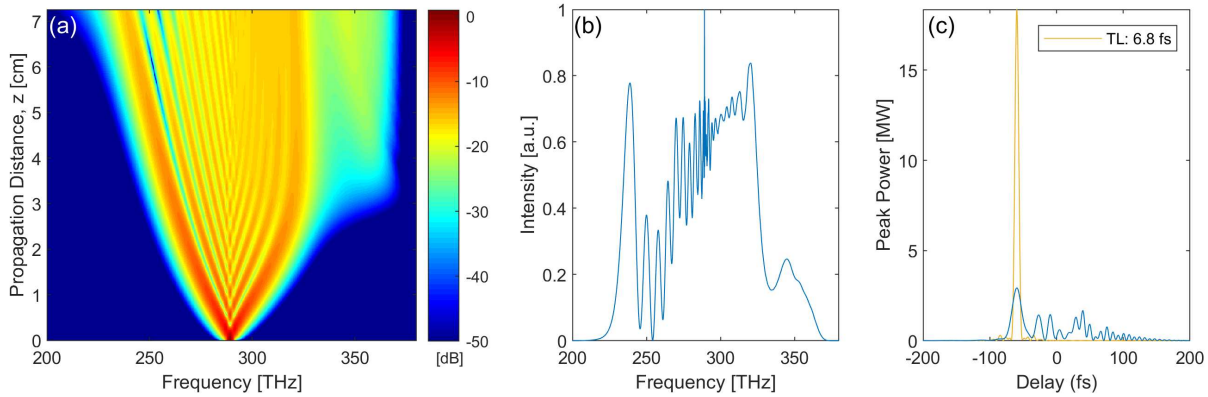

Figure 5.9: Numerical simulation of nonlinear propagation for the transform-limited launch pulse exhibited in Fig. 5.7(a), with pulse energy of 140nJ and duration 209 fs. (a) Spectral intensity along the fiber. (b) Output spectral intensity, supporting a 7 fs pulse. (c) Output pulse after GDD compensation.

Next, we allow for lowering seed pulse peak power with temporal chirp, but do not apodize the spectrum. Figure 5.10(b) shows the Y-Fi amplifier output spectrum characterized by SHG-FROG, which supports a 117 fs pulse. The asymmetry in the spectrum, relative to a standard ANDi oscillator output [72], is due to the high gain in the Y-Fi fiber amplifier at 1030nm. This spectrum is numerically chirped with the addition of 28,300 fs^2 of GDD, in order to generate an output spectrum supporting 19 fs pulses - a similar duration to the pulses measured in Fig. 5.7. The launch pulse peak intensity is low enough to avoid the onset of wavebreaking. However, the sharp features in the launch pulse spectrum lead to a spectral evolution containing significant

higher order spectral phase. Once again, a quadratic compressor is not able to cleanly compress the pulse (Fig. 5.10(e)).

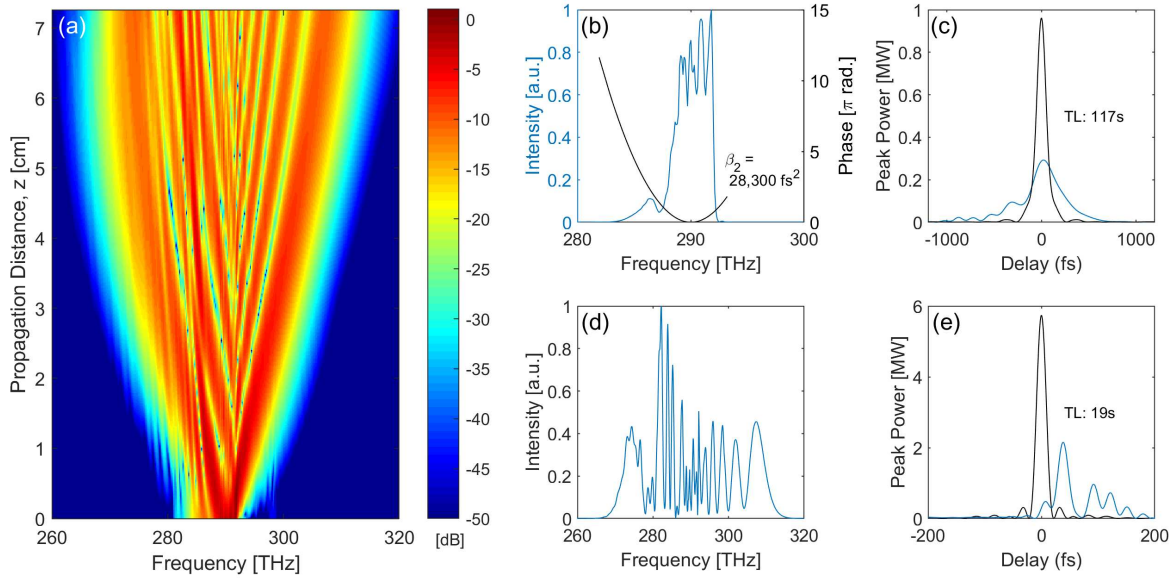

Figure 5.10: Numerical simulation of nonlinear propagation for a chirped seed pulse that does not have a smooth spectral profile. (a) Spectral intensity along the fiber. (b) Launch pulse spectrum & phase: measured Y-Fi HP amplifier spectrum (supporting a 117fs pulse), with numerical addition of 28,300 fs^2 of GDD. (c) Temporal launch pulse (blue), exhibiting structure on the leading (red) side of the pulse. TL pulse (black) supported by the spectrum in (b). (d) Simulated output spectrum, supporting a 19 fs pulse. (e) Output pulse, after GDD compensation (blue); transform-limit (black).

As a further confirmation of the efficacy of our approach, we plot the compressed peak power in Fig. 5.11 for three seed conditions: transform-limited, positively chirped, and negatively chirped. The TL seed is a 210 fs FWHM Gaussian pulse, with energy 140 nJ. For each temporal seed pulse, we plot the transform-limited peak power, and the peak power after quadratic compression. Just as a Gaussian pulse's peak amplitude is 94% of the peak amplitude of a square pulse of the same energy and FWHM duration, by way of analogy, we compute the relative peak amplitude of our quadratically-compensated pulses compared to the peak amplitude of the perfectly-compensated version of themselves. What becomes clear is that the TL pulse rapidly loses the ability to become phase-compensated with a simple compressor after about 2.5cm of propagation. This agrees with the spectral evolution plotted in Fig. 5.9, where we see wave-

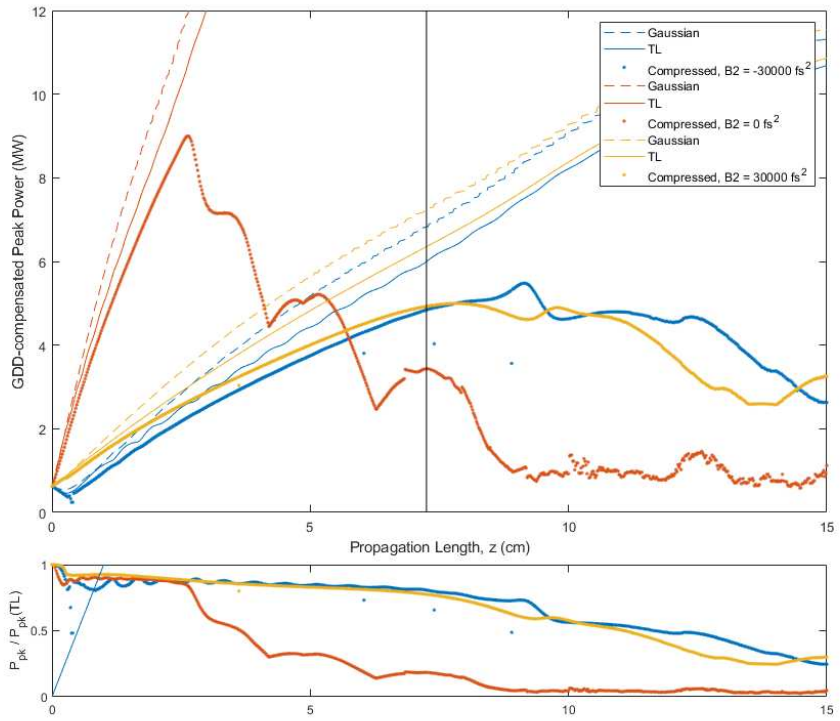

Figure 5.11: (a) Numerical simulation of compressed pulse peak power, for the 7.4nm full-width-half-maximum experimental pulse spectrum shown in figures 1(a) and 2(a), using 3 different launch pulse chirps: +30,000 fs^2 (yellow), 0 (red), -30,000 fs^2 (blue). For each launch pulse, we show the transform-limited peak power (solid line), the GDD-compensated peak power (dotted), and a Gaussian pulse peak power (dashed), where the Gaussian is given the same FWHM as the TL pulse. Black line shows the experimental fiber length. (b) Ratio of GDD-compensated peak power vs. TL pulse peak power, showing the degree of adherence of quadratic compression to complete compression as function of propagation.

breaking become fully developed between 2.5-3cm of propagation. With a short fiber, one could extract 9 MW of peak power from a TL seed pulse and a simple compressor.

In comparison, the chirped launch pulses allow for peak powers near the transform limit for a longer propagation distance. Moreover, the deviation from fully-compensated peak power exhibits a much slower transition than in the TL seed pulse case. As we argue in this paper, this approach relaxes the experimental constraints on fiber length and mounting, and also enables faster fiber replacement in the case of damage.

5.2.4 Discussion

The goal of the research presented here is to enable high energy throughput in (nearly) single-mode fiber. We do away with intricate fiber design and impractically short fiber lengths. Instead, we shape the launch pulse, and apply variable chirp in order to restrain nonlinear pulse evolution to the SPM-dominated regime, which can be subsequently dechirped with a simple compressor. Robustness is increased first by choice of a standard, solid-core step-index fiber. Secondly, chirped launch pulses present reduced peak power at the entrance fiber face.

The case of a negatively-chirped seed pulse presents an intuitive advantage. As discussed, under normal dispersion, the spectrum first narrows. As this takes place, the pulse's temporal duration remains constant. A "turnaround point" occurs when the narrowing spectrum supports a TL pulse matching the actual temporal duration. In other words, the chirped launch duration becomes transform-limited through the shedding of bandwidth. Beyond this point, the pulse undergoes spectral broadening, with newly generated bandwidth positively chirped by the fiber's normal dispersion profile. This is demonstrated in Fig. 5.8(d), where the turnaround occurs at about 0.5cm into the fiber. The plot of GDD-compensated peak power (Fig. 5.11) shows a small dip corresponding to this loss of bandwidth. Under negative chirp, we aim to exploit the fact that we can control this TL location along the static fiber length. In principle, this means that the compressor only needs to account for spectral phase that is accumulated after the turnaround point. Therefore, negative pre-chirp allows a practical fiber length to mimic the performance of a shorter fiber and a compressed launch pulse.

A positively-chirped launch pulse, however, accumulates dispersion across its launch bandwidth over the entire fiber length. It would seem disadvantageous to use a larger-than-necessary launch bandwidth in this case, relative to a TL pulse of the same temporal duration. Nevertheless, the launch spectrum used in this paper appears narrow enough that this is not an issue. The experimental seed pulse durations are only chirped by a factor of two (Fig. 5.7(a)), which is enough to exert fine control over nonlinear pulse evolution, but not enough to drastically impact linear phase accumulation.

No matter its sign, pre-chirp becomes a useful tool in the laboratory - one can experimentally find the amount of pre-chirp needed to still give a cleanly compressed pulse downstream. The cost of increasing seed chirp is less SPM and subsequently a longer compressed pulse. Depending on one's experiment, the desired balance point between the cleanest compressed pulse and the shortest compressed pulse can then be selected.

Large launch bandwidths may not benefit from either chirping strategy. With positive chirp, the spectrum will sample the fiber's higher order dispersion along the whole fiber length, which creates compression issues. Moreover, a grating compressor will add third-order dispersion, which will be more noticeable for a larger launch bandwidth. With negative chirp, the asymmetry of third-order dispersion may prevent the pulse from coming to a symmetric spectral focus. This could lead to added structure in the subsequent SPM-broadened spectrum, with associated additional spectral phase. One must also evaluate how much bandwidth is worth destroying only to then regenerate it on the path toward a broader spectrum.

Our experimental results indicate the new bandwidth remains highly coherent. While SPM, wavebreaking (WB), and stimulated Raman scattering (SRS) can all generate new spectral components within the pulse envelope, Heidt *et al.* report that [80] the latter effect, in concert with Four Wave Mixing (FWM), is the driving decoherence mechanism of super-continuum generated in the normal dispersion regime. The greater concern is quite possibly pulse energy fluctuation. A recent study by Genier *et al.* [98] examined the mapping of noise in the seed pulse into the noise and coherence of the broadened spectrum for all-normal dispersion (ANDi) fiber broadening, finding that the SC RIN is typically lower than seed RIN, but that seed RIN can lead to decoherence. Our seed laser, the Y-Fi HP from KM Labs, specifies a shot-to-shot pulse energy fluctuation of $< 1\%$ (0.1%). Nevertheless, the low reconstruction error based on our SHG-FROG measurements indicates a strong degree of coherence.

We also attempted this pulse compression strategy with visible pulses, derived from second-harmonic generation of the Y-Fi output in a 1mm BBO crystal, chirped with a Martinez compressor, and broadened in Nufern PM-S405-XP. In this case, negatively-chirped launch pulses

did outperform positively-chirped pulses, with output durations compressed to ~50 fs albeit significant pulse pedestals. We note the compressor used SF10 prisms, and results would be improved by switching to fused silica. However, we abandoned this strategy after discovering significant spectral fluctuation above coupled powers of a few hundred milliwatts.

We believe that the number of high energy, moderate bandwidth amplified laser sources currently appearing on the market could benefit from a spectral-broadening strategy like the one presented here in order to generate sub-100 fs pulses. Due to the intrinsic limitation of gain bandwidth in most laser media, it is practically much easier to amplify moderate bandwidths and then broaden the spectrum. Furthermore, amplifying with broad-bandwidth gain media such as Titanium Sapphire leaves the pulse spectrum subject to gain narrowing, presenting a tradeoff between energy and transform-limited duration. Other amplifier sources employing nonlinear pulse propagation, such as parabolic-pulse amplifiers and the recently characterized gain-managed Yb:fiber amplifier, can both amplify and broaden the pulse spectrum such that it is compressible to 30-50 fs durations. By employing the strategy presented here, using some spectral apodization and pulse duration control, these pulses could be extended to sub-20 fs durations. The main difficulty with such an approach is how the large bandwidths on the input pulse pick up higher order dispersion along the entire fiber length.

Finally, this approach should scale up with pulse energy as one increases the fiber mode-field diameter. There are a number of passive PM double-clad fibers (DCFs) currently available that are meant to mode-match corresponding DCF gain fibers. Carefully launching the seed pulse onto the TEM00 mode of the fiber will mimic single-mode propagation and ought to allow for 0.5 - 1 microjoule pulses to be compressed from 100's of femtoseconds to a few tens of femtoseconds.

5.3 Conclusion

In conclusion, we have demonstrated two techniques capable of converting typical ytterbium laser pulses with transform-limited durations exceeding 100 fs into sub-30 fs pulses. Corresponding peak powers exceed 1 MW. These schemes both employ 10/125 polarization - main-

taining fiber, which is relatively easy to work with and preserves single spatial mode operation and linear polarization very well. The first method employs nonlinear fiber amplification in a regime that combines parabolic pulse amplification with red-shifting gain bandwidth. The second method utilizes a chirped seed pulse scheme in combination with standard, nearly single-mode fiber, and is shown to enable compression at >100nJ pulse energies. By avoiding expensive fibers for pulse broadening and pulse shapers for compression, as well as the spatial inhomogeneities of bulk broadening, we demonstrate a high throughput and low cost system that can enable ultrafast applications with all the benefits of standard glass fiber, such as durability, low cost, and a clean, TEM00 mode profile at the output.

Author Contributions

K.A.W. designed research for the experiment in Section 5.1; K.A.W. and R.A.B. designed research for the experiment in Section 5.2. K.A.W. performed research, wrote numerical simulations, and analyzed data.

CHAPTER 6

DEMONSTRATION OF 1D RESOLUTION ENHANCEMENT WITH MP-SPIFI

In this chapter images generated with the first MP-SPIFI microscope are presented. This microscope was built based on the principles outlined in prior chapters, using a home-built femtosecond fiber laser source for illumination. Two-photon excitation mechanisms were demonstrated for both coherent and incoherent signal contrast mechanisms, using second harmonic generation and two-photon excitation fluorescence, respectively. These imaging capabilities under two-photon excitation are presented for both biological and inorganic samples.

6.1 Experimental parameters of the MP-SPIFI microscope

The microscope system was illuminated by pulses from a nonlinear fiber amplifier centered at 1065 nm [67], seeded by an all-normal dispersion fiber oscillator using Yb-doped gain fiber [71]. Temporal compression in a folded Martinez compressor resulted in near transform-limited durations of approximately 150 fs at an average power ranging from 900 mW to 1.3 W and a repetition rate of 52.5 MHz. The beam from the laser was collimated and expanded to a beam size of 8.85 mm (full-width at half-maximum of the intensity). The beam was brought to a line focus on the modulation mask with an achromatic cylindrical lens (ThorLabs, ACY-254-150-B) oriented such that the beam is focused in the vertical (y) direction only. The mask plane was re-imaged to the object plane in two stages, first with a 1:1 image relay system composed of two achromatic lenses (ThorLabs AC254-100-C-ML) in a 4-f configuration, and again with an image relay system consisting of a tube lens (ThorLabs AC254-150-C-ML) and an infinity-corrected objective lens. Data presented in this work were collected with a 0.8 NA objective lens (Zeiss, N-Achroplan 50x/0.8 NA Pol), such that the mask is imaged to the object region with demagnification of 46.5×. The SPIFI modulation mask used in this work had a density parameter $\Delta_k = 70/\text{mm}$. Imperfections in disk mounting lead to an additional phase accumulated in $S(t)$

as a function of mask rotation. The process used to remove disk aberration phase is discussed in the next chapter. All images displayed here were collected in the epi-direction with a long-pass dichroic beamsplitter placed between the tube lens and the objective lens (Semrock, FF875-Di01). Fluorescent light from the HeLa specimen was collected in the epi-direction through a short-pass filter (Semrock, FF720/SP) and a 500 nm long-pass filter (Chroma, ET500lp). Filtered optical signals were spatially integrated with a sensitive photo-multiplier tube (Hamamatsu 7422P-40), electronically amplified with a wide-band amplifier, and digitized on a data acquisition card (National Instruments) at a rate typically eight times faster than the fourth temporal harmonic of the carrier frequency ν_o. To generate 2D images, the sample was scanned in the vertical direction.

6.2 Point Spread Function Measurements

To demonstrate that MP-SPIFI provides images with frequency support beyond the diffraction limit for contrast mechanisms with both real and virtual energy states, we imaged TPEF from 100-nm-diameter fluorescent nanodiamonds (FNDs), and SHG from 200-nm-diameter barium-titanate oxide (BTO) crystals. The objects were illuminated with femtosecond laser pulses centered at a wavelength of 1065 nm and focused by a 0.8 NA objective lens. For both TPEF and SHG, the predicted spatial resolution for MP-SPIFI order $q = 1$ through $q = 4$ are 666 nm, 333 nm, 222 nm, and 167 nm, although these estimates assume a uniform transfer function.

Since the BTO crystals were larger than the predicted spatial resolution of the fourth-order MP-SPIFI image, we used FNDs to determine the spatial resolution of the imaging system. Figure 6.1(d) shows the recovered OTF for each SPIFI order, scaled to the lateral spatial frequency domain. It is clear that lateral spatial frequency information beyond the conventional limit is contained in all MP-SPIFI orders for $q > 1$. The corresponding PSFs are displayed in Fig. 6.1(e). Using the Raleigh criterion for spatial resolution, we determined the spatial resolution for the first-, second-, and fourth-order PSFs to be 949 nm, 491 nm, and 362 nm respectively (Fig. 6.5). We note that the third-order PSF suffers from a dual-lobe structure, where each lobe of the

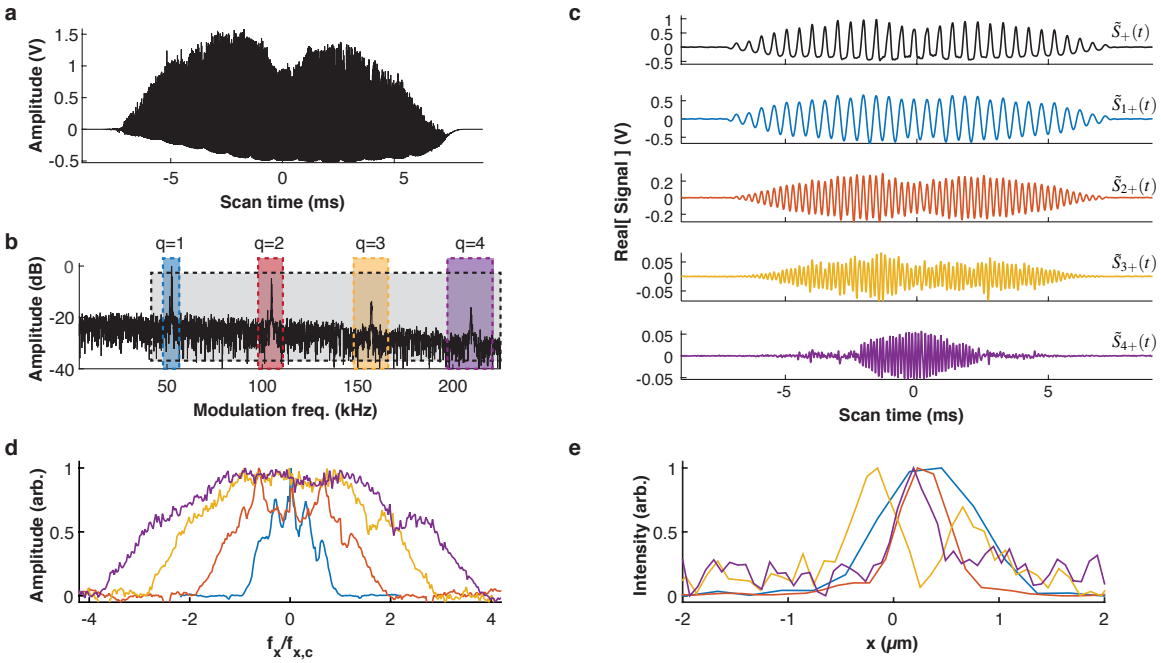

Figure 6.1: MP-SPIFI provides increased lateral spatial frequency support. (a) The average of 1000 temporal measurements of SHG from 200-nm-diameter BTO particles. Note that there is no DC offset S_0(t) because the amplifier was set to AC coupling. (b) A Fourier transform of the mean signal with respect to scan time reveals each MP-SPIFI image encoded at a different carrier frequency. (c) The complex temporal trace, $S_{q+}(t)$, was recovered for each SPIFI order by digitally filtering each harmonic in the modulation frequency domain with a square window, as shown in (b). To obtain $S_+(t)$, the digital filter was set to retain all four image orders. All five complex traces were demodulated such that the fundamental carrier frequency is 2 kHz as opposed to ~52 kHz. (e) Experimental MTFs for each MP-SPIFI image measured from 100-nm-diameter fluorescent nanodiamonds (FND).The q-th order image spans the spatial frequency range $[-q\,f_{x,c}, q\,f_{x,c}]$. (f) PSFs for each MP-SPIFI order. The spatial resolution computed from each PSF are listed in the text. Reprinted from Ref. [51].

third-order PSF has spatial resolution of 468 nm. This modulated PSF arises when higher-order diffracted beams from the binary modulation mask interfere with the first- and zero-order beams in the object plane, and is discussed in the next chapter.

6.3 Biological, Multimodal, and Polarization-Dependent Signal Collection

We demonstrated super-resolved multiphoton imaging of biological media by imaging TPEF from polymerized tubulin fibers (i.e. microtubules) tagged with with Alexa 546 in a mitotic HeLa cell, and SHG from collagen fibers in fixed rabbit tendon (Fig. 6.2). One-dimensional MP-SPIFI images were collected in the horizontal dimension as the specimen was scanned vertically to

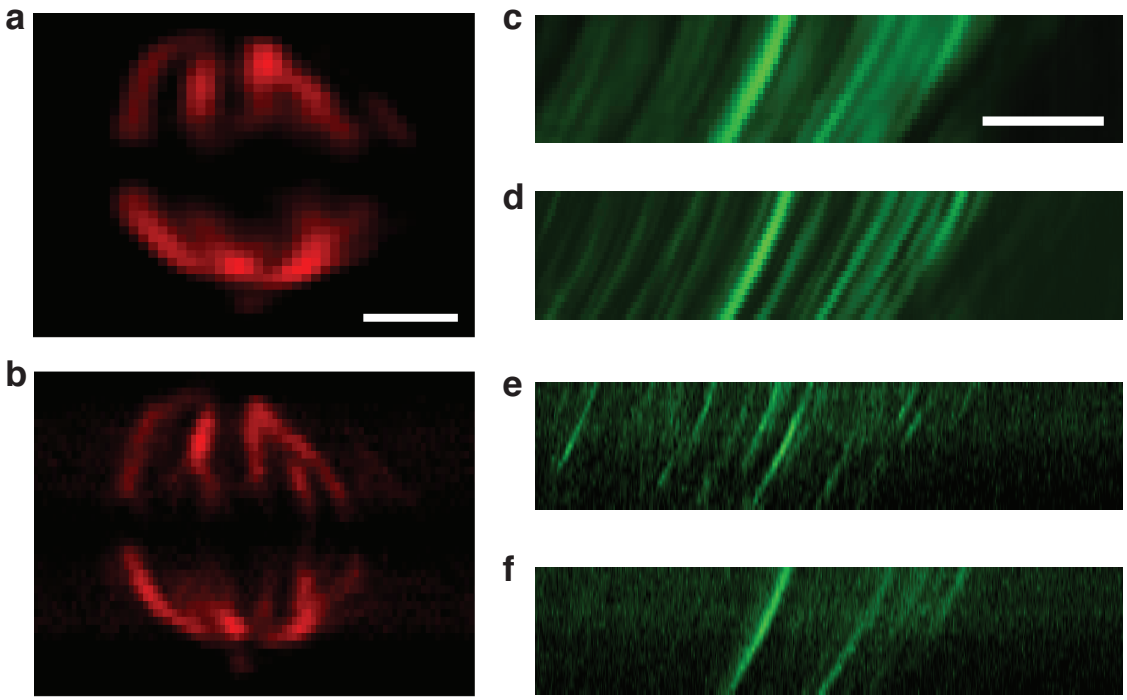

Figure 6.2: TPEF and SHG images collected from biological media with MP-SPIFI. (a) First- and (b) second-order MP-SPIFI images of TPEF from a mitotic HeLa cell immunostained with primary antibodies against alpha tubulin and secondary antibodies tagged with Alexa 546. Scale bar: 3 μm. (c)–(f) First through fourth order images of SHG from fixed, 16-μm-thick rabbit tendon. Scale bar: 10 μm. All images were collected at 0.8 NA with laser pulses centered at 1065 nm. TPEF was collected in the epi direction and SHG was collected in the forward-scattered direction. Reprinted from Ref. [51].

form a two-dimensional (2D) image. Resolution enhancement occurs only in the horizontal dimension in this illumination scheme.

To demonstrate multimodal super-resolved imaging with MP-SPIFI, we simultaneously imaged photoluminescence (PL) and SHG from CdTe solar cells (Fig. 6.3). Due to the opacity of the CdTe cells, both contrast mechanisms were collected in the epi-direction. Figures 6.3(a)–(d) display the first- through fourth-order SHG-SPIFI images, and the corresponding PL-SPIFI images are shown in Fig. 6.3(e)–(h). Comparison of the images for each MP-SPIFI order makes it clear that the spatial resolution is enhanced in both SHG and PL simultaneously, although the resolution appears to be different for these two contrast modes beyond the second-order data. The reason for this discrepancy is unclear at this time, though we note that the relatively long

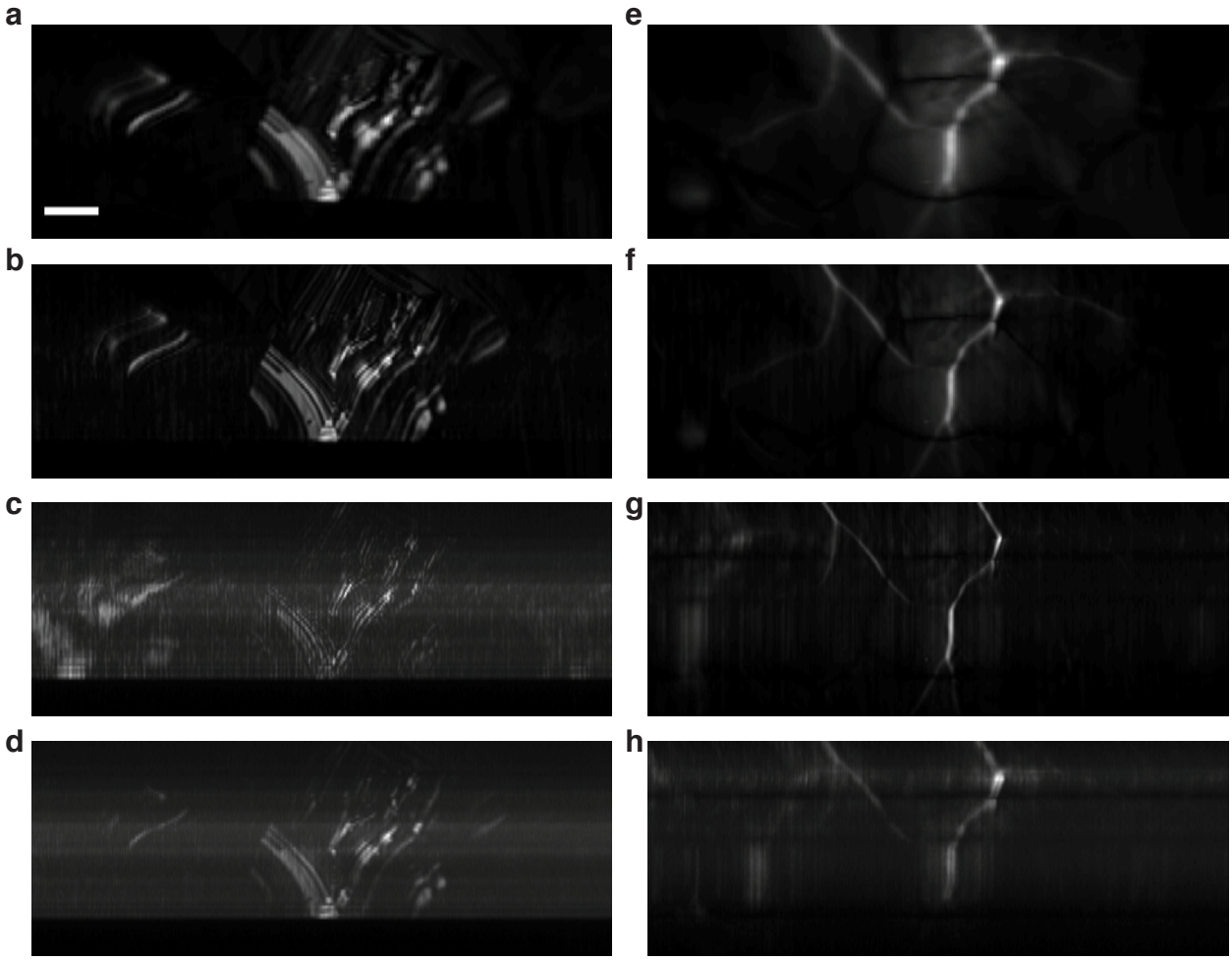

Figure 6.3: Multimodal super-resolved images of SHG and PL from CdTe solar cells. (a)–(d) First through fourth order SHG images. (e)–(h) Corresponding PL images. Scale bar: 10 μm. Reprinted from Ref. [51].

lifetime of the PL contrast mechanism, as well as diffusion of excited carriers may be responsible for these differences.

To demonstrate the polarization sensitivity that is inherent to coherent nonlinear scattering mechanisms, we rotated the linear polarization state of the collimated laser beam before being focused onto the mask. Although depolarization is to be expected at high numerical apertures, we found that clear differences in contrast occurred for SHG images. Figure 6.4 displays a CdTe solar cell for two different linear polarization states. The polycrystalline structure of the solar cell has numerous grain boundaries where carrier recombination occurs and photolumines-

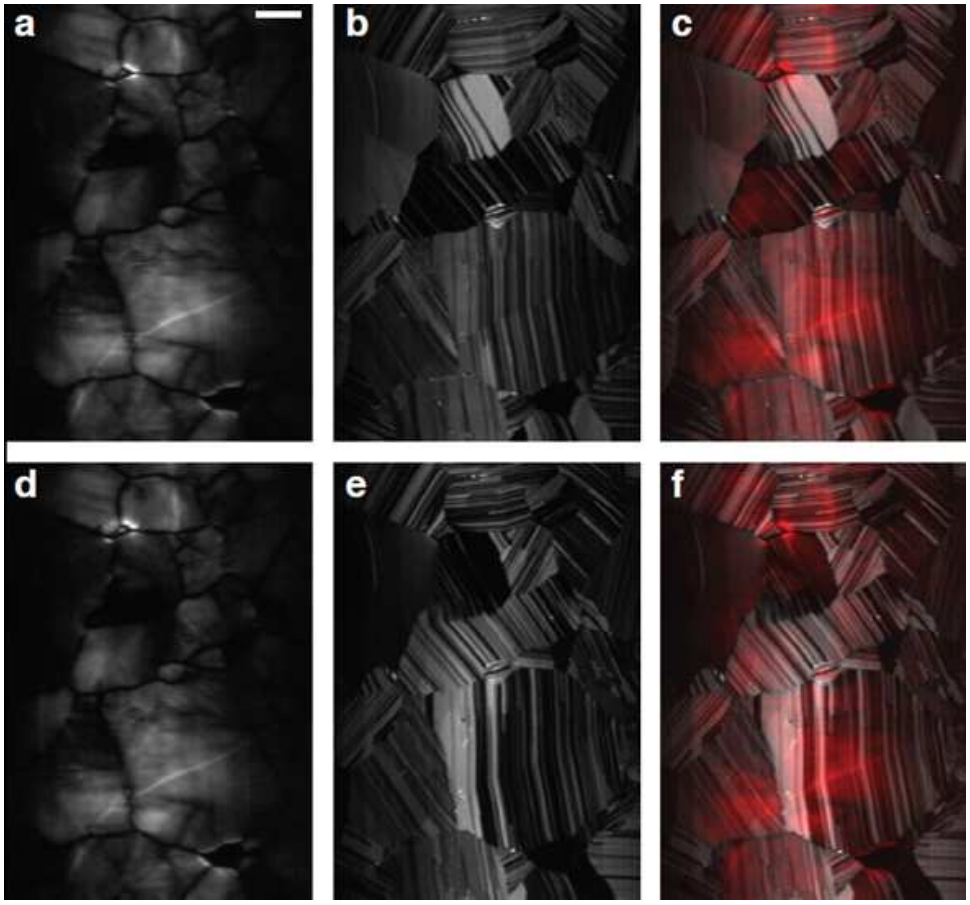

Figure 6.4: Linear polarization sensitivity in a CdTe solar cell. Images in the top row and bottom row were acquired with a difference in polarization state of 123^{o} at the input to the microscope. Images (a) and (d) are due to photoluminescence and do not display great variation with polarization state. Images (b) and (e) are due to second-harmonic generation; the polycrystalline spatial morphology displays clear differences in signal with polarization state. Images (c) merges the information in (a) and (b); image (f) merges the information in (d) and (e). The PL signal is false-colored red. Panel(f) is reprinted with permission from Ref. [99] ©The Optical Society.

cence is generated. Each grain itself is crystalline in nature and supports second harmonic generation, with a dependence on the polarization state of the incident laser beam.

6.4 Sample Preparation

Samples used for point spread function measurements were 200 nm $BaTi0_3$ particles (product number 1148DY, Nanostructured & Amorphous Materials, Houston TX) for SHG, and 100 nm fluorescent nanodiamonds (ND-400NV-100nm-10mL, Adamas Nanotechnologies, Raleigh NC) for TPEF. In both cases the insoluble nanoparticles, suspended in water, were diluted, disaggre-

gated in an ultrasonic bath, drop cast onto a microscope slide, and cover-slipped after the water had evaporated. HeLa cells were seeded onto glass coverslips and fixed when they reached ~70% confluency. Cells were rinsed rapidly with 37 C 1X PHEM buffer (60 mM PIPES, 25 mM HEPES, 10 mM EGTA, 4 mM $MgSO_4$, pH 7.0) followed by lysis at 37 C for 5 min in freshly prepared lysis buffer (1X PHEM + 0.5% Triton-X-100). Cells were then fixed on the bench top for 3 min using ice cold methanol (95% methanol + 5 mM EGTA) followed by an additional 20 min methanol fixation at 20 C. At room temperature, cells were then rehydrated with 1X PHEM then rinsed 3×5 min in PHEM-T (1X PHEM + 0.1% Triton-X-100) and blocked in 10% boiled donkey serum (BDS) in PHEM for 1 hr at room temperature. Microtubules were labeled with anti-alpha tubulin primary antibodies (Sigma-Aldrich, St. Louis, MO) diluted in 5% BDS for 12 hr at 4 C. Following primary antibody incubation, cells were rinsed 3×5 min in PHEM-T and then incubated for 45 min at room temperature with secondary antibodies conjugated to Alexa 546 (Life Technologies). Cells were then rinsed 3×5 min in PHEM-T, incubated in a solution of 2 ng/mL 4,6-diamidino-2-phenylindole (DAPI) diluted in PHEM, rinsed again (3×5 minutes), and then mounted onto microscope slides in an anti-fade solution containing 90% glycerol and 0.5% N-propyl gallate. Coverslips were sealed with nail polish to affix them to the slides. The polycrystalline, large grained CdTe sample was grown by close spaced sublimation (CSS), treated with $CdCl_2$, and polished, effectively "sealing" small grains (~2 μm) after growth. The sample was polished using an ion beam technique.

6.5 Data analysis

Data analysis was performed in MATLAB (The MathWorks, Natick, NJ). Each 1D line image was reconstructed by computing the fast Fourier transform (FFT) of the measured temporal data $S(t)$ to obtain the MP-SPIFI images in the modulation frequency domain, i.e., $S(\nu_t)$. Each MP-SPIFI order was recovered by numerically filtering at the positive carrier frequency. The filtered data, $S_q(\nu_t)$, was inverse transformed to obtain $S_{q+}(t)$. The complex temporal trace was then demodulated by the relative carrier frequency, $q\nu_o$, and the temporal axis was calibrated according to the relation $f_x(t) = q\kappa\, t/M$ to obtain $S_{q+}(f_x)$. The coupling coefficient κ between

modulation frequency and space was calibrated by measuring light transmitted through a 2 μm slit in the object plane as a function of lateral position [53]. The centroid of the measured distribution was computed as a function of lateral position. This allowed the quantity describing the relationship between lateral position and carrier frequency, κ, to be recovered empirically.

6.6 MP-SPIFI Resolution

The Raleigh resolution criterion was used to benchmark the spatial resolution from the experimental PSFs shown in Fig. 6.1. The left panel in Fig. 6.5 shows two copies of the simulated PSF for the first-order ($q = 1$) MP-SPIFI image, computed with the vector focusing model described in Section 3.3.6. Raleigh resolution is defined as the distance that a copy of the PSF must be shifted in order for its peak to coincide with a zero in the unshifted PSF. In the measured PSFs data, the shot noise background makes it difficult to interpret where the first zero of the PSF is located. Instead of directly detecting this zero we fit a Gaussian profile to the measured PSF. In the ideal case of a uniform OTF, the measured PSF would be proportional to $|\mathrm{sinc}(x)|$. However the OTF is neither uniform, nor is it a Gaussian, so fitting a $\mathrm{sinc}(x)$ or a Gaussian to the PSF results in deviations from the measured PSF. This is shown explicitly in the right panel of Fig. 6.5, where we have fit a both a Gaussian and a $|\mathrm{sinc}(x)|$ to the simulated PSF. We find that for the numerically simulated PSF, the half-width at 10.4% of the maximum of the Gaussian profile corresponds to the first zero in the computed PSF. We used this metric to compute the spatial resolution of our experimental data.

Using the vector focusing model we computed the spatial resolution at the HW@10.4% maximum for first- through fourth-order MP-SPIFI images to be 818 nm, 427 nm, 300 nm, and 240 nm respectively. For comparison, the HW@10.4% maximum for 2P-LSM is 429 nm. This is nearly identical to the x-resolution for the second-order MP-SPIFI image. Moreover, as the y-resolution in 2P-SPIFI is formed by full aperture line focusing with two-photon excitation, we should expect it to approach the 2P-LSM resolution with point focusing. Therefore with line scanning in y, and projections in x, the Q=2 image in 2P-SPIFI is approximately isotropically resolved. Whereas the x-resolution in the Q=1 image corresponds to a *linear* coherent brightfield

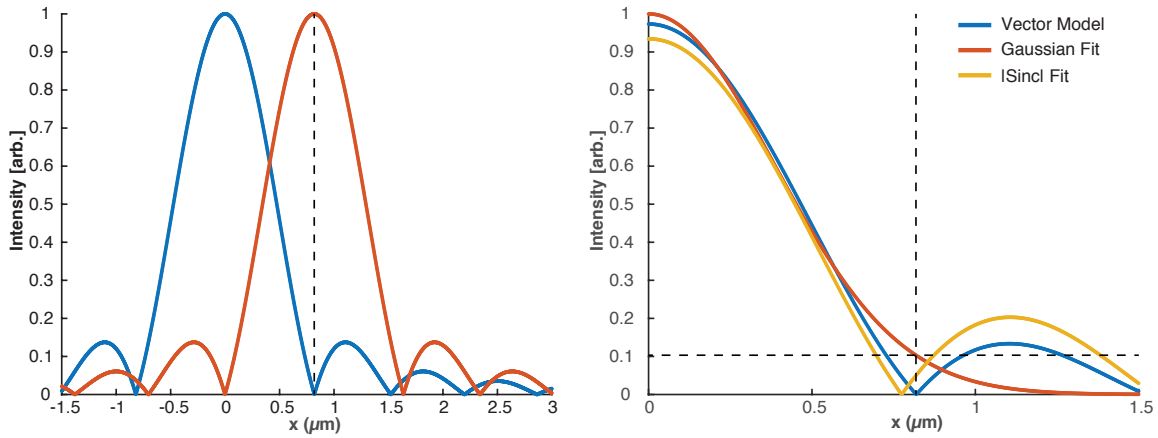

Figure 6.5: MP-SPIFI resolution metric. The left panel shows two copies of the simulated PSF for the first-order ($q = 1$) MP-SPIFI image, computed with the vector focusing model. Raleigh resolution is defined as the distance that a copy of the PSF must be shifted in order for its peak to coincide with a zero in the unshifted PSF. In the right panel, we have fit a both a Gaussian and a $|\mathrm{sinc}(x)|$ to the simulated PSF. We find that for the numerically simulated PSF, the half-width at 10.4% of the maximum of the Gaussian profile corresponds to the first zero in the computed PSF. We used this metric to compute the spatial resolution of our experimental data. Reprinted from Ref. [51].

system at $\lambda = 1065$ nm, images Q=3 and greater can display resolution beyond the two-photon LSM capability in the x-dimension. Finally, as a benchmark for our numerical recipe, we also compared the half-width at 1/e for full-aperture focusing to the analytic expression in Ref. [100], and found that the value of 285 nm from the simulation to be in good agreement with the value of 300 nm using the analytic expressions.

6.7 Comparison with MP-LSM

The ability to resolve fine spatial features in an image depends on both the shape and the extent of the spatial frequency support of the OTF. To evaluate the relative imaging performance of MP-SPIFI compared to conventional laser-scanning microscopy (LSM) techniques, the OTFs of these methods were computed using the vector focusing numerical model for two-photon SPIFI (2P-SPIFI), and two- and three-photon LSM. Intensities were computed for an illumination wavelength of 1065 nm, 0.8 NA, and linearly-polarized light aligned with the vertical (y) direction. For 2P-SPIFI, the widths of the intensity distributions in the pupil plane were mod-

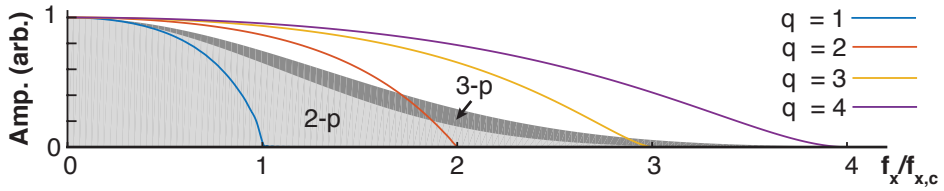

Figure 6.6: Comparison of the OTF in multiphoton laser scanning microscopy and two-photon SPIFI. The shaded gray regions indicate the frequency support for two- and three-photon laser scanning microscopy. Solid lines indicate the frequency support in 2P-SPIFI. All OTFs were computed with the Debye integral using $\lambda = 1065$ nm and 0.8 NA. Reprinted from Ref. [51].

eled after the MP-SPIFI system reported here. To compute the MP-SPIFI signal, we assumed a point emitter located at the focal point of the objective lens, $\mathbf{r}_0 = (0,0,0)$. The point emitter was modeled by a Dirac-δ distribution, $\delta(\mathbf{r}-\mathbf{r}_0)$. Since the contrast distribution we consider is a delta function, we need only compute the intensity at $\mathbf{r}_0$ to obtain the MP-SPIFI signal:

$$S(t) = \langle [I(\mathbf{r},t)]^2\, \delta(\mathbf{r}-\mathbf{r}_0)\rangle_{\mathbf{r}} = [I(\mathbf{r}_0,t)]^2 \tag{6.1}$$

For the simulated TP-SPIFI data presented in Fig. 6.6, we considered a second-order nonlinearity ($\eta = 2$), and included only first-order diffraction from the modulation mask, where $a_0 = 1/2$ and $a_1 = 1/\pi$ were set by the diffraction efficiency of a square grating.

For the multiphoton LSM calculation, the beam size in the vertical dimension of the 2P-SPIFI microscope was used as the radius of the circularly-symmetric Gaussian distribution, resulting in a fill factor of ~2 [38]. The lateral spatial frequency support was then computed from the illumination intensity for each imaging type. The resulting spatial frequency support is shown in Fig. 6.6, where the shaded gray regions indicate the spatial frequency support of each LSM mode, while solid lines indicate the spatial frequency support for each 2P-SPIFI order.

What is clear in Fig. 6.6 is that MP-SPIFI imaging collects significantly more information content (high SNR) at high spatial frequencies than multiphoton LSM, thus providing the ability to extract significantly more spatial information. As the scan time progresses in 2P-SPIFI, the focusing of the transmitted diffracted orders is perturbed by the circular objective pupil,

which shapes the spatial frequency support of the OTF. The OTFs associated with 2P-SPIFI extend to greater spatial frequency extent for the second-order nonlinear interaction than either two- or three-photon LSM. Moreover, the amplitude of the high spatial frequency content for 2P-SPIFI is significantly higher than for multiphoton LSM. The result is that 2P-SPIFI captures significantly more fine spatial information about an image than multiphoton LSM.

Author Contributions

This chapter uses text from Ref. [51]. The author contribution statement from Ref. [51] is adapted here: J.J.F. and R.A.B. designed research. J.J.F. and K.A.W. built microscope. J.J.F., K.A.W. and A.M.A.M. collected data. J.J.F., K.A.W. and R.A.B. analyzed data. J.J.F., K.A.W., and R.A.B. wrote the paper. S.R.D. designed the laser source and S.R.D. and K.A.W. constructed the laser source. A.M.A.M. and D.H.L. provided CdTe solar cells for imaging; K.F.D. and J.G.D. provided HeLa cells for imaging. M.D.Y. and J.A.S. provided ray-tracing tools and custom detection optics. J.J.F. and K.A.W. made figures. J.J.F. and K.A.W. contributed equally to this work.

CHAPTER 7

LIMITATIONS IN RECONSTRUCTING SUPER-RESOLVED IMAGES

The experimental results presented in the previous chapter were a promising development toward the goal of a multiphoton microscope that can image biological samples with super-resolving capabilities for both coherent and incoherent multiphoton contrast mechanisms. Our initial demonstration succeeded in showing that spatial frequency components beyond the pass-band of an illumination system can still be probed in a specimen through the combination of spatial frequency projections and a multiphoton excitation. However, numerous obstacles can prevent the image formation process from achieving the theoretical limit of resolution enhancement that is available through the NA, wavelength, and nonlinear order. In this chapter we discuss physical limitations caused by shot noise, depolarization under high NA focusing, and the low-pass spatial frequency filter due to the circular pupil. The latter plays multiple roles in reducing the achievable resolution enhancement, especially at high lateral spatial frequency, where it both reduces energy throughput and expands the vertical focal width of the scanning beams. We also discuss technical limitations related to imperfect rotation with a real motor, mask patterning constraints, and lens aberration.

7.1 Pupil Apodization of Scanning Diffracted Orders

The effect of a circular pupil clipping the horizontally focused, vertically collimated diffracted beams has been discussed at length in Sections 3.3.3 - 3.3.5 for scalar fields, and again in Section 4.5 for volume illumination. Here, we compute the effects of the circular pupil using the Debye-Wolf integral for vector fields at high NA. This numerical model was discussed in Section 2.8 and it's application to the case of MP-SPIFI input fields was developed in Section 3.3.6. We use the experimental parameters of the microscope described in Chapter 6 as inputs to our model.

7.1.1 Energy transmission vs. scan time

First, the throughput energy of the beams with scan time was computed with an overlap integral. The energy loss experienced by the diffracted beams causes a reduction in the modulation depth of the illumination intensity pattern, reducing the amplitude of each MP-SPIFI order with respect to the background DC signal. We computed the energy transmission as a function of scan time by numerically integrating the amplitude of the diffracted fields over the circular pupil of the objective lens:

$$e_j(t) = \int_0^{2\pi} \mathrm{d}\phi \int_0^{\theta_{max}} \mathrm{d}\theta \, \sin\theta \, E_{\infty,j}(\phi,\theta,t) \tag{7.1}$$

Here $E_{\infty,j}(\phi,\theta,t)$ is the time-dependent far-field on the reference sphere of an ideal high-NA lens given by Eqn. (3.83). The reference sphere admits a maximum semi-aperture angle θ_{max} given by Eqn. (2.87), and the circular boundary described by the polar angle $\theta = \theta_{max}$ on the reference sphere serves as the circular pupil, as described in Section 3.3.6.

The relative energy transmission curves are shown in Fig. 7.1, where it is clear that the diffracted modes ($j = 1$) contribute less to the overall energy of the illumination intensity as the beam traverses the pupil of the objective lens.

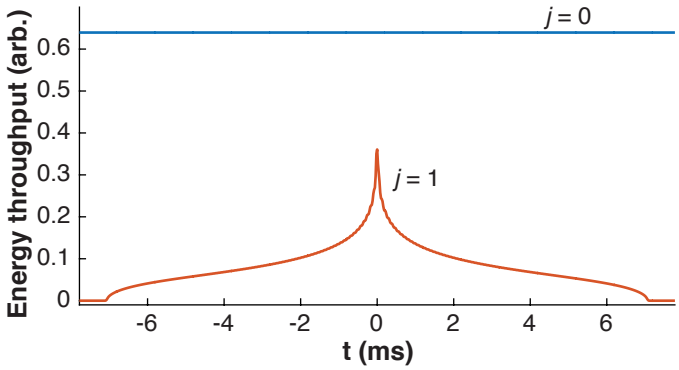

Figure 7.1: Simulated energy transmission of the diffracted orders through the objective lens. Relative energies are normalized by the total transmitted energy at scan time t=0, when both diffracted orders are overlaid in the lateral dimension. Reprinted from Ref. [51].

7.1.2 Vignetting of diffracted illumination beams

To numerically investigate the vertical frequency support passed by the objective lens as a function of scanning diffracted order position in the pupil, we again employed the Debye-Wolf integral as applied to our experimental MP-SPIFI microscope. While the time-stationary zero-order diffracted field is centered in the aperture and is brought to a diffraction-limited tight line focus in the vertical dimensions, the scanning diffracted fields $|j| \geq 1$ experience a time-varying truncation of their vertical distribution in the circular aperture. A numerical calculation

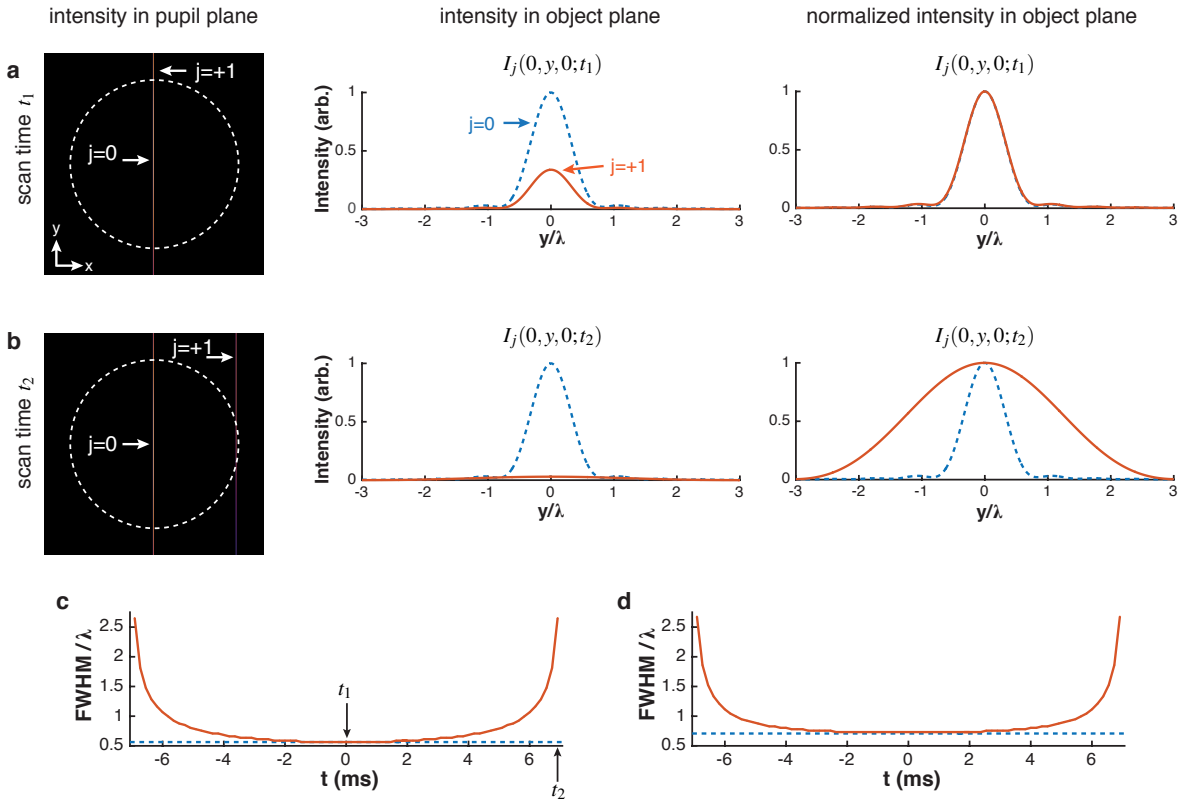

Figure 7.2: Vertical spatial frequency support vs. scan time. (a) At zero scan time, the diffracted beams and the undiffracted beam fill the objective lens pupil in the vertical dimension. In the focal plane the width of the light sheet in the vertical dimension is diffraction limited for both the diffracted and undiffracted beams. (b) At higher scan times, when the diffracted order approaches the maximum spatial frequency supported by the lens, the vertical spatial frequency content is significantly reduced by the circular pupil. Consequently, the $j = 1$ light sheet is not diffraction limited. This reduces the intensity of the diffracted beam in the focal plane, thus reducing the contrast of the illumination intensity fringes. The width of the light sheet changes with scan time, and varies slightly differently for (c) x-polarized and (d) y-polarized input light. Reprinted from Ref. [51].

of each diffracted field in the transverse focal plane, $E_{s,j}$, as a function of scan time, confirms the increasing loss of vertical spatial frequency support as the pupil fields scan from center to edge of the circular aperture. The width of the line focus in the vertical dimension at the sample plane therefore increases with the magnitude of scan time, $|t|$. Thus, for orders $|j| \geq 1$, the peak amplitude available for excitation in the focal plane decreases by two mechanisms - not only is the energy transmitted through the aperture decreasing, but the transverse extent of the focal fields is growing in the vertical dimension.

We computed the illumination intensity in the transverse plane located in the focus of the illumination objective ($z = 0$) for several scan times, considering only the $j = 0$ and $j = \pm 1$ beams. From Fig. 7.2 it is clear that as the first-order diffracted beams scan away from the optic axis in the lateral (x) dimension, the vertical spatial frequency support decreases and causes a corresponding broadening of the illumination beams in the vertical dimension.

7.2 Depolarization

Depolarization as a function of scan time can cause a reduction in the contrast of the illumination intensity fringes, and is dependent upon the polarization state of the beams in the pupil plane, and the polarization dependence of the contrast mechanism. Again, the Debye-Wolf integral was used with experimental microscope parameters to investigate depolarization in the focal plane of the illumination light sheet for linearly-polarized input light (Fig. 7.3). We find that not only can the depolarization cause reduction in the amplitude of the OTF with scan time, but that the shape of the OTF depends on the input polarization state.

7.3 Image Blurring due to Disk Rotation Error

The modulator described in Section 3.2 is fundamental to the image formation process in MP-SPIFI. Using an inertial device like a rotating wheel comes with certain challenges, especially for high resolution microscopy. These challenges are not insurmountable; both confocal microscopes and spinning platters in computer hard drives have also had to engineer solutions for the integration of spinning disks and high-NA focal volumes. In this section, we examine two

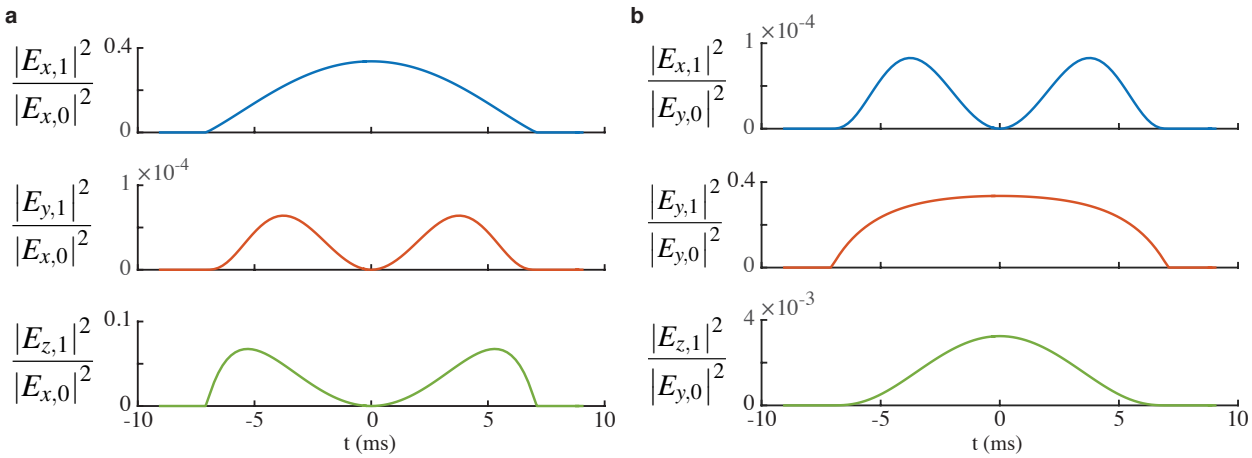

Figure 7.3: Depolarization of linearly-polarized input electric fields vs. scan time. The polarization state in the pupil plane was aligned in the (a) x-direction and (b) y-direction. Depolarization of the first diffracted order ($j = 1$) is shown by plotting the ratio of the intensities in each spatial dimension to the intensity of the input polarization state for the zero order beam. Depolarization at high spatial frequencies causes a reduction in the contrast of the illumination intensity, which can reduce the SNR. Reprinted from Ref. [51].

problems we have faced using the spinning Lovell reticle for high-resolution microscopy with MP-SPIFI: velocity fluctuations and pattern centration error. If left unchecked, each can have a deleterious effect on the microscope's resolving power. We discuss the physical origin of each problem, and the practical measures we have developed to minimize their impact. We find that addressing these problems yields FFT image reconstructions that are close to the theoretical limit in resolving power with improved signal-to-noise.

To reconstruct SPIFI data with the FFT algorithm, it is imperative that the sweep in projected spatial frequencies, and their spatial phases, be perfectly linear. In practice, this is difficult to achieve for two reasons. First of all, the motor does not spin at a uniform velocity. Secondly, it is difficult to perfectly overlap the printed modulator's pattern origin with that of the motor's axis of rotation. We will examine the effect of these two issues using a spectrogram analysis. The spectrogram is subsequently used to provide a correction to the measured data [101]. These corrections restore linearity to the data and allow for a cleaner reconstruction with the FFT algorithm.

It is helpful to start by visualizing a light source focused to a single point on the disk. For example, we can use the point $(x_o, 0)$, which corresponds to the center position of the line focus used for SPIFI modulation. (Let us assume for simplicity that we have a mask with gray-scale printing, so there are no effects from binary modulation). A point focus on the spinning-disk modulator should experience a singular modulation frequency, as described in Section 3.2. Under perfect conditions, the modulated light should produce a measured signal that is a perfect cosine function, which we can simply write as $S(t) = \frac{1}{2} + \frac{1}{2}\cos\left(2\pi f_o t\right)$. The temporal modulation frequency at that position is $f_o = \Delta_k \nu_r x_o$, given by Eqn. (3.16), where ν_r is the motor rotation rate in cycles/second [Hz]. Let us now explore what happens when the modulation frequency f_o deviates from linearity.

7.3.1 Non-concentric Disk Mounting

Ideally, the motor and reticle pattern share the same coordinate system. However, when the Lovell pattern's origin is offset from the motor spindle's axis of rotation, a laser point focus sitting at polar position $(r_o, 0)$ in the motor's frame of reference will not experience a uniform modulation frequency running past it due to the spinning disk. Instead, it will experience an excursion from the local modulation frequency, $f(r_o)$, as it is forced to "walk" into neighboring rings, with modulation $f(r_o + \delta r(t))$, before ultimately returning to its starting point after one spindle rotation. This means that collected light for the laser focus at location x_0 is spread into multiple modulation frequency bins, and therefore it's positional resolution is degraded. The deviation in modulation frequency for the point focus at $(x_o, 0)$ due to this spatial misalignment can be written as:

$$\begin{aligned} f(t) &= \Delta_k \nu_r \left[x_o + \delta x(t)\right] \\ f(t) &= f_o + \delta f(t) \end{aligned} \tag{7.2}$$

This error has been colloquially termed "wobble" in our lab due to the visual appearance of poorly-mounted disks while rotating.

7.3.2 Fluctuations in Disk Velocity

The motor does not spin at a uniform velocity. It is an inertial device, and requires small corrections from a PID controller to maintain a mean velocity equivalent to the setpoint. In MP-SPIFI, these departures from the mean velocity also map into a variation in the local modulation frequency for a given point focus. In the case of zero wobble, where a point focus stays perfectly within a ring of a singular printed modulation frequency, fluctuations in motor velocity will cause that singular printed pattern to generate a small bandwidth of temporal modulation frequencies imprinted onto the transmitted light. Just as in the case of wobble, this washes out the resolution, as neighboring points share the same modulation frequency for different sectors of the disk, and thus their signals values are integrated together in the same temporal frequency bins. These aberrations are especially noticeable when looking at point emitters in the higher image orders in MP-SPIFI. The perturbed modulation frequency for the point focus at $(x_o, 0)$ due to this temporal jitter can be written as:

$$\begin{aligned} f(t) &= \Delta_k \, x_o \, [\nu_r + \delta\nu_r(t)] \\ f(t) &= f_o + \delta f(t) \end{aligned} \tag{7.3}$$

It is clear upon inspection that motor velocity deviation, like the mask centration error, manifests as a spread in modulation frequency for a point focus at the mask.

7.3.3 Correction Model

Equations (7.2) & (7.3) show that wobble error and motor velocity fluctuations cause a point focus to be assigned a spread of modulation frequencies over one rotation of the disk. In the experiment, these are happening simultaneously. Therefore, in general, we have:

$$f(t) = \Delta_k \, [\nu_r + \delta\nu_r(t)] \, [x_o + \delta x(t)] \tag{7.4}$$

However, we can exploit differences in these errors to isolate and measure them separately. In that case, Equation (7.4) reduces to either (7.3) or (7.2), which are mathematically identical. Assuming this is the case, we briefly describe a spectrogram correction scheme that can be used for both errors. In order to account for the deviations represented by $\delta f(t)$, we rewrite the measured signal for a point focus at position x_o on the disk as a cosine whose phase argument consists of a linear component at the mean modulation frequency, f_o, and a small fluctuating component:

$$S(t) = \frac{1}{2} + \frac{1}{2}\cos\left(\Phi(t)\right), \tag{7.5}$$

$$\Phi(t) = 2\pi\left[f_o t + \delta f(t)\right] = 2\pi f_{\text{inst}}\, t \tag{7.6}$$

These measurements can be made by picking off the beam after the disk and integrating on a photodiode. The recorded signal, according to our model, should be the cosine function given in Eqn. (7.5). Once digitized, an FFT of this real-valued signal should produce positive & negative sidebands with conjugate spectral symmetry. A digital bandpass filter at the positive sideband generates a complex analytic signal, which is represented with the positive frequency component of the Euler expansion:

$$S_+(t) = \frac{1}{4}\mathrm{e}^{\mathrm{i}\Phi(t)} \tag{7.7}$$

In order to remove this fluctuation from the measurement, we first recognize that our digitized signal, after positive sideband filtering, is simply a vector of complex values. Based on Equation 7.7, the frequency components in our signal are available through $\Phi(t)$, which can be accessed numerically by isolating the phase component of the complex signal vector. In the case that $\delta f(t) = 0$, and a phase unwrapping algorithm is successful, then the phase term $\Phi(t)$ is a straight line with slope $2\pi f_o$. One way to measure deviations in frequency is to fit a line to the unwrapped $\Phi(t)$, and subtract it, leaving the deviation $\delta\Phi(t) = 2\pi\delta f(t)$. Another approach that bypasses phase unwrapping involves building a spectrogram through the use of the short-time Fourier transform (STFT). By sliding a window along $S_+(t)$, and computing the FFT of the

windowed time trace, the local instantaneous frequency can be extracted as the centroid of the frequency components present within the window at delay τ. Since instantaneous frequency can be accessed from the phase by taking the temporal derivative in Eqn. (7.6), it follows that the phase deviation can be computed from the instantaneous frequency, after subtracting f_o, by integration:

$$\delta\Phi(t) = 2\pi \int_0^t \delta f(t)\mathrm{d}t \tag{7.8}$$

Once $\delta\Phi(t)$ has been computed, it remains to use this information to apply a correction to the signal vector. In digitized form, our result can be applied as a conjugated phase to the measured signal:

$$S_+[t_n] = |S_+[t_n]|\mathrm{e}^{\mathrm{i}\angle S_+[t_n]} \times \mathrm{e}^{-\mathrm{i}\delta\Phi[t_n])} \tag{7.9}$$

$$= |S_+[t_n]|\mathrm{e}^{\mathrm{i}2\pi f_o t_n} \tag{7.10}$$

The corrected signal vector now has a linear phase, and therefore it's Fourier Transform will now display a narrower spectral linewidth at the modulation frequency f_o, as we will show in the next section.

7.3.4 Measuring Disk Errors: Joint Wobble & Velocity Corrections

To form a complete characterization of the modulator error, we need to measure $\delta v_r(t)$ and $\delta x(t)$. Fortunately, we can isolate the measurement of each in the lab. The mask mounting is a deterministic error that is the same for every rotation of the disk. Velocity fluctuations, however, are assumed to be stochastic, and need to be measured in tandem with every data acquisition.

To characterize the velocity fluctuations, we added a single-frequency encoder ring around the perimeter of the disk (visible in Figure 7.4). The width of the encoder track on the perimeter of the disk is wide enough to keep a point focus from walking out of its track due to any disk-mounting error. The encoder modulation frequency does not vary with radial position within

its track, and is therefore immune to disk-mount error. We monitored this encoder frequency with a tightly focused CW laser and a photodiode.

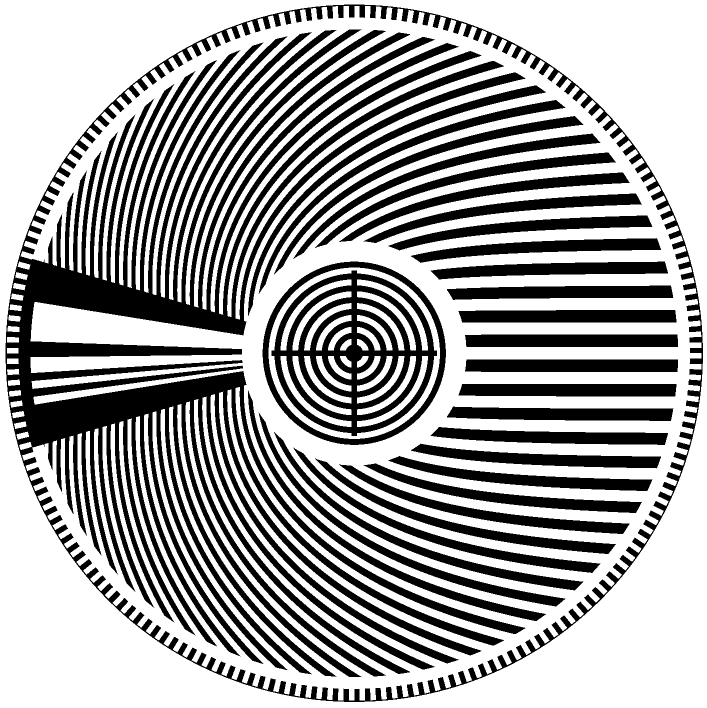

Figure 7.4: SPIFI disk with enhancements for error correction, including perimeter encoder for monitoring velocity fluctuations, 13 digit Barker sequence for precision retriggering, and cross-hair & bulls-eye for improved concentric mounting to chuck. Barker sequence & cross-hairs are enlarged, and encoder ring frequency & reticle chirp parameter are reduced, for easy visualization.

Experimentally, a third source of error in our disk modulator results from timing jitter in the trigger signal that starts data acquisition for each trace in a set. To counteract this, we printed a timing sequence on the far side of the disk, where the highest spatial frequencies are positioned on the reticle (Figure 7.4). These spatial frequencies were expendable, as they were higher than the cutoff frequency of our image relay system aperture. The timing sequence consisted of a set of length-13 Barker sequences, of varying sizes. Barker sequences were developed in order to generate autocorrelations with very low sidelobes relative to the peak. For a set of traces, the Barker sequence is windowed, and computationally autocorrelated with a stored reference

sequence. The temporal pixel shift in each trace was refined with a parabolic peak sub-pixel shifting algorithm, and then applied as a phase shift to the signal in the conjugate domain.

The joint measurement of wobble & velocity error is performed directly at the disk, bypassing any optical aberration in the microscope. Two laser foci were used; a point focus was generated on the SPIFI reticle to measure wobble, and a second point focus was generated on the encoder ring. Both modulated laser beams were picked off with mirrors after the disk, directed onto photodiodes, preamplified, and digitized. An ensemble of 100 time traces was acquired simultaneously in each channel. The motor used in our experiments was a feedback-stabilized brushless DC electric motor (Faulhaber, 2057S012BK1155). The feedback was generated by internal Hall sensors, and PID control was implemented with a paired external position & velocity controller (Faulhaber, MCBL3006),

The post-processing, performed in Matlab, proceeded as follows, for each encoder trace & SPIFI trace pair in the ensemble. First, the triggering errors were corrected using the Barker autocorrelation sequence in the SPIFI channel (Fig. 7.5(c)). Next, the fundamental carrier was isolated in each channel with an FFT and digital bandpass filter. For the encoder channel, a spectrogram was computed using the real part of each resultant complex time trace, the centroid frequency at each spectrogram delay was calculated, the carrier at 33 kHz was subtracted, and the resulting frequency deviation vector was turned into a time-varying phase with cumulative integration, as described in the previous section. This inverse phase was then applied to the SPIFI trace (Fig. 7.5(d)) before computing a spectrogram to track wobble frequency deviation.

Because the wobble correction scheme was previously published [101], we compare it's performance to that of the dual velocity and wobble correction scheme discussed here. These results are displayed in Fig. 7.5(e) - (h). In Fig. 7.5(e), the instantaneous frequency in each of the 100 SPIFI time traces is plotted in black, and then in gray for the velocity-corrected time traces. The mean instantaneous frequency for each case is then overlaid in cyan and red, respectively. The standard deviation for the two cases is plotted in Fig. 7.5(f). Adding the encoder informa-

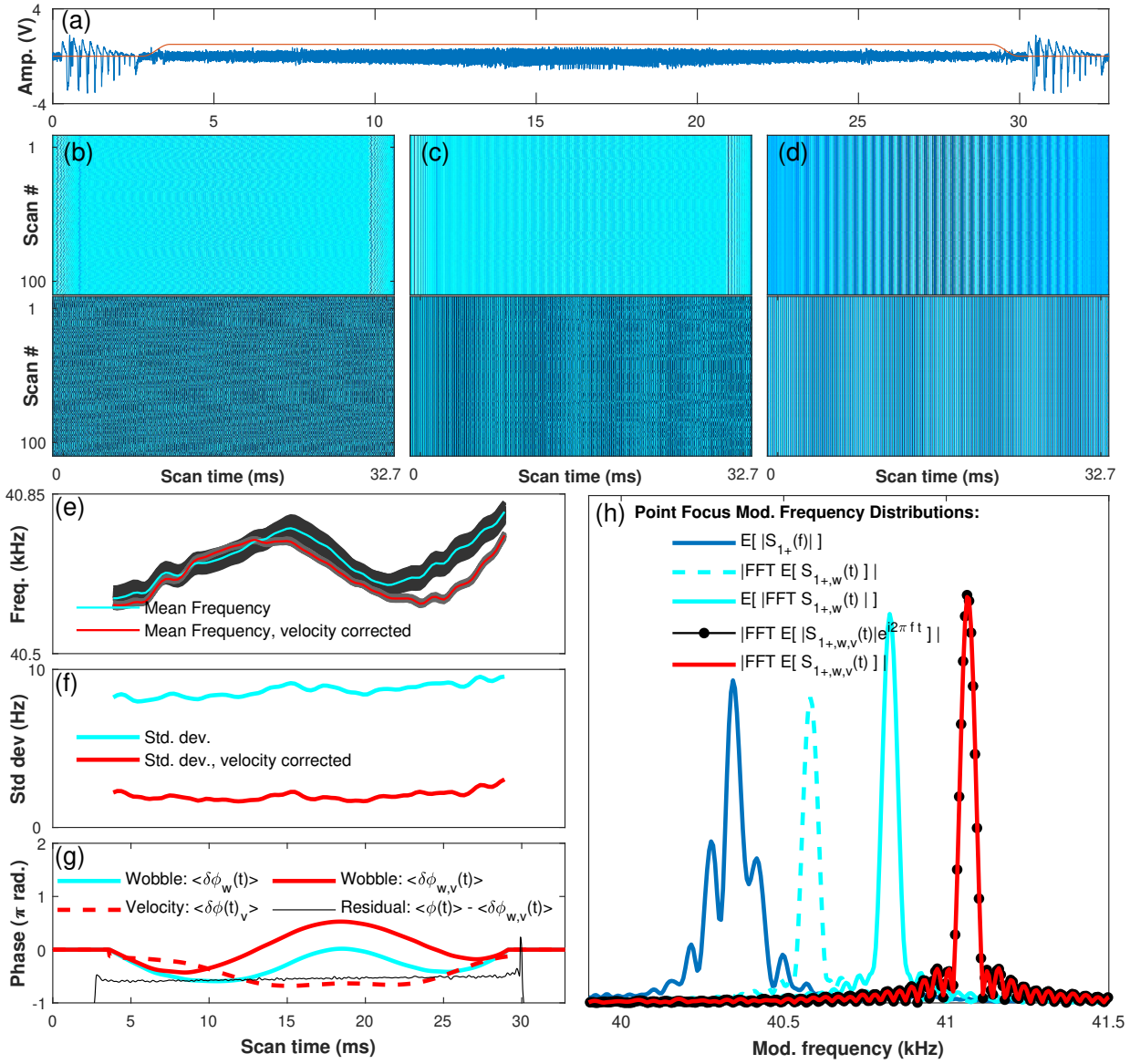

Figure 7.5: Mask Characterization Scheme. (a) A single time trace for a point focus on the SPIFI reticle, with Barker sequence visible on edges. (b) Ensemble of 100 traces for SPIFI (top) and encoder (bottom) channels. (c) Ensemble after retriggering using Barker sequence. (d) Ensemble after correcting for motor velocity fluctuations using encoder channel. (e) Computed instantaneous modulation frequency due to mask mounting error (wobble). Mean values are overlaid on results from each time trace. (f) Standard deviation from mean instantaneous frequency. (g) Accumulated phase computed from mean frequency variation. (h) Modulation frequency distributions: averaged raw data (blue), dewobbled & temporally averaged (cyan,dashed), dewobbled & Fourier averaged (cyan), dewobbled & deacclerated & temporally averaged (red), transform-limited distribution with a pure tone carrier (black dots), for the data in red. Distributions were offset from the carrier at 40.7 kHz for clarity. Using the mapping $x_o = f_o/(v_r \Delta_k)$, the 3 corrected datasets measure 22.2, 21.9, & 20.7 μm (FWHM), respectively.

tion to the wobble correction measurement reduces the standard deviation about the mean center frequency (≈ 40.7kHz) from approximately 9Hz to 2.5Hz. Therefore, the modulation frequency variation is reduced from a few parts in ten-thousand (0.0002-0.0003) to less than a part in ten-thousand (<0.0001). Meanwhile, a close look at the computed average phase corrections in Fig. 7.5(g) shows that there exists a deterministic velocity variation on every rotation of the disk, lying within the expected stochastic variations. This is likely due to the motor PID controller output in a steady state control cycle, accounting for fixed variations in the physical load distribution. Wobble correction without velocity correction (cyan) in fact measures both the wobble error and this deterministic component of the velocity deviation. Isolating the wobble error (solid red) by removing velocity error produces an intuitive measurement, where the modulation frequency excursion from disk mounting has the form of a single-cycle sinusoid, as expected since the disk must return to its starting point after one rotation. The residual phase (black) on the time trace after subtracting the two measured errors is quite flat, indicating all error has been removed.

The modulation frequency distribution due to the laser point focus on the disk, plotted in Fig. 7.5(h), provides a final verification of the joint correction scheme. The Fourier magnitude of the signal is displayed after varying levels of correction, showing reconstructed images of the laser spot size in a manner akin to point spread function measurements under varying degrees of aberration. The raw data is clearly corrupted with modulation labeling error (blue). For data with wobble correction only (cyan), the temporal mean over the ensemble (cyan, dashed) results in a lower image amplitude than taking the mean Fourier magnitude (cyan, solid), because velocity fluctuations (visible in Fig. 7.5(c)) create fringe jitter which in turn decreases the signal envelope when averaging. The jointly corrected data performs best (red). We have overlaid this result with the FFT of the same temporal envelope with a synthetic, pure carrier (black dots), showing that the dual correction scheme essentially obtains its transform limited distribution width. Using the mapping $x_o = f_o/(\nu_r \Delta_k)$, the 3 corrected datasets measure 22.2, 21.9, & 20.7 μm (FWHM), respectively.

In conclusion, we remark that our disk error correction schemes provide complementary improvements to the linearity of the projection-imaging scheme used in SPIFI, which in turn open the doorway to a cleaner SNR image reconstruction via temporal averaging. While we have used the modulation frequency perspective for this analysis, we can cast the two corrections schemes in terms of the projected spatial frequency as well. Velocity correction answers the question, "Which grating density was projected at time t?", whereas the wobble correction scheme answers the question, "Which grating phase was projected at time t?" Because SPIFI is predicated on a linear increase in both grating density and grating phase as a function of disk rotation, these corrections enable the FFT image reconstruction algorithm to generate images closer to its theoretical limits.

These results demonstrate the efficacy of our correction models, implemented by measuring laser beams in transmission with high SNR and low NA focusing at the disk. Despite the relatively small nature of these deviations, their correction produces sharper images. However, the advantage of this scheme becomes more pronounced when applied to data measured through the microscope, especially when looking at weak signals from fine features. We demonstrate this next.

7.4 Shot Noise in Single Pixel Imaging

Shot noise is a fundamental physical limitation in any imaging technique. For single-pixel imaging, shot noise has an enhanced role due to the spatial multiplexing of signal light $\beta(\mathbf{r})$ collected on a single pixel detector. Because light from all illuminated spatial positions is integrated on a single pixel, increased shot noise from bright sample locations is spread across all locations in the reconstructed image. This is a well-known fundamental issue with single pixel imaging. For example, it has also been observed in fluorescent imaging using radiofrequency-tagged emission (FIRE) [54], another imaging method that uses spatial frequency-modulated illumination to form images.

In SPIFI or FIRE, the noise floor in the modulation frequency (spatial) domain is determined by the shot noise from the time-averaged total light intensity measured on the photodetector,

$\overline{\langle\beta(\mathbf{r},t)\rangle_{\mathbf{r}}}$. In MP-SPIFI, each image order contributes a portion of this total light intensity, with an SNR scaling as $\langle\beta_q(\mathbf{r},t)\rangle_{\mathbf{r}} / \overline{\langle\beta(\mathbf{r},t)\rangle_{\mathbf{r}}}$. Since the best-resolved image orders (e.g. q=3 or q=4) also have the weakest amplitudes, there is ample motivation to improve SNR by enhancing signal or reducing noise. In our experimental results in the previous chapter, images of TPEF collected from HeLa cells truncated at second-order due to a large noise floor that restricted our ability to collect higher-order images. Images of SHG from rabbit tendon had a significantly larger SNR due to increasing the power of the illumination laser by ~50%, making the fourth-order signal detectable above the shot noise floor.

7.4.1 Ensemble averaging in a Poisson random process

For weak signals, it is often necessary to acquire a set of time traces and perform averaging to boost SNR. For example, the point spread functions presented in Figure 6.1, from our initial demonstration of MP-SPIFI [51], were computed from 1000 line images. The data processing protocol for experimental images in the prior chapter involved applying the wobble correction phase to each complex analytic signal vector in the ensemble, performing an FFT, and then averaging the magnitude of the FFT to generate an image. Averaging line images in the modulation frequency (spatial) domain reduced the variance of the shot noise floor, but did not lower its DC level.

We subsequently found that averaging measurement data in the time (spatial frequency) domain reduces both the variance *and* the DC level of the noise floor, resulting in improved SNR for higher-order SPIFI images. In order to achieve this, motor velocity error had to be corrected, or else fringes in the temporal waveforms would wash out upon averaging over an ensemble. This was the primary motivation for characterizing disk velocity error.

To understand the difference in the DC level of the ensemble-averaged spatial-domain noise floor, it is helpful to consider a SPIFI measurement to be a random process. Each time increment sampled by the digitizer integrates the photons collected from the physical interaction of projecting one angular increment of the disk onto the sample. The overlap integral of the sample and the k^{th} projection is a unique random variable, $\mathbf{S}[t_k]$ with rate value, α_k. The reason for

assigning randomness to the collected signal photon count in digitizer period T is fundamentally related to the quantized nature of the electromagnetic field. Photon arrival times - even for a uniform classical field - at an optical detector are not perfectly uniform; rather, the exact time period between successive arrivals exhibits random fluctuation. The Poisson probability distribution can be derived from this model of random behavior. For our optical detector, it describes the probability of counting n photons in a time period T:

$$P(n,T) = \frac{(\alpha T)^n \mathrm{e}^{-\alpha T}}{n!} \tag{7.11}$$

The SPIFI time trace is thus a sequence of Poisson random variables, which forms a Poisson random process. In SPIFI, the image lies in the Fourier transform of the collected time trace, and as such, it is a transformation over the entire Poisson process. Deriving a best estimate of the Fourier transformed random process is a very complicated task. Instead, it is much simpler and more intuitive to work with each Poisson random variable directly, in the time domain, where their properties are easily exploited. One useful property of the Poisson distribution is that the maximum-likelihood estimate of an independent & identically distributed (i.i.d.) sampling of a Poisson random variable is simply given by the sample mean [102]. For SPIFI, this means that averaging an ensemble of i.i.d. time traces, in the time domain, will produce an ML estimate of the measured value for each time increment. While this is not the ML estimate of the *object* we wish to reconstruct, computing the MLE of the measurement nevertheless maps into an object reconstruction with improved noise rejection. The physical intuition for this is clear - by reducing an ensemble of time traces to its MLE at each time point, corresponding to an average of each column in Figure 7.5(d), we reduce the noise present in the time trace. For Poisson-distributed shot noise, which has a uniform spectral distribution, we have effectively lowered the DC-level of this uniform spectral noise at every frequency bin in our digitized spectrum.

7.4.2 PSF noise reduction aided by disk error correction

To illustrate the difference in ensemble averaging of the measurement data as opposed to the reconstructed images, we refer the reader to point spread function data in Figure 7.6. The left-hand column displays second harmonic generation (SHG) point spread functions measured with a $200\mu m$ Barium Titanate ($BaTiO_2$) particle as the point emitter. For this measurement, 100 time traces were acquired. The reconstructed PSFs for the image orders $q = 1-4$ are plotted for the two different ensemble averaging schemes. While there is not much difference for the brighter image orders (e.g. $q = 1$ and $q = 2$), when we look at the higher image orders (e.g. $q = 3$ and $q = 4$) the effect of the reduced DC noise floor using measurement-domain averaging is evident.

For this data, the ability to average SPIFI traces in the temporal domain is predicated on the experimental ability to minimize or remove stochastic timing error between traces in the ensemble. Our experiment produces two forms of temporal error - motor velocity fluctuations, and trigger jitter. Deviations in the timing of the rapidly varying carrier frequency from trace to trace can result in deconstructive interference when ensemble members are added together. At the wings of the time trace, this is especially problematic, since a reduction in the mean envelope amplitude directly equates to a decrease in high spatial frequency support - and thereby, a loss in image resolution. The experimental goal is, therefore, to improve SNR through temporal averaging, while being careful not to lose sample spatial frequency information by poor handling of stochastic temporal fluctuations. We applied the same error correction scheme described in Section 7.3. The wobble phase error, being a deterministic error, was computed and saved to file. The illumination laser was once again focused to a line at the disk, and relay imaged to the microscope sample plane for SPIFI imaging. The encoder ring was measured simultaneously by a CW laser on a second channel, and recorded without passing through the microscope. The modulation frequency deviation due to motor velocity was computed for each SPIFI time trace using the encoder trace, in the exact same manner as described for the wobble measurement. After correcting the trigger & velocity error for each complex SPIFI time trace,

the traces were averaged in time, followed by multiplication with the stored wobble correction phase.

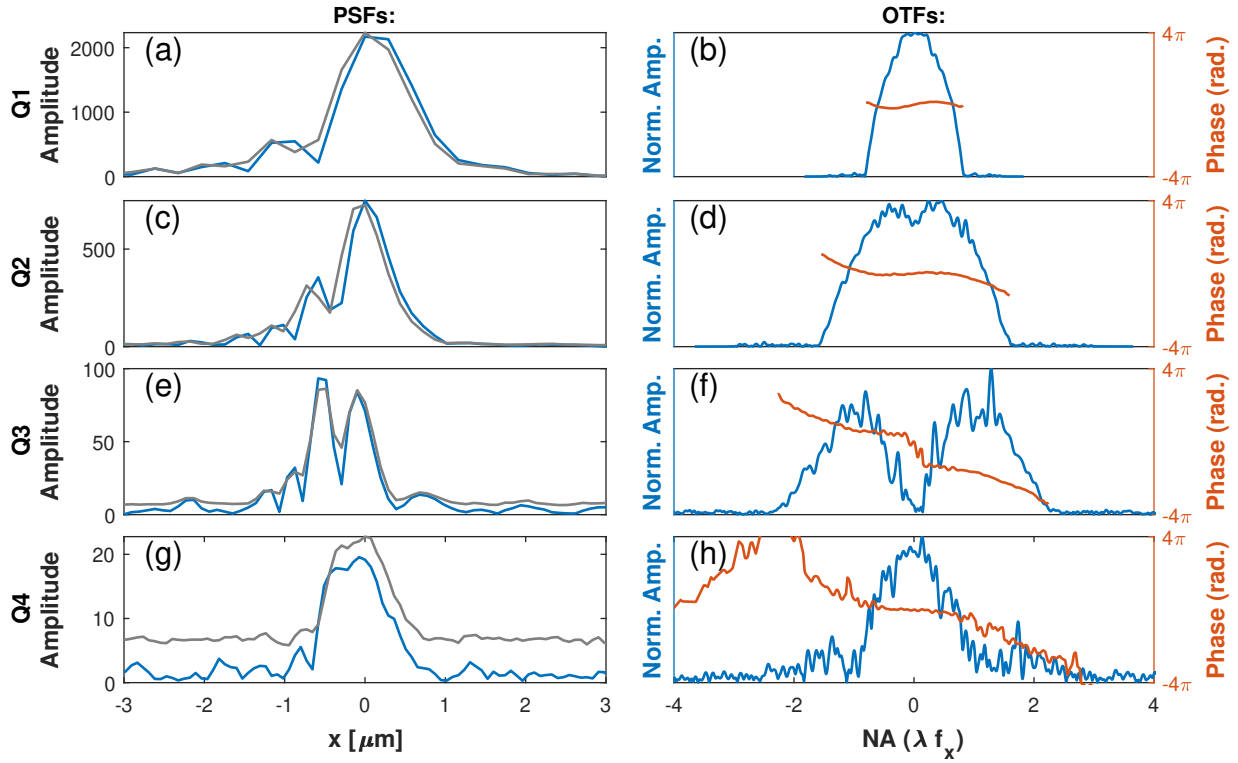

Figure 7.6: Second Harmonic Generation Point Spread Functions for MP-SPIFI. Data is an average of 100 traces. The PSF and the corresponding complex OTF from which it was derived are plotted for each image order, Q. In the left column, the gray trace is the wobble-corrected PSF computed without velocity correction, averaged in the modulation frequency (image) domain, whereas the blue trace is the wobble- and velocity-corrected trace, averaged in the time (spatial frequency) domain. Temporal averaging reduces the noise floor, which is most noticeable for high-order images with low peak amplitudes. In the right hand column, the optical transfer function's magnitude and phase is plotted for each fully-characterized PSF.

We note in passing that one could equivalently acquire data by performing stop-and-hold for each angular increment on the mask, and digitizing the noisy DC output signal at some sampling rate to produce N independent & identical distributed (i.i.d.) realizations of the random variable $\mathbf{S}[t_k]$. This would bypass issues with triggering and velocity, with the tradeoffs of acquisition speed, drift, and greater exposure to low-frequency noise [56].

7.5 Binary Printing and Higher-order Diffraction

While the improvements in signal-to-nose ratio and modulation-frequency labeling error demonstrated above are quite helpful, an inspection of the point spread functions in Figure 7.6 demonstrate additional issues with our imaging scheme. In theory, each additional image order, Q, should display finer resolution than the previous. This appears true looking from the first-order image to the second (Q1 to Q2). However, we see in panel (c) that the third-order image, Q3, has a bifurcated nature, which upon convolution with the object, will reveal distorted imaging (see Figs. 6.2, 6.3 for example of this). The fourth-order image, Q4, is clearly less well-resolved than even the second-order image. In this section, we form a link between the binary printing pattern of our modulator disk, and the PSF distortions visible in standard MP-SPIFI images. We also introduce a spatial filtering technique that can be used to remove these distortions.

Before proceeding, we also note the presence of coma in the PSFs in Figure 7.6. We attribute this to optical aberration in the $4f$ image relay system, as it was not present in measurements at the disk (Fig. 7.5). Optical aberrations are discussed in Sec. 7.6. For the discussion of binary mask diffraction in this section, we will focus on the width of the main lobe in the PSFs.

In Chapter 3 we formed an analysis of our binary modulator that cast the transmitted field in terms of a set of odd-harmonic diffracted orders. The a_j amplitude coefficients for the first diffracted orders, computed using Eqn. (3.25), are listed in Table 7.1. Of particular importance is the negative sign on the third diffracted orders. We shall see that even though the overall intensity in the third diffracted orders is very weak ($|a_3|^2 = .011$), the fact that they mix with the strong zero order creates a strong impact on the Q=3 and Q=4 OTFs. The negative sign causes zero-crossings in these OTFs, which map into modulations in the magnitude of the PSFs.

The point spread functions for each image order for the microscope discussed in Ch. 6, computed using the vector field model (section 3.3.6), are plotted in Fig. 7.7. Each PSF has been demodulated from its sideband, and normalized.

Table 7.1: Fourier series harmonic amplitudes (up to $j = 5$) for a 50% duty cycle binary periodic structure.

j	0	1	2	3	4	5
a_j	$\frac{1}{2}$	$\frac{1}{\pi}$	0	$\frac{-1}{3\pi}$	0	$\frac{1}{5\pi}$
a_j^2	0.25	0.101	0	0.011	0	0.004

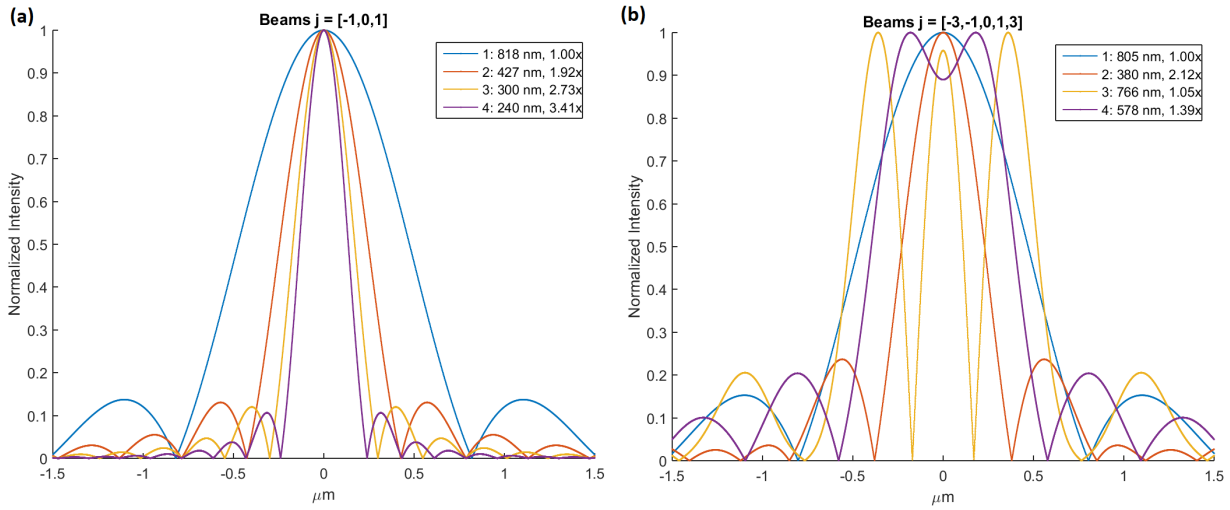

Figure 7.7: Point spread functions computed using the Debye integral with y-polarized light. Left Panel: the PSF for each image order Q, where the imaging system passes only the zero-order and first-order diffracted beams from the mask. Right Panel: PSFs including third-diffracted order beams, corresponding to the experimental situation in [51]. The half-width at the first zero is listed for each PSF, and the relative enhancement to the Q1 PSF.

7.5.1 Diffracted Order Amplitudes

We can generalize Eqn. (3.25) to account for the case where the binary mask pattern contains a duty cycle other than 50%. The coefficients for each Fourier series component are then given by the equation:

$$a_j(\Delta) = \Delta \,\mathrm{sinc}(j\,\Delta), \quad j \in \mathbb{Z} \tag{7.12}$$

where Δ is the square wave duty cycle. Practically, the series can be truncated at an N^{th} order, above which the amplitude coefficients become vanishingly small relative to the measurement noise floor. As expected, the decomposition of a square wave is comprised of odd harmonics of the fundamental. The final row in Table 7.1 is a measure of how much energy is carried

away in each diffracted order. Note that only half of the total energy incident on the mask is transmitted, while the rest is lost to reflection - a significant motivation for the laser sources described in Ch. 5. An analysis of the effect of diffracted orders $j > 1$ is discussed in the next section, including the interesting effect of changing the signum function threshold, which is equivalent to changing the duty cycle of the periodic binary printed pattern.

7.5.2 PSF Engineering with Mask Duty Cycle

The coefficients $H_q(t)$ in Eqn. (3.113) each contain a linear combination of amplitude and window products for all of the pair-wise plane wave combinations, $v_j^* v_k$, that produce an intensity modulation oscillating at the q^{th} harmonic. To demonstrate this, Table 7.2 lists the H_q terms for the two cases of linear and 2-photon excitation ($\eta = 1,2$), respectively, and where the number of beams is limited to the case of $j = \{-1,0,1\}$. We have replaced the binary gating function Π_{x_j} with a 'relaxed' gating function u_j, which can represent a window with softer edges, such as a raised-cosine or super-Gaussian shape. This is justified on the grounds that the scalar model doesn't account for depolarization or vignetting through the objective lens, which reduce the amplitude at scan times near the cutoff.

Table 7.2: Optical Transfer Functions, $H_q(t)$ for a SPIFI microscope with only the diffracted orders $j = \{-1,0,1\}$ propagating to the sample plane. Col. (1): Linear Excitation, $\eta = 1$. Col. (2): Two-Photon Excitation, $\eta = 2$.

	(1) $\eta = 1, N = 1$	(2) $\eta = 2, N = 1$
$H_0(t)$	$a_0^2 + 3\,a_1^2\,u_1^2(t)$	$6a_1^4 u_1^4(\mathrm{t}) + 12a_1^2 a_0^2 u_1^2(\mathrm{t}) + a_0^4$
$H_1(t)$	$4\,a_0\,a_1\,u_1(t)$	$24a_1^3 a_0 u_1^3(\mathrm{t}) + 8a_1 a_0^3 u_1(\mathrm{t})$
$H_2(t)$	$a_1^2\,u_1^2(t)$	$8a_1^4 u_1^4(\mathrm{t}) + 12a_0^2 a_1^2 u_1^2(\mathrm{t})$
$H_3(t)$	0	$8a_0 a_1^3 u_1^3(\mathrm{t})$
$H_4(t)$	0	$2a_1^4 u_1^4(\mathrm{t})$

In the linear case, it is easy to see by examination of the coefficients a_j that the first cosine term is due to the interference between each of the first diffracted orders with the zero order,

whereas the second cosine term is due to interference between just the first diffracted orders. In the nonlinear case, it is a bit more complicated, as squaring the linear intensity mixes contributions from the three beam pairs into various cosine terms.

What is the effect of including higher diffracted orders $|j| > 1$ on the set of images $S_q(x)$? The degree of impact depends on the unique transfer function, $H_q(f_x)$, for each image band. Let us examine the 3rd and 4th harmonic images, for the case of a second-order nonlinearity ($\eta = 2$), as a case study in the effects of higher order diffraction. For simplicity, we will expand our collection of beams to include 3rd order diffraction only, so that $N = 3$ in Eqn (3.113). This is justified since, in practice, 5th order beams were not detected experimentally, as they did not have enough appreciable energy to be detected above the noise floor. The nonlinear intensity $I^2(\mathbf{r}, t)$ now has components at integer multiples of the carrier up to $12\nu_o$, since $2\eta N = 12$. The resultant OTFs are listed in Table 7.3:

Table 7.3: Optical Transfer Functions, $H_q(t)$ for MP-SPIFI with a Two-Photon Excitation, $\eta = 2$, and diffracted orders $j = \{-3, -1, 0, 1, 3\}$ from a 50% duty cycle modulator.

H_0	$6a_1^4u_1^4(\mathrm{t}) + 8a_1^3a_3u_1^3(\mathrm{t})u_3(\mathrm{t}) + 24a_1^2a_3^2u_1^2(\mathrm{t})u_3^2(\mathrm{t}) + 12a_1^2a_0^2u_1^2(\mathrm{t}) + 6a_3^4u_3^4(\mathrm{t})$ $+12a_3^2a_0^2u_3^2(\mathrm{t}) + a_0^4$
H_1	$24a_1^3a_0u_1^3(\mathrm{t}) + 24a_1^2a_3a_0u_1^2(\mathrm{t})u_3(\mathrm{t}) + 48a_1a_3^2a_0u_1(\mathrm{t})u_3^2(\mathrm{t}) + 8a_1a_0^3u_1(\mathrm{t})$
H_2	$8a_1^4u_1^4(\mathrm{t}) + 24a_3a_1^3u_1^3(\mathrm{t})u_3(\mathrm{t}) + 24a_3^2a_1^2u_1^2(\mathrm{t})u_3^2(\mathrm{t}) + 12a_0^2a_1^2u_1^2(\mathrm{t}) + 24a_3^3a_1u_1(\mathrm{t})u_3^3(\mathrm{t})$ $+24a_0^2a_3a_1u_1(\mathrm{t})u_3(\mathrm{t})$
H_3	$8a_1^3a_0u_1^3(\mathrm{t}) + 48a_1^2a_3a_0u_1^2(\mathrm{t})u_3(\mathrm{t}) + 24a_3^3a_0u_3^3(\mathrm{t}) + 8a_3a_0^3u_3(\mathrm{t})$
H_4	$2a_1^4u_1^4(\mathrm{t}) + 24a_3a_1^3u_1^3(\mathrm{t})u_3(\mathrm{t}) + 12a_3^2a_1^2u_1^2(\mathrm{t})u_3^2(\mathrm{t}) + 24a_3^3a_1u_1(\mathrm{t})u_3^3(\mathrm{t})$ $+24a_0^2a_3a_1u_1(\mathrm{t})u_3(\mathrm{t})$
H_5	$24a_0a_3a_1^2u_1^2(\mathrm{t})u_3(\mathrm{t}) + 24a_0a_3^2a_1u_1(\mathrm{t})u_3^2(\mathrm{t})$
H_6	$8a_1^3a_3u_1^3(\mathrm{t})u_3(\mathrm{t}) + 24a_1^2a_3^2u_1^2(\mathrm{t})u_3^2(\mathrm{t}) + 8a_3^4u_3^4(\mathrm{t}) + 12a_0^2a_3^2u_3^2(\mathrm{t})$
H_7	$24a_0a_1a_3^2u_1(\mathrm{t})u_3^2(\mathrm{t})$
H_8	$12a_1^2a_3^2u_1^2(\mathrm{t})u_3^2(\mathrm{t}) + 8a_1a_3^3u_1(\mathrm{t})u_3^3(\mathrm{t})$
H_9	$8a_0a_3^3u_3^3(\mathrm{t})$
H_{10}	$8a_1a_3^3u_1(\mathrm{t})u_3^3(\mathrm{t})$
H_{11}	0
H_{12}	$8a_1^3a_3u_1^3(\mathrm{t})u_3(\mathrm{t}) + 24a_1^2a_3^2u_1^2(\mathrm{t})u_3^2(\mathrm{t}) + 8a_3^4u_3^4(\mathrm{t}) + 12a_0^2a_3^2u_3^2(\mathrm{t})$

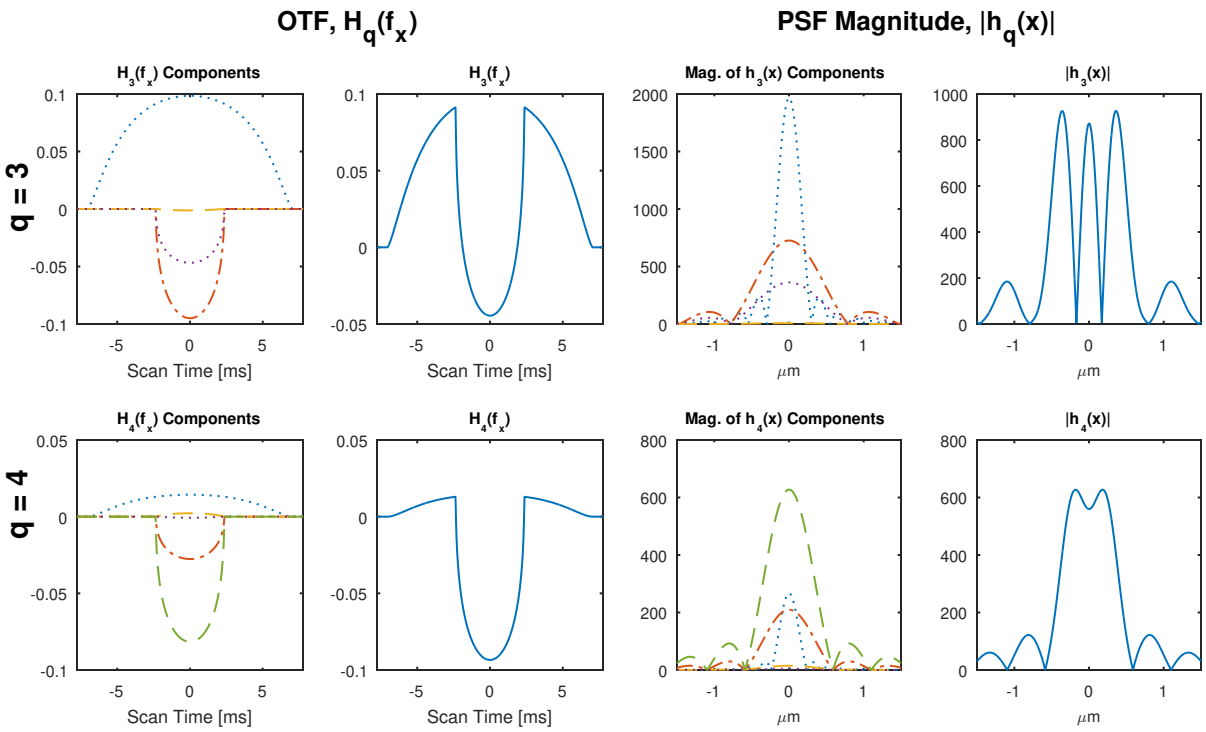

Figure 7.8: Point Spread Functions for SPIFI image orders $q = 3$ and $q = 4$, as calculated by a numeric model, for the scenario of a 50% duty cycle mask, with up to third-diffracted order beams imaged onto the sample ($N = 3$), and a 2nd order nonlinear optical interaction ($\eta = 2$). The individual terms plotted in the first panel for each image order correspond to each term in the linear sum of $H_3(f_x)$ and $H_4(f_x)$, given in Table 7.3. The spatial axis for each PSF is downshifted and appropriately rescaled by q. Experimental parameters such as wavelength, objective lens, and mask parameter Δk were drawn from the experiment described in Ref. [51]. Reprinted from Ref. [62] with permission.

We see that given the nonlinearity and the number of diffracted beams, many beam pairs $v_j^* v_k$ can contribute to a given optical transfer function. In Figure (7.8), we have plotted the transfer functions and point spread functions for the two images, $S_3(x)$ and $S_4(x)$, for the case of a 50% duty cycle mask. The first panel in each case plots the contribution from each of the terms in the linear sum comprising $H_q(f_x)$; the second panel displays the sum. Similarly, the third panel displays the magnitude of the Fourier transform for each component, and the final panel displays the magnitude of the complete point spread function.

There are two main observations we can make about this example. First of all, we see that the presence of the $j = \{-3, 3\}$ beams serves to distort images $S_3(x)$ and $S_4(x)$, by producing

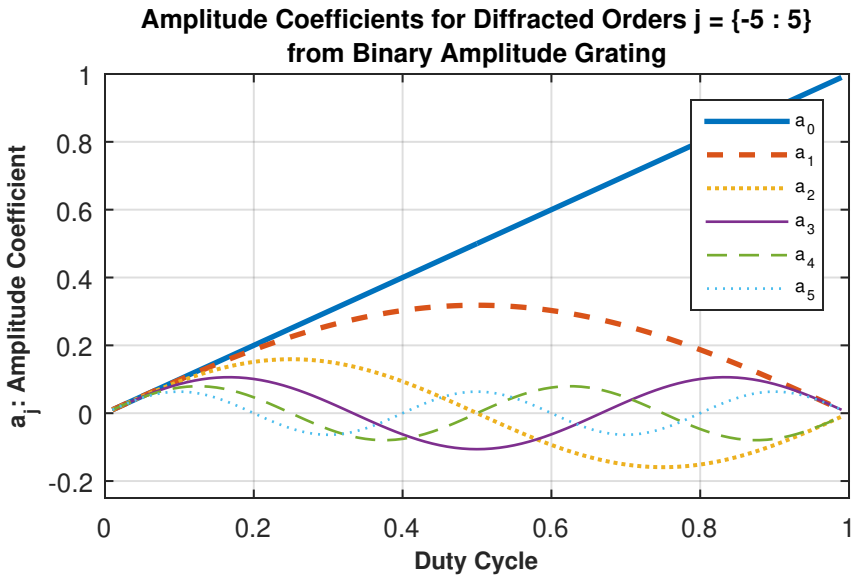

Figure 7.9: Diffracted order beam coefficients as a function of duty cycle. Implementation of Eqn. (7.12). Reprinted from Ref. [62] with permission.

extra modulations in the point spread functions. This can be traced directly back to the negative sign of the $j = \{-3,3\}$ fields, imparted by the mask. We see how the combination of positive and negative terms in H_3 and H_4 generate overall OTFs that have zero crossings. These zero crossings then map to point spread functions, $|h_3(x)|$ and $|h_4(x)|$, that have modulations in their main lobes. The case of $|h_3(x)|$ looks especially troublesome for imaging.

A natural question arises: can one engineer the mask to remove the negative sign in diffracted beams contributing to certain images? To investigate this, we extended our model to account for custom specification of the mask duty cycle. Varying the duty cycle does not change the fundamental modulation frequencies for each radial circle on the mask, but it does alter the Fourier coefficients needed to synthesize that binary pattern. The diffracted order beam coefficients, calculated from Eqn. (7.12), are plotted in Figure (7.9) as a function of duty cycle. Note that we define a high duty cycle as transmitting more than half of the light incident on the grating, meaning that the printed chrome covers $< 50\%$ of the cycle.

Five duty cycles were chosen for investigation - 25%, 33%, 50%, 67% and 75% - because they each extinguish at least one of the the first four diffracted beams: whereas the 50% duty

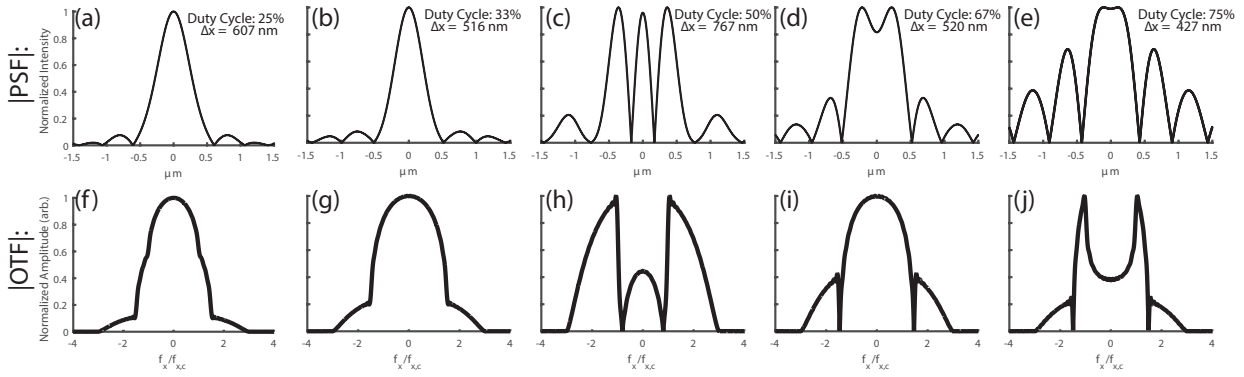

Figure 7.10: PSFs and OTFs for SPIFI image order q = 3, as a function of mask duty cycle, with diffracted orders N = 3 and nonlinearity $\eta = 2$. Duty cycles are: (a) 25%, (b) 33%, (c) 50%, (d) 67%, and (e) 75%. Reprinted from Ref. [62] with permission.

cycle mask extinguishes even orders, the 33% and 67% masks extinguish every third order, and the 25% and 75% duty cycles extinguish every fourth order. It turns out that the lower duty cycle masks maintain positive coefficients on the first 3 diffracted orders. Another nice practical feature of the lower duty cycle masks is that the zero-order beam has lower amplitude, which should lower its dominating shot noise contribution in an experimental setup. $|H_3(f_x)|$ and $|h_3(x)|$ are plotted in Figure (7.10) for these five cases.

We see in Figure (7.10) a wide variability in the PSF and OTF for the same SPIFI image, q = 3. The 50%, 67%, and 75% duty cycle cases have OTFs with negative contributions from a_j coefficients. These OTFs in turn produce PSFs with central lobe modulations and relatively large sidelobes. In contrast, the 25% and 33% masks produce only non-negative a_j coefficients for the included beams, $|j| \leq 3$. As one would expect, the linear sum of terms comprising H_3 adds constructively, and the point spread functions $h_3(x)$ have smooth central lobes and relatively small sidelobes. However, it should be noted that while removing negative a_j coefficients from the system smooths out the PSFs, the resolution offered by the PSF is not as fine as the PSF due to the first diffracted orders alone. This is because each successively higher diffracted order has a progressively faster transit across the pupil. For example, let us consider the 33% duty cycle case, which produces diffracted orders $j = [-2,-1,0,1,2]$, but $a_3 = 0$. Although both the

$j = \pm 1$ and $j = \pm 2$ orders sweep through the entire lateral spatial frequency range of the pupil, the $j = \pm 2$ orders exit the pupil at a time when the $j = \pm 1$ beams are still only 2/3 the way from pupil center to pupil edge. The resultant coherent addition of signal from the $j = \pm 2$ orders to the signal from the $j = \pm 1$ orders is a lump in the middle two-thirds of the total scan. This is evident in Figure 7.10(g). The scan envelope, which is directly related to the OTF, appears to have increased information in the middle relative to the wings, and therefore its Fourier Transform results in a PSF that is not as narrow as the case of the $j = \pm 1$ beams alone, where the signal envelope is somewhat flatter across the entire span. Consequently, point spread functions produced with multiple diffracted orders, even with all positive a_j coefficients, are not as narrow as those produced by the $j = \{-1, 0, 1\}$ beams alone. For the experimental system in Ch. 6, with a 50% duty cycle mask and the assumption of no diffracted orders beyond $j = \pm 1$, we numerically calculate a theoretical resolution of 300 nm for SPIFI order q =3. In contrast, the 25% and 33% duty cycle masks presented here, where we explicitly include orders $|j| > 1$, have theoretical resolutions of 607nm and 516nm, respectively.

In conclusion, we present a means of selectively tuning a SPIFI binary reticle in order to shape the various point spread functions that are simultaneously present in a multiphoton SPIFI microscope. We find that suppressing diffracted orders with negative coefficients can be quite helpful in constructing smooth, localized point spread functions. While the total elimination of diffracted orders greater than $j = \pm 1$ offers a pathway to the narrowest super-resolved point spread functions that MP-SPIFI can currently offer, the exertion of duty cycle control offers a powerful tool for ensuring clean point spread functions in the presence of higher diffracted orders from a binary printed mask.

7.5.3 PSF Engineering with Spatial Filtering

An alternative approach to improved point spread function behavior in MP-SPIFI makes use of a spatial filter to remove unwanted diffracted orders from the mask. This idea is represented in Figure 7.11, where we plot the intensity distribution in an image conjugate plane to the objective's back aperture, for the system described in [51]. We placed an adjustable mechanical

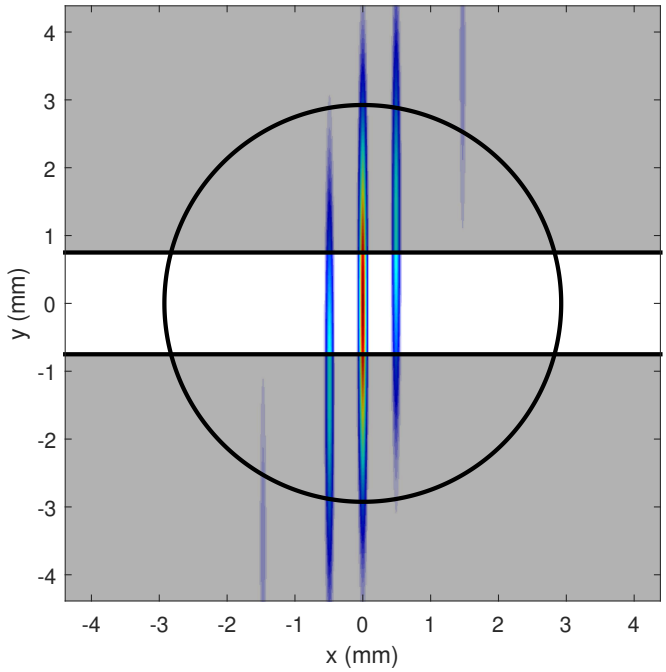

Figure 7.11: Spatial filter in system pupil plane for removing unwanted diffracted orders. Intensity of diffracted orders is plotted at scan time $t = 2$ ms for the system described in [51]. Black circle represents the demagnified image of the objective lens' back aperture. Shaded gray boxes represent mechanical beam stops.

slit (VA100, Thorlabs) in this plane to reject higher diffracted orders from the mask ($|j| \geq 2$). We note that in this case, the mask contains a standard 50% duty cycle, and therefore only odd diffracted orders are present. The spatial filter acts in the y-dimension only, ensuring that the first diffracted orders still scan out to the full NA of the objective lens in x. We exploit the fact that each diffracted order's center position has a fixed vertical offset that scales with order, j, in order to remove these orders for all scan times, as the diffracted beams only translate horizontally with the polar-coordinate modulator we use.

Point spread function measurements using 200nm Barium-titanate particles are displayed in Figures 7.12 & 7.13. In the first dataset,the slit is blocking some, but not all, of the third diffracted orders. We see that the contribution of the third diffracted orders (j=3) to the third image image order (Q=3) is reduced, as the bifurcated nature of the PSF has given way to a sin-

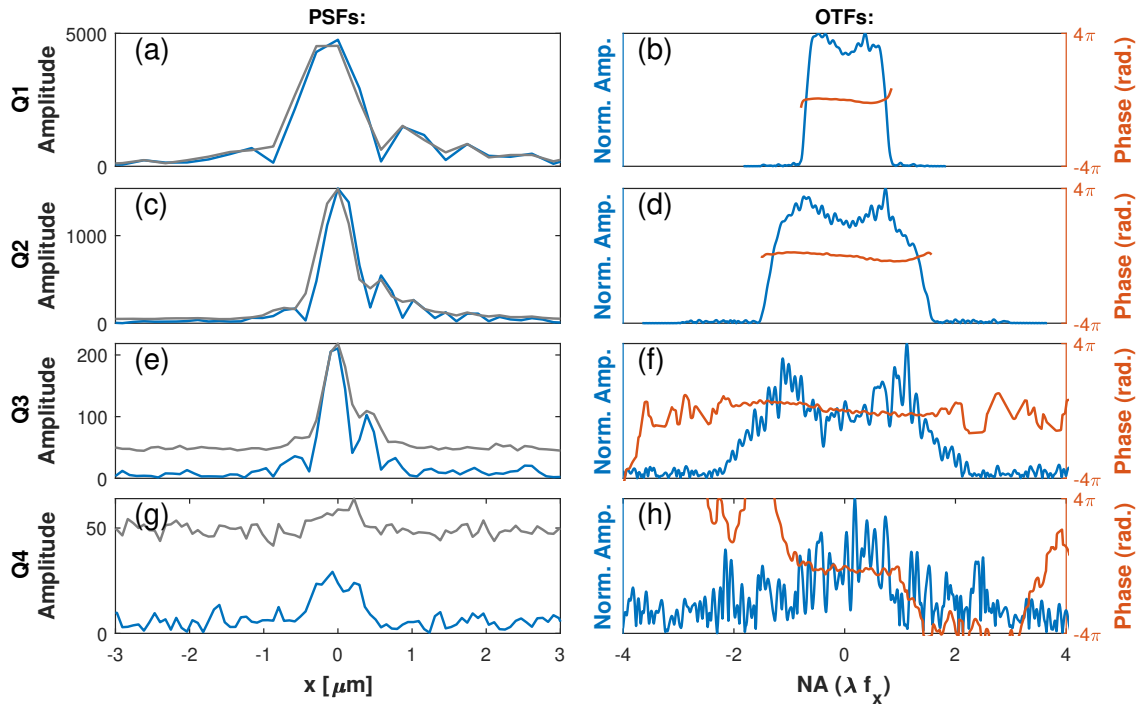

Figure 7.12: Second Harmonic Generation Point Spread Functions for MP-SPIFI, with 3rd diffracted orders partially rejected by spatial filter. Data is an average of 100 traces. The PSF and the corresponding complex OTF from which it was derived are plotted for each image order, Q. In the left column, the gray trace is the wobble-corrected PSF computed without velocity correction, averaged in the modulation frequency (image) domain, whereas the blue trace is the wobble- and velocity-corrected trace, averaged in the time (spatial frequency) domain. FWHM values are 841nm, 370nm, & 339 nm for the Q1-Q3 PSF distributions.

gle main lobe width narrower than the Q=2 PSF. The fourth-order image, Q4, is barely visible due to the intensity loss from the slit, but we do see at least a small signal thanks to the temporal averaging scheme. However, it does not appear to achieve narrower resolution, as it is still corrupted by the strong influence of j=3 beams mixing with the j=0 beam. Recalling Figure 7.8, where the lower-left panel shows the relative impact of each beam pair contributing to the Q4 image in the unfiltered microscope, we see that the components formed with j=3 beams exist over a shorter scan time, but have a stronger magnitude than the single term contributed by the mixing of the j=±1 beams. Further evidence of the lingering presence of the j=3 beams is visible in the amplitude of the OTFs, where we see a small dip in the middle third of the distribution -

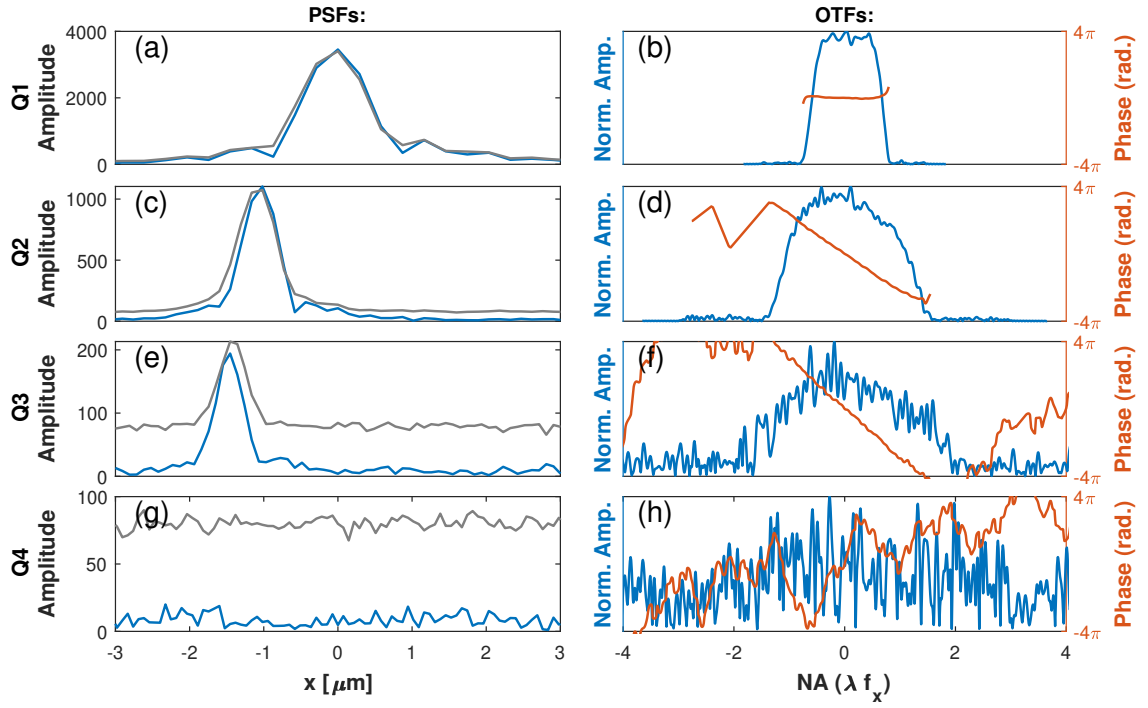

Figure 7.13: Second Harmonic Generation Point Spread Functions for MP-SPIFI, with 3rd diffracted orders fully rejected by spatial filter. Clean PSFs for images order q = 1-3 result. Moreover, PSF width scales with q as in the ideal case given by Equation (3.119). However, object information in the signal for image order q = 4 is too weak to detect. Data is an average of 100 traces of the same point emitter used in Fig. 7.12. Lateral shifts of the point spread functions with q are due to a small error in the demodulation frequency applied.

direct evidence of both the negative sign and the quicker scan duration of the third diffracted orders passing through the system pupil.

By reducing the slit width further, we can completely extinguish the third diffracted orders. The PSF dataset in Fig. 7.13 demonstrates this. The dip in the OTFs has disappeared, and the PSFs for Q1 through Q3 have a smooth envelope extending to 1x, 2x, and 3x the NA of the lens, and clean PSFs that narrow with order as in the ideal case presented by Equation (3.119). However, the Q4 PSF has disappeared completely, indicating that the system SNR is too weak to see the single contributing term from the j=±1 diffracted orders. We see that a tradeoff for such aggressive spatial filtering is a reduced nonlinear excitation capability. A smaller slit means less transmitted laser energy, and a softer line focus at the sample. These effects act in concert to lower the available peak power. The heavy losses in MP-SPIFI at the disk and the spatial fil-

tering plane motivate the need for higher average power, higher peak power laser sources that can perform nonlinear line-geometry imaging with sufficient peak power. These efforts were discussed in Chapter 5.

7.6 Optical Aberration in the 4f Image Relay

Another systematic error is traditional optical aberration in the 4-f image relay system. In this case, the imaging system, including lenses, coverslip, and sample mounting medium, can impart small shifts in the one-to-one mapping from object space (the mask) to image space (at the sample). In SPIFI, the cosine projections across x that are used to gather x image information are sensitive to aberrations such as coma. We will now show how these aberrations in the x dimension are encoded in MP-SPIFI measurements and can be corrected for with a point spread function measurement.

Aberration can be modeled as an additional spatial map applied to the field in the back aperture of the objective lens. For MP-SPIFI, we recall the diffracted fields in the pupil plane of the 4f image relay, given by Equation (3.33), and tack on an horizontal aberration phase term in scaled pupil coordinates so that it corresponds to the CTF: $\phi_a(x_p/\lambda f_1)$:

$$E_{j,p} = \quad \frac{1}{\mathrm{i}\lambda f_1}\Pi_{m_j} a_j \mathrm{e}^{\mathrm{i}2\pi j f_{g_x}(t)\, x_o} \hat{E}_i\left(\frac{x_p}{\lambda f_1} - j f_{g_x}(t)\,, \frac{y_p}{\lambda f_1} - j f_{g_y}\right) \mathrm{e}^{\mathrm{i}\phi_a(x_p/\lambda f_1)} \tag{7.13}$$

For simplicity, we will use the scalar model in which the field transferred to the focal plane of the objective lens is unobstructed by the pupil (Eqn. (3.56)). Moreover, we will ignore the spatial profiles of the field and simply utilize the plane wave components. Thus $\hat{E}_i(x,y) = \delta(x)\delta(y)$, and $E_{j,p} \to \upsilon_{j,p}$. Invoking Eqn. (2.79) to transfer the field to the focal plane of the objective lens, which has focal length f_2:

$$\upsilon_{j,s}\left(x_s, y_s, t\right) = \frac{1}{\mathrm{i}\lambda f_2}\int_{x_p}\int_{y_p} \upsilon_{j,p}\left(x_p, y_p, t\right) \mathrm{e}^{-\mathrm{i}2\pi\left[\frac{x_s}{\lambda f_2}x_p + \frac{y_s}{\lambda f_2}y_p\right]} \mathrm{d}x_p \mathrm{d}y_p \tag{7.14}$$

$$= -\frac{f_1}{f_2} a_j \Pi_{x_j} \mathrm{e}^{\mathrm{i}2\pi j\left[f_{g_x}x_o - \frac{f_1}{f2}f_{g_x}x_s - \frac{f_1}{f_2}f_{g_y}y_s\right]} \mathrm{e}^{\mathrm{i}\phi_a(j f_{g_x})} \tag{7.15}$$

The linear intensity in the focal plane due to interference from the zero and first diffracted orders is:

$$I = |v_0 + v_p + v_m|^2 \tag{7.16}$$

$$= \left[|v_0|^2 + |v_p|^2 + |v_m|^2\right] + \left[v_0^* v_p + v_m^* v_0\right] + \left[v_0 v_p^* + v_0^* v_m\right] + \left[v_m^* v_p\right] + \left[v_m v_p^*\right] \tag{7.17}$$

$$= I_{DC} + I_p + I_m + I_{2p} + I_{2m} \tag{7.18}$$

where we used "p" to refer to intensity terms located at the positive first harmonic sideband, "2p" for the positive second harmonic sideband, "m" for the negative first and "2m" for the negative second harmonic sidebands. The nonlinear illumination intensity due to a two photon process is:

$$I^{NL} = I^2 = \left(I_{DC} + I_p + I_m + I_{2p} + I_{2m}\right)^2 \tag{7.19}$$

$$= I_0^{NL} + I_{1+}^{NL} + I_{1-}^{NL} + I_{2+}^{NL} + I_{2-}^{NL} + I_{3+}^{NL} + I_{3-}^{NL} + I_{4+}^{NL} + I_{4-}^{NL} \tag{7.20}$$

Where the various harmonic sideband terms are:

$$I_0^{NL} = I_{DC}^2 + 2I_p I_m + 2I_{2p} I_{2m}$$

$$I_{1+}^{NL} = 2I_{DC} I_p + 2I_m I_{2p} \tag{7.21}$$

$$I_{1-}^{NL} = 2I_{DC} I_m + 2I_p I_{2m} \tag{7.22}$$

$$I_{2+}^{NL} = 2I_{DC} I_{2p} + I_p^2 \tag{7.23}$$

$$I_{2-}^{NL} = 2I_{DC} I_{2m} + I_m^2 \tag{7.24}$$

$$I_{3+}^{NL} = 2I_p I_{2p} \tag{7.25}$$

$$I_{3-}^{NL} = 2I_m I_{2m} \tag{7.26}$$

$$I_{4+}^{NL} = I_{2p}^2 \tag{7.27}$$

$$I_{4-}^{NL} = I_{2m}^2 \tag{7.28}$$

Examining the positive sideband components in terms of field interactions, and using $v_0^* = v_0$ and $|v_m|^2 = |v_p|^2$:

$$I_{1+}^{NL} = 2v_0(I_{DC} + |v_p|^2)(v_p + v_m^*)$$
$$\propto e^{i2\pi f_{g_x} x_o} e^{-i2\pi \frac{f1}{f2} f_{g_x} x_s} \left[e^{i\phi_a(f_{g_x})} + e^{-i\phi_a(-f_{g_x})} \right] \tag{7.29}$$

$$I_{2+}^{NL} = v_0^2 \left[v_p^2 + v_m^{*^2} + 2(1 + I_{DC}/v_0^2) v_m^* v_p \right]$$
$$\propto e^{i2\pi 2 f_{g_x} x_o} e^{-i2\pi \frac{f1}{f2} 2 f_{g_x} x_s} \left[e^{i2\phi_a(f_{g_x})} + e^{-i2\phi_a(-f_{g_x})} + 2(1 + I_{DC}/v_0^2) e^{i\phi_a(f_{g_x})} e^{-i\phi_a(-f_{g_x})} \right] \tag{7.30}$$

$$I_{3+}^{NL} = 2v_0 \left[v_m^* v_p^2 + v_m^{*^2} v_p \right]$$
$$\propto e^{i2\pi 3 f_{g_x} x_o} e^{-i2\pi \frac{f1}{f2} 3 f_{g_x} x_s} \left[e^{i2\phi_a(f_{g_x})} e^{-i\phi_a(-f_{g_x})} + e^{-i2\phi_a(-f_{g_x})} e^{i\phi_a(f_{g_x})} \right] \tag{7.31}$$

$$I_{4+}^{NL} = (v_m^* v_p)^2$$
$$\propto e^{i2\pi 4 f_{g_x} x_o} e^{-i2\pi \frac{f1}{f2} 4 f_{g_x} x_s} e^{i2\phi_a(f_{g_x})} e^{-i2\phi_a(-f_{g_x})} \tag{7.32}$$

If we decompose the aberration function into the sum of an even and an odd function, $\phi_a = \phi_e + \phi_o$, and use the properties that $\phi_e(-f_{g_x}) = \phi_e(f_{g_x})$ and $\phi_o(-f_{g_x}) = -\phi_o(f_{g_x})$, we see that for three types of phase term groupings there is a simplification:

$$\text{Group 1:} \quad e^{i\phi_a(f_{g_x})} + e^{-i\phi_a(-f_{g_x})} = e^{i\phi_o(f_{g_x})} 2\cos\left(\phi_e(f_{g_x})\right) \tag{7.33}$$

$$\text{Group 2:} \quad e^{i\phi_a(f_{g_x})} e^{-i\phi_a(-f_{g_x})} = e^{i2\phi_o(f_{g_x})} \tag{7.34}$$

$$\text{Group 3:} \quad e^{i2\phi_a(f_{g_x})} e^{-i\phi_a(-f_{g_x})} +$$
$$e^{-i2\phi_a(-f_{g_x})} e^{i\phi_a(f_{g_x})} = e^{i3\phi_o(f_{g_x})} 2\cos\left(\phi_e(f_{g_x})\right) \tag{7.35}$$

Using these three simplified terms in (7.29) - (7.32),

$$I_{1+}^{NL} \propto e^{i2\pi f_{g_x}\left[x_o - \frac{f1}{f2}x_s\right]}\left[e^{i\phi_o(f_{g_x})}2\cos\left(\phi_e(f_{g_x})\right)\right] \tag{7.36}$$

$$I_{2+}^{NL} \propto e^{i2\pi 2 f_{g_x}\left[x_o - \frac{f1}{f2}x_s\right]}\left[e^{i2\phi_o(f_{g_x})}2(1+I_{DC}/v_0^2) + e^{i4\phi_o(f_{g_x})}2\cos\left(4\phi_e(f_{g_x})\right)\right] \tag{7.37}$$

$$I_{3+}^{NL} \propto e^{i2\pi 3 f_{g_x}\left[x_o - \frac{f1}{f2}x_s\right]}\left[e^{i3\phi_o(f_{g_x})}2\cos\left(\phi_e(f_{g_x})\right)\right] \tag{7.38}$$

$$I_{4+}^{NL} \propto e^{i2\pi 4 f_{g_x}\left[x_o - \frac{f1}{f2}x_s\right]}\left[e^{i4\phi_o(f_{g_x})}\right] \tag{7.39}$$

The important result is that odd aberration phase functions $\phi_o(f_{g_x})$, such as coma, scale with image order q in the same way that wobble and acceleration phase errors do. Phase functions with an even form, $\phi_e(f_{g_x})$, such as defocus and spherical aberration, manifest differently for each image order q. The fact that these aberrations are encoded in the complex intensity for each image order means that they can be inverted by a good point spread function measurement in order to improve reconstructed images.

If a microscope system exhibits only odd-function aberration phase terms, $\phi_a \approxeq \phi_e$, then the aberration phase present in each image order reduces to:

$$I_{1+}^{NL} \propto e^{i\phi_a(f_{g_x})} \tag{7.40}$$

$$I_{2+}^{NL} \propto e^{i2\phi_a(f_{g_x})} \tag{7.41}$$

$$I_{3+}^{NL} \propto e^{i3\phi_a(f_{g_x})} \tag{7.42}$$

$$I_{4+}^{NL} \propto e^{i4\phi_a(f_{g_x})} \tag{7.43}$$

Thus, a measurement of the OTF phase for the first image order can simply be multiplied by image order, q, and inverted in order to apply a correction to the higher image orders. As we demonstrated with wobble error and velocity error, the inverse aberration phase can be applied to data to generate sharper images.

For an experimental demonstration of system aberration phase dominated by an odd functional form, where the aberration phase scales with q, we refer the reader to the complex OTFs displayed in Fig. 7.12, where the cubic polynomial phases clearly impart characteristic coma to the associated PSFs for image orders q=1-3. Another example is depicted in Fig. 7.6, where data

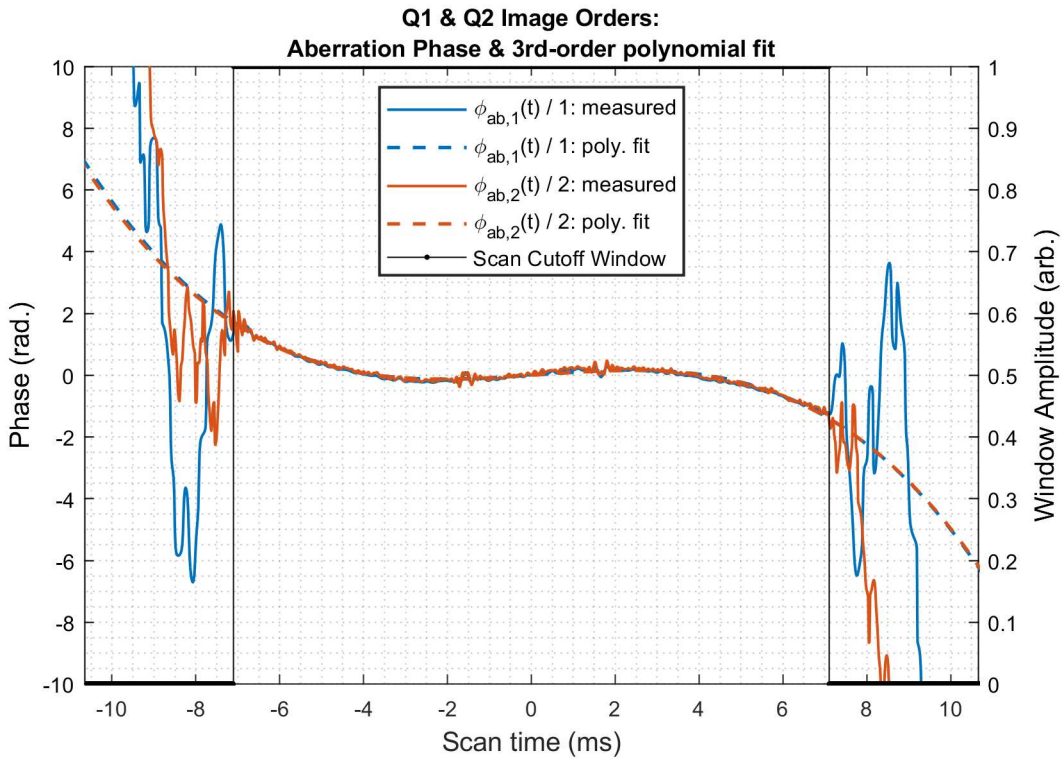

Figure 7.14: Measured Aberration Phase for Second Harmonic Generation Optical Transfer Functions, using a 200nm $BaTiO_3$ particle, with 3rd order polynomial fit. Phases for image orders Q1 and Q2 are overlaid, scaled by Q, showing they measure the same quantity. Note that phase error due to mask wobble and motor acceleration is already removed from the data; only the residual phase error due to optical aberration is shown here.

for images $q = 1$ and $q = 2$ have an odd aberration function that again looks like a third-order polynomial. The measured residual aberration phase for these OTFs is displayed in Fig. 7.14. The plots show the residual phase after removing phase errors due to mask wobble and motor acceleration. The residual phase, which we attribute to system aberration, is scaled by q for each OTF order before plotting. The plotted results demonstrate good agreement with the model outlined in this section for the case when lateral aberration functions are predominantly odd in functional form.

Author Contributions

J.J.F. applied the vector focusing model to the study of depolarization and transmitted energy at the focal plane, and developed the wobble correction scheme. K.A.W. developed joint

velocity and wobble correction scheme, analyzed data as a Poisson random process, and redesigned masks to measure all timing errors. K.A.W., J.J.F. and R.A.B. analyzed effects of higher diffracted orders, and wrote the paper in Ref. [62]. K.A.W. analyzed lateral microscope aberration. K.A.W. performed all research and data analysis in this chapter. Sections 7.1, 7.2 and 7.4 use text from Ref. [51] and Sections 7.5.1 and 7.5.2 use text from Ref. [62]. J.J.F. made Figures 7.1 – 7.3 and K.A.W. made Figures 7.4 – 7.14.

CHAPTER 8

2D LATERAL SUPER-RESOLUTION WITH MP-SPIFI

We now present a technique for generating laterally isotropic super-resolved multiphoton images with a multiphoton spatial frequency modulated imaging (MP-SPIFI) microscope. As we have discussed, MP-SPIFI is an optical super-resolution technique that can be widely applied to various contrast mechanisms, whether a real-state electronic transition, such as fluorescence, or a virtual-state nonlinear scattering mechanism, such as SHG or THG. However, the innate resolution enhancement is limited to one dimension. Moreover, it is difficult to form images with the full theoretical resolution of the microscope due to extraneous diffracted orders from the modulator, and the fact that high spatial frequency information is typically gathered with very low SNR relative to the low spatial frequency information.

In this chapter, we demonstrate two important advances in the imaging capabilities of an MP-SPIFI microscope. First, we demonstrate a novel synthesis algorithm for 1D SPIFI measurement data, which stitches together the information in each of q image orders produced by MP-SPIFI. The composite image generated by the algorithm exhibits both high SNR and the full available horizontal resolution enhancement from the information contained in the data. Second, we extend the super-resolving properties of MP-SPIFI into both lateral dimensions. To achieve this, we combine transverse and rotational scanning of the object, in order to form a set of measurements in the object's spatial frequency space that span f_x and f_y isotropically. These data are coherently combined into a composite set of information and deconvolved, before applying a final inverse Fourier transform to reconstruct an image with isotropic resolution enhancement in the (x, y) plane.

8.1 Synthesizing a 1D Image from all MP-SPIFI Image Orders

8.1.1 Processing the Measured Signal for each Image Order

In this section, we provide a synopsis of the data processing scheme for MP-SPIFI signals discussed throughout this work. First of all, after isolating the image at each positive sideband

harmonic frequency $q\nu_o$ of the Fourier transformed measured signal using a digital bandpass filter, the resultant complex time traces after inverse Fourier transform are:

$$S_{q+}(t) = \int I^2_{q+}(x,t)\, C(x) \mathrm{d}x \tag{8.1}$$

$$= H_q(t) \mathrm{e}^{\mathrm{i}2\pi q \nu_o t} \int \mathrm{e}^{-\mathrm{i}2\pi q f_{g_x}(t) x} C(x) \mathrm{d}x \tag{8.2}$$

$$= H_q(t) \mathrm{e}^{\mathrm{i}2piq\nu_o t} \hat{C}\left(q f_{g_x}(t)\right) \tag{8.3}$$

where $I^2_{q+}(x,t)$ is the complex two-photon intensity component that deposits object information into the q^{th} harmonic sideband [51, 62]. The shaping functions, $H_q(t)$, are the result of combinations of various diffracted order amplitudes, a_j, and windowing functions $\Pi_{x_j}(t)$, which are due to the mask pattern and the microscope pupil.

In the absence of measurement errors, the diffracted orders imaged from the mask create a sinusoidal spatial frequency pattern at the sample plane that increases in spatial frequency linearly with time. However, errors in the optical system can cause these projected spatial frequency patterns to deviate from linearity with time, as discussed in Ch. 7. One such error is lateral phase-shifting in the projected interference patterns due to mask mounting error, created when the mask pattern is not precisely centered on the axis of rotation [101]. A second systematic error is traditional optical aberration in the 4-f image relay system. In this case, the imaging system, including lenses, coverslip, and sample mounting medium, can impart small shifts in the one-to-one mapping from object space (the mask) to image space (at the sample). Fortunately, these errors are deterministic and measurable. We can include these phase errors in the measured signal by writing

$$S_{q+}(t) = H_q(t) \mathrm{e}^{\mathrm{i}q[\phi_a(f_{g_x}(t)) + \phi_m(f_{g_x}(t))]} \mathrm{e}^{\mathrm{i}2\pi q \nu_o t} \hat{C}\left(q f_{g_x}(t)\right) \tag{8.4}$$

After demodulating each complex time trace to baseband, and applying the inverse of the measured aberration & mask phase errors as discussed in Sec. 7.3 and 7.6, each complex trace is

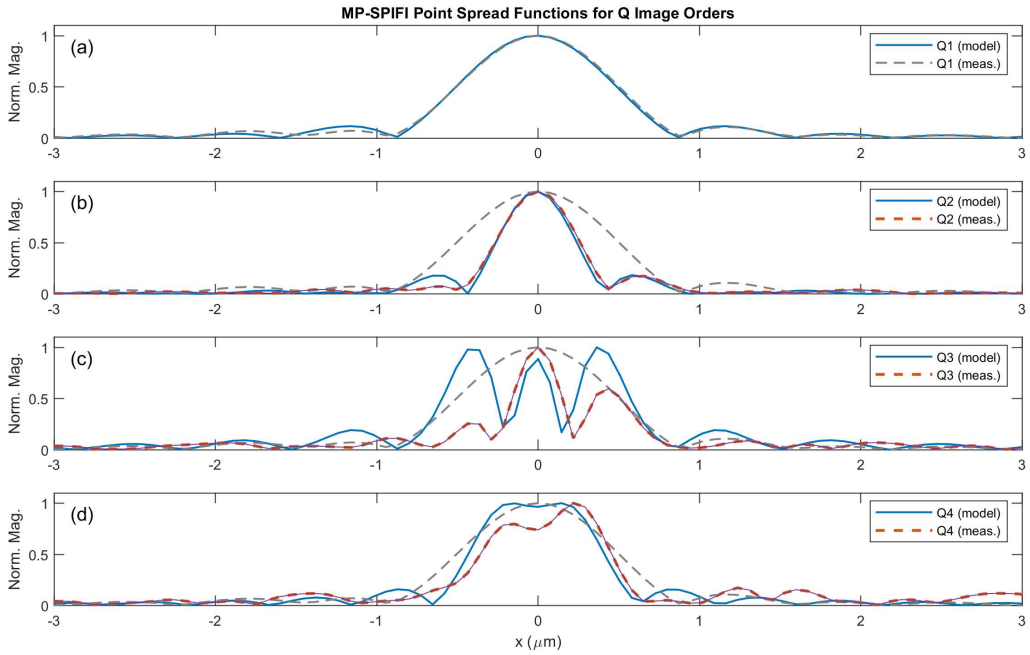

Figure 8.1: Measured & Simulated Point Spread Functions. (a)-(d) MP-SPIFI image orders 1-4. Data is acquired by detecting SHG from a single 200nm $BaTiO_3$ grain. The calculated PSF for this imaging system using the vector focusing model (blue) described in [51] is compared with the measured and processed PSF data (red, dashed). The envelope of the first-order image is plotted in (b)-(d) as a gray dashed line, illustrating that the thresholding operation using this widest PSF retains the finer features of the narrower PSFs in (b)-(d).

reduced to $S_{q+} = H_q(t)\hat{C}\left(qf_{g_x}\right)$. Since the shaping functions H_q are formed from the time period in which the $j = \pm 1$ diffracted orders are within the system pupil, we can write them as functions of time, or equivalently, as functions of the fundamental grating frequencies formed at each time: $H_q(t) \rightarrow H_q\left(f_{g_x}\right)$. Now, making the substitution $f_x = qf_{g_x}$, the signals can equivalently be written $S_{q+} = H_q(f_x/q)\hat{C}(f_x)$. The axis dilation in $H_q(f_x/q)$ is performed numerically by mapping the S_{q+} time traces, which are on a common time grid, onto f_x grids which are scaled by q. The traces are then interpolated onto a common f_x grid.

A Fourier transform of each OTF H_q returns the point spread function h_q. In the ideal case where only the $j \in -1,0,1$ diffracted orders propagate to the sample plane, the PSFs will narrow as image order q increases. However, in practice, PSFs $h_3(x)$ and $h_4(x)$ do not follow this trend, due to the presence of $j = \pm 3$ diffracted orders in the sample region. This PSF distortion

is discussed at length in Section 7.5. In Fig. 8.1 we plot both measured and simulated SHG point spread functions, demonstrating the PSF distortions in image orders $q = 3$ and $q = 4$. The measured PSFs have been corrected for wobble and velocity error from the mask, and aberration in the $4f$ image relay, yet still display the influence of higher diffracted orders on the imaging process. The measured PSFs are in very good agreement with the simulation, which used the vector focusing model described in Section 3.3.6.

8.1.2 Coherently Summing the Processed Signals for each Image Order

In this section, we discuss our strategy for generating a single information-bearing signal that contains the information contributed from each image order in MP-SPIFI. This strategy employs a windowing scheme to mitigate the deleterious impact of higher diffracted orders from the binary mask, discussed in Sec. 7.5. It then employs a Wiener deconvolution to equally weight the contribution of each spatial frequency projection in the imaging system.

After removing phase errors from the data, as described in Ch. 7, the complex trace for each image order, S_{q+} contains the same pure carrier frequency, albeit oscillating under different envelopes. This set of traces can then be summed to formed a single, composite trace without fear of information loss due to destructive interference:

$$S_\Sigma(f_x) = \sum_q S_{q+}(f_x) = \hat{C}(f_x) \sum_q H_q(f_x/q) = \hat{C}(f_x)\, H_\Sigma(f_x) \tag{8.5}$$

This single trace brings together the strengths of each image order. It contains high SNR information at low spatial frequencies from the first image order, S_{1+}. It also contains high spatial frequency information, albeit at lower SNR, thanks to the higher image orders, S_{3+} and S_{4+}. Together, a composite trace exhibits both high SNR and high resolution. This composite signal contains a new composite OTF, $H_\Sigma(f_x) = \sum_q H_q(f_x/q)$, which is depicted in Figures 8.4 and 8.3.

A thresholding operation can also be applied to help remove noise in the set of signals before summing. This strategy exploits the high SNR of the $q = 1$ image by first identifying which pixels lie below a threshold in the $q = 1$ image, and then zeroing those identified pixel locations across

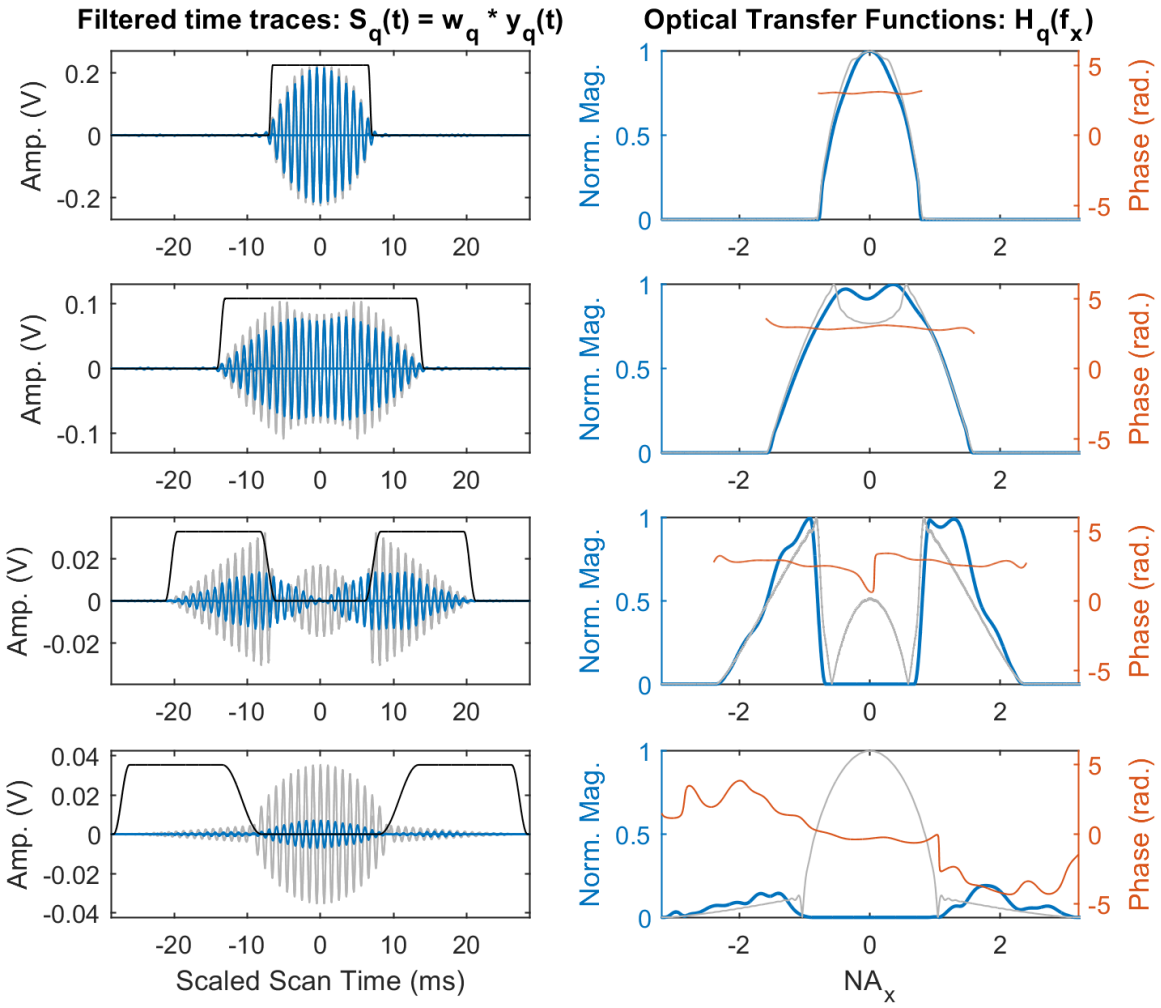

Figure 8.2: Left Column: Measured complex time traces (real part), downshifted to a slow carrier frequency for visibility (blue). Computed complex time traces (real part) using the vector model in [51] for comparison (gray). Windowing function used to extinguish information from scan times when the $j = \pm 3$ diffracted orders are within the system pupil (black). The measurement time axis has been scaled by q for each order's time trace, in descending order from $S_{1+}(t)$ at top to $S_{4+}(t)$ at bottom. **Right Column:** Complex optical transfer functions formed by taking the magnitude (blue) and phase (red) of the complex time traces on the right, with model magnitude in gray. The windows have been applied to the magnitudes. The increasing spatial frequency support with q is visible (top to bottom) on the uniform spatial frequency axis, $NA_x = f_x/\lambda$.

all image orders. For the data presented in this chapter, a threshold is set to 2% of the peak value in the $q = 1$ image. This process avoids loss of information, because image orders $q \geq 2$ are more finely resolved than $q = 1$. In the point spread functions in Fig. 8.1, the envelope of

the first-order image is plotted in (b)-(d) as a gray dashed line, illustrating that the thresholding operation using this widest PSF retains the finer features of the narrower PSFs in (b)-(d).

Windowing Strategy

Because our masks are printed in binary fashion for practical purposes, the sequence of gratings has a square wave profile, as opposed to a cosine profile. Therefore, odd harmonics of the first diffracted orders are generated, as discussed in Sec. 3.2. The third diffracted orders, $j = \pm 3$, present a specific practical problem, as they contain negative field coefficients, and generate zero-crossings in the amplitudes of the complex signal envelopes S_{q+} for the $q = 3$ and $q = 4$ image orders, evident in Fig. 7.8 and discussed at length in Sec. 7.5. This leads to distortion and failure to reach the available resolution in the corresponding PSFs, as seen in both measured and simulated data presented in Figure 8.1.

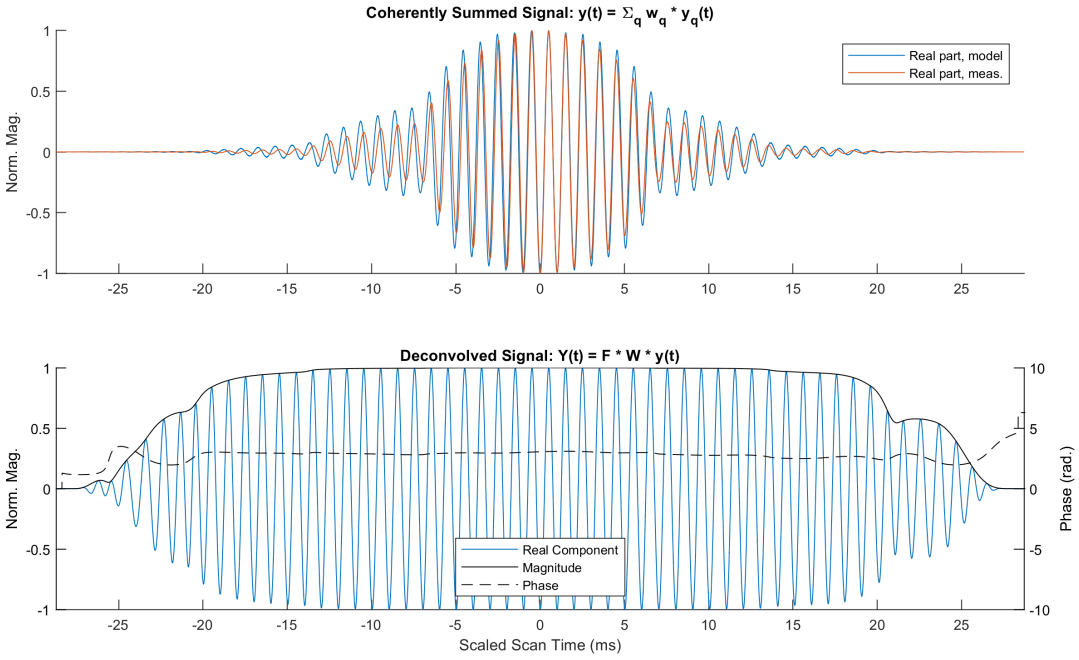

Figure 8.3: Coherently Summed Temporal Signal from PSF dataset. **Top:** Real part of the coherently summed signal, displaying aberration-free summation of the (downshifted) carrier frequency. The magnitude of this data is shown in Fig. 8.4 (top). **Bottom:** The summed signal after deconvolution, using the deconvolution filter in Fig. 8.4 (bottom).

To counteract the effect of the third diffracted orders, we make use of the fact that they exit the 4f system pupil earlier than the first diffracted orders. The cutoff time scales as $1/j$, so they are present for scan times $t = [-t_c/3 : t_c/3]$, where t_c is the cutoff time. We therefore impose a window function that zeroes S_{3+} and S_{4+} during these scan times (Fig. 8.2, left column, black). There is no loss of information, since the S_{1+} and S_{2+} traces already contain the same information at higher SNR. We have therefore forced S_{3+} and S_{4+} to yield only the desired high spatial frequency information from interference between the $j \in \{-1, 0, 1\}$ beams; information which is unique to those image orders. The windows, for all image orders, also zero out noise in the region beyond the known cutoff time for the $j = \pm 1$ diffracted orders. This modification to the composite OTF can be written $H_\Sigma = \sum_q W_q(f_x) H_q(f_x/q)$.

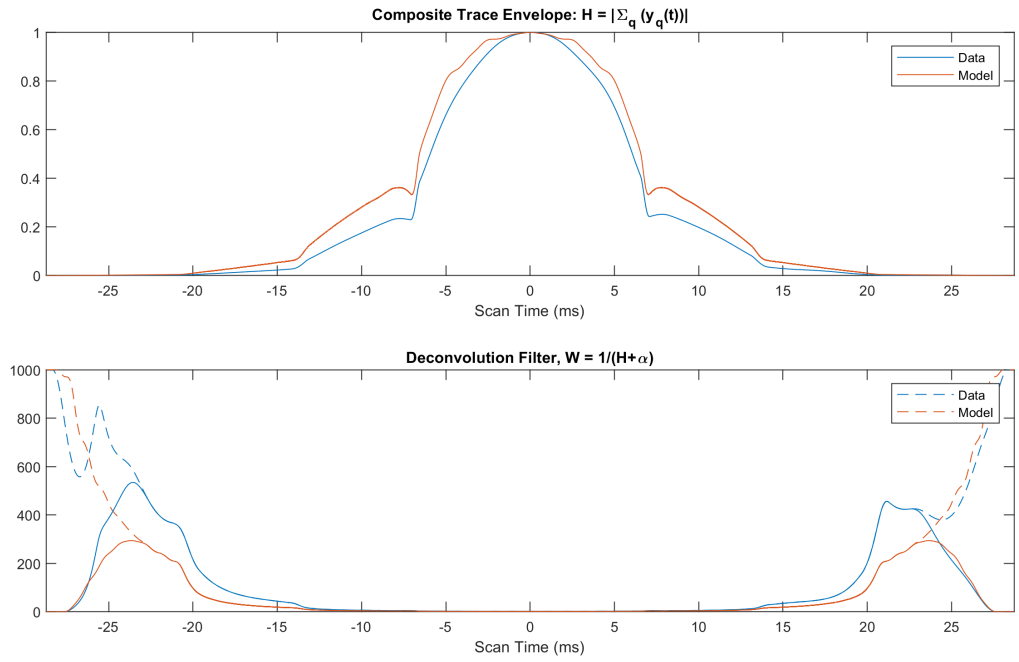

Figure 8.4: MP-SPIFI composite support & deconvolution filter. **Top:** Magnitude of composite time trace formed by coherent summation of the windowed PSF time traces in Fig. 8.2. This forms the system OTF, $H_\Sigma(f_x)$. **Bottom:** The deconvolution filter $G(f_x)$ formed from H_Σ (dashed) in Eqn. (8.6), and multiplied by a raised-cosine roll-off filter (solid).

Figure 8.3(a) shows the composite signal formed from summing the windowed complex traces in the left column Figure 8.2. Figure 8.4(a) shows the envelope of the composite signal, $|H_\Sigma|$. For reference, we plot the OTF formed in the same way from our vector model [51] for this microscope. The large variation in signal amplitude from each image order is evident. This leads naturally to a deconvolution strategy in order to equalize the contributions of each excitation spatial frequency. We employ a simple, real-valued Wiener filter of the form

$$G(f_x) = \frac{1}{|H_\Sigma| + \alpha_r} \tag{8.6}$$

using a normalized version of $|H_\Sigma|$, and where α_r is a regularization parameter that is tuned to suppress noise at high spatial frequencies. This filter is visible in Figure 8.4(b). Figure 8.3(b) displays the deconvolved signal.

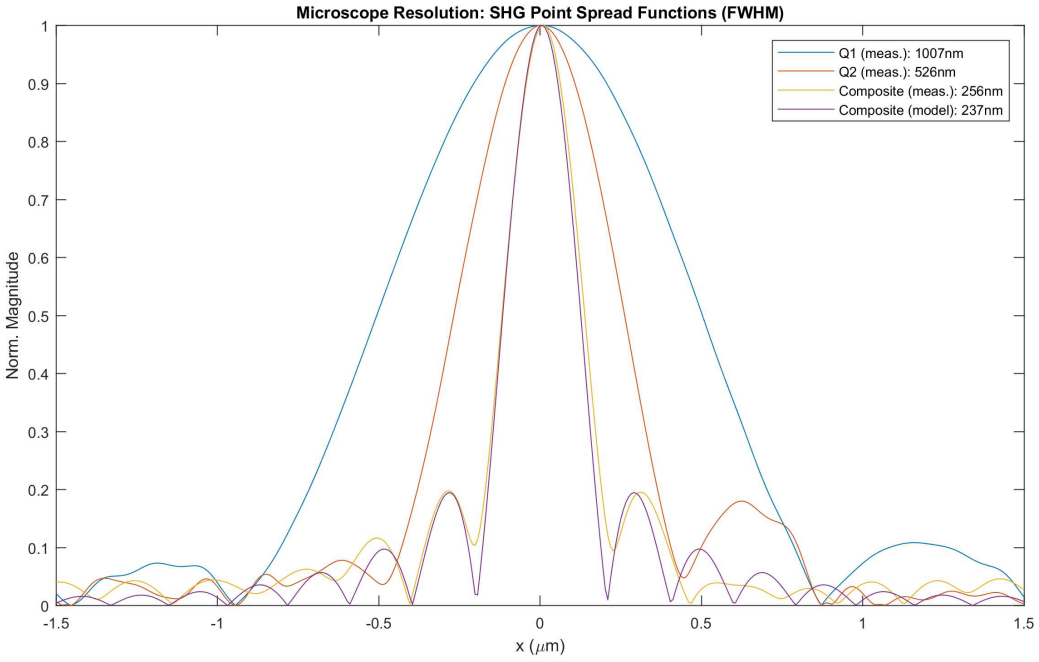

Figure 8.5: Composite Point Spread Function for Second Harmonic Generation contrast mechanism. For reference, the 1^{st} and 2^{nd} order PSFs from this dataset are displayed (red,blue), along with the modeled PSF using the coherent addition process (yellow). The coherently-combined image order data produces an SHG point spread function (256 nm FWHM) that nearly reaches the theoretical limit (237 nm FWHM).

The image formed by this process is found by Fourier transform of the composite signal after deconvolution, and taking the magnitude:

$$\hat{C}(x) = |\mathscr{F}^{-1}\{G(f_x)S_\Sigma(f_x)\}| \tag{8.7}$$

$$= |\mathscr{F}^{-1}\{G(f_x)\,H_\Sigma(f_x)\,\hat{C}(f_x)\}| \tag{8.8}$$

For the point spread function measurement data used in Figures 8.2, 8.4, and 8.3, the image is presented in Fig. 8.5. For the 0.8 NA objective lens used in the microscope, the system resolution is very close to that predicted by our vector focusing model. Most importantly, the measured PSF resolves at $2x$ the second-order image alone, which serves as a benchmark for the resolution of standard point-focus two-photon microscopy.

8.2 Synthesizing a 2D Image with Isotropic Resolution using Object Rotations

The natural framework for extending the super-resolving capabilities of SPIFI and MP-SPIFI is rotation about the z-axis. This is because the frequency support in transverse frequency space (f_x, f_y) is anamorphic for the higher image orders, where $f_{x_{max}} < f_{y_{max}}$.

Transverse rotation has been utilized on prior implementations of SPIFI. Lateral - tomographic SPIFI [103] implements an elegant concept wherein the line focus at the modulator is expanded in y to form a collimated beam at the sample, with vertical columns through the beam profile each labeled with a unique modulation frequency. In effect, each modulation frequency recorded by the detector contains an integration of signal information from the sample interaction with that vertical slice of the beam. This is directly analogous to Computed Tomography (CT), where one dimension of the object information is integrated at the detector (one difference being that CT takes place in the lateral-axial plane). Drawing on the parallel with CT, transverse rotation of the vertically-labeled whole-beam illumination forms a set of 1D data traces, which can be stacked into a sinogram. The sinogram can then be converted into a 2D image using a standard back-projection algorithm. This approach does indeed generate a 2D image with only a single scan axis (transverse rotation). Although this paper does not explore

the second-order image recorded with linear SPIFI excitation, it is straightforward to show that the second-order image contains twice the spatial-frequency coverage, and that this results in uniform resolution enhancement across the (x, y) image. However, the main drawback of this technique for multiphoton purposes is the very large average power required to generate nonlinear signal under wide-field illumination, which can be on the order of Watts. Indeed, other schemes for widefield super-resolved SHG have also faced this impractical cost of implementation [30, 104].

A second concept for SPIFI [105] implemented a single 90-degree rotation of standard line-scanning, projecting fringes first in x, then y. Maintaining a line focus allows for easy generation of nonlinear signal. However, this method lessens, but does not remove, the object-resolution asymmetry in x vs. y. For higher-order SPIFI images (e.g., Q = 4) which contain the greatest resolution enhancement, there will be noticeably poorer resolution along the 45-degree and 135-degree diagonals of the image, relative to along the x & y axes. This results in an "X" shaped point spread function for a point object.

A third concept, Fourier Computed Tomography (FCT) [106], implemented a transverse rotation of a SPIFI line focus with a finely-stepped angular spacing. Again, a CT-like back-projection algorithm was applied to the data, except this time the back-projection took place in the Fourier domain (hence the FCT moniker). While conceptually elegant, this method generates images with radially-varying azimuthal resolution. To understand the physical meaning of this statement, it is helpful to think about a point object near the origin, and another far away from the origin. At the origin, a point object will be illuminated by 1D spatial frequency projections that are rotated through all transverse angles ϕ_i, spanning from 0 to 180 degrees, with $\Delta\phi_i$ on the order of 1 degree. However, far from the origin, a point object may only be illuminated by a few rotated line foci, depending on its radial distance, the thickness of the rotated line focus, and the overlap between adjacent rotated versions of the line focus. The result of this few-angle illumination is that the distant point object will have enhanced resolution along the radial direction (the direction of the spatial frequency projections), but only standard

diffraction-limited resolution in the azimuthal direction (the direction orthogonal to the projections). Indeed, this is borne out in the data presented in [106], where the asymmetric resolution in (x, y) from y-scanning the line focus has simply been turned into an asymmetric resolution in (r, ϕ). The significant difference between y-scanning vs. ϕ-scanning lies in the total frequency support spanned by the imaging process. In y-scanning, the resultant 2D image has a clearly asymmetric frequency support. In ϕ-scanning, the magnitude of the spatial frequency content has a circularly-symmetric profile. However, this metric is a bit deceiving in regards to imaging performance. For isotropic resolution enhancement across the entire illumination field of view, the local frequency support at each position (x, y) must be the same.

While each of these approaches offers merit for various imaging tasks, the difficult task of generating uniform transverse super-resolution under multiphoton-excitation SPIFI calls for new suitable imaging methods. We can summarize the fundamental requirements as the following. One, rotation of the enhanced frequency support that occurs along x due to the nonlinear projections. Two, an expanded field of view relative to FCT, in which all spatial points in a large circular area are illuminated by SPIFI 1D projections, for all angular orientations. Third, illumination peak intensity is high enough to generate nonlinear signal.

8.2.1 Isotropic Support with Cartesian Scanning and Sparse Rotation

In order to create such isotropically super-resolved images, we have developed a concept that ensures the spatial frequency support is both equivalent at all locations in the (x, y) image, and roughly circular in shape. Moreover, we did this with a line-focus illumination profile, to enable nonlinear signal generation at reasonable laser powers. This ensured a super-resolved, shift-invariant imaging system for multiphoton excitation.

The idea works by acquiring SPIFI line images that are scanned in the (y, ϕ) two - dimensional space - a finely-sampled line scan in y and a sparse angular rotation in ϕ. Each finely-sampled line scan in y creates a 2D image with asymmetric frequency support, since MP-SPIFI creates images with $f_{x_{max}} > f_{y_{max}}$. By rotating the sample about the optic axis, and repeating the vertical line scan, the enhanced support in f_x of the imaging process is able to probe the

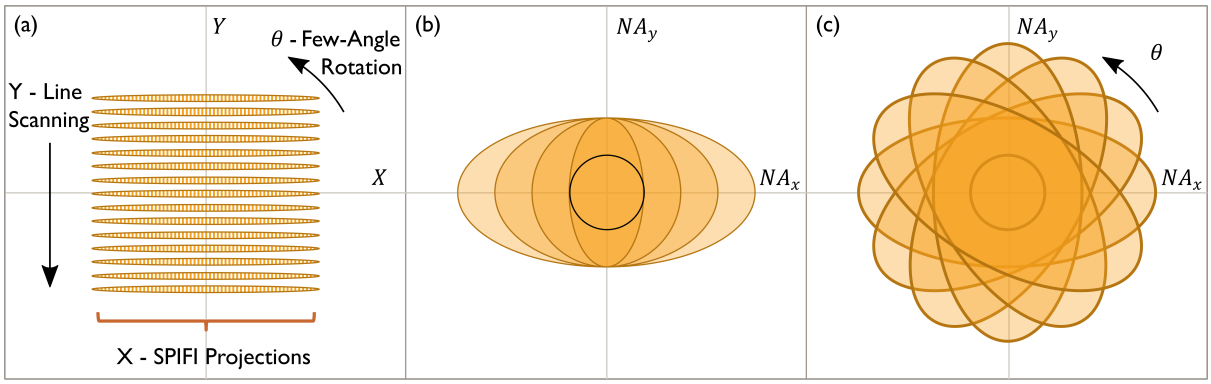

Figure 8.6: Coherent Summing of 1D and 2D Fourier Image Information (Schematic). (a) Visualization of SPIFI spatial frequency projections along x, under a line-focus envelope translated in y, and then repeated after rotation in ϕ. (b) Asymmetric frequency support along the f_x direction, for a y-scanned 2D image at $\phi = 0$. Cartoon of the frequency support for each image order under two-photon illumination shows the increasing support in f_x and constant support in f_y relative to the passband of the objective lens (black circle). (c) Rotation of the object, or the illumination, allows this asymmetric support to probe previously inaccessible portions of the object's Fourier spectrum.

object's spatial frequency content at any angle set by the user. While the step size δy is set in the standard way by the PSF of the line focus, the step size $\delta\phi$ is set by the degree of asymmetry between $f_{x_{max}}$ and $f_{y_{max}}$. The goal is to rotate the elliptically-shaped frequency support, in as few steps as possible, such that the transverse spatial frequency space (f_x, f_y) is filled out in a roughly circular fashion. This strategy is somewhat similar to that employed in structured illumination microscopy (SIM) [4, 35]. We note for reference that while traditional SIM is implemented with wide field illumination and detection, and requires discrete phase-stepping of a fixed-frequency spatial frequency projection to isolate complex intensity, MP-SPIFI is a line-illumination and single-pixel detection approach, with a continuously increasing and phase-shifting set of spatial frequency projections that automatically yield a complex intensity upon FFT.

To demonstrate the applicability of this idea, we set up a multiphoton SPIFI microscope to detect two-photon excitation fluorescence (TPEF). Because MP-SPIFI has been demonstrated to work equivalently well for coherent harmonic scattering processes like SHG and incoherent scattering processes like the fluorescence demonstrated here [51], it is straightforward to ex-

tend this current concept from TPEF to SHG and THG images. However, with HG, one should be careful to manipulate the polarization state with each sample rotation, so that though the intensity pattern rotates, the electric field polarization components project onto the sample the same way each time. This can be accomplished with a half-wave plate rotated to $\phi/2$ for an object rotation of ϕ.

8.2.2 Mathematical Model

To include 2D object information in our model, we first assume that the two-photon intensity distribution in the focal plane maintains a static line-focus profile $P(y)$ for all scan times. This is despite the time-varying apodization of the scanning vertical line cursors that takes place in the back aperture of the objective lens. This assumption is loosely justified when accounting for the fact that the undiffracted ($j = 0$) beam remains on-axis, and focused with the full vertical support of the objective lens, for all scan times, combined with the fact that the undiffracted beam contributes strongly to the intensity in the first and second image orders ($q = 1, 2$), which in turn have strong magnitudes relative to the higher image orders (e.g., $q \geq 3$) [51, 62]. A rigorous account of actual profile variation with time is covered in detail in Chapters 3 and 4.

The 1D line image at each y position will be formed through the order-stitching process discussed earlier, given by Eqn. (8.8). Expanding Eqns. (8.1)-(8.3) to include the line focus geometry and vertical object scanning:

$$S_{q+}(t, y_0) = \int I^{(2)}_{q+}(x, y)\, C(x, y - y_0)\, \mathrm{d}x\, \mathrm{d}y \tag{8.9}$$

$$= H_q(t)\, \mathrm{e}^{\mathrm{i}2\pi q v_o t} \int P(y)\, \mathrm{e}^{-\mathrm{i}2\pi q f_{g_x}(t) x}\, C(x, y - y_0)\, \mathrm{d}x\, \mathrm{d}y \tag{8.10}$$

A Fourier transform over y_0, along with demodulation and dilation along f_x to bring each of the q image orders to the same axis at baseband, yields the set of q complex signals:

$$S_{q+}(f_x, f_{y0}) = -H_q(f_x/q)\hat{P}(f_{y0})\hat{C}\left(f_{g_x}, -f_{y0}\right), \tag{8.11}$$

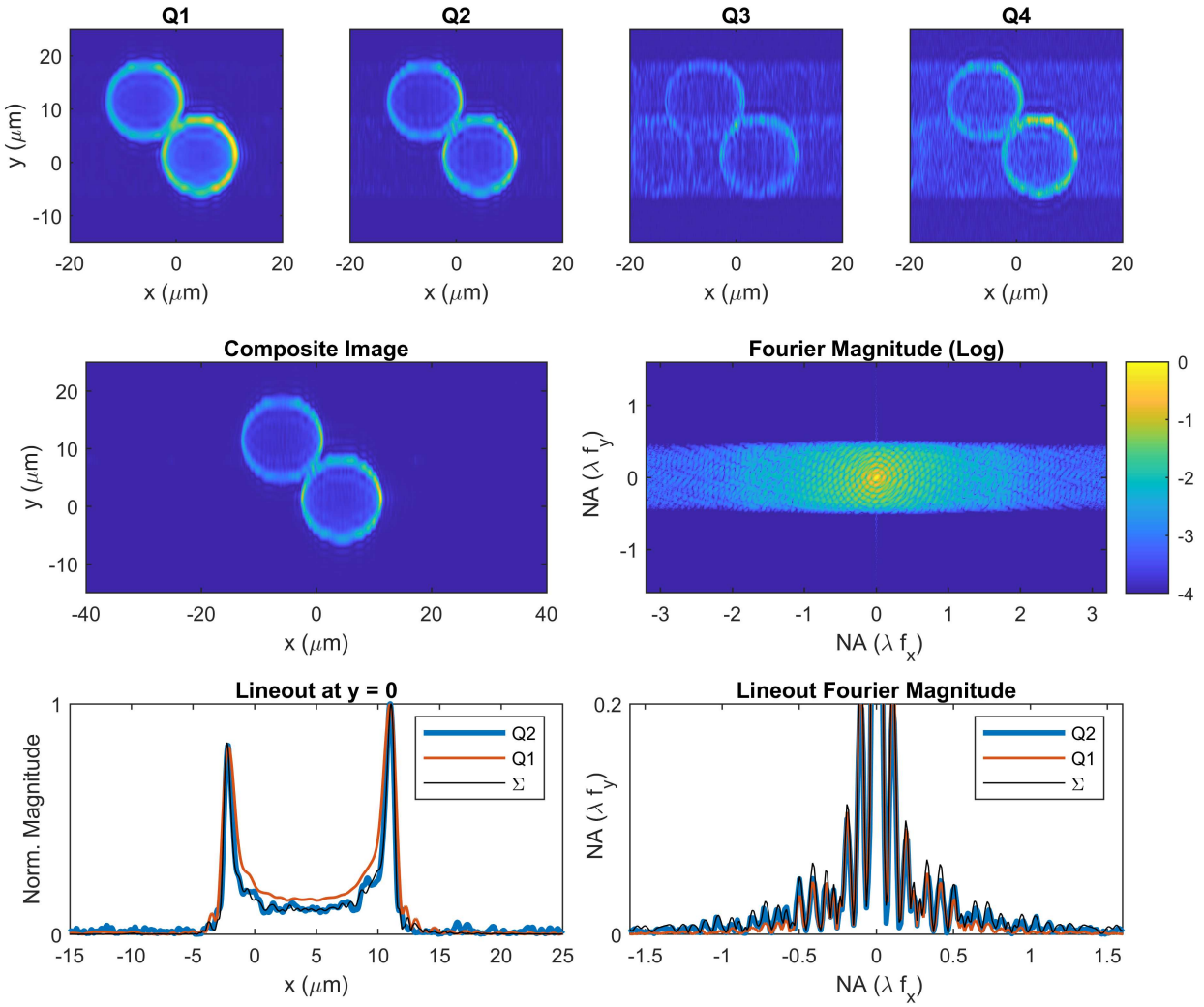

Figure 8.7: Top: Images of 15μm fluorescent shell-stained spheres obtained under two-photon illumination, isolated at harmonic sidebands after FFT of the datastream. The higher order images are dominated by shot noise due to the brighter lower order images. Images $q = 3$ and $q = 4$ struggle to display enhanced resolution in x due to the presence of higher-order diffraction from the modulator disk, and because this particular object has vanishing spatial frequency content beyond approximately NA = 2 NA_{obj}. **Middle:** Composite image formed by windowing away information corrupted by higher-order diffraction and then combining images Q1-Q3 in the spatial frequency domain and deconvolving. Q4 was neglected because its windowed contribution was only noise. The Fourier magnitude of the composite image clearly displays the asymmetric support given by the imaging process, the effect of which is seen in the image where the stained shell is blurred in the y-direction relative to x. **Bottom:** A cross-section of the bead along $y = 0$, and a zoom-in of its Fourier magnitude. The composite image is resolving the shell at least as well as the 2^{nd}-order image, while suppressing noise as well as the 1^{st}-order image.

As before, we sum over the q complex traces with increasing spatial frequency information available along f_x. Our assumption of equivalent vertical profiles $P(y)$ allows $\hat{P}(f_{y0})$ to move outside the sum. Coherent summation over q yields the single 2D information array:

$$S_\Sigma(f_x, f_{y0}) = -H_\Sigma(f_x)\hat{P}(f_{y0})\hat{C}\left(f_{g_x}, -f_{y0}\right), \tag{8.12}$$

Multiplying Eqn. (8.12) by deconvolution filters $G_x(f_x)$ and $G_y(f_{y0})$ to account for the spectral shapes of H_Σ and $\hat{P}(f_{y0})$, respectively, returns a 2D Fourier-space object estimate with roughly rectangular support.

$$\hat{C}(f_x, f_{y0}) = G_x(f_x)\, G_y(f_{y0})\, H_\Sigma(f_x)\, \hat{P}(f_{y0})\, \hat{C}\left(f_{g_x}, -f_{y0}\right) \tag{8.13}$$

We now turn to the task of rendering an object reconstruction with isotropic resolution enhancement. Rotation of the object (or the illumination) allows the asymmetric support to probe previously inaccessible portions of the object's Fourier spectrum, as indicated in Fig. 8.6(c). To implement our sparse-rotation scheme, we recognize that a rotation of the object by an angle ϕ_n results in rotated support, such that the spatial frequency variables in (8.13) are replaced with f'_{x_n} and f'_{y0_n}, which are given by the well-known rotational transformation:

$$f'_{x_n}(f_x, f_{y0}, \phi_n) = \quad f_x \cos(\phi_n) + f_{y0} \sin(\phi_n) \tag{8.14}$$

$$f'_{y0_n}(f_x, f_{y0}, \phi_n) = -f_x \sin(\phi_n) + f_{y0} \cos(\phi_n) \tag{8.15}$$

The number of rotations necessary to cover a circular region depends on the relative bandwidths of the focal support in f_y and the nonlinear SPIFI projections in f_x. The coherent summation of the complex data recorded for each angle, followed by Fourier transform, returns an objection with a laterally-uniform enhanced resolution. A deconvolution filter, H_ϕ, can be constructed to properly divide each pixel by the amount of information contributed from each image. In the limiting case of rectangular blocks of data, this would be a filter with integer values

only. The final reconstructed image can be written:

$$\hat{C}_{\Phi}(x,y) = |\mathscr{F}^{-1}\{H_{\phi}\sum_{n}\hat{C}\left(f'_{x_n}, f'_{y0_n}\right)\}| \tag{8.16}$$

where the subscript Φ indicates that this object reconstruction is a summation over a set of n rotated estimates given by (8.13) and (8.14)-(8.15).

8.2.3 Experimental Setup

To test our system, we utilized 15μm fluorescent shell-stained polystyrene beads, which are large and easy to locate, yet have a thin feature (the stained shell) providing the ability to determine system resolution (FocalCheck Fluorescence Microscope Test Slide #1, F36909, ThermoFisher). The microscope was equipped with a Zeiss 50x 0.8NA air-immersion objective lens, and a 150mm achromatic tube lens to relay image the mask to the sample. The sample was rotated to a set of six angles (0,30,60,90,120,150 degrees), and at each orientation, the sample was scanned vertically to acquire a stack of SPIFI line images which together generated a 2D image. Each of the six images has an enhanced spatial frequency bandwidth occurring in the direction of its rotation angle. It should be noted that the data could have been equivalently acquired by rotating the illumination pattern and keeping the sample stationary. However, this would have added a great deal of complexity to the instrument.

To detect the TPEF signal light emitted by the sample, a dichroic filter (Semrock FF775-Di01) and interference filter (Semrock, FF01-720/SP-25) were used to isolate the TPEF from the illumination light. The laser source was a custom-built ANDi style fiber laser [71] and subsequent nonlinear amplifier [67] emitting 110fs fs pulses at 62.7 MHz repetition rate, centered at 1060nm, with up to 2.2 W of average power available for the microscope. The isolated TPEF signal was directed onto a PMT (Hamamatsu 7422P-40), and the subsequent electronic current signal was pre-amplified (Femto DHPCA-100), passed through an anti-aliasing filter, and then digitized on a data acquisition board (National Instruments, PCI-6110 card with BNC 2090A panel). Data was sampled at roughly 4x the Nyquist frequency for the highest modulation fre-

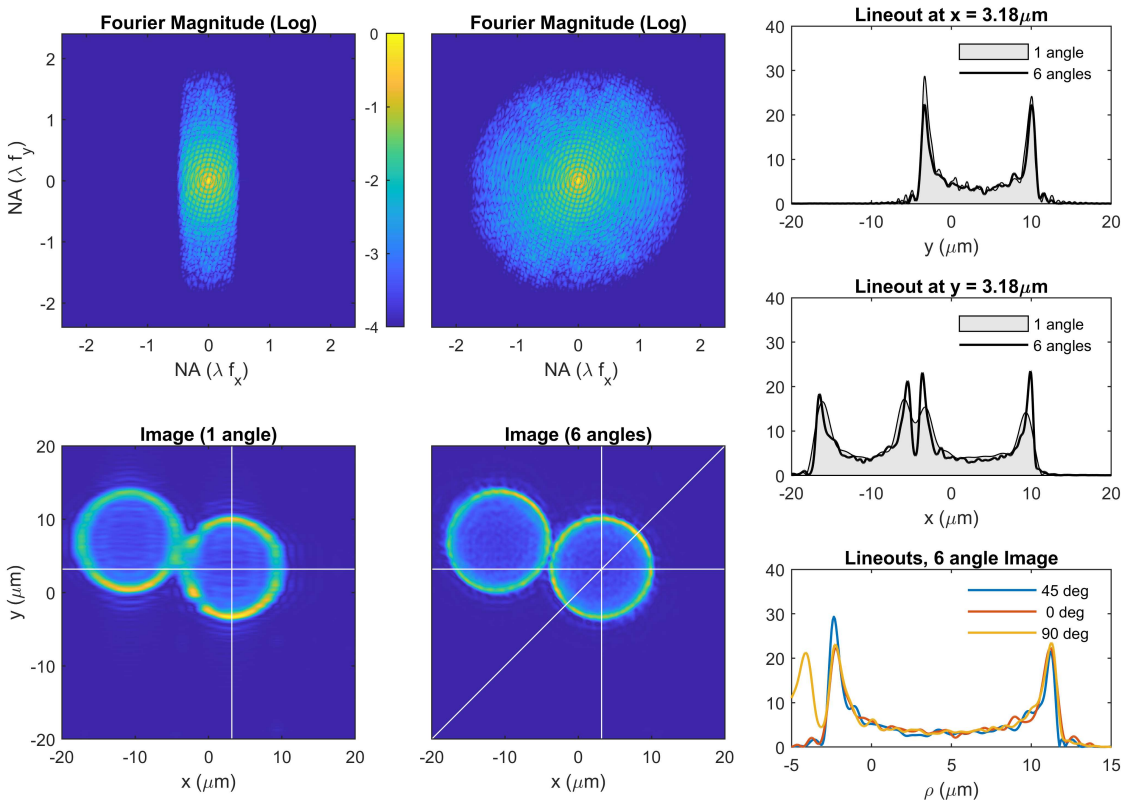

Figure 8.8: (a) Fourier magnitude and (c) image at rotation angle $\phi = 90$ degrees. (b) Fourier magnitude and (d) image due to summation of image data at 6 angles: 0, 30, 60, 90, 120, and 150 degrees. (e)-(g): Lineouts at various orientations, corresponding to white lines in (c) & (d). (e) Vertical lineout at x = 3.18μm, showing that the 1-angle and 6-angle image reconstructions resolve the fluorescent shell equally well. (f) Horizontal lineout at y = 3.18μm, showing that the 6-angle reconstruction is resolving the adjacent shells in an a superior fashion due to the added support with rotation. (g) 3 lineouts of the 6-angle image, at 0, 45 and 90 degrees, meant to demonstrate that the resolution enhancement has been made isotropic.

quency in the highest image order, which corresponds to 2 MHz sampling for a fourth-order image centered near 250 kHz. A 500 kHz analog anti-aliasing filter was used at the DAQ to ensure high-frequency noise was not mapped into the signal band. Simultaneously, an encoder signal on the SPIFI disk was recorded in order to track velocity fluctuations in the disk.

To mount the sample, we built a stage assembly affording both rotational and translational degrees of freedom. First, we mounted a clear-aperture motorized rotation stage (Newport, PR50CC) onto a motorized, 3-axis translation stage (Newport LTA motors in x,y, on an ASI z-stage). Secondly, a manual x-y translation stage with a clear aperture (Thorlabs, CXY1) was at-

tached to the rotation stage, and finally, the microscope slide was fixed to the top of this manual stage. The manual stage allowed us to center the feature of interest on or near the rotational axis of the PR50CC. Meanwhile, the 3-axis motorized stage was used to bring the object into focus, center the rotation stage to the illumination, and perform y-scanning of the object. The motorized rotation stage performed the sparse angular rotations of the object. However, because the PR50CC motor was not a high-precision microscope stage, each time the object was rotated, the object underwent transverse shift and defocus relative to the illumination pattern. The z-stage was used after each rotation to refocus the object before recording the y-scan. Transverse shifts were handled in post-processing.

8.2.4 Data Processing and Results

The processing performed on the ensemble of 1D signal vectors acquired at each (y, ϕ) position follows the procedure outlined in section 8.1. Next, for each rotation angle ϕ, the 2D (x, y) image data was interpolated from an asymmetric grid (2048 x 121 with grid spacing $\mathrm{d}x = 73$ nm and $\mathrm{d}y = 1\mu$m) onto a symmetric 2048 x 2048 grid with grid spacing $\mathrm{d}y = \mathrm{d}x = 73$ nm. Instead of deconvolving the line focus profile $P(y)$, a super-Gaussian filter was applied in the y-direction to square up the support while losing some of the natural support in y. However, we note that this lost information is recovered through the x support as it is rotated.

Figure 8.7 depicts the image reconstruction at a single angle $\phi = 0°$ for a pair of 15μm fluorescently shell-stained polystyrene spheres under two-photon illumination. The object reconstruction given by inverse Fourier transform of (8.13) displays finer resolution in x than y, as in previously reported MP-SPIFI data [51], but with superior SNR due to coherent combination of the individual image orders, q. The asymmetric frequency support formed by summation over the image orders q is depicted schematically in Figure 8.6(b).

Next, the $n-1$ subset of images corresponding to $\phi = 30$, 60, 90, 120, and 150 degrees were derotated to the same orientation as the first image at $\phi = 0°$ using Matlab's *imrotate* function. Each image in the derotated subset was transversely shifted to achieve coregistration with the first image, using a cross-correlation calculation followed by a sub-pixel shifting routine, in or-

der to counteract imperfections in the mechanical rotation of the stage during data acquisition. The n images were then coherently summed in the spatial frequency domain. A deconvolution filter H_ϕ was formed by taking the reciprocal of the sum of the rotated region of support formed by $G_y(f_{y0})\hat{P}(f_{y0})$, which in this initial demonstration we replaced with a super-Gaussian filter of order four with half-maximum at NA = 0.4. Pixel values below 0.01 in the super-Gaussian filter were replaced with infinity, so that the reciprocal produced zeros at those pixels. After multiplying H_ϕ by the summed object spatial frequency content, a final, radial super-Gaussian filter was applied with order two and a half-maximum at NA = 1.6. The shell-stained beads appear to be information-limited to about 1.6 NA, which is twice the NA of the objective lens. This filter served to limit noise in the reconstructed object, and can be considered part of H_ϕ in (8.16).

The results of our sparse-angle image synthesis are displayed in Fig. 8.8. In the left hand column, the Fourier magnitude and corresponding image at rotation angle $\phi = 90°$ are displayed. The Fourier space content has greater support in the f_y direction, and the resulting image shows resolution enhancement in the y direction. The center column displays the results of the sparse angle synthesis scheme presented here. The Fourier space magnitude how has equivalent support in all radial directions, and the corresponding image demonstrates isotropic resolution enhancement. The right hand column dissects this enhancement in more detail by examining lineouts along the $\phi = 0°$, $\phi = 45°$, and $\phi = 90°$ directions. The vertical lineout shows that the 1-angle and 6-angle image reconstructions resolve the fluorescent shell equally well, as expected by the large frequency support in the vertical direction in both cases. The horizontal lineout shows that the 6-angle reconstruction is resolving the adjacent shells in an a superior fashion due to the added support with rotation. Finally, the diagonal lineout is further demonstrating that the resolution enhancement has been made isotropic.

8.3 Conclusion

In this chapter we have demonstrated two important advances in the capabilities of multi-photon spatial frequency modulated imaging (MP-SPIFI). First, we have shown that the multi-image information given by the technique can be combined to render a single 1D line image

that has the dual benefits of the full super-resolving capability of the higher-order nonlinear projections and the superior SNR of the lower image orders. Secondly, we have demonstrated that a sparse angular rotation scheme combined with Cartesian line scanning generates a set of 2D images which can be coherently combined to produce a single image with the MP-SPIFI resolution enhancement occurring isotropically and uniformly throughout the field of view.

Author Contributions

K.A.W. developed the strategies for synthesizing image-order information into one composite image, and for extending the super-resolving capability from 1D to 2D. K.A.W. designed research, performed research, and analyzed data.

CHAPTER 9

SUMMARY AND FUTURE WORK

In this work, we have demonstrated a novel method for super-resolved imaging of microscopic specimens, which goes by the name of multiphoton spatial frequency modulated imaging (MP-SPIFI). MP-SPIFI uses the combination of a temporal sequence of spatial cosine illumination patterns, nonlinear optical excitation mechanisms, and single pixel integration of signal light in the far-field to produce image information with spatial frequency bandwidth exceeding the passband of the illumination system. This extra spatial frequency content in turn produces images with finer spatial detail than otherwise obtainable in a standard multiphoton laser-scanning microscope. Remarkably, this method works whether the excitation mechanism occurs through a real-state or a virtual-state energy transition. While myriad highly-developed super-resolution techniques already exist for real-state transitions, mostly for the case of fluorescence, the main implication of our work is that the suite of coherent nonlinear scattering mechanisms that are routinely probed in multiphoton microscopy, such as second-harmonic and third-harmonic generation and various forms of coherent Raman scattering, can now be deployed at enhanced spatial resolution in tandem with real-state transitions such as multiphoton fluorescence. This is an exciting development in the broad effort to establish imaging tools for interrogating biological specimens in a label-free manner.

With the advances presented in this work, MP-SPIFI is poised to make further headway in the field of multiphoton microscopy. One important step for MP-SPIFI microscopy will be extending the technique to nonlinear contrast mechanisms that provide both structural and chemical information about the specimen. Coherent Raman scattering microscopy techniques such as CARS and SRS provide this information, but these coherent nonlinear contrast mechanisms have not yet benefited from a super-resolution capability that is robust and worth the effort of adopting at scale. The chemical specificity of Raman vibrational modes is an important

means of exploiting native molecular contrast without resorting to fluorescent dyes or genetically expressed fluorescent proteins.

Many coherent Raman scattering contrast mechanisms use two-color excitation to selectively stimulate Raman vibrational modes in a given sample. To extend MP-SPIFI imaging to these contrast mechanisms, the microscope will need to be integrated with broadband or wavelength-tunable femtosecond pulsed laser sources such as optical parametric amplifiers (OPAs) or optical parametric oscillators (OPOs). These sources offer synchronized pulse trains at tunable pairs of center wavelength. However, these sources need to be tailored to the illumination requirements in MP-SPIFI in order to optimally generate coherent Raman signals. For example, the sources need to operate at repetition rates at or above approximately eight times the highest modulation rate generated in the MP-SPIFI modulation process (often, above 1 MHz) while also providing sufficient fluence in a line focus geometry such that nonlinear processes can be driven and detected without significant integration times.

Looking ahead, the future of label-free imaging will include imaging thick samples both *ex vivo* and *in vivo*. MP-SPIFI line focus illumination can be scanned axially through the sample to generate 3D images, as discussed in this work. However, clever ideas for gathering axial sample information without scanning would allow for faster image acquisition. For example, exploiting the holographic information that is available in the CHIRPT configuration and applying it to coherent nonlinear scattering mechanisms can provide a novel approach to gathering axial information without scanning. In this regard, the growing body of work in model-based image reconstruction, also known as inverse problems, can be harnessed to generate images in situations where the FFT algorithm has known limitations. While the FFT offers speed and ease of use, we have shown that experimental parameters such as motor speed or mask pattern centration have errors which lead to a violation of the assumptions involved in using the FFT, such as linear discretization of the transform variables. Numerical solutions based on minimum mean-squared error or maximum likelihood estimation and their myriad algorithmic implementations can provide a more flexible framework for image reconstruction. One poten-

tial tradeoff with these techniques is increased computational time and power. Nevertheless, there is vast room to explore various combinations of illumination patterns and model-based image reconstructions in order to extract 3D sample information and speed the advent of super-resolved imaging in thick samples.

Imaging thick samples should develop in tandem with scattering investigations. An important question to answer is, how well does the super-resolving mechanism of fringe projection perform in highly scattering samples? Robustness to scattering is one of the main reasons that people select multiphoton microscopy for imaging certain samples. It is encouraging that MP-SPIFI benefits from the same ballistic signal gating mechanism as standard MP-LSM microscopy, and does not rely on delicately prepared field polarization states for it's resolution enhancement mechanism. Initial examinations of SPIFI cosine illumination pattern formation through scattering media have begun in our laboratory for linear excitation, although we have not yet extended these to the multiphoton case. Should nonlinear fringe formation prove robust at multiple scattering lengths, MP-SPIFI would provide an interesting platform for extending super-resolution to thicker biological samples.

For those who have patiently read to the very end, I thank you for your interest, and hope that the time spent leads to new ideas in your own scientific journey.

BIBLIOGRAPHY

[1] Jean Livet, Tamily A. Weissman, Hyuno Kang, Ryan W. Draft, Ju Lu, Robyn A. Bennis, Joshua R. Sanes, and Jeff W. Lichtman. Transgenic strategies for combinatorial expression of fluorescent proteins in the nervous system. *Nature*, 450(7166):56–62, Nov 2007.

[2] Guy Cox and Colin J.R. Sheppard. Practical limits of resolution in confocal and non-linear microscopy. *Microscopy Research and Technique*, 63(1):18–22, 2004.

[3] T. Wilson. Resolution and optical sectioning in the confocal microscope. *Journal of Microscopy*, 244(2):113–121, 2011.

[4] M. G. L. Gustafsson. Surpassing the lateral resolution limit by a factor of two using structured illumination microscopy. *Journal of Microscopy*, 198(2):82–87, 2000.

[5] Stefan W Hell and Jan Wichmann. Breaking the diffraction resolution limit by stimulated emission: stimulated-emission-depletion fluorescence microscopy. *Opt. Lett.*, 19(11):780–782, 1994.

[6] Thomas A. Klar, Stefan Jakobs, Marcus Dyba, Alexander Egner, and Stefan W. Hell. Fluorescence microscopy with diffraction resolution barrier broken by stimulated emission. *Proceedings of the National Academy of Sciences*, 97(15):8206–8210, 2000.

[7] E Betzig. Proposed method for molecular optical imaging. *Opt. Lett.*, 20(3):237–239, 1995.

[8] Eric Betzig, George H Patterson, Rachid Sougrat, O Wolf Lindwasser, Scott Olenych, Juan S Bonifacino, Michael W Davidson, Jennifer Lippincott-Schwartz, and Harald F Hess. Imaging Intracellular Fluorescent Proteins at Nanometer Resolution. *Science*, 313(5793):1642–1645, 2006.

[9] Michael J Rust, Mark Bates, and Xiaowei Zhuang. Sub-diffraction-limit imaging by stochastic optical reconstruction microscopy (STORM). *Nat Meth*, 3(10):793–796, oct 2006.

[10] Utku Baran, Wan Qin, Xiaoli Qi, Goknur Kalkan, and Ruikang K. Wang. Oct-based label-free in vivo lymphangiography within human skin and areola. *Scientific Reports*, 6(1):21122, Feb 2016.

[11] YongKeun Park, Christian Depeursinge, and Gabriel Popescu. Quantitative phase imaging in biomedicine. *Nature Photonics*, 12(10):578–589, Oct 2018.

[12] Sixian You, Haohua Tu, Eric J. Chaney, Yi Sun, Youbo Zhao, Andrew J. Bower, Yuan-Zhi Liu, Marina Marjanovic, Saurabh Sinha, Yang Pu, and Stephen A. Boppart. Intravital imaging by simultaneous label-free autofluorescence-multiharmonic microscopy. *Nature Communications*, 9(1):2125, May 2018.

[13] Sixian You, Ronit Barkalifa, Eric J. Chaney, Haohua Tu, Jaena Park, Janet Elise Sorrells, Yi Sun, Yuan-Zhi Liu, Lin Yang, Danny Z. Chen, Marina Marjanovic, Saurabh Sinha, and Stephen A. Boppart. Label-free visualization and characterization of extracellular vesicles in breast cancer. *Proceedings of the National Academy of Sciences*, 116(48):24012–24018, 2019.

[14] Xiyi Chen, Oleg Nadiarynkh, Sergey Plotnikov, and Paul J. Campagnola. Second harmonic generation microscopy for quantitative analysis of collagen fibrillar structure. *Nature Protocols*, 7(4):654–669, Apr 2012.

[15] P J Campagnola and C.-Y. Dong. Second harmonic generation microscopy: principles and applications to disease diagnosis. *Laser & Photonics Reviews*, 5(1):13–26, 2011.

[16] Delphine Débarre, Willy Supatto, Ana-Maria Pena, Aurélie Fabre, Thierry Tordjmann, Laurent Combettes, Marie-Claire Schanne-Klein, and Emmanuel Beaurepaire. Imaging lipid bodies in cells and tissues using third-harmonic generation microscopy. *Nature Methods*, 3(1):47–53, Jan 2006.

[17] Chi Zhang and Ji-Xin Cheng. Perspective: Coherent raman scattering microscopy, the future is bright. *APL Photonics*, 3(9):090901, 2018.

[18] J.X. Cheng and X.S. Xie. *Coherent Raman Scattering Microscopy*. Series in Cellular and Clinical Imaging. CRC Press, 2016.

[19] Stephen A. Boppart, Sixian You, Lianhuang Li, Jianxin Chen, and Haohua Tu. Simultaneous label-free autofluorescence-multiharmonic microscopy and beyond. *APL Photonics*, 4(10):100901, 2019.

[20] Yi Sun, Sixian You, Haohua Tu, Darold R. Spillman, Eric J. Chaney, Marina Marjanovic, Joanne Li, Ronit Barkalifa, Jianfeng Wang, Anna M. Higham, Natasha N. Luckey, Kimberly A. Cradock, Z. George Liu, and Stephen A. Boppart. Intraoperative visualization of the tumor microenvironment and quantification of extracellular vesicles by label-free nonlinear imaging. *Science Advances*, 4(12):eaau5603, 2018.

[21] Andrew K Dunn, Vincent P Wallace, Mariah Coleno, Michael W Berns, and Bruce J Tromberg. Influence of optical properties on two-photon fluorescence imaging in turbid samples. *Appl. Opt.*, 39(7):1194–1201, 2000.

[22] W Denk, J H Strickler, and W W Webb. Two-photon laser scanning fluorescence microscopy. *Science*, 248(4951):73–76, 1990.

[23] Demirhan Kobat, Michael E Durst, Nozomi Nishimura, Angela W Wong, Chris B Schaffer, and Chris Xu. Deep tissue multiphoton microscopy using longer wavelength excitation. *Opt. Express*, 17(16):13354–13364, 2009.

[24] Dimitre G. Ouzounov, Tianyu Wang, Mengran Wang, Danielle D. Feng, Nicholas G. Horton, Jean C. Cruz-Hernández, Yu-Ting Cheng, Jacob Reimer, Andreas S. Tolias, Nozomi Nishimura, and Chris Xu. In vivo three-photon imaging of activity of gcamp6-labeled neurons deep in intact mouse brain. *Nature Methods*, 14(4):388–390, Apr 2017.

[25] Gael Moneron and Stefan W. Hell. Two-photon excitation sted microscopy. *Opt. Express*, 17(17):14567–14573, Aug 2009.

[26] Maria Ingaramo, Andrew G. York, Peter Wawrzusin, Oleg Milberg, Amy Hong, Roberto Weigert, Hari Shroff, and George H. Patterson. Two-photon excitation improves multifocal structured illumination microscopy in thick scattering tissue. *Proceedings of the National Academy of Sciences*, 111(14):5254–5259, 2014.

[27] Peter W. Winter, Andrew G. York, Damian Dalle Nogare, Maria Ingaramo, Ryan Christensen, Ajay Chitnis, George H. Patterson, and Hari Shroff. Two-photon instant structured illumination microscopy improves the depth penetration of super-resolution imaging in thick scattering samples. *Optica*, 1(3):181–191, Sep 2014.

[28] Omid Masihzadeh, Philip Schlup, and Randy A Bartels. Enhanced spatial resolution in third-harmonic microscopy through polarization switching. *Opt. Lett.*, 34(8):1240–1242, 2009.

[29] Jing Liu, Il-Hoon Cho, Yi Cui, and Joseph Irudayaraj. Second Harmonic Super-resolution Microscopy for Quantification of mRNA at Single Copy Sensitivity. *ACS Nano*, 8(12):12418–12427, 2014.

[30] Mikko J Huttunen, Aazad Abbas, Jeremy Upham, and Robert W Boyd. Label-free super-resolution with coherent nonlinear structured-illumination microscopy. *J Opt*, 19(8):085504, 2017.

[31] E. Abbe. Beiträge zur theorie des mikroskops und der mikroskopischen wahrnehmung. *Archiv für Mikroskopische Anatomie*, 9(1):413–468, Dec 1873.

[32] H. Volkmann. Ernst abbe and his work. *Applied Optics*, 5:1720–1731, Nov 1966.

[33] Barry R. Masters. Ernst abbe and the foundation of scientific microscopes. *Opt. Photon. News*, 18(2):18–23, Feb 2007.

[34] S W Hell and M Kroug. Ground-state-depletion fluorscence microscopy: A concept for breaking the diffraction resolution limit. *Applied Physics B*, 60(5):495–497, 1995.

[35] Mats G L Gustafsson. Nonlinear structured-illumination microscopy: Wide-field fluorescence imaging with theoretically unlimited resolution. *Proc. Nat. Acad. Sci.*, 102(37):13081–13086, 2005.

[36] Stefan Bretschneider, Christian Eggeling, and Stefan W. Hell. Breaking the diffraction barrier in fluorescence microscopy by optical shelving. *Phys. Rev. Lett.*, 98:218103, May 2007.

[37] Robert D. Guenther. *Modern Optics*. John Wiley & Sons, 1990.

[38] L Novotny and B Hecht. *Principles of Nano-Optics*. Cambridge University Press, 2nd edition, 2012.

[39] Leonard Mandel and Emil Wolf. *Optical Coherence and Quantum Optics*. Cambridge University Press, 1995.

[40] Jerome Mertz. *Introduction to Optical Microscopy*. Cambridge University Press, 2nd edition, 2019.

[41] Joseph Goodman. *Introduction to Fourier Optics*. Roberts & Company, 3rd edition, 2004.

[42] Arnold Sommerfeld. *Optics: Lectures on Theoretical Physics, Vol. IV*. Academic Press, Inc., 1st paperback edition, 1964. Translated by Otto Laporte and Peter Moldauer.

[43] E. Wolf. Electromagnetic diffraction in optical systems. i. an integral representation of the image field. *Proceedings of the Royal Society of London. Series A, Mathematical and Physical Sciences*, 253(1274):349–357, 1959.

[44] B. Richards and E. Wolf. Electromagnetic diffraction in optical systems. ii. structure of the image field in an aplanatic system. *Proceedings of the Royal Society of London. Series A, Mathematical and Physical Sciences*, 253(1274):358–379, 1959.

[45] Emil Wolf and Yajun Li. Conditions for the validity of the debye integral representation of focused fields. *Optics Communications*, 39(4):205–210, 1981.

[46] M Born and E Wolf. *Principles of Optics: Electromagnetic Theory of Propagation, Interference and Diffraction of Light*. Cambridge University Press, 7th edition, 1999.

[47] Jakob J. Stamnes and Bjørn Spjelkavik. Focusing at small angular apertures in the debye and kirchhoff approximations. *Optics Communications*, 40(2):81–85, 1981.

[48] Ernst Abbe Hon. Vii.—on the estimation of aperture in the microscope. *Journal of the Royal Microscopical Society*, 1(3):388–423, 1881.

[49] Masud Mansuripur. Abbe's sine condition. *Opt. Photon. News*, 9(2):56–60, Feb 1998.

[50] Patrick A. Stockton, Jeffrey J. Field, Jeff Squier, Ali Pezeshki, and Randy A. Bartels. Single-pixel fluorescent diffraction tomography. *Optica*, 7(11):1617–1620, Nov 2020.

[51] Jeffrey J. Field, Keith A. Wernsing, Scott R. Domingue, Alyssa M. Allende Motz, Keith F. DeLuca, Dean H. Levi, Jennifer G. DeLuca, Michael D. Young, Jeff A. Squier, and Randy A. Bartels. Superresolved multiphoton microscopy with spatial frequency-modulated imaging. *Proceedings of the National Academy of Sciences*, 113(24):6605–6610, 2016.

[52] James Cooley and John Tukey. An algorithm for the machine calculation of complex Fourier series. *Math. Comp.*, (19):297–301, 1965.

[53] Greg Futia, Philip Schlup, David G Winters, and Randy A Bartels. Spatially-chirped modulation imaging of absorption and fluorescent objects onsingle-element optical detector. *Opt. Express*, 19(2):1626–1640, 2011.

[54] Eric D Diebold, Brandon W Buckley, Daniel R Gossett, and Bahram Jalali. Digitally synthesized beat frequency multiplexing for sub-millisecond fluorescence microscopy. *Nat Photon*, 7(10):806–810, 2013.

[55] Scott S Howard, Adam Straub, Nicholas G Horton, Demirhan Kobat, and Chris Xu. Frequency-multiplexed in vivo multiphoton phosphorescence lifetime microscopy. *Nat Photon*, 7(1):33–37, 2013.

[56] Jesse W. Wilson and Randy A. Bartels. Rapid birefringent delay scanning for coherent multiphoton impulsive raman pump–probe spectroscopy. *IEEE Journal of Selected Topics in Quantum Electronics*, 18(1):130–139, Jan 2012.

[57] David G. Winters and Randy A. Bartels. Two-dimensional single-pixel imaging by cascaded orthogonal line spatial modulation. *Opt. Lett.*, 40(12):2774–2777, Jun 2015.

[58] Jeffrey J Field, David G Winters, and Randy A Bartels. Plane wave analysis of coherent holographic image reconstruction by phase transfer (CHIRPT). *Journal of the Optical Society of America A*, 32(11):2156–2168, 2015.

[59] Jeffrey S. Sanders, Ronald G. Driggers, Carl E. Halford, and Steven T. Griffin. Imaging with frequency-modulated reticles. *Optical Engineering*, 30(11):1720 – 1724, 1991.

[60] D.J. Lovell. Electro-optical position indicator system, 1961. US Patent 2,997,699.

[61] Zibang Zhang, Xueying Wang, Guoan Zheng, and Jingang Zhong. Hadamard single-pixel imaging versus fourier single-pixel imaging. *Opt. Express*, 25(16):19619–19639, Aug 2017.

[62] Keith A. Wernsing, Jeffrey J. Field, Scott R. Domingue, Alyssa M. Allende-Motz, Keith F. DeLuca, Dean H. Levi, Jennifer G. DeLuca, Michael D. Young, Jeff A. Squier, and Randy A. Bartels. Point spread function engineering with multiphoton SPIFI. In Thomas G. Brown, Carol J. Cogswell, and Tony Wilson, editors, *Three-Dimensional and Multidimensional Microscopy: Image Acquisition and Processing XXIII*, volume 9713, pages 17 – 26. International Society for Optics and Photonics, SPIE, 2016.

[63] Rainer Heintzmann and Mats G L Gustafsson. Subdiffraction resolution in continuous samples. *Nat Photon*, 3(7):362–364, 2009.

[64] Jeffrey J. Field, Keith A. Wernsing, Jeff A. Squier, and Randy A. Bartels. Three-dimensional single-pixel imaging of incoherent light with spatiotemporally modulated illumination. *J. Opt. Soc. Am. A*, 35(8):1438–1449, Aug 2018.

[65] Jeffrey J Field, David G Winters, and Randy A Bartels. Single pixel fluorescent imaging with temporally labeled illumination patterns. *Optica*, 3(9):971–974, 2016.

[66] Daniel J Higley, David G Winters, Gregory L Futia, and Randy A Bartels. Theory of diffraction effects in spatial frequency-modulated imaging. *J. Opt. Soc. Am. A*, 29(12):2579–2590, 2012.

[67] Scott R Domingue and Randy A Bartels. Nonlinear fiber amplifier with tunable transform limited pulse duration from a few 100 to sub-100-fs at watt-level powers. *Opt. Lett.*, 39(2):359–362, 2014.

[68] Zhanwei Liu, Zachary M. Ziegler, Logan G. Wright, and Frank W. Wise. Megawatt peak power from a mamyshev oscillator. *Optica*, 4(6):649–654, Jun 2017.

[69] Pavel Sidorenko, Walter Fu, and Frank Wise. Nonlinear ultrafast fiber amplifiers beyond the gain-narrowing limit. *Optica*, 6(10):1328–1333, Oct 2019.

[70] Scott R. Domingue and Randy A. Bartels. Overcoming temporal polarization instabilities from the latent birefringence in all-normal dispersion, wave-breaking-extended nonlinear fiber supercontinuum generation. *Opt. Express*, 21(11):13305–13321, Jun 2013.

[71] Andy Chong, Joel Buckley, Will Renninger, and Frank Wise. All-normal-dispersion femtosecond fiber laser. *Opt. Express*, 14(21):10095–10100, 2006.

[72] K. Kieu, W. H. Renninger, A. Chong, and F. W. Wise. Sub-100 fs pulses at watt-level powers from a dissipative-soliton fiber laser. *Opt. Lett.*, 34(5):593–595, Mar 2009.

[73] M. E. Fermann, V. I. Kruglov, B. C. Thomsen, J. M. Dudley, and J. D. Harvey. Self-similar propagation and amplification of parabolic pulses in optical fibers. *Phys. Rev. Lett.*, 84:6010–6013, Jun 2000.

[74] Christophe Finot, John M. Dudley, Bertrand Kibler, David J. Richardson, and Guy Millot. Optical parabolic pulse generation and applications. *IEEE Journal of Quantum Electronics*, 45(11):1482–1489, 2009.

[75] V. I. Kruglov, A. C. Peacock, J. D. Harvey, and J. M. Dudley. Self-similar propagation of parabolic pulses in normal-dispersion fiber amplifiers. *J. Opt. Soc. Am. B*, 19(3):461–469, Mar 2002.

[76] Vladimir I. Kruglov and John D. Harvey. Asymptotically exact parabolic solutions of the generalized nonlinear schrödinger equation with varying parameters. *J. Opt. Soc. Am. B*, 23(12):2541–2550, Dec 2006.

[77] Rudiger Paschotta, Johan Nilsson, Anne C Tropper, and David C Hanna. Ytterbium-doped fiber amplifiers. *IEEE J. Quantum Electron*, 33(7):1049–1056, jul 1997.

[78] Chenfei Hu, Jeffrey J. Field, Varun Kelkar, Benny Chiang, Keith Wernsing, Kimani C. Toussaint, Randy A. Bartels, and Gabriel Popescu. Harmonic optical tomography of nonlinear structures. *Nature Photonics*, 14(9):564–569, Sep 2020.

[79] John M. Dudley, Goëry Genty, and Stéphane Coen. Supercontinuum generation in photonic crystal fiber. *Rev. Mod. Phys.*, 78:1135–1184, Oct 2006.

[80] Alexander M. Heidt, James S. Feehan, Jonathan H. V. Price, and Thomas Feurer. Limits of coherent supercontinuum generation in normal dispersion fibers. *J. Opt. Soc. Am. B*, 34(4):764–775, Apr 2017.

[81] Jan Schulte, Thomas Sartorius, Johannes Weitenberg, Andreas Vernaleken, and Peter Russbueldt. Nonlinear pulse compression in a multi-pass cell. *Opt. Lett.*, 41(19):4511–4514, Oct 2016.

[82] Kilian Fritsch, Markus Poetzlberger, Vladimir Pervak, Jonathan Brons, and Oleg Pronin. All-solid-state multipass spectral broadening to sub-20 fs. *Opt. Lett.*, 43(19):4643–4646, Oct 2018.

[83] Chih-Hsuan Lu, Yu-Jung Tsou, Hong-Yu Chen, Bo-Han Chen, Yu-Chen Cheng, Shang-Da Yang, Ming-Chang Chen, Chia-Chen Hsu, and A. H. Kung. Generation of intense supercontinuum in condensed media. *Optica*, 1(6):400–406, Dec 2014.

[84] Chih-Hsuan Lu, Tobias Witting, Anton Husakou, Marc J.J. Vrakking, A. H. Kung, and Federico J. Furch. Sub-4 fs laser pulses at high average power and high repetition rate from an all-solid-state setup. *Opt. Express*, 26(7):8941–8956, Apr 2018.

[85] Marcus Seidel, Gunnar Arisholm, Jonathan Brons, Vladimir Pervak, and Oleg Pronin. All solid-state spectral broadening: an average and peak power scalable method for compression of ultrashort pulses. *Opt. Express*, 24(9):9412–9428, May 2016.

[86] K. F. Mak, M. Seidel, O. Pronin, M. H. Frosz, A. Abdolvand, V. Pervak, A. Apolonski, F. Krausz, J. C. Travers, and P. St. J. Russell. Compressing μj-level pulses from 250 fs to sub-10 fs at 38-mhz repetition rate using two gas-filled hollow-core photonic crystal fiber stages. *Opt. Lett.*, 40(7):1238–1241, Apr 2015.

[87] Yuan Liu, Haohua Tu, and Stephen A. Boppart. Wave-breaking-extended fiber supercontinuum generation for high compression ratio transform-limited pulse compression. *Opt. Lett.*, 37(12):2172–2174, Jun 2012.

[88] S. R. Domingue and R. A. Bartels. Nearly transform-limited sub-20-fs pulses at 1065 nm and >10 nj enabled by a flat field ultrafast pulse shaper. *Opt. Lett.*, 40(2):253–256, Jan 2015.

[89] K. L. Corwin, N. R. Newbury, J. M. Dudley, S. Coen, S. A. Diddams, K. Weber, and R. S. Windeler. Fundamental noise limitations to supercontinuum generation in microstructure fiber. *Phys. Rev. Lett.*, 90:113904, Mar 2003.

[90] Zhaoming Zhu and Thomas G. Brown. Effect of frequency chirping on supercontinuum generation in photonic crystal fibers. *Opt. Express*, 12(4):689–694, Feb 2004.

[91] Valdas Sirutkaitis Julius Vengelis, Vygandas Jarutis. Extension of supercontinuum spectrum, generated in polarization-maintaining photonic crystal fiber, using chirped femtosecond pulses. *Optical Engineering*, 57(1):016102–1 – 016102–10, 2018.

[92] Haohua Tu, Yuan Liu, Xiaomin Liu, Dmitry Turchinovich, Jesper Lægsgaard, and Stephen A. Boppart. Nonlinear polarization dynamics in a weakly birefringent all-normal dispersion photonic crystal fiber: toward a practical coherent fiber supercontinuum laser. *Opt. Express*, 20(2):1113–1128, Jan 2012.

[93] Selcuk Akturk, Xun Gu, Mark Kimmel, and Rick Trebino. Extremely simple single-prism ultrashort-pulse compressor. *Opt. Express*, 14(21):10101–10108, Oct 2006.

[94] K. J. Blow and D. Wood. Theoretical description of transient stimulated raman scattering in optical fibers. *IEEE Journal of Quantum Electronics*, 25(12):2665–2673, Dec 1989.

[95] Ilaria Cristiani, Riccardo Tediosi, Luca Tartara, and Vittorio Degiorgio. Dispersive wave generation by solitons in microstructured optical fibers. *Opt. Express*, 12(1):124–135, Jan 2004.

[96] Govind P. Agrawal. *Nonlinear Fiber Optics (Fourth Edition)*. Academic Press, fourth edition edition, 2006.

[97] Sonia Boscolo, Frederic Chaussard, Esben Andresen, Hervé Rigneault, and Christophe Finot. Impact of initial pulse shape on the nonlinear spectral compression in optical fibre. *Optics & Laser Technology*, 99:301 – 309, 2018.

[98] Etienne Genier, Patrick Bowen, Thibaut Sylvestre, John M. Dudley, Peter Moselund, and Ole Bang. Amplitude noise and coherence degradation of femtosecond supercontinuum generation in all-normal-dispersion fibers. *J. Opt. Soc. Am. B*, 36(2):A161–A167, Feb 2019.

[99] Jeffrey J. Field, Keith A. Wernsing, Jeff A. Squier, and Randy A. Bartels. Toward deep-tissue super-resolution microscopy. *Opt. Photon. News*, 27(12):40–40, Dec 2016.

[100] Warren R. Zipfel, Rebecca M. Williams, and Watt W. Webb. Nonlinear magic: multiphoton microscopy in the biosciences. *Nature Biotechnology*, 21(11):1369–1377, Nov 2003.

[101] Jeffrey J. Field and Randy A. Bartels. Digital aberration correction of fluorescent images with coherent holographic image reconstruction by phase transfer (CHIRPT). In Thomas G. Brown, Carol J. Cogswell, and Tony Wilson, editors, *Three-Dimensional and Multidimensional Microscopy: Image Acquisition and Processing XXIII*, volume 9713, pages 61 – 68. International Society for Optics and Photonics, SPIE, 2016.

[102] Yudi Pawitan. *In All Likelihood: Statistical Modelling and Inference Using Likelihood*. Oxford University Press; 1st edition, 2001.

[103] Philip Schlup, Greg Futia, and Randy A Bartels. Lateral tomographic spatial frequency modulated imaging. *Applied Physics Letters*, 98(21):211115, 2011.

[104] Huttunen M.J. and A. Kiviniemi. Nonlinear label-free super-resolution microscopy using structured illumination. In Astratov V., editor, *Label-Free Super-Resolution Microscopy. Biological and Medical Physics, Biomedical Engineering*, pages 289–312. Springer, Cham, 2019.

[105] Nathan Worts, John Czerski, Jason Jones, Jeffrey J. Field, Randy Bartels, and Jeff Squier. Simultaneous multi-dimensional spatial frequency modulation imaging. *International Journal of Optomechatronics*, 14(1):1–17, 2020.

[106] Patrick A. Stockton, Keith A. Wernsing, Jeffrey J. Field, Jeff Squier, and Randy A. Bartels. Fourier computed tomographic imaging of two dimensional fluorescent objects. *APL Photonics*, 4(10):106102, 2019.

APPENDIX A

NOTATION

A guide to the reader is provided for the symbolic notation used in this work. The main body of this work details electric field behavior in a microscope. The symbols used in that description are detailed here. In some cases, symbols may have a dual use found in Ch. 5, where effort was made to match the standard notation in the field of ultrafast lasers.

Table A.1: Notation used to describe general propagation and manipulation of electromagnetic waves, predominantly derived or explained in Ch. 2. Symbols are listed in order of appearance in Ch. 2.

Symbol	SI Units	Meaning
E	V/m	Electric field
H	A/m	Magnetic field
D	C/m^2	Electric flux density
B	N/(A·m)	Magnetic flux density
ϵ_0	C/(V·m)	Dielectric permittivity of vacuum
μ_0	N / A^2	Magnetic permeability of vacuum
P	C/m^2	Material Polarization
M	A/m	Material Magnetization
J	A/m^2	Electric current density
σ	A/(V·m)	Material Conductivity
n	-	Index of refraction
c	m/s	Speed of light in vacuum
E	V/m	Complex electric field distribution
k	rad./m	Angular spatial frequency (wavenumber)
ω	rad./s	Angular temporal frequency
$\mathbf{S}$	W/m^2	Poynting vector
I	W/m^2	Optical intensity
$\mathcal{F}$	-	Fourier Transform
$\mathcal{H}$	-	Angular Spectrum (Fresnel) Propagator
$f_\perp$	1/m	Transverse spatial frequency

Table A.2: Table of selected Greek alphabetical symbols used to describe electric field behavior in a SPIFI microscope used in this work.

Symbol	Meaning
α_k	k^{th} rate parameter in a Poisson random process
α_r	Regularization parameter
β	Optical signal light
Δ_k	Proportionality constant relating printed number of cycles to radial position on mask
η	Order of nonlinear interaction light
θ	Polar angle in spherical coordinate system
θ_j	Mask diffraction angle for j^{th} order
κ	Proportionality constant relating temporal modulation rate to radial position on mask
λ	Wavelength
ν	Temporal frequency
ν_r	Mask rotation frequency
Π	Rectangle 'Boxcar' Function
ρ	Radius in cylidrical coordinate system
φ	Azimuthal angle in cylindrical coordinate system
ϕ	Azimuthal angle in polar or spherical-polar coordinate systems
ϕ_a	Aberration phase error
Φ	Temporal phase error due to modulator
ξ	transverse linear polarization angle relative to $\hat{x}$
Ω	Solid angle

Table A.3: Table of selected English alphabetical symbols used to describe electric field behavior in a SPIFI microscope used in this work.

Symbol	Meaning
a_j	Amplitude of j^{th} diffracted order
C	Specimen spatial contrast distribution
f_{g_x}	Horizontal grating spatial frequency on the mask
f_{g_y}	Vertical grating spatial frequency on the mask
G	Wiener filter
H_q	SPIFI 1D transfer function at the q^{th} sideband
H_Σ	Composite 1D OTF
j	Index for diffracted orders from SPIFI modulator
m	Mask function
M	Magnification
NA	Numerical Aperture
OTF	Optical transfer function
p	Electric field spatial profile component
P	Intensity spatial profile component
$\mathcal{P}$	Pupil spatial distribution
PSF	Point spread function
q	Index for harmonics of SPIFI center modulation frequency
S	Signal produced by integration at single pixel detector
u_j	Relaxed pupil gating function for jth diffracted order
v	Electric field plane wave component
V	Intensity plane wave component
w	Gaussian beam radius